

FLORIDA STATE UNIVERSITY  
COLLEGE OF ARTS AND SCIENCE

THE PHOTOPRODUCTION OF STRANGENESS IN  $\gamma P \rightarrow \Lambda K^+ \pi^+ \pi^-$  WITH CLAS AT  
JEFFERSON LAB

By  
HUSSEIN AL GHOUL

A Dissertation submitted to the  
Department of Physics  
in partial fulfillment of the  
requirements for the degree of  
Doctor of Philosophy

2016

Hussein Al Ghouh defended this dissertation on April 12, 2016.  
The members of the supervisory committee were:

Paul Eugenio  
Professor Directing Dissertation

James Justus  
University Representative

Volker Crede  
Committee Member

Simon Capstick  
Committee Member

Alexander Ostrovidov  
Committee Member

Horst Wahl  
Committee Member

The Graduate School has verified and approved the above-named committee members, and certifies that the dissertation has been approved in accordance with university requirements.

To my family

# ACKNOWLEDGMENTS

لا حسب كالتواضع و لا شرف كالعلم

The quote above is an Arabic proverb and it translates to: **”There is no virtue higher than humility, and there is no honor higher than knowledge”**.

My journey in graduate school started in the summer of 2010 when I left Lebanon to the United States. As I waved goodbye to my family, my father took me to the side and told me to remember the quote above. It has since never left my mind. Over five years later, I now find myself finishing up my thesis, cleaning out my desk, and getting ready to say goodbye to my wonderful family at the physics department here at FSU, without whom none of this could have been possible. From family to friends and teachers, this journey would have not been successful without you. I thank you.

This work was by no means a one man’s job. There is a number of people who have contributed and helped in the execution of the analysis and have offered much appreciated insight and assistance. A special thank you to the scientists and graduate students in the g12 run group for their feedback and comments. From the very first stages of this analysis, the group, initially led by Dennis Weygand, were very helpful with their productive feedback and encouragement. To Johann, MK, Rafael and Will for being very helpful and providing me with the necessary tools to perform this analysis successfully. Also a big thank you to the GlueX collaboration members for guiding me during my stay at Jefferson lab. I would have been much less productive without the assistance of Mark Ito, Beni Zihlmann, Michael Staib, and other members of the Hall D staff and engineers. Constructing the Time of Flight was the most thrilling and fulfilling thing I’ve done in graduate school, and it would have not been such a rewarding experience without the help and guidance of the GlueX collaboration members and their patience with me. I would also like to thank members of the hadronic physics group at FSU especially Dr. Alexander Ostrovidov, Mukesh, and Aristeidis, for giving me advice and allowing me to annoy them with my questions. Also thank you to Dr. Volker Crede for his input on my research, and his students Priya, Chris and Zulkaida for our numerous physics discussions and casual office talks.

All the things I learned in graduate school were the fruit of my relationship with my advisor Dr. Paul Eugenio. He is a wonderful teacher who puts his students' interest in front of his, thus making sure they get all the help they need. Paul, you have been very generous with your time and funding, giving me advice when I would ask for help and sending me to numerous conferences and workshops. Your company has extensively benefited me on an academic level and a personal level. I will be the researcher I strive to become one day because of your guidance and support. Thank you.

To my parents, Amenah and Mohammad. The two most influential people in my life. They sacrificed a lot so my siblings and I would become the people we are right now. Through all the hardships that we went through as a family, they always provided a warm home for me to grow into the man I am right now. Dad, you invested a lot into my future and I can not thank you enough. You told me multiple times that the one thing no one can take away from us is knowledge, and today I wholeheartedly believe that I have made you proud. I wouldn't be the man I am right now without your constant support and love. Mom, your unconditional and limitless love for me is what keeps me going. Your pride in me will always be my greatest reward.

To my sister Zahra, thank you for making the first few years in graduate school easier for me and for giving me advice on how to proceed. I owe my success to your constant encouragement and belief in me. I keep looking up to you and I strive to become the scientist and teacher that you are right now. You are not just my sister, but also my friend and teacher.

To my siblings Zeinab, Hassan, fatima and Iman, thank you for the numerous joyful phone calls and skype sessions over the weekends. You made sure I did not feel the distance between us by always talking to me and letting me know that you are there for me.

To my new family, the Wakils, Bassam, Gwyn and Brandon, thank you for taking me in as a member of your family. You have given me a home away from home, and have been in every step of my journey in graduate school. I am grateful to have met you and I strive to keep making you proud of me.

Last but not least, a big thank you to my wonderful wife, Samantha, without whom I would not have gotten so far. Samantha, you are the reason I am here right now. I am so thankful that we have found each other. Your ambitious and hard working nature is inspirational and it is you who inspires every decision I make. I love you.

# TABLE OF CONTENTS

List of Tables . . . . .	ix
List of Figures . . . . .	x
List of Acronyms . . . . .	xviii
Abstract . . . . .	xix
<b>1 INTRODUCTION</b>	<b>1</b>
1.1 The Standard Model . . . . .	3
1.2 Quantum Chromodynamics . . . . .	4
1.3 The Constituent Quark Model . . . . .	8
1.4 Strange Mesons . . . . .	15
1.5 Also In This Document . . . . .	21
<b>2 EXPERIMENTAL SETUP</b>	<b>22</b>
2.1 The CEBAF Accelerator . . . . .	23
2.2 Hall B Photon Tagger . . . . .	24
2.3 Experimental Target . . . . .	26
2.4 The CLAS Detector . . . . .	27
2.4.1 Start Counter . . . . .	28
2.4.2 Superconducting Toroidal Magnet . . . . .	29
2.4.3 Drift Chambers . . . . .	30
2.4.4 Time of Flight . . . . .	32
2.4.5 Čerenkov Counter . . . . .	33
2.4.6 Event Trigger and Data Acquisition . . . . .	34
2.4.7 Event Reconstruction . . . . .	35
<b>3 DATA ANALYSIS</b>	<b>39</b>
3.1 Exclusive $\gamma p \rightarrow pK^+\pi^+\pi^-[\pi^-]$ Event Selection . . . . .	39
3.1.1 Kinematic Corrections . . . . .	39
3.1.2 Event Vertex and Timing Cuts . . . . .	41
3.1.3 Beta Cuts . . . . .	43
3.1.4 Beam Energy . . . . .	44
3.1.5 Kinematic Fitting . . . . .	45
3.2 Final Event Selection . . . . .	48
3.2.1 $\Lambda \rightarrow p\pi^-$ Selection . . . . .	49
3.2.2 Baryon Background Reduction . . . . .	52
3.2.3 Eliminating Particle Misidentification . . . . .	53
3.2.4 Momentum Transfer Cut . . . . .	56
3.3 Features of the Final $\gamma p \rightarrow \Lambda K^+\pi^+\pi^-$ Sample . . . . .	59

<b>4</b>	<b>PARTIAL WAVE ANALYSIS FORMALISM</b>	<b>64</b>
4.1	Introduction . . . . .	64
4.2	Decay Amplitudes . . . . .	69
4.3	Production Amplitudes . . . . .	72
4.4	Summary . . . . .	76
<b>5</b>	<b>PARTIAL WAVE ANALYSIS PROCEDURE AND RESULTS</b>	<b>77</b>
5.1	Experimental Acceptance . . . . .	77
5.2	Fitting Procedure . . . . .	87
5.2.1	The FSU PWA Toolkit . . . . .	87
5.2.2	Preparation of the $\gamma p \rightarrow \Lambda K^+ \pi^+ \pi^-$ Dataset . . . . .	89
5.2.3	Minimization of The Likelihood Function and Error Estimation . . . . .	89
5.2.4	Wave Selection . . . . .	93
5.2.5	Fit Quality . . . . .	98
5.3	Fit Results . . . . .	99
5.3.1	The Total Intensity . . . . .	99
5.3.2	$1^+S$ Waves . . . . .	100
5.3.3	$1^-P$ Waves . . . . .	105
5.3.4	$2^+D$ Waves . . . . .	108
5.3.5	$2^-S$ Waves . . . . .	109
5.3.6	Predicted Distributions . . . . .	112
<b>6</b>	<b>SUMMARY</b>	<b>118</b>
<b>Appendix</b>		
<b>A</b>	<b>EXTENDED PWA RESULTS</b>	<b>120</b>
A.1	PWA Fit with $0^-S$ waves . . . . .	120
A.1.1	$1^+S$ Waves . . . . .	121
A.1.2	$1^-P$ Waves . . . . .	122
A.1.3	$2^+D$ Waves . . . . .	123
A.1.4	Predicted Distributions . . . . .	124
A.2	PWA Fit with 50 MeV Bins . . . . .	127
A.2.1	$1^+S$ Waves . . . . .	128
A.2.2	$1^-P$ Waves . . . . .	129
A.2.3	$2^+D$ Waves . . . . .	130
A.2.4	Predicted Distributions . . . . .	131
<b>B</b>	<b>THE GLUEX EXPERIMENT</b>	<b>134</b>
B.1	The 12 GeV Upgrade . . . . .	134
B.2	The GlueX Detector . . . . .	135
B.3	The Time of Flight Detector . . . . .	137
<b>C</b>	<b>DETACHED VERTEX SIMULATION</b>	<b>142</b>
<b>D</b>	<b>THE K-MATRIX FORMALISM</b>	<b>145</b>
<b>E</b>	<b>WIGNER-D FUNCTIONS</b>	<b>149</b>

**F CLEBSCH-GORDAN COEFFICIENTS** **151**

References . . . . . 153

Biographical Sketch . . . . . 157

# LIST OF TABLES

1.1	Parameters in the standard model. . . . .	4
1.2	The quantum numbers of light quarks. . . . .	10
1.3	The quantum numbers of light quarks. . . . .	13
1.4	A compilation of all the strange mesons with masses between 1 GeV and 2 GeV as reported by Reference[16]. <b>States in red are ones that have been observed in photoproduction experiments.</b> The significantly high volume of states that still await confirmation is noticeable . . . . .	18
3.1	A summary of the event counts before and after each cut used to select the final sample $\gamma p \rightarrow \Lambda K^+ \pi^+ \pi^-$ events for PWA. . . . .	62
5.1	The full set of isobars considered to contribute to the invariant mass distributions of $K^+ \pi^-$ and $\pi^+ \pi^-$ subsystems. Isobars that were present in our data, and were essential for the success of the PWA, are marked in red. . . . .	94
5.2	The full set of waves expected to contribute in the partial wave analysis. Waves in red correspond to the ones that we included in the final fit where the best results were obtained. The check marks indicate the region where a wave is included in the partial wave analysis. Keep in mind that except for the flat background, every wave has two reflectivities. . . . .	97
6.1	Summary of the resonant structures observed in the partial waves, along with any possible states that could account for them. . . . .	119
A.1	The full set of waves included in this partial wave analysis. The check marks indicate the region where a wave is included in the partial wave analysis. Keep in mind that except for the flat background, every wave has two reflectivities. . . . .	120
A.2	The full set of waves included in this partial wave analysis. The check marks indicate the region where a wave is included in the partial wave analysis. Keep in mind that except for the flat background, every wave has two reflectivities. . . . .	127

# LIST OF FIGURES

1.1	An infographic of the standard model of particle physics, including the recently discovered Higgs boson. (Courtesy of CERN Webfest) . . . . .	2
1.2	Experimentally measured values of the coupling $\alpha_s$ from various experiments confirming the theoretically expected behavior at high energies. [16] . . . . .	7
1.3	An illustration of the quark antiquark pair in a potential. The quark has a spin $\vec{s}_1$ and the antiquark has a spin $\vec{s}_2$ and they couple together with an angular momentum $\vec{l}$ . Image source [12] . . . . .	11
1.4	Illustration of the SU(3) spectrum of $\mathbf{J}^{\mathbf{P}} = 1^-$ mesons. . . . .	16
1.5	Illustration of the SU(3) spectrum of $\mathbf{J}^{\mathbf{P}} = 1^-$ exotic mesons. . . . .	16
1.6	Features of the $K^- \pi^+ \pi^-$ system produced via diffractive dissociation of kaons in $K^- p \rightarrow p K^- \pi^+ \pi^-$ at COMPASS. [12] . . . . .	19
1.7	Features of a $K^- \pi^+ \pi^-$ produced in hypercharge exchange reaction $\pi^- p \rightarrow \Lambda K^+ \pi^- \pi^0$ using the CERN 2 m hydrogen bubble chamber. [29] . . . . .	19
1.8	A Feynman Diagram illustrating the isobar model interpretation of a $\gamma p \rightarrow \Lambda K^+ \pi^+ \pi^-$ decay. The incoming photon interacts with the proton, which in turn leaves as a $\Lambda$ that later decays to a $p \pi^-$ , then by exchanging a $K^+$ with the meson vertex, a resonance X is peripherally produced. X then decays to an isobar Y and a bachelor particle. . . . .	20
2.1	An aerial view of Jefferson Lab. Image source [36] . . . . .	22
2.2	Schematic CEBAF accelerator overview, including modifications for the 12 GeV update. Image source [37] . . . . .	23
2.3	A cross section view of Superconducting Radio Frequency (SRF) Niobium cavities. The Standing waves are tuned so that each bunch of electrons will get a continuous accelerating electric force when it passes through the cavities. Image source [36] . . . . .	24
2.4	Side view of the Hall B photon tagger. Electrons bent into the focal plane by the dipole magnet, pass through the E-counters where their energies are measured, then through the t-counters where their timing is measured. Image source [39] . . . . .	26
2.5	A schematic diagram of the g12 target. Image source [41] . . . . .	26
2.6	Three dimensional computer rendering of CLAS. Image source [36] . . . . .	27
2.7	Computer rendering of the start counter. Image source [36] . . . . .	28
2.8	An illustration of CLAS's superconducting toroidal magnet. Image source [42] . . . . .	29

2.9	(A) Contours of the magnetic field generated by the torus in the mid plane between two coils. (B) Magnetic field vectors for the CLAS torus transverse to the beam in a plane centered on the target. Image source [36] . . . . .	30
2.10	A cross sectional cut through the CLAS detector showing the position of different regions of the DC. Dashed lines outline the position of the toroidal magnet. Image source [43] . . . . .	31
2.11	A schematic of a section of the drift chambers showing two superlayers. The sense wires are positioned in the center and the field wires are positioned at each corner of the cell. The arrow depicts the track of a charged particle as it passes through the drift chambers, and the shadowed hexagons represent the hit cells. Image source [43]	32
2.12	The time of flight detector subsystem used in each CLAS sector. The four panels are made of 57 scintillator paddles of different lengths . Image source [36] . . . . .	33
2.13	Computer rendering of the Čerenkov counter showing its position relative to the R2 drift chamber and th Torus magnet. Image source [36] . . . . .	34
2.14	A schematic of one of the fixtures of the six Čerenkov modules showing the path of the Čerenkov light from an electron track. The light is first reflected off the surface of an elliptical mirror which in turn reflects it onto a hyperbolic mirror that finally collects the light into a photomultiplier tube. Image source [36] . . . . .	35
2.15	Illustrated are three distinct coincidence trigger criteria. $ECP_{inner}$ and $ECP_{total}$ represent a photon signal above threshold for the inner layer of the EC and entire EC respectively. $ECP_{inner}$ and $ECP_{total}$ represent an electron signal above threshold for the inner layer of the EC and entire EC respectively. $ST_{0,1,2,3}$ are the four TDC signals for the start counter. Image source [42] . . . . .	36
2.16	The path of a charged particle going through a magnetic field. When the radius of curvature is large when compared with the sagitta, the radius of curvature can be approximated by $r \approx \frac{l^2}{2s}$ . . . . .	37
2.17	$\beta$ of every track in run 56855 as a function of track momentum. Image source [43]	38
3.1	The z and r distributions of $pK^+\pi^+\pi^-[\pi^-]$ events. The blue region indicates the selected events. . . . .	42
3.2	The z and r distributions of $pK^+\pi^+\pi^-[X]$ events. The green region indicates the selected events. . . . .	43
3.3	The difference in start counter time to the RF-corrected tagger vertex time of $pK^+\pi^+\pi^-[\pi^-]$ events. The green region indicates the selected events. . . . .	44
3.4	The <i>beta</i> distribution of $pi^+$ for all events. The darker blue region indicates the selected events. . . . .	45
3.5	The beam profile of the $pK^+\pi^+\pi^-[X]$ events. The brown area indicates the selected events. . . . .	46

3.6	The missing mass squared off ( $pK^+\pi^+\pi^-$ ) distribution. The region between the two red lines indicates the fitted events. The dark gray region in Figure (b) represents the selected events. The shaded areas in Figures (c) and (d) represent the selected fitted events and the discarded fitted events respectively. . . . .	47
3.7	The pulls of the kinematic fit related to the momenta of the particles. They are centered close to zero and have a sigma close to 1. . . . .	49
3.8	The invariant masses of ( $p\pi^-$ ) and ( $p[\pi^-]$ ) systems. Peaks around $1.1 \text{ GeV}/c^2$ are clear indications of $\Lambda$ baryons. . . . .	50
3.9	The 2 dimensional plot of the invariant masses of ( $p\pi^-$ ) and ( $p[\pi^-]$ ) (a), The invariant mass distribution of the ( $p\pi^-\pi^-$ ) system (b). Events in bright blue in (b), correspond to the sample enclosed in the yellow box in (a). . . . .	51
3.10	The invariant mass of ( $p\pi^-$ ) versus the invariant mass of ( $p\pi^-$ ). Events enclosed inside the red boxes correspond to the $\Lambda$ selection. . . . .	51
3.11	The invariant mass of $K^+\pi^+\pi^-$ (a), $K^+\pi^-$ (b), and $\pi^+\pi^-$ (c) for the exclusive $\gamma p \rightarrow \Lambda K\pi^+\pi^-$ sample following the $\Lambda$ selection. . . . .	52
3.12	The invariant mass of $\Lambda\pi^+$ versus the invariant mass of $K^+\pi^-$ . . . . .	53
3.13	The invariant mass of $\Lambda\pi^+$ . The area in brown corresponds to selected events. . .	54
3.14	The invariant mass of $K^+\pi^+\pi^-$ (a), $K^+\pi^-$ (b), and $\pi^+\pi^-$ (c) for the exclusive $\gamma p \rightarrow \Lambda K\pi^+\pi^-$ sample following the sigma elimination cut. . . . .	55
3.15	An illustration of the relation between momentum and PID. The momenta of proton, $\pi$ and K (x-axis) are plotted against their respective $\beta$ 's (y-axis). . . . .	56
3.16	A two dimensional plot of the mass of $\pi^+\pi^-$ as a function of the momenta of kaons. The $K_s$ is clearly more prominent in the higher momentum region. . . . .	56
3.17	The invariant mass of $K^+\pi^+\pi^-$ (a), $K^+\pi^-$ (b), and $\pi^+\pi^-$ (c) for the exclusive $\gamma p \rightarrow \Lambda K\pi^+\pi^-$ sample following the K momentum cut. . . . .	57
3.18	The momentum transfer $t$ . . . . .	58
3.19	Exponential fits for the $t'$ distribution over the full $K\pi\pi$ mass range (a), in the low mass region between 1 and 1.6 GeV (b), and in the high mass region between 1.6 and 2.2 GeV (c). the values of the slopes are -0.5763, -0.6076, and -0.5415 respectively. . . . .	60
3.20	Features of the data: the invariant mass of $K^+\pi^-$ in (a), $\pi^+\pi^-$ in (b), and $K^+\pi^+\pi^-$ in (c) for various $t'$ selections. The final event sample uses the $t'$ cut shown in blue.	61
3.21	The invariant mass of the final $K^+\pi^+\pi^-$ sample used in the partial wave analysis (a), and the dalitz plot of this selected sample (b). . . . .	62

3.22	Dalitz distributions for the low $K\pi\pi$ mass region ( <b>top</b> ), and high mass region <b>bottom</b> . Green regions on the left correspond to events used in the Dalitz plots on the right. . . . .	63
4.1	A Feynman Diagram illustrating the isobar model interpretation of a $\gamma p \rightarrow \Lambda K^+ \pi^+ \pi^-$ decay. The incoming photon exchanges a $K^+$ with the proton, which in turn leaves as a $\Lambda$ that later decays to a $p\pi^-$ , and peripherally produces a resonance X. X then decays to an isobar Y and a bachelor particle which could be either a $\pi^+$ or a $K^+$ . The isobar then decays to $\pi^+\pi^-$ or $K^+\pi^-$ . . . . .	66
4.2	The definition of the Gottfried-Jackson reference frame (blue) and the Helicity reference frame (red) used in the calculation of decay amplitudes. . . . .	67
4.3	The variation of the decay amplitude of the $1^+D, \rho K^+$ as a function of the invariant mass of the $K^+\pi^+\pi^-$ system for accepted Monte Carlo events ( <b>left</b> ) and raw Monte Carlo events ( <b>right</b> ). The blue lines correspond to the positive reflectivity $1^+D, \rho K^+$ wave, while the red lines corresponds to the negative reflectivity of the same wave. Notice that the decay amplitudes of both reflectivities on the right are almost identical making it hard to distinguish them in this plot. . . . .	73
5.1	The momentum transfer $ t $ (a) and the excess momentum transfer $ t' $ (b) for the raw Monte Carlo sample. Both distributions are fitted to an exponential function thus yielding slopes of 0.615 and 0.679 for the accepted and raw Monte Carlo samples respectively. . . . .	79
5.2	Dalitz distributions for the low $K\pi\pi$ mass region ( <b>top</b> ), and high mass region <b>bottom</b> for the raw Monte Carlo dataset. Green regions on the left correspond to events used in the Dalitz plots on the right. . . . .	80
5.3	The CLAS acceptance for the $\gamma p \rightarrow \Lambda K^+ \pi^+ \pi^-$ events as a function of $K^+\pi^+\pi^-$ mass. . . . .	81
5.4	The momentum transfer $ t $ distribution of the data (a) and of the accepted Monte Carlo (b). The slopes are in approximate agreement at 0.554 for data and 0.558 for the accepted Monte Carlo. . . . .	81
5.5	Dalitz distributions for the low $K\pi\pi$ mass region ( <b>top</b> ), and high mass region <b>bottom</b> for the accepted Monte Carlo dataset. Green regions on the left correspond to events used in the Dalitz plots on the right. . . . .	82
5.6	The Gottfreid-Jackson angles for the data and Monte Carlo Samples. The flat <b>blue</b> distribution is the $\cos\theta_{GJ}$ of $(\pi^+\pi^-)$ in (b) and $(K^+\pi^-)$ in (d) for the raw Monte Carlo sample, while the <b>green</b> distributions are the $\cos\theta_{GJ}$ of $(\pi^+\pi^-)$ in (b) and $(K^+\pi^-)$ in (d) for the accepted Monte Carlo. . . . .	83
5.7	The Gottfreid-Jackson angles for the data and Monte Carlo Samples. The flat <b>blue</b> distribution is the $\phi_{GJ}$ of $(\pi^+\pi^-)$ in (b) and $(K^+\pi^-)$ in (d) for the raw Monte Carlo sample, while the <b>green</b> distributions are the $\phi_{GJ}$ of $(\pi^+\pi^-)$ in (b) and $(K^+\pi^-)$ in (d) for the accepted Monte Carlo. . . . .	84

5.8	The $(\phi_{lab}, \theta_{lab})$ angular distributions of all detected particles for both the data and the accepted Monte Carlo events. . . . .	85
5.9	The $(\phi_{lab}, \theta_{lab})$ angular distributions of all detected particles for both the data (right) and the accepted Monte Carlo (left) events, plotted as so to reflect the geometry of the CLAS detector. . . . .	86
5.10	The values of the likelihood function at its minimum for each bin in the fit we are presenting. The red point indicates the location of the bin which we used in our tracking process. A total of hundred fits were performed in that bin to determine the minimum of the likelihood function. . . . .	100
5.11	The acceptance corrected total intensity of all the partial waves in the fit. To determine the total intensity, the coherent sum of all the partial waves is calculated.	101
5.12	The acceptance corrected total intensity of all $1^+S$ waves included in this fit. This intensity includes the coherent sum of amplitudes of $1^+S$ wave decaying to a $\rho(770)K^+$ or a $K^*(892)\pi^+$ . . . . .	102
5.13	The acceptance corrected total intensities $1^+S$ waves decaying to $\rho(770)K^+$ (a) and $K^*(892)\pi^+$ (b). . . . .	103
5.14	The acceptance corrected intensities of the $1^+S$ with a relativistic Breit-Wigner fit of the low mass structure in $1^+S, K^*(892)\pi^+$ (a) and a K-matrix fit of both structures in $1^+S, \rho(770)K^+$ (b). . . . .	104
5.15	The acceptance corrected total intensity of all $1^-P$ waves included in this fit. This intensity includes the coherent sum of amplitudes of $1^-P$ wave decaying to a $\rho(770)K^+$ or a $K^*(892)\pi^+$ . . . . .	106
5.16	The acceptance corrected total intensities $1^-P$ waves decaying to $\rho(770)K^+$ (a) and $K^*(892)\pi^+$ (b). . . . .	107
5.17	The acceptance corrected total intensity of all $1^-P$ waves included in this fit. This intensity includes the coherent sum of amplitudes of $1^-P$ wave decaying to a $\rho(770)K^+$ or a $K^*(892)\pi^+$ . . . . .	108
5.18	The acceptance corrected total intensity of all $2^+D$ waves included in this fit. This intensity includes the coherent sum of amplitudes of $2^+D$ wave decaying to a $\rho(770)K^+$ or a $K^*(892)\pi^+$ . . . . .	109
5.19	The acceptance corrected total intensities $2^+D$ waves decaying to $\rho(770)K^+$ (a) and $K^*(892)\pi^+$ (b). . . . .	110
5.20	The acceptance corrected intensity of the $2^+DK^*(892)\pi^+$ wave fitted with a mass-dependent relativistic Breit-Wigner and a second degree polynomial. . . . .	111
5.21	The acceptance corrected total intensity of all $2^-S$ waves included in this fit. This intensity includes the coherent sum of amplitudes of $2^-S$ wave decaying to a $f_2(1270)K^+$ or a $K_2^*(1432)\pi^+$ . . . . .	112

5.22	The acceptance corrected total intensities $2^+D$ waves decaying to $K_2^*(1430)\pi^+$ (a) and $f_2(1430)K^+$ (b). . . . .	113
5.23	The acceptance corrected intensity of the $2^-SK_2^*(1430)\pi^+$ wave fitted with a mass-dependent relativistic Breit-Wigner and a second degree polynomial. . . . .	114
5.24	Features of the fitted data events (blue) and the predicted distributions (red points) for the $\gamma p \rightarrow \Lambda K^+\pi^+\pi^-$ sample. . . . .	115
5.25	The measured (blue) and predicted (red points) angular distributions in the Gottfried-Jackson frame. . . . .	116
5.26	The measured (blue) and predicted (red points) angular distributions in the Helicity frame. The angular distributions of the $K^+\pi^-$ system were determined using the $K^+$ as a spectator, and those of the $\pi^+\pi^+$ system were determined using the $\pi^+$ as a spectator. . . . .	117
A.1	The acceptance corrected total intensity of all $1^+S$ waves included in this fit. This intensity includes the coherent sum of amplitudes of $1^+S$ wave decaying to a $\rho(770)K^+$ or a $K^*(892)\pi^+$ . . . . .	121
A.2	The acceptance corrected total intensities $1^+S$ waves decaying to $\rho(770)K^+$ (a) and $K^*(892)\pi^+$ (b). . . . .	121
A.3	The acceptance corrected total intensity of all $1^-P$ waves included in this fit. This intensity includes the coherent sum of amplitudes of $1^-P$ wave decaying to a $\rho(770)K^+$ or a $K^*(892)\pi^+$ . . . . .	122
A.4	The acceptance corrected total intensities $1^-P$ waves decaying to $\rho(770)K^+$ (a) and $K^*(892)\pi^+$ (b). . . . .	122
A.5	The acceptance corrected total intensity of all $1^-P$ waves included in this fit. This intensity includes the coherent sum of amplitudes of $1^-P$ wave decaying to a $\rho(770)K^+$ or a $K^*(892)\pi^+$ . . . . .	123
A.6	The acceptance corrected total intensities $2^+D$ waves decaying to $\rho(770)K^+$ (a) and $K^*(892)\pi^+$ (b). . . . .	123
A.7	Features of the fitted data events (blue) and the predicted distributions (red points) for the $\gamma p \rightarrow \Lambda K^+\pi^+\pi^-$ sample. . . . .	124
A.8	The measured (blue) and predicted (red points) angular distributions in the Gottfried-Jackson frame. . . . .	125
A.9	The measured (blue) and predicted (red points) angular distributions in the Helicity frame. The angular distributions of the $K^+\pi^-$ system were determined using the $K^+$ as a spectator, and those of the $\pi^+\pi^+$ system were determined using the $\pi^+$ as a spectator. . . . .	126
A.10	The acceptance corrected total intensity of all $1^+S$ waves included in this fit.	

	This intensity includes the coherent sum of amplitudes of $1^+S$ wave decaying to a $\rho(770)K^+$ or a $K^*(892)\pi^+$ . . . . .	128
A.11	The acceptance corrected total intensities $1^+S$ waves decaying to $\rho(770)K^+$ (a) and $K^*(892)\pi^+$ (b). . . . .	128
A.12	The acceptance corrected total intensity of all $1^-P$ waves included in this fit. This intensity includes the coherent sum of amplitudes of $1^-P$ wave decaying to a $\rho(770)K^+$ or a $K^*(892)\pi^+$ . . . . .	129
A.13	The acceptance corrected total intensities $1^-P$ waves decaying to $\rho(770)K^+$ (a) and $K^*(892)\pi^+$ (b). . . . .	129
A.14	The acceptance corrected total intensity of all $1^-P$ waves included in this fit. This intensity includes the coherent sum of amplitudes of $1^-P$ wave decaying to a $\rho(770)K^+$ or a $K^*(892)\pi^+$ . . . . .	130
A.15	The acceptance corrected total intensities $2^+D$ waves decaying to $\rho(770)K^+$ (a) and $K^*(892)\pi^+$ (b). . . . .	130
A.16	Features of the fitted data events (blue) and the predicted distributions (red points) for the $\gamma p \rightarrow \Lambda K^+ \pi^+ \pi^-$ sample. . . . .	131
A.17	The measured (blue) and predicted (red points) angular distributions in the Gottfried-Jackson frame. . . . .	132
A.18	The measured (blue) and predicted (red points) angular distributions in the Helicity frame. The angular distributions of the $K^+ \pi^-$ system were determined using the $K^+$ as a spectator, and those of the $\pi^+ \pi^+$ system were determined using the $\pi^+$ as a spectator. . . . .	133
B.1	Schematic CEBAF accelerator overview, including modifications for the 12 GeV update. . . . .	135
B.2	Schematic CEBAF accelerator overview, including modifications for the 12 GeV update. . . . .	137
B.3	Schematic of a layer of the Time of Flight detector. Blue colored bars represent the full width - full length modules. The green colored bars represent the half width modules, and the red colored bars represent the half length modules. The white box in the middle represents the beam hole. . . . .	139
B.4	An illustration of the different steps of polishing that the light guides had to go through. Several sand papers were used in the process, leading to the shades variation observed above. . . . .	140
B.5	The method used to attach PMT to light guides is illustrated in this photo. After the Silicon RTV was applied, the PMT/Light guide joint was held together using the device shown in this photo. Constant pressure had to be applied to the joint to ensure best results. . . . .	140

B.6	The completed time of flight proudly fashioned in garnet and gold (FSU's official colors), as it gloriously resides in its final position. . . . .	141
C.1	Distributions of the distance between the $\Lambda$ vertex and the event vertex for the Data sample (a) and the accepted Monte Carlo sample (b). . . . .	144
F.1	The Clebsch-Gordan coefficients table with the Wigner-d functions and the spherical harmonics $Y_l^m$ . Image source [16]. . . . .	152

# LIST OF ACRONYMS

ADC	Analog to digital converter.
CC	Čherenkov counter.
CEBAF	Continuous Electron Beam Accelerator Facility.
CLAS	CEBAF Large Acceptance Spectrometer.
CM	Center of Mass.
CODA	CEBAF Online Data Acquisition.
A1C	Event reconstruction software used by the CLAS collaboration.
CQM	Constituent Quark Model.
DAQ	Data Acquisition System.
DC	Drift Chambers.
EC	Electromagnetic Calorimeters.
g12	The code name of the experiment used in this analysis.
GEANT	Simulation software used to describe the passage of elementary particles through matter.
GENR8	An event generator used to generate phase space events.
CERN	European Organization for Nuclear Research.
GJ	The Gottfried-Jackson frame.
GPP	A utility used in CLAS simulations to simulate data resolutions and efficiencies.
GSIM	A GEANT based package that simulates the geometry of CLAS.
JLAB	Jefferson Laboratory.
LINAC	Linear accelerator.
LQCD	Lattice Quantum Chromodynamics.
MC	Monte Carlo simulations.
MINUIT	Numerical minimization utility developed by CERN.
PDG	Particle data group.
PID	Particle Identification.
PMT	Photo multiplier tube.
PWA	Partial Wave Analysis.
QCD	Quantum Chromodynamics.
QED	Quantum Electrodynamics.
RF	Radio Frequency.
ST	Start Counter.
TOF	Time of Flight detector.

# ABSTRACT

The available information about strange excited mesons is limited and most of the observed states have been reported but not confirmed. While the low mass region (1.0 - 1.5 GeV) has been extensively studied in the past and states such as the  $K_1(1270)$ ,  $K_1(1400)$ , and  $K^*(1410)$  have been confirmed by a handful of experiments, little is known about the spin-parity structure of resonances in the higher  $K\pi\pi$  mass region (1.5-2.0 GeV). Past experiments have used hadron beams to gain access to the  $K\pi\pi$  system, and have provided extensive information about strange states that made mapping their spectrum possible. Except for the  $K^*(892)$ , none of the excited strange states has been photoproduced before. We perform a partial wave analysis on a photoproduced  $K^+\pi^+\pi^-$  system produced off a  $\Lambda$  baryon using the CLAS detector at Jefferson Lab. Using a photon beam incident on a liquid hydrogen target, we are able to reconstruct 16K events of the  $\gamma p \rightarrow \Lambda K^+\pi^+\pi^-$  topology. Results from initial data selection confirmed the dominance of two decay modes for a  $K\pi\pi$  resonance: the  $K^*(892)\pi$  and the  $\rho(770)K^+$ . A PWA was carried out in the helicity formalism using the reflectivity basis in the isobar model to parametrize the decay amplitudes of the resonances. Resonating structures are found in the  $1^+S$  wave primarily coupling to  $K^*\pi^+$  with a mass of  $1.35 \text{ GeV}/c^2$  and to  $\rho(770)K^+$  with a lower mass structure around  $1.33 \text{ GeV}/c^2$  and a higher mass resonance around  $1.73 \text{ GeV}/c^2$ . The  $1^-P$  also exhibited a significant resonating behavior with a mass of  $1.43 \text{ GeV}/c^2$  coupling primarily to the  $K^*(892)\pi^+$  decay mode. Also observed, an enhancement around  $1.49 \text{ GeV}/c^2$  in the  $2^+D$  wave strongly coupling to  $K_2^*(1430)\pi^+$ , and an enhancement in the  $2^-S$  wave around  $1.76 \text{ GeV}/c^2$  coupling primarily to  $K_2^*(1430)\pi^+$ .

# CHAPTER 1

## INTRODUCTION

The evolution of particle physics, as a field that studies the fundamental properties of matter, has been an ongoing process for the past hundred years. The rise of quantum mechanics and the birth of Einstein's special relativity laid down the foundation for a better understanding of the fundamental forces that govern the subatomic world, starting with atomic physics and Rutherford's planetary model of the atom. On a quest to understand the basic structure of the atom, following the discovery that an atom consists of electrons and protons, Rutherford devised an experiment in 1911 to study the "plum pudding" model suggested by J.J. Thomson. In this model, the electrons and protons were suggested to uniformly mix throughout the atom. Rutherford theorized that if Thomson's model would be correct, only if the mass of the atom was spread throughout the atom's structure. In his experiment, high velocity alpha particles were bombarded on a thin film of gold atoms. Rutherford observed that while most of the alpha particles went through the film, some were deflected backwards. He then went on to discard Thomson's model, reasoning that the only way alpha particles would deflect backwards is if the mass of the atom is concentrated in a nucleus. He then developed the planetary model [13], where the protons are located in the nucleus with electrons orbiting around the nucleus in a planetary form.

Less than three years later, Niels Bohr improved on Rutherford's model suggesting that electrons orbit around the nucleus in stable "stationary" orbits. He also theorized that each orbit had an its own energy associated with it, and that light is emitted when an electron jumps from a higher to a lower orbit, and is absorbed when going in the opposite direction. While Bohr's model was able to explain the hydrogen atom spectrum, it failed for heavier atoms. The final atomic model was yet to be discovered. In 1932, James Chadwick discovered the neutron [14], a particle similar in mass to a proton but is uncharged. Shortly after this discovery, Heisenberg proposed the proton-neutron model for the nucleus, in which the proton and the neutron constitute the nucleus thus deeming Rutherford's proposal of "proton-electron" pair incorrect. The neutron and the proton were then considered manifestations of the same state, the nucleon.

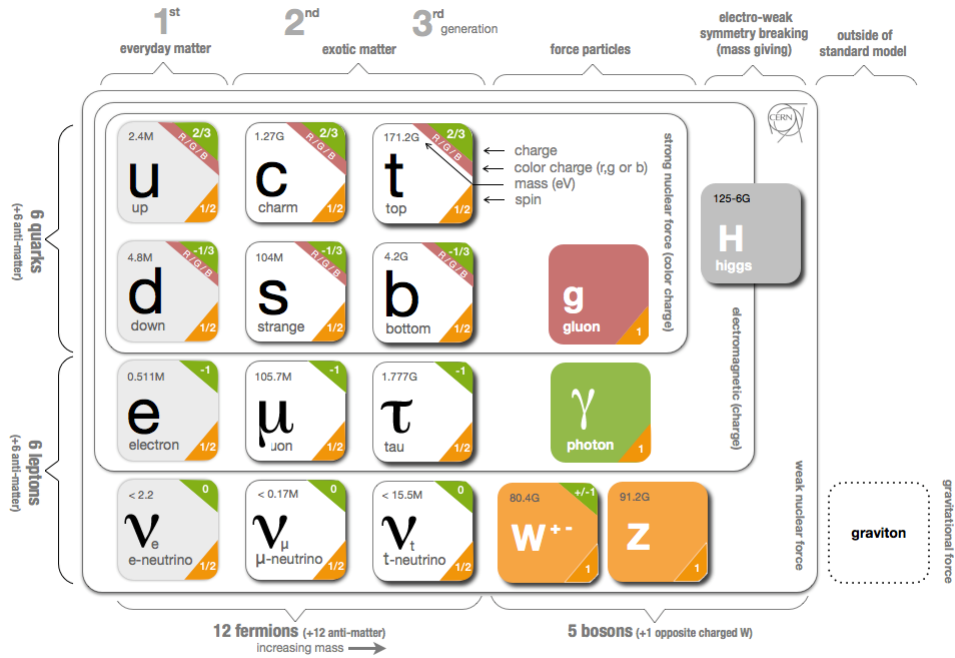


Figure 1.1: An infographic of the standard model of particle physics, including the recently discovered Higgs boson. (Courtesy of CERN Webfest)

Rutherford's discovery raised the question about the nature of the force that binds the protons and neutrons together. Being neutral, the neutron could not electro-statically bind to the protons. In 1934, Hideki Yukawa predicted the existence of a new force that binds the nucleons together mediated by the exchange of a new particle [7]. This new force was called the strong force of interaction. Yukawa's mediating particle was discovered in 1947 [15][11]. During the same year, an unidentified neutral "V" particle, to be later named the  $K^0$ , was discovered in a cloud chamber by Rochester and Butler in Manchester, England [23]. These events marked the start of modern particle physics, and for the next 70 years, physicists were able to identify a large spectrum of particles and provide concise information about their physical and quantum mechanical properties.

## 1.1 The Standard Model

The standard model is considered the framework that explains how the basic building blocks of matter interact. According to the standard model, everything in the universe is made of fundamental particles, governed by three fundamental forces. Developed in the early 1970s, it has been astonishingly successful at explaining almost all experimental results while also providing predictions of a wide variety of phenomena. So far, our understanding of the universe has relied on four fundamental forces: gravitational force, electromagnetic force, the weak force and the strong force. These forces have different strengths and work over different ranges. The gravitational force has an infinite range and is considered the weakest among these forces. The electromagnetic is stronger than gravity, but has an infinite range. The weak and strong forces dominate the subatomic world, working at very small ranges. The strong force is the strongest of all four fundamental interactions.

The weak, strong, and electromagnetic forces result from the exchange of force-carriers, called bosons. The strong force, for instance, is carried by a boson called the "gluon", the weak force is mediated by the "W" and "Z" bosons, while the electromagnetic force is carried by the photon. According to the standard model, the most fundamental building blocks of matter are the quarks. Quarks interact via the strong force by exchanging gluons. Similar to Leptons, they are spin-1/2 particles, also known as fermions, and obey Pauli's exclusion principle. In other words, quarks, like other fermions, cannot occupy the same space at the same time (quantum mechanically speaking, no two fermion can be described by the same quantum numbers). The standard model is thus divided into three sections: quarks, leptons, and bosons. Quarks, like leptons, come in pairs. Quarks are grouped up and down, charm and strange, and top and bottom. These quarks are proposed to carry a special kind of charge called the color charge. The color charge can be either red, green, or blue. The electron, muon, and tau each have an associated low mass, uncharged particle called a neutrino. Like protons and neutrinos, the electron is a stable particle and is present in almost all matter. The tau and muon, on the other hand, are unstable and are found in decay processes. The bosons, which we've already described as force carriers, are spin-1 particles. The strong force carriers, the gluons, can interact with themselves, since they carry the color charge that they couple to. The photons, on the other hand, cannot interact with other photons, since their electromagnetic charge is zero. Figure 1.1 shows the three sections of the standard model and the properties of the particles in it, including

Table 1.1: Parameters in the standard model.

Parameters	Number	Comments
Masses of Quarks	6	u, d, s (light) c, b (heavy) t=175 ±6 GeV
Masses of Leptons	6	e, $\mu$ , $\tau$ $M_{\nu_e, \nu_\mu, \nu_\tau}$
Mass of $W^\pm$	1	80.3 GeV
Mass of Z	1	91.2 GeV
Mass of Gluons, photons		0 (Gauge Symmetry)
Mass of Higgs	1	125.09±0.21 GeV
Coupling $\alpha_s$	1	$\approx 1$ for energies $\leq 1$ GeV
Coupling $\alpha_{EM}$	1	1/137 (=1/128.9 at $M_Z$ )
Coupling $G_F$	1	$10^{-5} GeV^{-2}$
Weak Mixing Angles	3	$\theta_1, \theta_2, \theta_3$
CP Violating Phase	1	$\delta$
Strong CP Parameter	1	$\Theta$

the most recently discovered Higgs Boson [34].

## 1.2 Quantum Chromodynamics

Quantum chromodynamics, familiarly called QCD, is a gauge field theory that describes the strong interactions of colored quarks and gluons, and is the SU(3) component of the SU(3)×SU(2)×U(1) standard model of particle physics. In a way, QCD is viewed an expansion of Quantum Electrodynamics (QED), having three different kinds of charge, labeled by "color", whereas QED has only one kind of charge. The color charge of QCD is analogous to the electric charge of QED. It is thus not related to any physical properties of the quarks and gluons. Addi-

tionally, the color charges are conserved in all physical processes, and are carried by the gluon. The parity conserving, time-inversion invariant, QCD Lagrangian has the form [1]

$$\mathcal{L}_{QCD} = -\frac{1}{4}(F_{\mu\nu}^i)^2 + \bar{\psi}(i\gamma^\mu D_\mu - m_q)\psi \quad (1.1)$$

where  $\psi$  is the quark field and  $\bar{\psi} = \psi^\dagger\gamma_0$  is the anti-quark field. The fermionic part in Equation 1.1 is the covariant Dirac operator  $M = i\gamma^\mu D_\mu - m_q$  with the quark mass  $m_q$ . The field strength,  $F_{\mu\nu}^i$ , is defined as

$$F_{\mu\nu}^i = \partial_\mu A_\nu^i - \partial_\nu A_\mu^i + gf^{ijk}A_\mu^j A_\nu^k \quad (1.2)$$

where  $f^{ijk}$  are the structure constants of the symmetry group. When comparing the field strength in QCD to that in QED, one notices the extra  $gf^{ijk}A_\mu^j A_\nu^k$  term. This term describes the ability of the gluon to interact not only with quarks and antiquarks, but also with other gluons.

When compared to QED, the response of gluons to color charge, as determined by the QCD coupling constant, is much more vigorous than the response of photons to electric charge. The gluons can also change the color charge into another. All possible color charges are allowed yet this charge is always conserved. The gluons, therefore, are able to carry unbalanced color charges. For instance, if a gluon can transform a blue charged quark into red, it must carry a red charge and an anti-blue charge. This would seem to require the existence of  $3 \times 3 = 9$  different color gluons, however the color-SU(3) singlet, that is suggested to respond equally to all charges, is dropped from the set if we are to have a perfectly color-symmetric theory. This conclusion was luckily validated by experiment. This profound property of gluons also suggests that they are capable of interacting with each other, unlike the photons which are electrically neutral. A famous consequence of this property is color confinement.

Confinement in QCD is the idea that the force between quarks does not decrease with distance. The idea of confinement lies in forbidding the free propagation of color charges, instead just keeping them inside the color neutral states (mesons and baryons). In practical terms, one can imagine the quarks connected by a string. When the quarks move further away from each other, the string stretches tight. This results in an increase in the gluonic field until the potential reaches a pair production threshold thus favoring the production of a spontaneous pair than to

continue separating the quarks. As a result, one can think of the inter-quark potential in QCD as

$$V(r) = -\frac{4}{3} \frac{\alpha_s(r)}{r} + kr \tag{1.3}$$

where  $\alpha_s$  is the QCD running coupling, and  $k$  is the QCD string tension. The first term is a Coulomb-like potential and the second is a confining potential. The Coulomb part is called the *Lüscher* term [1] and plays a crucial theoretical role even if it is not very important in heavy quark spectroscopy. Color confinement in QCD is true for low energy scales, where the momentum transfer is low, but in the higher energy scale quarks acquire asymptotic freedom and are well described by perturbation theory.

The discovery of asymptotic freedom by Gross, Wilczek, and Politzer provided a very well rounded explanation to the puzzling idea that even though quarks are confined inside colorless hadrons, experimental results from various high energy electron-proton collisions found that the interaction between the quarks at such energy is weak. Discovered by David Gross, Frank Wilczek, and David Politzer in 1973, asymptotic freedom explained how the attraction between quarks grows weaker as they approach each other, and conversely becomes stronger as they move away from each other. Using perturbation theory, once higher-order corrections are added, the strength of interaction between the quarks can be seen as highly dependent on the magnitude of "Q" the energy momentum transfer between the quarks. This strength can be expressed as the coupling factor  $\alpha_s$  [2][3]

$$\alpha_s \equiv \frac{\bar{g}(q)^2}{4\pi} = \frac{c}{\ln(q/\Lambda)} + \dots \tag{1.4}$$

where  $c$  is calculable constant and  $\Lambda$  is the QCD mass scale. Figure 1.3 shows experimental measures of the effective gauge coupling  $\alpha_s$  from high energy scattering experiments. While perturbation theory seems to be generally reliable at high energies, its expansion starts to fall apart as we move towards the other end of the energy scale. Two approaches were developed to calculate strong forces and the dynamics of light bound systems at low energies: Chiral perturbation theory and Lattice QCD.

Chiral perturbation theory is an effective field theory of QCD. In general, the basic idea of effective field theory is to treat the light particles as relevant degrees of freedom, while the heavy

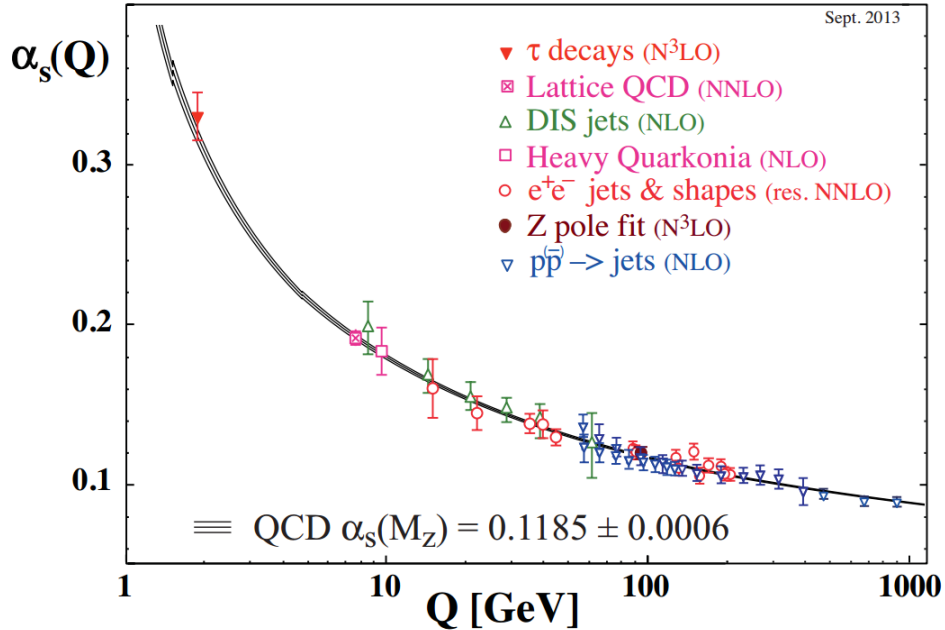


Figure 1.2: Experimentally measured values of the coupling  $\alpha_s$  from various experiments confirming the theoretically expected behavior at high energies. [16]

particles are reduced to static sources. The dynamics of effective field theory are described by an effective Lagrangian which is essentially formulated in terms of light particles and incorporates all important symmetries and symmetry-breaking patterns. Chiral perturbation theory makes use of the fact that at low energies hadrons are the only relevant degrees of freedom due to confinement. It is thus convenient in the low energy level to replace the QCD Lagrangian with an effective Lagrangian that uses pion, kaons and other light mesons as effective degrees of freedom. ChPT has been successful at calculating light meson mass, but is affected by the broken symmetry due to the non-vanishing mass of the quarks [6]. For a more comprehensive read on ChPT, refer to References [4][5].

Lattice QCD is a non-perturbative approach to carrying out QCD calculations. The primary goal of lattice QCD is to test whether quantum chromodynamics is the correct theory for strong interactions. Generally speaking, QCD has been surprisingly successful at describing large energy - large momentum transfer - processes, making it a reliable theory for strong interactions. However, quantitative confirmation is still lacking. Perturbative approaches to QCD in the low energy region ( $\leq 1$  GeV) are problematic because the strong interaction coupling

$\alpha_s$  starts approaching 1. Thus, perturbation theory in  $\alpha_s$  becomes unreliable. Determining the basic properties of quark bound states thus becomes extremely complicated. Lattice QCD was introduced many years ago as a frame work to address the problems that QCD faces in the low energy scale. Briefly speaking, LQCD is obtained by the quantization of the space-time dimensions. In LQCD, the four-dimensional space-time continuum is replaced by a hyper-cubic lattice, and the quark and gauge fields are restricted to the lattice points. Simulations of lattice QCD have six unknown input parameters: the coupling  $\alpha_s$  and the masses of the up, down, strange, charm, and bottom quarks (the top quark is eliminated from lattice simulations because it is too short-lived to form bound states). Once these have been fixed in terms of six precisely measured masses of hadrons, the properties of various other particles made up of these quarks and gluon can be determined. Following recent improvements in computational technology, lattice studies have become more popular, and have determined the static and dynamic properties of bound quark systems more precisely [10].

### 1.3 The Constituent Quark Model

Our knowledge of mesons and our understanding of strong interactions have gone several revisions ever since Yukawa introduced the pion to explain the interaction between nucleons. Our current understanding of the strong force is inspired by what QCD offers, however we have seen that at low energies, finding solutions for the QCD Lagrangian becomes more complicated with color confinement. And even though QCD does provide a theory for strong interactions, we know very little about the physical states of the theory. To a large extent, our knowledge of hadron physics is based on phenomenological models, in particular the constituent quark model (CQM). Introduced over 30 ago, the constituent quark model, with its phenomenological structure, allows for describes color singlet hadrons as bound states of quark and antiquarks. This model has been surprisingly successful at describing these hadrons as particle that are made of valence quarks. However, while most QCD-motivated models offer insight on other states predicted to exist by QCD that are not quark bound states, the quark model does not possess such a property. More precisely, QCD predicts the existence of a broader spectrum of states, ones that are made solely of gluons (*glueballs*), or states which have both constituent quarks and excited gluonic degrees of freedom (*hybrids*). The constituent quark model, however, has had the most success in describing the structure of hadrons.

Hadrons are divided into two categories, mesons and baryons. Mesons were first introduced by Yukawa when he postulated the existence of the pion as the exchange boson responsible for the strong interaction between nucleons. Tens of years later, with high energy accelerator experiments, a large pool of mesons and baryons appeared, thus leading to confusion among particle physicists. In an important breakthrough, Gell-mann [8] and Zweig [9] postulated that mesons and baryons were in fact composite objects. Initially only the up, down and strange mesons were included in the model, but eventually the charm, top, and bottom quarks were also included. In the CQM, mesons are made of a quark-antiquark pair, while the baryons were made of three quarks. We will discuss how mesons and baryons are arranged in the constituent quark model in what follows, but first we need to recall some of the quantum numbers that are conserved in strong interaction

- **Q** Electric charge.
- **B** Baryon number.
- **S** strangeness.
- **J** Angular momentum.
- **I** Isospin.
- **P** Parity.
- **C** Charge conjugation.
- **G** G-parity.

These quantum numbers are used to construct various meson and baryon states in the constituent quark model. Some of these numbers are carried by the light quarks themselves (Table 1.2). Since the meson is made of a quark-antiquark pair, only two total spins are possible,  $S = 0$  or  $S = 1$

$$\begin{aligned}
 S = 0 & \quad \frac{1}{\sqrt{2}}(\uparrow_1\downarrow_2 - \downarrow_1\uparrow_2) \\
 S = 1 & \quad \frac{1}{\sqrt{2}}(\uparrow_1\downarrow_2 + \downarrow_1\uparrow_2)
 \end{aligned}
 \tag{1.5}$$

Table 1.2: The quantum numbers of light quarks.

Quark	B	Q	J	S	I	I <sub>z</sub>
u	$\frac{1}{3}$	$\frac{2}{3}$	$\frac{1}{2}$	0	$\frac{1}{2}$	$+\frac{1}{2}$
d	$\frac{1}{3}$	$-\frac{1}{3}$	$\frac{1}{2}$	0	$\frac{1}{2}$	$-\frac{1}{2}$
s	$\frac{1}{3}$	$-\frac{1}{3}$	$\frac{1}{2}$	-1	0	0

where  $\uparrow_{1,2}$  and  $\downarrow_{1,2}$  represent the projection of the spin 1/2 in the z direction. The total spin is determined using

$$\vec{S} = \vec{s}_1 + \vec{s}_2 \rightarrow S = 0, 1 \quad (1.6)$$

In addition to the total spin, we can have orbital angular momentum  $\vec{L}$  between the  $q\bar{q}$  pair. Then when combining this angular momentum with the total spin, we can determine the total angular momentum  $\vec{J}$

$$\vec{J} = \vec{L} + \vec{S} \quad (1.7)$$

Following the spin coupling rules one obtains the possible magnitudes of the total angular momentum  $\vec{J}$ ,

$$|\mathbf{L} - \mathbf{S}| \leq \mathbf{J} \leq |\mathbf{L} + \mathbf{S}| \quad (1.8)$$

The magnitude  $\mathbf{J}$  is one of the most essential quantum numbers used to classify meson and baryon states. Using  $\mathbf{S}$ ,  $\mathbf{L}$ , and  $\mathbf{J}$  the states can be written in spectroscopic notation as  $^{2\mathbf{S}+1}\mathbf{L}_{\mathbf{J}}$ . The relative orbital angular momentum between the quark and antiquark can be zero or any positive integer, its notation is letter based, using S for  $\mathbf{L} = 0$ , and P for  $\mathbf{L} = 1$ , and so on. Using the information from table 1.2, we are able to use these quantum numbers to construct various  $\mathbf{J}^{\mathbf{PC}}$  quantum numbers for meson states.

**Parity:** The parity of the  $q\bar{q}$  system depends on the intrinsic parity of its constituents, as well as the behavior of the wavefunction under inversion of axes. The wavefunction of this system is separated into a radial component and an angular component represented by the spherical  $Y_{lm}$  functions.

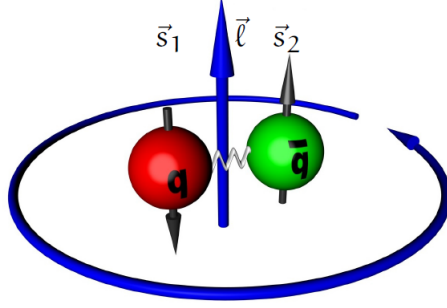


Figure 1.3: An illustration of the quark antiquark pair in a potential. The quark has a spin  $\vec{s}_1$  and the antiquark has a spin  $\vec{s}_2$  and they couple together with an angular momentum  $\vec{l}$ . Image source [12]

$$\psi(\vec{r}) = \mathbf{R}(r)Y_{lm}(\theta, \phi) \quad (1.9)$$

Mathematically, the parity is a reflection operator, and if the wavefunctions are eigenstates of the parity, then

$$\mathbf{P}\psi(\vec{r}) = \psi(-\vec{r}) = \eta_P\psi(\vec{r}) \quad (1.10)$$

Since applying the parity twice is supposed to give the original state back, the eigenvalues of parity  $\eta_P$  can be  $\pm 1$ . While  $\mathbf{R}$  is left unchanged, the parity operation transforms the angular part into  $Y_{lm}(\pi - \theta, \phi + \pi)$ , it can thus be shown that

$$Y_{lm}(\pi - \theta, \phi + \pi) = (-1)^l Y_{lm}(\theta, \phi) \quad (1.11)$$

Finally, since quarks are fermions, they have opposite intrinsic parity. This leads to the parity of a meson becoming

$$\mathbf{P}(q\bar{q}) = (-1)^{L+1} \quad (1.12)$$

**Charge Conjugation:** The charge conjugation, C, is responsible of interchanging a particle with its antiparticle. By definition, only states which are their antiparticles are C-parity eigen-

states. In a  $q\bar{q}$  system, the C-parity operation is carried out by inverting the coordinates as well as inverting the spin projections. This reverses several properties of the particle such as charge and magnetic moment. Clearly, in order for a particle to be an eigenstate of C-parity it needs to be electrically neutral. For a  $q\bar{q}$  spin triplet state, the inversion of the spin projection makes no contribution to the C-parity eigenvalue, but for a singlet state, a minus sign is encountered. If we consider the  $\pi^0$  for example, the C-parity operator gives

$$C|\pi^0\rangle = \eta_C|\pi^0\rangle \quad (1.13)$$

$\eta_C$  in this case can be  $\pm 1$ . If we consider a meson built from a quark and its antiquark, the total wavefunction including the spatial and spin factors is

$$\psi(\vec{r}, \vec{s}) = \mathbf{R}(r)Y_{lm}(\theta, \phi)\chi(\vec{s}) \quad (1.14)$$

The charge conjugation operator in this case replaces the quark with its antiquark, and reverses the direction of  $\vec{r}$ , thus leading to a factor of  $(-1)^{L+1}$ . This operator also flips the spin component, leading to a factor of  $(-1)$  for the  $\mathbf{S} = 0$  case and a factor of  $(+1)$  for the  $\mathbf{S} = 1$  case. This translates to a factor of  $(-1)^{\mathbf{S}+1}$ , which when combined with the spatial factor gives,

$$C(q\bar{q}) = (-1)^{\mathbf{L}+\mathbf{S}} \quad (1.15)$$

Clearly, charged particles are not eigenstates of C, given that the antiparticle of a positively charged particle is its negative counterpart and vice versa. However, if we apply the C operator followed by a rotation in isospin, then charged particles become eigenstates of this operator. The G-parity operator is defined as

$$G = C \exp[i\pi I_y] \quad (1.16)$$

where C is the C-parity of the neutral member of the isospin triplet and  $I_y$  is the y-component of the isospin operator. The eigenvalues of G for a given state are

$$G(q\bar{q}) = (-1)^{\mathbf{S}+\mathbf{L}+\mathbf{I}} \quad (1.17)$$

Using these quantities, we can build several  $q\bar{q}$  states. We commonly combine them with a standard notation of  $\mathbf{J}^{\mathbf{PC}}$ . The combinations below represent states that are allowed by the constituent standard model

Table 1.3: The quantum numbers of light quarks.

State	S	L	J	P	C	$\mathbf{J}^{\mathbf{PC}}$	Mesons				Name
$^1\mathbf{S}_0$	0	0	0	-	+	$0^{-+}$	$\pi$	$\eta$	$\eta'$	K	pseudoscalar
$^3\mathbf{S}_1$	1	0	0	-	-	$1^{--}$	$\rho$	$\omega$	$\phi$	$K^*$	vector
$^1\mathbf{P}_1$	0	1	1	+	-	$1^{+-}$	$b_1$	$h_1$	$h_1'$	$K_1$	pseudo-vector
$^3\mathbf{P}_0$	1	1	0	+	+	$0^{++}$	$a_0$	$f_0$	$f_0'$	$K_0^*$	scalar
$^3\mathbf{P}_1$	1	1	1	+	+	$1^{++}$	$a_1$	$f_1$	$f_1'$	$K_1$	axial vector
$^3\mathbf{P}_2$	1	1	2	+	+	$2^{++}$	$a_2$	$f_2$	$f_2'$	$K_2^*$	scalar

$$\mathbf{J}_{\text{CQM}}^{\mathbf{PC}} = 0^{-+}, 0^{++}, 1^{--}, 1^{+-}, 2^{--}, 2^{-+}, 2^{++}, 3^{--}, 3^{+-}, 3^{-+}, \dots \quad (1.18)$$

Table 1.3 provides more details about these states and their nomenclature. However, as we previously discussed, QCD predicts the existence of states that are not  $q\bar{q}$  bound states. As it turns out, QCD predicts the existence of hybrid states ( $q\bar{q}g$  states), glueballs (gg states), and tetraquark states ( $q\bar{q}q\bar{q}$  states). Commonly referred to as states with exotic quantum numbers, the set below represents these states

$$\mathbf{J}_{\text{non-CQM}}^{\mathbf{PC}} = 0^{--}, 0^{+-}, 1^{-+}, 2^{+-}, 2^{-+}, 3^{-+}, \dots \quad (1.19)$$

These latter states can not be described by a simple  $q\bar{q}$  model. They have been a prime interest of the particle physics community for the past few years, leading to the development of a number of experiments worldwide, including the experiment presented in this thesis. Exotic states are not the topic of this thesis, however it is important to recall that while strange states can not have exotic quantum numbers (no C-charge), strange companions of exotic unflavored states are expected.

**Isospin, Strangeness, and the Eightfold Way:** The idea of isospin was introduced by Heisenberg in 1936. He proposed the isospin as a new quantum number to denote the 2 possible states of a nucleon as either a proton or a neutron. The nucleon, with isospin  $\frac{1}{2}$ , has  $2I + 1 = 2$  possible orientations in isospin space. The isospin vector  $\vec{I}$  has three components denoted  $I_1$ ,  $I_2$ , and  $I_3$ . In analogy to spin S, the third component of the isospin  $I_3$  distinguishes between the proton and the neutron. The latter has an  $I_3 = -\frac{1}{2}$ , while the former has an  $I_3 = +\frac{1}{2}$ . The

most convenient way to write the value of  $I$  and  $I_3$  for a given state is by using  $|I, I_3\rangle$ . Then the proton and the neutron are

$$\text{proton } \left| \frac{1}{2}, \frac{1}{2} \right\rangle \quad \text{neutron } \left| \frac{1}{2}, -\frac{1}{2} \right\rangle \quad (1.20)$$

In the quark model, isospin symmetry arises from the nearly identical masses of the up and down quarks. The neutron, for example, can become a proton when one of the down quarks is replaced by an up quark. Therefore, these quarks are also assigned  $I_3$  values, with the up having  $I_3 = +\frac{1}{2}$  and the down quark having  $I_3 = -\frac{1}{2}$ . Note that, all the other heavier quarks have a zero isospin. The charge of a state  $|I, I_3\rangle$  can be related to its isospin via

$$q = e(I_3 + \frac{1}{2}) \quad (1.21)$$

where  $e$  is the charge of an electron. Isospin symmetry can also be extended to other particle, such as mesons. The isospin of  $q\bar{q}$  states could be 0 or 1 for unflavored states, and  $\frac{1}{2}$  for states with a strange quark. For example, pions are  $q\bar{q}$  states that can be constructed by only using the up and down quarks. Similar to the way spin-1/2 states are constructed, we can construct 3 pion isospin states from the combination of two isospin-1/2 quarks.

$$\begin{aligned} -u\bar{d} \text{ state} : \quad & \left| \frac{1}{2}, \frac{1}{2} \right\rangle = |I = 1, I_3 = 1\rangle \rightarrow \pi^+ \\ d\bar{u} \text{ state} : \quad & \left| -\frac{1}{2}, -\frac{1}{2} \right\rangle = |I = 1, I_3 = -1\rangle \rightarrow \pi^- \\ \frac{u\bar{u} - d\bar{d}}{\sqrt{2}} \text{ state} : \quad & \frac{\left| \frac{1}{2}, -\frac{1}{2} \right\rangle - \left| -\frac{1}{2}, \frac{1}{2} \right\rangle}{\sqrt{2}} = |I = 1, I_3 = 0\rangle \rightarrow \pi^0 \end{aligned} \quad (1.22)$$

The quantum number "Strangeness" was first introduced by Gell-mann in the 1950's as a way to explain the strange behavior of newly discovered particles. Several particle accelerator experiments at the time were observing a particle that seemed heavier than the nucleon and pion. They were termed strange because they were produced in strong interactions yet decayed weakly. Gell-mann suggested that this new quantum number is conserved in strong interaction but it may not be conserved in weak interactions. He later proposed the existence of the strange quark, a quark heavier than the up and down quarks and has a strangeness  $S = -1$ . Gell-mann

then used this new quantum number to come up with a new scheme to arrange particles based on their strangeness and their charges and he called it the "Eightfold way".

The eightfold way is a mathematical scheme derived from group theory. It was independently developed by Murray Gell-mann and Yuval Ne'eman in 1961. At the time, a pool of meson had been discovered, and their quark contents were being deduced their decay process. Using the eightfold way, Gell-Mann arranged the mesons in the hexagon shown in Figure 1.4. The particles on the top of the hexagon are the kaons (K), and both contain one strange antiquark, they thus have a +1 strangeness. Going down the hexagon, one strange quark is added to the state, so the particles on the middle row, called the rhos ( $\rho$ ), phi ( $\phi$ ) and omega ( $\omega$ ), contain no strange quarks. The particles on the bottom are the antiparticles of the mesons on the top row.

A down quark is replaced by an up quark when going across the hexagon from left to right. The  $K^{*0}$  for instance, is made up of a down quark and a strange antiquark, it thus has the composition ( $d\bar{s}$ ). To its right is the  $K^{*+}$  which has the composition  $u\bar{s}$ . The  $\rho^-$  on the middle row is a  $d\bar{u}$ , the  $\rho^0$  in the center is a mixture of  $d\bar{d}$  and  $u\bar{u}$  and the  $\rho^+$  is a  $u\bar{d}$ . The  $\phi$  and the  $\omega$ , in the center of the hexagon, also contain mixtures of  $d\bar{d}$  and  $u\bar{u}$ , as well as some  $s\bar{s}$ , they therefore have a zero strangeness.

The letter Q on the bottom denotes the charge of the meson. Using the charges of their constituent quarks, shown in Table 1.2, and recalling that antiquarks have opposite charges to their quarks, the charged of the mesons can be obtain by simply adding the charges of their  $q\bar{q}$  constituents. The set of these 9 mesons is called a nonet, and mesons with similar  $\mathbf{J}^{\mathbf{P}(\mathbf{C})}$ 's belong to the same nonet. Therefore all the mesons that we know belong to nonets. This could also be extended to states with exotic quantum numbers. Figure 1.5, shows the nonet for exotic states with their strange companions. These strange states are expected to be produced with the same mechanism that regular strange states are produced, they are therefore expected to mix with regular  $q\bar{q}$  states.

## 1.4 Strange Mesons

The quark model has been surprisingly successful at explaining the existence of light mesons in the mass region between 1 and 2  $GeV/c^2$ . It has provided a reliable framework for understanding light  $q\bar{q}$  states, including strange states. Although the leading  $q\bar{q}$  states have been extensively studied and reported in the past, most of the non-leading  $q\bar{q}$  states still lack iden-

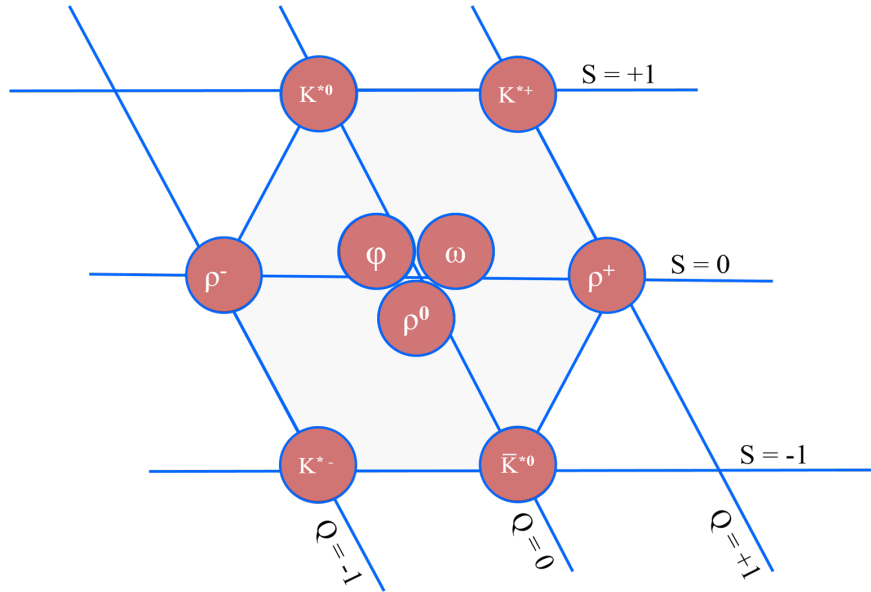


Figure 1.4: Illustration of the SU(3) spectrum of  $\mathbf{J}^{\mathbf{P}} = 1^-$  mesons.

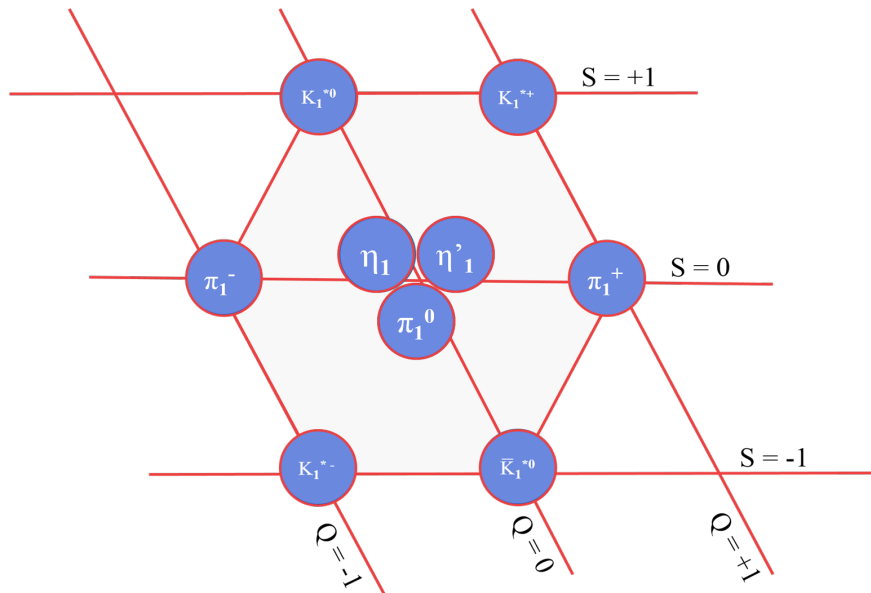


Figure 1.5: Illustration of the SU(3) spectrum of  $\mathbf{J}^{\mathbf{P}} = 1^-$  exotic mesons.

tification and confirmation, especially strange excited states. This limitation not only exhibits serious implications on the quark model, but also affects the identification of non- $q\bar{q}$  such as glueballs and hybrid states that are predicted to mix well with ordinary states. Strange mesons are an ideal place to study the properties of  $q\bar{q}$  states. The absence of glueballs and hybrid state mixing makes the experimental situation less confusing. Additionally, the general dominance of two decay modes allows access to numerous states with only two isobars.

The available information about strange excited mesons is limited and most of the observed states have been reported but not confirmed. While the low mass region (1.0 - 1.5 GeV) has been extensively studied in the past and states such as the  $K_1(1270)$ ,  $K_1(1400)$ , and  $K^*(1410)$  have been confirmed by a handful of experiments [30][32][33][12], little is known about the spin-parity structure of the higher  $K\pi\pi$  mass region (1.5-2.0 GeV) [26]. The  $K(1630)$ , for instance, is still a mystery and its spin-parity structure is yet to be determined. Information about the mass and the width of the  $K_1(1650)$  is also limited, and this state requires further investigation. Past experiments have used hadron beams to gain access to the  $K\pi\pi$  system. Table 1.4 gives an overview of our current mapping of the strange meson spectrum. The lack of confirmation for a significant volume of states is noticeable especially in the higher mass region. Additionally, there seems to be a tendency to combine states of the same spin-parity together in this region, even when the masses and widths from various experiments differ significantly. This is noticed with the  $K_1(1650)$ , having a reported mass of 1650 MeV from one experiment [25], and 1800 MeV from another [30].

Most of the data about excited strange mesons available today has been acquired by experiments using either a pion or a kaon beam. Diffractive dissociation of kaon, in particular, has provided significant results especially in the low mass region of the  $K\pi\pi$  system. The most recent results from a diffractive dissociation experiment are available in Reference [12]. Using the COMPASS spectrometer at CERN, a kaon beam of energies up to 200 GeV/c was incident on a liquid hydrogen target, producing a  $K^-\pi^+\pi^-$  system off a recoil proton. A partial wave analysis was performed on a data sample of around 270K events, resulting in the confirmation of the  $K_1(1270)$ ,  $K_1(1400)$ , and the  $K_2^*(1430)$ , with a pool of other higher mass states. Another example of kaon beam experiments comes from the ACCMOR collaboration, with a kaon beam up to 63 GeV/c energies also incident on a liquid hydrogen, resulting in events in the order of 200K. A partial wave analysis extracted several states that still require confirmation. One of the first conclusive measurements of strange mesons in a  $K\pi\pi$  system was performed at the SLAC

Table 1.4: A compilation of all the strange mesons with masses between 1 GeV and 2 GeV as reported by Reference[16]. **States in red are ones that have been observed in photoproduction experiments.** The significantly high volume of states that still await confirmation is noticeable .

$J^P$	Name	Mass (GeV)	Width (GeV)	M, $\Gamma$ in $K\pi\pi$	Note
	<i>K</i>	0.494	Stable	$\times$	
$0^-$	K(1460)	1.460	0.260	1.460 $\Gamma$ 0.260	Needs Confirmation
	K(1830)	1.830	0.250	$\times$	Needs Confirmation
$0^+$	$K_0^*(1430)$	1.425	0.270	$\times$	
	$K_0^*(1950)$	1.945	0.201	$\times$	Needs Confirmation
$1^-$	<i>K*(892)</i>	0.892	0.051	$\times$	
	$K^*(1410)$	1.414	0.232	$\times$	
	$K^*(1680)$	1.717	0.322	$\times$	
$1^+$	$K_1(1270)$	1.272	0.090	1.270 $\Gamma$ 0.090	
	$K_1(1400)$	1.403	0.174	1.410 $\Gamma$ 0.195	
	$K_1(1650)$	1.650	0.150	1.800 $\Gamma$ 0.250	Needs Confirmation
$2^-$	$K_2(1580)$	1.580	0.110	1.580 $\Gamma$ 0.110	Needs Confirmation
	$K_2(1770)$	1.773	0.186	1.780 $\Gamma$ 0.210	
	$K_2(1820)$	1.816	0.276	1.840 $\Gamma$ 0.230	needs confirmation
$2^+$	$K_2^*(1430)$	1.426	0.099	1.421 $\Gamma$ 0.100	
	$K_2^*(1980)$	1.973	0.373	$\times$	Needs Confirmation
$3^-$	$K_3(1780)$	1.776	0.159	$\times$	

accelerator with a 13 GeV/c kaon beam incident on liquid hydrogen target. A total of 72K events were obtained and a partial wave analysis was performed leading to the first evidence for the  $1^+$  and  $0^-$  states [20]. Also from SLAC, the first observation of the  $K_1(1410)$  and  $K_1(1770)$  states [31] using the LASS spectrometer, by performing a partial wave analysis on a sample of 7K  $\bar{K}^0\pi^+\pi^-$  events .Alternatively, pion beams have also been used to extract excited strange states from a  $K\pi\pi$  produced off a  $\Lambda$  [29]. Suffering from low statistics, the latter experiment

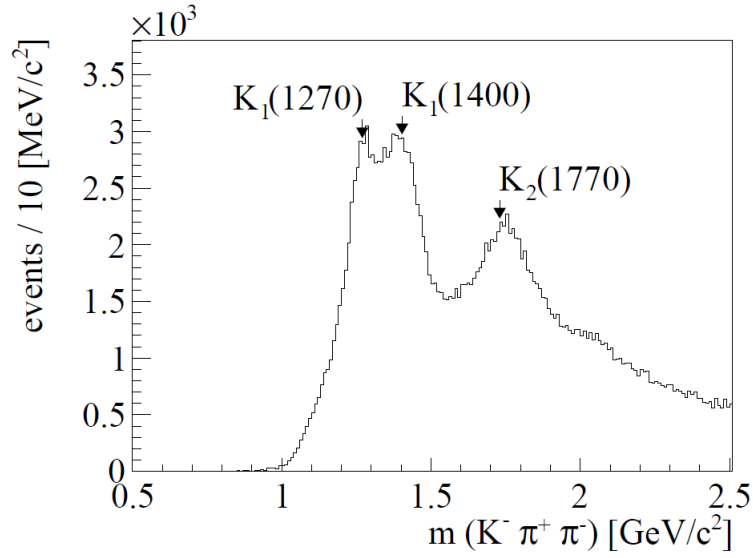


Figure 1.6: Features of the  $K^-\pi^+\pi^-$  system produced via diffractive dissociation of kaons in  $K^-p \rightarrow pK^-\pi^+\pi^-$  at COMPASS. [12]

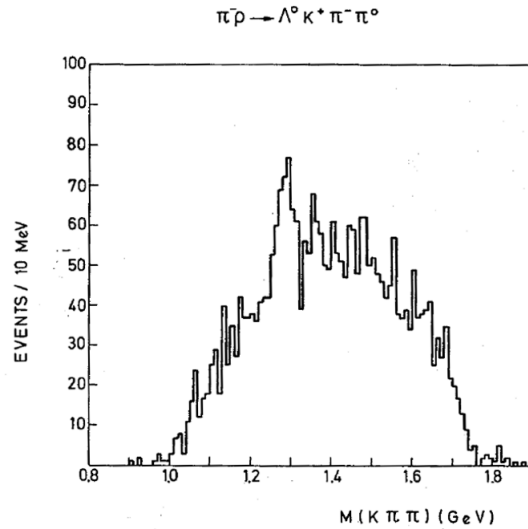


Figure 1.7: Features of a  $K^-\pi^+\pi^-$  produced in hypercharge exchange reaction  $\pi^-p \rightarrow \Lambda K^+\pi^-\pi^0$  using the CERN 2 m hydrogen bubble chamber. [29]

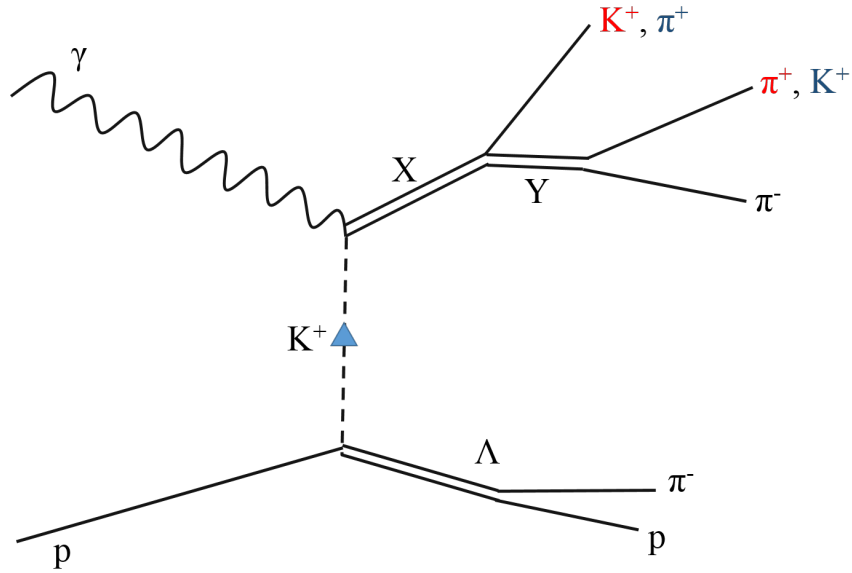


Figure 1.8: A Feynman Diagram illustrating the isobar model interpretation of a  $\gamma p \rightarrow \Lambda K^+ \pi^+ \pi^-$  decay. The incoming photon interacts with the proton, which in turn leaves as a  $\Lambda$  that later decays to a  $p\pi^-$ , then by exchanging a  $K^+$  with the meson vertex, a resonance  $X$  is peripherally produced.  $X$  then decays to an isobar  $Y$  and a bachelor particle.

only resulted in the observation of a the  $K_1(1270)$  state around 1.3 GeV.

Results from the diffractive dissociation of kaons into  $K\pi\pi$  have greatly contributed to the mapping of the strange meson spectrum over the past 40 years. Photoproduction, on the other hand, has never been used to study excited strange mesons. Except for the  $K^*(892)$ , none of the excited strange states has been photoproduced before. A partial wave analysis of a photoproduced  $K\pi\pi$  system is performed for the first time in this thesis. The data was acquired from the g12 experiment at Jefferson Lab using the CEBAF Large Acceptance Spectrometer (CLAS). A beam of photons with energies up to 5.45 GeV was incident on a liquid hydrogen target causing the production of about 16K  $\gamma p \rightarrow \Lambda K^+ \pi^+ \pi^-$  events. A partial wave analysis of the produced meson system, which will be presented in Chapter 5, showed clear evidence of several excited strange states.

A peripherally produced  $K\pi\pi$  system is guaranteed in photoproduction, mainly due to the strangeness the  $\Lambda$  baryon forces onto the meson vertex. Additionally, choosing events with the lowest possible momentum transfer ensures that the peripherally produced meson system is of

highest quality. The photoproduction picture in this analysis is as follows: a photon beam is incident on a proton target, producing a  $\Lambda$  baryon. The  $\Lambda$  then exchanges a  $K^+$  with the meson vertex thus producing a resonance that would later decay to  $K^+\pi^+\pi^-$  final state. The three body decay of the resonance is seen in the isobar model as a decay to an intermediate state (isobar) and a bachelor particle. The isobar then decays to the other two final state particles and a  $K\pi\pi$  system is produced. Figure 1.8 show the Feynman diagrams that represent the peripheral production of a  $K\pi\pi$  system with the exchange of a  $K^+$ . In these figures also, the intermediate state where an isobar  $Y$  decays to either  $\pi^+\pi^-$  and a bachelor  $K^+$  or to  $K^+\pi^-$  with a bachelor  $\pi^+$ . Previous studies have shown that two decay modes dominate the decay of most of the excited strange states, especially in the low mass region. We will show in this analysis that our results were in fact consistent with these studies, indicating the dominance of the  $\rho(770)K$  and  $K^*\pi$  decay modes.

## 1.5 Also In This Document

In addition to the work on analyzing photoproduction data to study strange mesons and perform the first partial wave analysis on a photoproduced  $K\pi\pi$  system, the author of this document took part in constructing the time of flight detector for the GlueX experiment at Jefferson Lab. The project was a year long effort of a number of other graduate and undergraduate students under the supervision of Dr. Paul Eugenio. All the components of the time of flight detector were built at Florida State University, then transported to Jefferson Lab for assembly. Component construction included the production of 84 2.5 m long scintillator modules with two readout photomultiplier tubes on either end, and 8 1.1m long scintillator modules with one readout photomultiplier tube attached to one end, as well as various miscellaneous frame components. More information on this project can be found in appendix B.

# CHAPTER 2

## EXPERIMENTAL SETUP

The dataset used in this analysis was obtained at the Thomas Jefferson National Accelerator Facility (Jefferson lab), using a photon beam delivered by the Continuous Electron Beam Accelerator Facility (CEBAF) into experimental hall B where the CEBAF Large Acceptance Spectrometer (CLAS) is hosted. The CLAS detector is designed to take electroproduction data directly, but can also take photoproduction data when an electron beam is delivered to an e-tagger (sitting upstream) which in turn generates a photon beam via bremsstrahlung radiation. For the g12 run, physics events were generated using a circularly polarized photon beam incident on an unpolarized liquid hydrogen target. A photon beam of energies up to 5.5 GeV was delivered to hall B, resulting in about 26.2 billion triggers of different topologies. The g12 dataset is considered the world's largest for meson photoproduction.



Figure 2.1: An aerial view of Jefferson Lab. Image source [36]

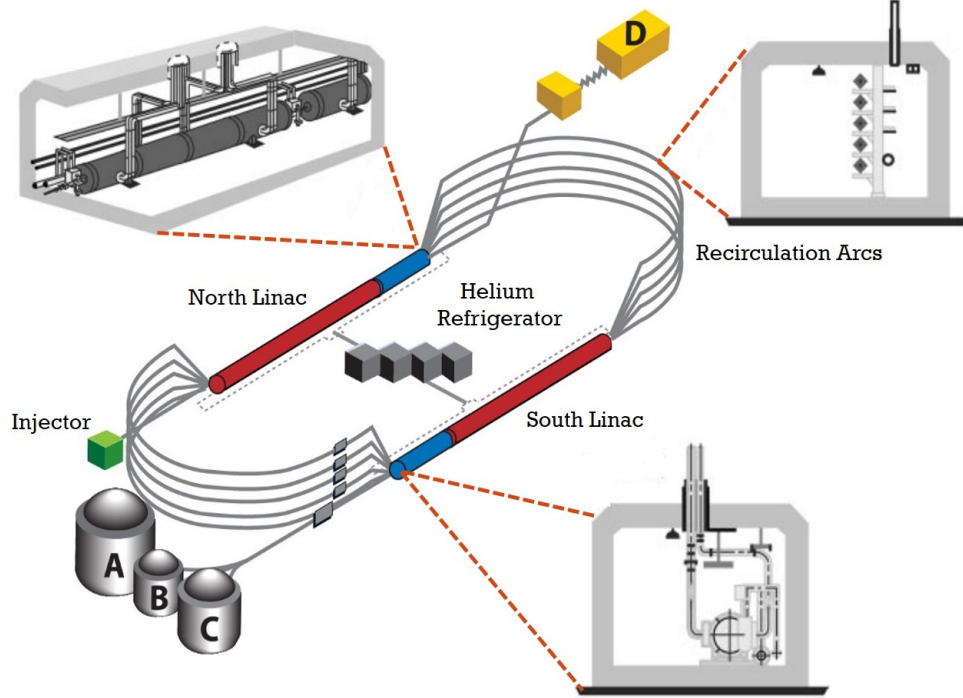


Figure 2.2: Schematic CEBAF accelerator overview, including modifications for the 12 GeV update. Image source [37]

## 2.1 The CEBAF Accelerator

The Continuous Electron Beam Accelerator Facility (CEBAF) is Jefferson lab’s main research facility. Constructed in the 1980’s, CEBAF was designed and built to explore the rules of interaction between quarks in the confinement regime [29]. CEBAF was originally designed to provide high quality, continuous-wave electron beam with up to 80% polarization, energies up to 6 GeV, and currents up to  $200 \mu\text{A}$ . It recently underwent a major upgrade increasing beam energies to 12 GeV and adding a new hall where a new experiment (GLueX) is currently taking place (Appendix B). CEBAF was the first accelerator facility in the world to make use of superconducting niobium radio-frequency (SRF) cavities, Figure 2.3, thus providing an acceleration gradient necessary for delivering high quality beam to three halls simultaneously. The accelerator’s final shape, including the recent upgrades, is depicted in Figure 2.2. The large scale design comprises two linear accelerators (linacs) connected by recirculation arcs at both ends, reminiscent of a racetrack, as shown in Figure 2.2.

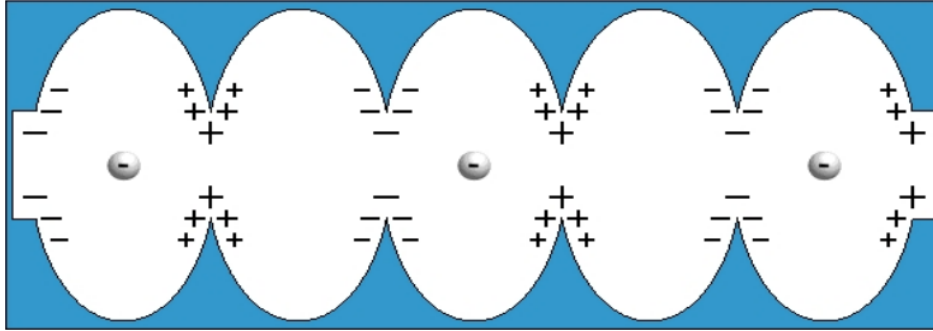


Figure 2.3: A cross section view of Superconducting Radio Frequency (SRF) Niobium cavities. The Standing waves are tuned so that each bunch of electrons will get a continuous accelerating electric force when it passes through the cavities. Image source [36]

Electrons are first produced inside the injector using a laser incident on a photo-cathode. The incident laser beam strikes the photo-cathode and knocks electrons off as a result of the photoelectric effect. The electric potential between the anode and the cathode then gives the electron an initial acceleration of 100 kV [19]. Since CEBAF delivers beam simultaneously and independently to three different halls, three different lasers set at different frequencies, are used. Electrons leave the injector in bunches about  $90 \mu\text{m}$  in length and separated by 667 picoseconds in time. After every trip through the linac, electrons pass through sets of magnets that bend them into the arcs according to their momenta. After every lap around the track, electron bunches acquire roughly 1200 MeV of kinetic energy and travel up to five times inside the accelerator before being delivered to the experimental halls. The beam switch-yard then takes care of delivering these bunches into each experimental hall, resulting in beam bunches every 2.004 ns. Three experimental halls are located at the south end of the CEBAF site, and the newly added hall D is located at the northern end as seen in Figure 2.2. Hall B is the smallest hall and houses the CEBAF Large Acceptance Spectrometer, the detector used in this analysis.

## 2.2 Hall B Photon Tagger

In order to produce a real photon beam necessary for photoproduction experiments, Hall B uses a tagging system or "tagger" that converts the incoming electron beam into a photon beam via bremsstrahlung radiation [21]. Electrons from the beam are incident on a very thin

radiator sheet, typically made of gold or copper and anchored in the pathway of the beam, thus passing through the Coulomb's fields of the nuclei causing them to decelerate and ultimately emit photons. Using a very thin radiator ensures that a single electron is correlated with a single photon. A dipole magnet produces a 1.75 T uniform fields that bends the scattered electrons downwards. A set of scintillators in the first layer detect the position of each scattered electron, while scintillators in the second layer measure the timing. Since the mass of gold is much higher than that of an electron, most of the momentum is transferred to the recoil electron and a negligible amount is absorbed by the nucleus. The energy of a photon can thus be measured with high precision via:

$$E_\gamma = E_e^i - E_e^f \quad (2.1)$$

where  $E_\gamma$  is the energy of the bremsstrahlung photon,  $E_e^i$  is the energy of the electron from the accelerator, and  $E_e^f$  is the energy of the electron after scattering through the radiator. After their travel through the radiator, the recoil electrons and the bremsstrahlung photons continue through a dipole "tagger" magnet that filters out the electrons [22]. A constant current is maintained across the magnet during the experiment for the photon tagging system to measure the energies of recoil electrons and to gain a coincidence signal for the CLAS detector. About 20-95% of the electron beam's energy is tagged, corresponding to 1.14 to 5.45 GeV for the incident 5.74 GeV electron beam energy of the g12 experiment.

Recoiled electrons are bent by this uniform-field dipole magnet onto a focal plane covered by two arrays of scintillators as shown in Figure 2.4. The first layer consists of 384 overlapping scintillator modules and is used to measure the energy of the scattered electrons, it is thus called the "E-Plane". A counter's main role is to register hits from recoiled electrons thus providing the Data Acquisition System (DAQ) with information about the position of the electron, which is sufficient to measure the energy. Below the E-Plane is another layer of scintillator modules, 61 in number, for measuring the timing of arrival of electrons bent into the focal plane, this is called the "t-plane". Information provided by the tagger counters is essential for CLAS users. Combining the tagger timing with times from particle tracks in CLAS gives the time of creation of the photon responsible for the physics event. The created photons finally pass through a 6.4 mm collimator upstream from the target followed by a set of sweeping magnets. These magnets bend any charged particles created by the photons hitting the collimator out of the beam's path.

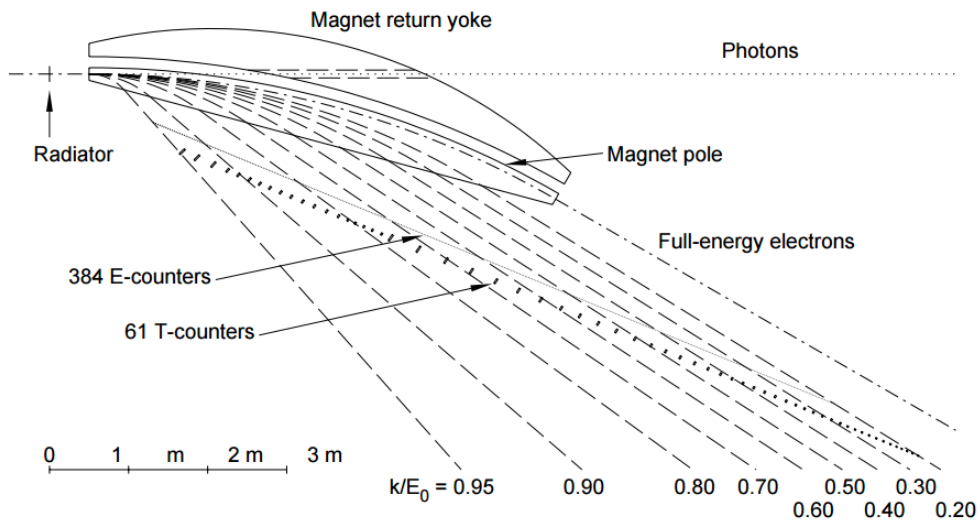


Figure 2.4: Side view of the Hall B photon tagger. Electrons bent into the focal plane by the dipole magnet, pass through the E-counters where their energies are measured, then through the t-counters where their timing is measured. Image source [39]



Figure 2.5: A schematic diagram of the g12 target. Image source [41]

## 2.3 Experimental Target

A liquid hydrogen target, pictured in Figure 2.5, was used during the g12 run period. Built at Jefferson lab and commissioned by another CLAS run group (g11), the target cell had a cylindrical shape and was 40 cm in length and 4 cm in diameter. The cell's walls and substructure

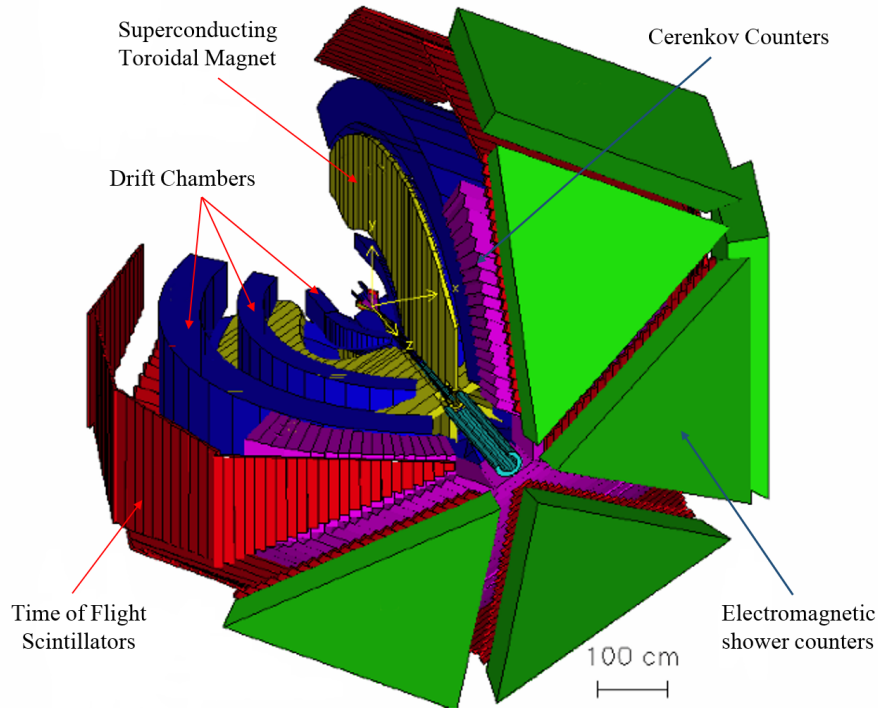


Figure 2.6: Three dimensional computer rendering of CLAS. Image source [36]

were made of aluminum, while the beam window was made of Kapton. Kapton was chosen for its superior performance under extreme temperatures and high levels of radiation. For the g12 run, the target was placed 90 cm upstream the detector to reduce the angular size of the forward hole in the detector thus increasing the efficiency of events at small deflection angles.

## 2.4 The CLAS Detector

The CEBAF Large Acceptance Spectrometer, CLAS, is a multi-particle almost  $4\pi$  spectrometer housed in Hall B at Jefferson Lab, Figure 2.6. Unlike detectors in other halls at Jefferson Lab, the CLAS detector is capable of tracking particles produced in electron-proton and photon-proton collisions over a large angular range [19]. The main components of the detector are combined around a superconducting toroidal magnet, which consists of six coils that divide the detection system into six sectors. Each sector consists of three separate Drift Chambers (DC) regions to determine the trajectories and momenta of charged particles, scintillation counters or Start Counter (SC) for time of flight and particle identification, Cerenkov Counters

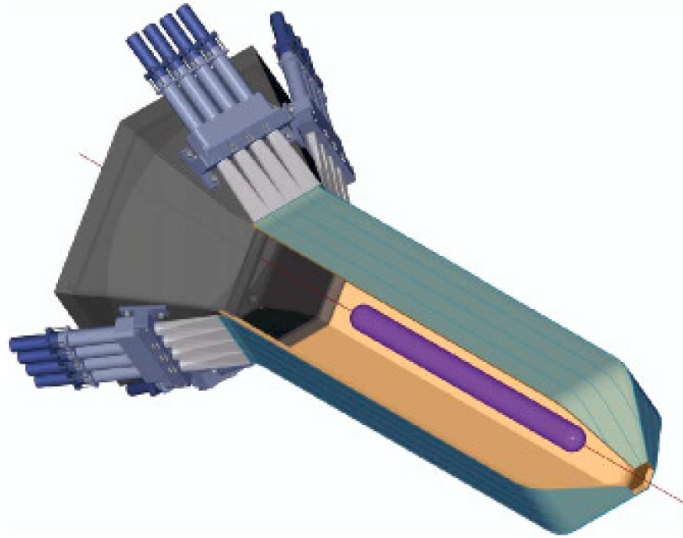


Figure 2.7: Computer rendering of the start counter. Image source [36]

(CC) for electron identification, and an Electromagnetic Calorimeter (EC) to identify showering particles such as electrons and protons.

### 2.4.1 Start Counter

The first detector component the charged tracks encounter in CLAS is the multi-segmented start counter surrounding the target cell, Figure 2.5. The start counter is made of 24 scintillator paddles arranged in a hexagonal array [27]. The upstream ends of the SC are attached to photomultiplier tubes while the downstream ends are bent inwards converging into a six-sided cone, thus providing coverage at smaller angles in  $\theta$ . The photomultiplier tubes provide TDC's and ADC's with information about the timing of a hit and the energy deposited into a paddle. The start counter also plays an important role in the trigger logic in coincidence with the tagger readout and the time of flight read out. Most particles registering hits in the start counter will ultimately register a hit in the time of flight detector thus providing necessary information to calculate the velocity of a particle. In addition to its triggering and timing role, the SC helps select the appropriate RF-beam bucket which leads to precise measurements of the photon-time, hence a precise vertex time [27]. Since these measurements are made for every track, events with multiple tracks give better timing estimates since they provide repeated measurements.

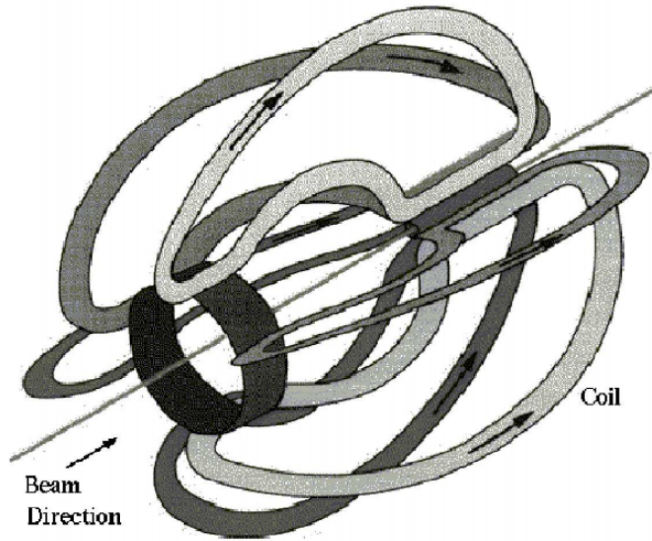


Figure 2.8: An illustration of CLAS's superconducting toroidal magnet. Image source [42]

### 2.4.2 Superconducting Toroidal Magnet

The heart of the CLAS detector is the superconducting toroidal magnet. It generates the magnetic field necessary to bend the trajectory of charged particles as they make their way through the detector. It is composed of six superconducting coils arranged around the beamline thus splitting the detector into six independent sectors [19]. Each coil is located in a separate cryostat, and is about 5 m long and 2.5 m wide with a  $60^\circ$  separation in the azimuthal direction. The magnet has the capacity to generate up to 3.5 T magnetic field and can support a 3861 A current [28]. The kidney shaped superconducting coils create a stronger field in the forward angles of the detector than in backward angles. Since the field is in the azimuthal direction and always transverse to the particle's momentum, positively charged particles are bent away from the beamline, while negatively charged particles are bent towards the beamline. Knowing the strength of the field, one can determine the momentum of the particle using its trajectory from the drift chambers.

For the g12 run. the magnet operated at a 1930 A current with a half-maximum field of 1.75 T [28]. Since higher magnetic fields tend to bend negatively charged tracks closer to the beamline and thus closer to CLAS's forward hole, a half-maximum field was chosen to reduce this effect. Figure 2.8 depicts the shape of the torus magnet installed inside the CLAS detector.

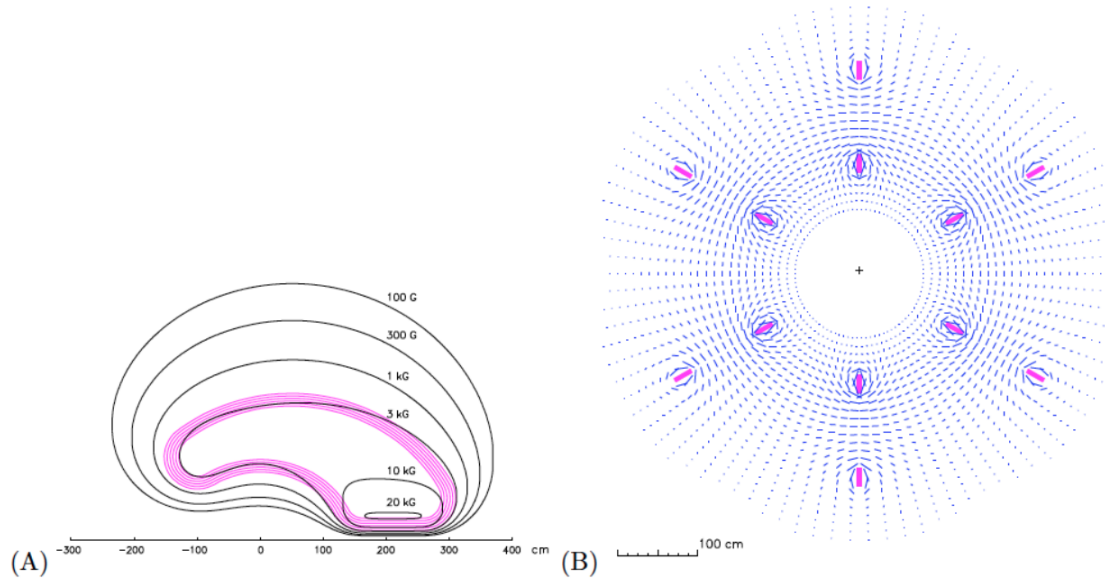


Figure 2.9: (A) Contours of the magnetic field generated by the torus in the mid plane between two coils. (B) Magnetic field vectors for the CLAS torus transverse to the beam in a plane centered on the target. Image source [36]

### 2.4.3 Drift Chambers

The drift chambers are used to determine the momenta of charged particles by tracking their trajectories. The structure of the toroidal magnet divides the drift chambers into six sectors, each of which is divided into three regions located at different distances from the target Figure 2.11. Region 1 (R1) is the closest to the target falling between the beamline and the torus coil in a Field-Free area. R1 is used to determine the initial direction of charged tracks. Region 2 (R2) is located between the torus coils, in the high magnetic field area, and is used to detect tracks at the point of maximum curvature to achieve good energy resolution. Region 3 (R3) falls outside the coils, in a low magnetic field area, and is used to measure the final position of the track before the time of flight counters, Cerenkov counters, and the electromagnetic calorimeters [28]. Each region has six separate chambers corresponding to the six layers of CLAS. Each chamber contains one axial superlayer made of sense wires strung parallel to the magnetic field, and one stereo superlayer with sense wires strung at an angle of  $6^\circ$  with respect to the axial wires [28]. The wires in these superlayers are arranged into a hexagonal pattern, with up to 192 sense wires per layer. A layer of guard wires surround every superlayer to minimize edge effects. There are

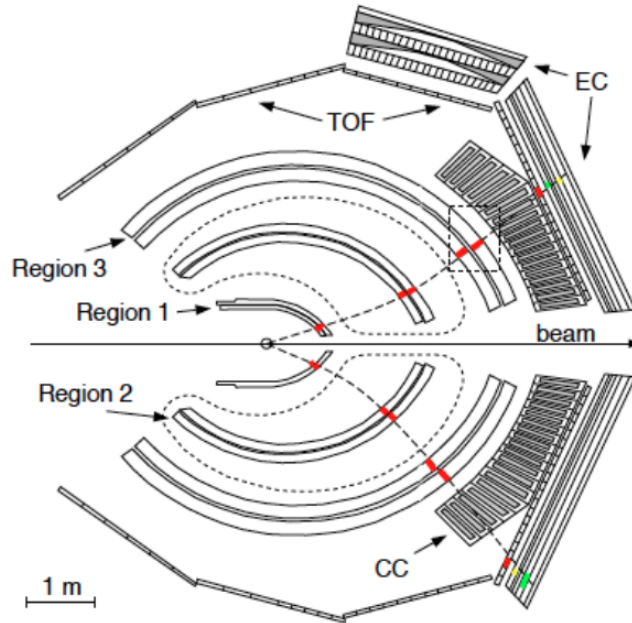


Figure 2.10: A cross sectional cut through the CLAS detector showing the position of different regions of the DC. Dashed lines outline the position of the toroidal magnet. Image source [43]

35148 hexagonal cells in total, capable of detecting particles of momenta greater than 0.2 GeV/c and covering a polar angle range from  $8^\circ$  to  $143^\circ$ .

As the charged particle travels through the drift chambers, it ionizes the gas molecules. The field wires, supplied with negative voltage serve as a cathode, while the sense wires hold positive charge and serve as the anode. Electrons from the ionized molecules make their way towards the sense wires and create a secondary ionization with the gas molecules, thus increasing the overall number of electrons and ions. Using the particle drift time information from the detected signals, the hit positions of the initial charged particles can be found. The gas within the drift chamber is a mixture of Ar and  $\text{CO}_2$ , 90/10 by volume. The gas mixture supports drift velocities of  $4\text{cm}/\mu\text{sec}$  and operates at very high voltages. The track resolution for the drift chambers was  $\delta P/P \leq 0.5\%$  for 1 GeV/c charged particles [28]. This resolution is enhanced at forward angles where the magnetic field is stronger, and falls off with increasing polar angles.

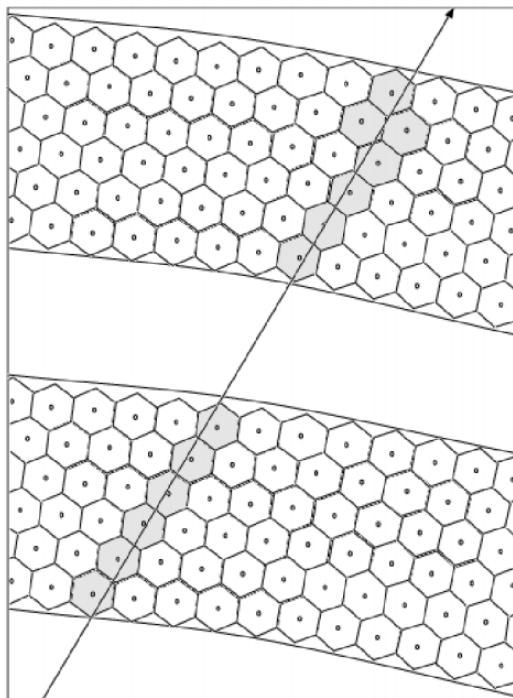


Figure 2.11: A schematic of a section of the drift chambers showing two superlayers. The sense wires are positioned in the center and the field wires are positioned at each corner of the cell. The arrow depicts the track of a charged particle as it passes through the drift chambers, and the shadowed hexagons represent the hit cells. Image source [43]

#### 2.4.4 Time of Flight

The Time of Flight (TOF) subsystem is essential for particle identification. Because of their fast response time, the Time of Flight counters can be used in conjunction with the start counter to help define trigger criteria for event recording. Whenever a track passes through one of the TOF paddles, a hit is registered and the time of arrival is determined. Having the trajectory from the drift chambers and the timing information from both the start counter and the time of flight, it is possible to explicitly determine the mass of a particle using:

$$m = \frac{p\sqrt{1 - \beta^2}}{\beta} \quad (2.2)$$

where  $m$  is the mass of the charged particle,  $p$  is its momentum, and  $\beta$  is the velocity of the particle when it hit the TOF paddle. Similar to other subsystems in CLAS, the Time of Flight is divided into six sectors mounted behind the Cerenkov counters about 5 m away from

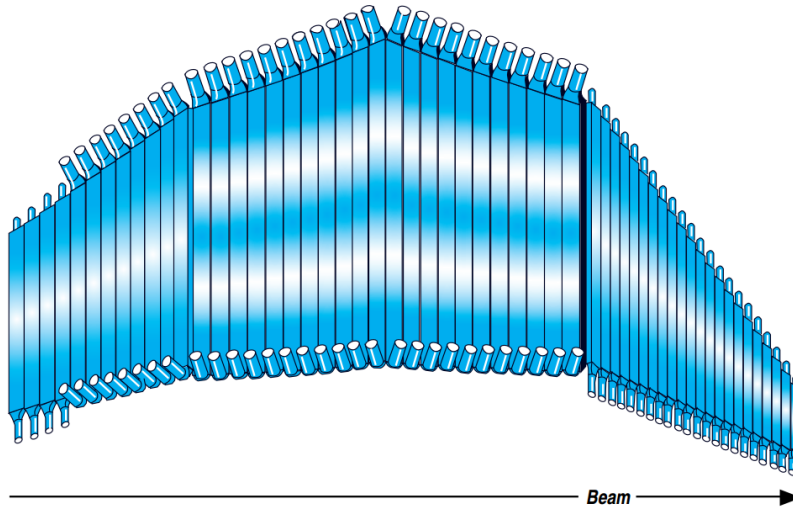


Figure 2.12: The time of flight detector subsystem used in each CLAS sector. The four panels are made of 57 scintillator paddles of different lengths . Image source [36]

the target [24]. Every sector in the TOF subsystem consists of 57 scintillator paddles divided into 4 panels or 3 polar angle regions as depicted in Figure 2.12. The first 23 paddles are 15 cm in width and are instrumented with 2 inches photomultiplier tubes, and are responsible for detecting particles with polar angles on the range of  $8.6^\circ$  to  $45.9^\circ$ . Paddles 24 through 53 are 22 cm in width and are instrumented with 3 inches photomultiplier tubes, and cover polar angles on the range of  $45.9^\circ$  to  $131.4^\circ$ . The last four paddles are 15 cm in width and are instrumented with 2 inches photomultiplier tubes, and cover polar angles on the range of  $134.2^\circ$  to  $141.0^\circ$ . All paddles are 5.08 cm thick and are made of BC-408 scintillating plastic and have photomultiplier tubes attached to both ends to read the signal. The timing resolution of the TOF depends on the length of the bar and averages to 140ps. This resolution provides a Pion/Proton separation up to 2.5 GeV/c in momentum and a Pion/Kaon separation up to 1.5 GeV/c in momentum.

#### 2.4.5 Čerenkov Counter

The CLAS Čerenkov counter are used for lepton/pion separation during particle identification. The Čerenkov counter is mounted around the third drift chamber region, and is segmented into six identical modules as shown in Figure 2.13. These sectors are capable of detecting leptons of polar angles on the range of  $8^\circ$  to  $45^\circ$ . Each module is made of 18 light collecting fixtures, with each fixtures accounting for a range of polar angle. A single fixture is made of two pairs of

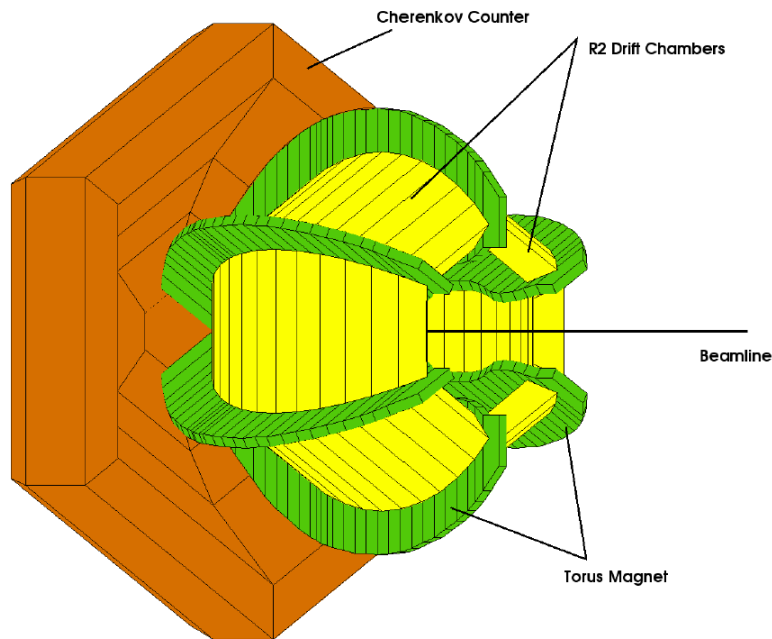


Figure 2.13: Computer rendering of the Čerenkov counter showing its position relative to the R2 drift chamber and th Torus magnet. Image source [36]

mirrors in opposing manner along the long axis of the CC module, Figure 2.14, and is filled with a perfluorobutane ( $C_4F_{10}$ ) gas medium with a 1.00153 index of refraction. Most light hadron, such as pions, travel at lower velocities and will not leave any trails of Čerenkov light in the CC. Leptons on the other hand, being much lighter than Hadrons, will travel closer to the threshold velocity thus emitting Čerenkov radiation providing means to distinguish them from pions. The Čerenkov counter is specifically important for experiments with electron beam, and was not used for the g12 run. For more information on the Čerenkov counter consult reference [35]

#### 2.4.6 Event Trigger and Data Acquisition

The CLAS data acquisition system uses a multi-layer suite of electronics to monitor the performance of different subsystems and collect signals. The presence of a signal in a single detector element is not necessarily an indication of a physics event. Some of these unwanted signals originate from cosmic radiation passing through the detector elements, others are a direct effect of electronics noise. To eliminate these background signals, a trigger system was used to determine which sets of signals constitute a physics event to be recorded for further

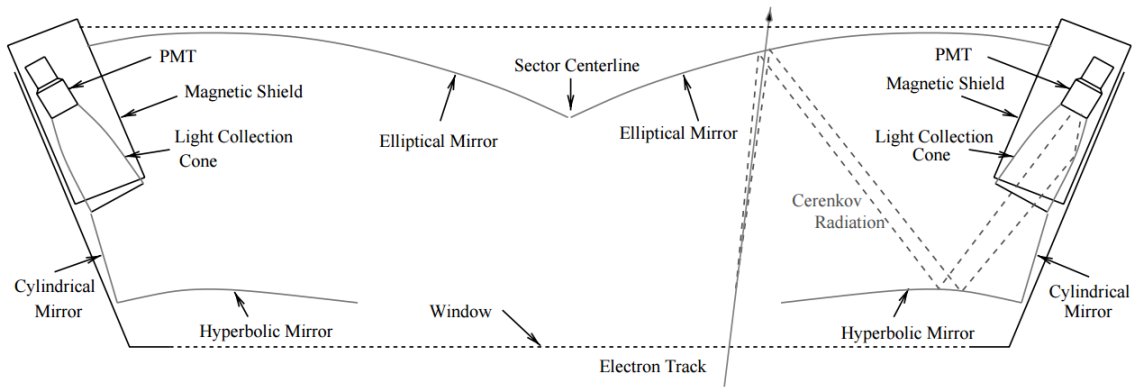


Figure 2.14: A schematic of one of the fixtures of the six Čerenkov modules showing the path of the Čerenkov light from an electron track. The light is first reflected off the surface of an elliptical mirror which in turn reflects it onto a hyperbolic mirror that finally collects the light into a photomultiplier tube. Image source [36]

analysis. Once an event was triggered, the data acquisition system collected the signals from all detector subsystems and cached them into disk. The recorded events were then copied to Jlab's tape-silo library for storage and further offline processing. The primary trigger required a 100 ns coincidence between the tagger, ST and TOF, it also required two-track events have high incident photon energy [68]. An example of the basic trigger logic used in data collection for a single sector is shown in Figure 2.15. More information about the trigger configuration for the g12 experiment can be found in reference [42][43].

The g12 trigger operated at a rate of 8 KHz thus recording events faster than any previous CLAS experiment. As a consequence, the g12 experiment acquired the largest photoproduction dataset to date totaling in 26 Billion triggers, about 126 TB in disk space, and averaging with a luminosity of  $68 \text{ pb}^{-1}$  [42].

### 2.4.7 Event Reconstruction

Events written to the tape-silo library by the Data Acquisition System can not be analyzed without getting reconstructed first. A program called "a1c" was used to reconstruct tracks and their subsequent particle identification by using information from the raw data on tape, this procedure is called "cooking". Information recorded from various detector subsystems is converted to readable form using "a1c" via "hit-based" tracking and "time-based" tracking. Event

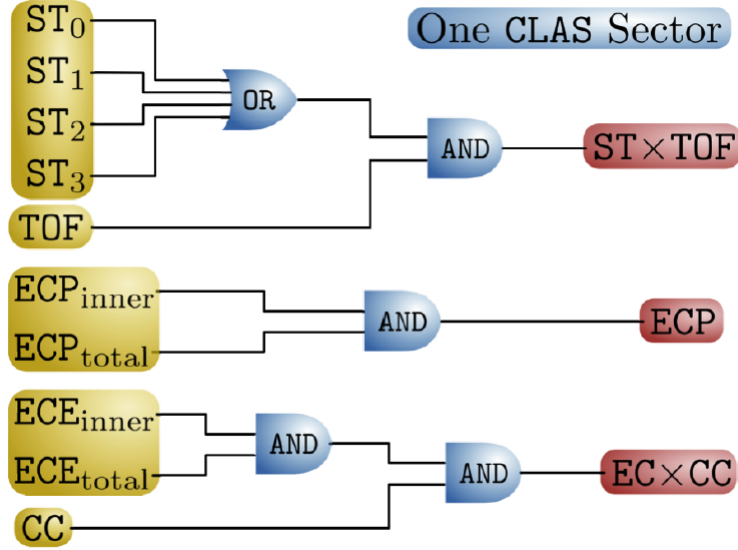


Figure 2.15: Illustrated are three distinct coincidence trigger criteria.  $ECP_{inner}$  and  $ECP_{total}$  represent a photon signal above threshold for the inner layer of the EC and entire EC respectively.  $ECP_{inner}$  and  $ECP_{total}$  represent an electron signal above threshold for the inner layer of the EC and entire EC respectively.  $ST_{0,1,2,3}$  are the four TDC signals for the start counter. Image source [42]

reconstruction starts with a "hit-based" tracking, during which the position of Drift Chamber wires that registered a hit are acquired. Adjacent hits in each superlayer are then assembled into clusters, and layers belonging to the same sector are linked together to produce track segments. Track segments from the three Drift Chamber regions are then combined to produce full "hit-based" trajectories. The curvature of this track gives the magnitude of its momentum by,

$$p = \frac{l^2 q B}{8s} \quad (2.3)$$

where  $p$  is the momentum of the track,  $q$  is the charge of the particle,  $l$  is the chord length,  $B$  is the magnetic field strength and  $s$  is the sagitta length. Different components of Eq. 2.3 are illustrated in Figure 2.16.

With trajectories now in hand, a "time-based" tracking is performed to connect a "hit-based" track to the appropriate Time of Flight panel. This kind of tracking is essential to eliminate any noise hits not associated with physical tracks. If a hit from the "hit-based" tracking is matched to a TOF panel, the time measurement from the TOF panel is used to set an upper limit to the

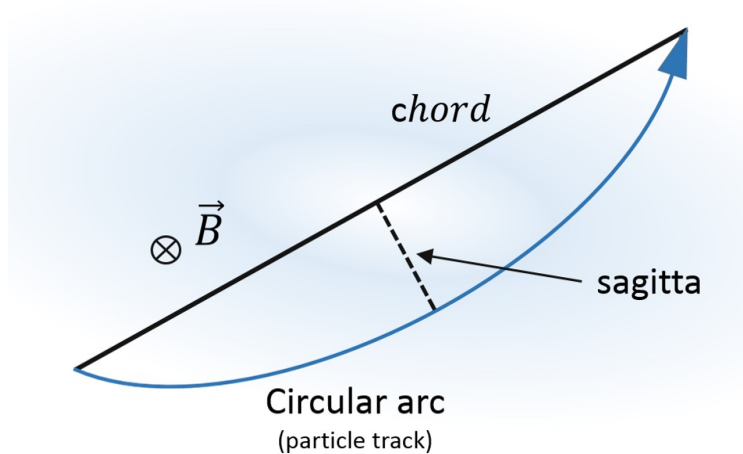


Figure 2.16: The path of a charged particle going through a magnetic field. When the radius of curvature is large when compared with the sagitta, the radius of curvature can be approximated by  $r \approx \frac{l^2}{2s}$ .

time of the drift-chamber hits. Using this upper limit, Drift Chamber hits associated with the track are checked for timing agreement, where each hit is required to be in increasing time order as the track moves away from the target. Hits that do not satisfy this condition are disregarded. With the bad hits now removed, the momentum of an individual track as well as the event vertex can be measured.

The final reconstruction step is assigning the reconstructed track to a known hadronic state based on its charge and mass. The mass of the track is calculated using Eq. 2.2, and the particle identification PID is determined by the following criteria:

$$PID = \begin{cases} \pi^\pm, & \text{if } m < 0.3 \text{ GeV and } q^\pm \\ K^\pm, & \text{if } 0.35 < m < 0.65 \text{ GeV and } q^\pm \\ p^\pm, & \text{if } 0.8 < m < 1.2 \text{ GeV and } q^\pm \\ d, & \text{if } 1.75 < m < 2.2 \text{ GeV} \end{cases} \quad (2.4)$$

Tracks with masses falling outside the defined PID regions are not identified and are labeled "unknown". The CLAS detector provides a Pion/Kaon separation up to 2 GeV in momentum and a Proton/Kaon separation up to 3 GeV as evident by Figure 2.17. These separation capabilities are crucial for analyses where a Kaon is in the final state including this analysis. A series

of cuts, outlined in Chapter 4, are performed to reduce the effect of the compromised PID at higher momenta.

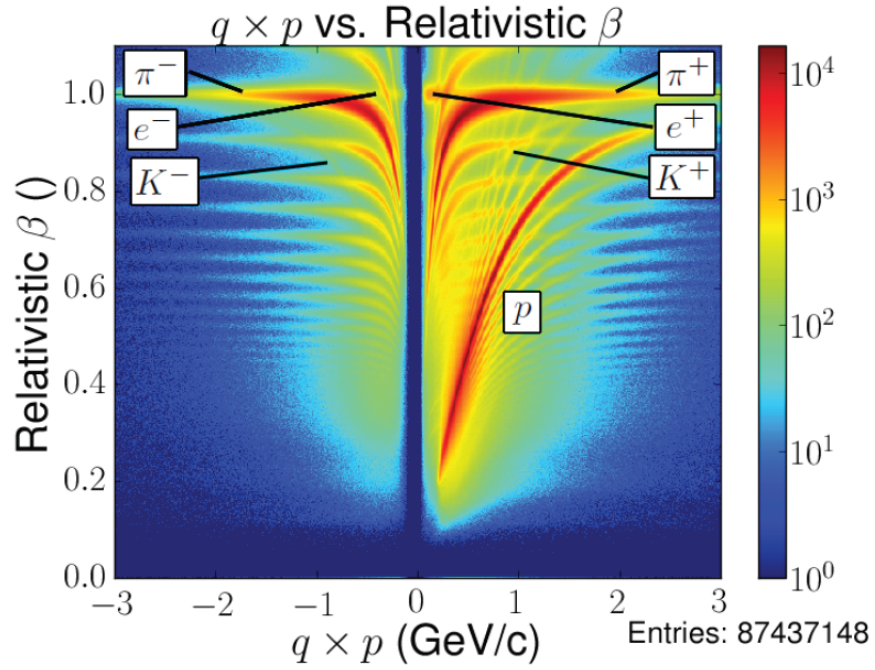


Figure 2.17:  $\beta$  of every track in run 56855 as a function of track momentum. Image source [43]

# CHAPTER 3

## DATA ANALYSIS

Event selection begins with establishing physically justified criteria to maximize the sample and minimize contamination from other reactions. This criteria comprises a set of conditions (cuts) that are based on our knowledge of the detector, the minimum production energy, and the kinematics of the topology under study. The first step is to select events that yield the production of 5 charged particles, or 4 charged particles with a missing particle. The missing particle - chosen to be missed to enhance the acceptance of this topology - is later reconstructed using the conservation of the four-momenta of the detected particles and the tagged photon energy. This is followed by a series of corrections that take into account any loss in energy and momentum a particle experiences as it travels through the detector. Kinematic fitting is then performed to enhance the measured kinematics of the particles, by constraining their energies and momenta to their known masses. A series of cuts is finally performed to reduce physics background and prepare a final data set for partial wave analysis. Reducing the physics background has a crucial role in the data selection due to its effect on the success of partial wave analysis.

### 3.1 Exclusive $\gamma p \rightarrow pK^+\pi^+\pi^-[\pi^-]$ Event Selection

We begin our data analysis by selecting  $\gamma p \rightarrow pK^+\pi^+\pi^-[\pi^-]$  events reconstructed from the skimmed g12 dataset [47]. From the 24.8B triggered events, only events with one proton, one possible  $K^+$ , one  $\pi^+$ , one or two  $\pi^-$ 's are selected. A possible kaon is either a real kaon as identified by the PART bank, or a high momentum pion ( $P_\pi > 2.0$  GeV). Events that pass this criteria are then treated with a series of corrections to account for any loss of energy and momenta. These corrections are not accounted for in the CLAS reconstruction software and are applied independently.

#### 3.1.1 Kinematic Corrections

Among the 24.8B triggered events produced in g12, about 24 million are selected. The CLAS reconstruction software does not account for any momentum or energy loss inside the

detector, therefore three independent packages are used to implement the energy and momentum corrections. These packages account for any uncertainties in the measured magnetic field, any change in the configuration of the target or the tagging magnet, and any errors in the track reconstruction of the detected particles. Below is a detailed explanation of how these packages work and what they correct for.

**Energy Loss:** During its trip inside the detector, a particle loses some of its energy and momentum as it interacts with various components of CLAS [48]. To account for these losses, a package called "Eloss" is implemented in the event selection code. This package considers the different materials a particle passes through as it travels from the target cell to the time of flight detector. It takes the particle momentum as calculated using the magnetic field between regions 1 and 3 in the drift chamber, and returns a corrected momentum using Bethe-Bloch formula [52] to relate the material characteristics and path length to energy loss. Since track reconstruction in CLAS uses information from the drift chambers, this correction can be quite substantial especially for low momentum particles and runs where the start counter is installed.

**Beam Energy Corrections:** The "BEC" package is used to correct for errors included in the calculation of the photon beam four-momentum. These errors are associated with hysteric behavior of the tagger magnet [50]. Any errors in the calculated bending magnetic field of the tagger for incoming electrons, would eventually propagate to the calculated four-momentum of the photon beam. This correction is essential for topologies with a missing particle, since the missing four-momentum is calculated using the photon beam momentum and energy.

**Momentum Correction:** The "Pcor" package is implemented in the event selection process to correct the momenta of detected charged particles. As discussed in Chapter 2, track reconstruction relies completely on the magnetic field map inside CLAS, which means that any deviations in the magnetic field need to be considered [50]. Small deviations of the real field from the provided mapped field to the reconstruction software usually arise due to our limited knowledge of the imperfections of the real field in CLAS as well as the misalignment of the drift chambers. The "Pcor" package fixes the momenta of the charged particles hence enhancing our knowledge of their track inside the detector.

The effect of these corrections on the momenta of different particles is illustrated in Figure 3.1. The mass dependence of these corrections can be clearly observed. Pions have up to 0.006 GeV correction in the lower momentum region. Protons have a correction up to 0.02 GeV in the higher momentum region and a correction up to 0.08 GeV in the lower momentum region.

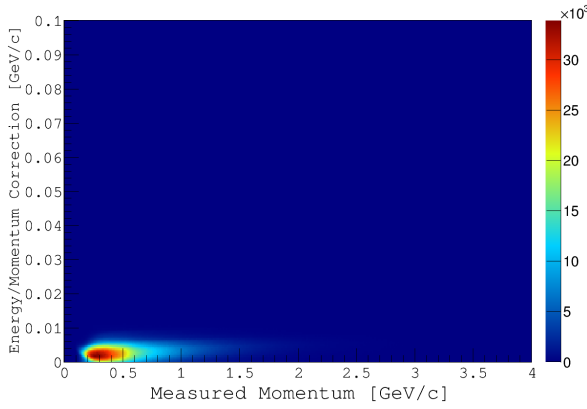
Similarly, kaons require a correction up to 0.05 GeV in the lower momentum region, and up to 0.02 GeV in the higher momentum region.

### 3.1.2 Event Vertex and Timing Cuts

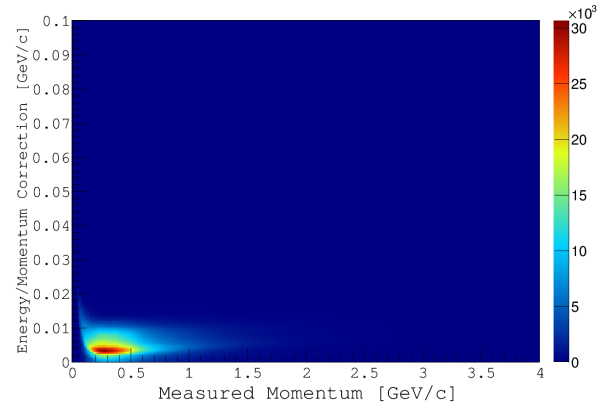
The target used for g12 was a 40 cm long, 4 cm in radius liquid hydrogen cell, placed 90 cm upstream inside the detector to enhance forward angle acceptance. To determine the position of the vertex of an event, reconstruction uses the distance of closest approach (DOCA) from neighboring charged tracks to extrapolate them back to their intersection point inside the target cell. This process can sometimes lead to badly reconstructed events due to equipment failures and changes in detector configuration, causing the beam to shift off target, thus producing tracks off the target cell walls and its support structure. To reduce the effect of this phenomenon, the following selections are performed:

1. The reconstructed vertex radius ( $r = \sqrt{x^2 + y^2}$ ) is selected to be  $< 2.5$ cm, taking into account the 5mm tracking resolution of g12.
2. The z position of reconstructed vertex is selected to fall in the (-110,-70) cm range.

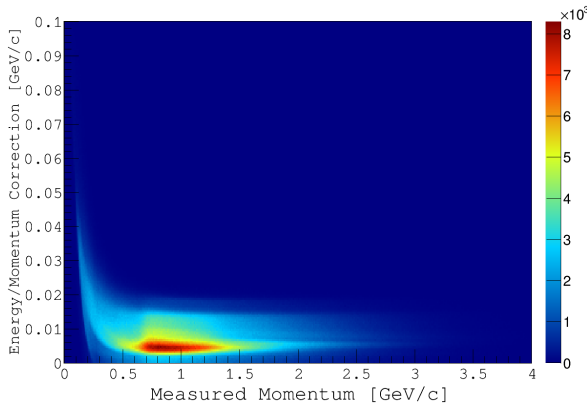
These selections ensure that the event vertex falls within the target cell and they eliminate any vertex position reconstruction inefficiencies. The selected green events are then subjected to vertex timing examination. In CLAS an event's start timing, or vertex timing, is determined using timing information from the accelerator and the start counter. The accelerator timing of the incoming electron is the most accurate timing known for an event in CLAS and is referred to as the RF time of the beam bucket. Once the timing of a scattering electron in the start counter is determined, it can be extrapolated to get its original RF beam bucket. The produced photon, therefore, acquires a time stamp that is later propagated to determine the event vertex timing. For a given CLAS event, a number of photons are considered acceptable candidates of the beam photon. Requiring that the incoming photon be close to the time-average of the measured tracks enforces the selection of the best candidate. About 12% of g12 events have more than two photons in the same beam bucket. However, most of these photons have different energies. Therefore, the triggering photon can be determined by selecting the photon with the highest energy in conjunction with its time proximity to the event vertex.



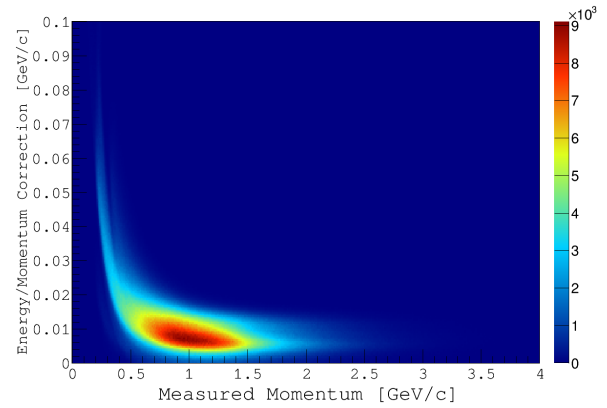
(a) Corrections' effect on  $\pi^-$  momenta.



(b) Corrections' effects on  $\pi^+$  momenta.



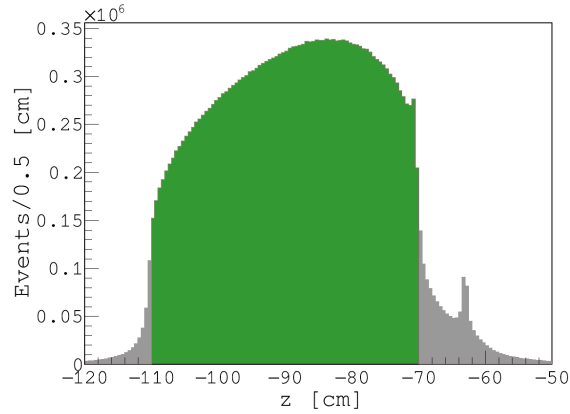
(c) Corrections' effects on  $K^+$  momenta.



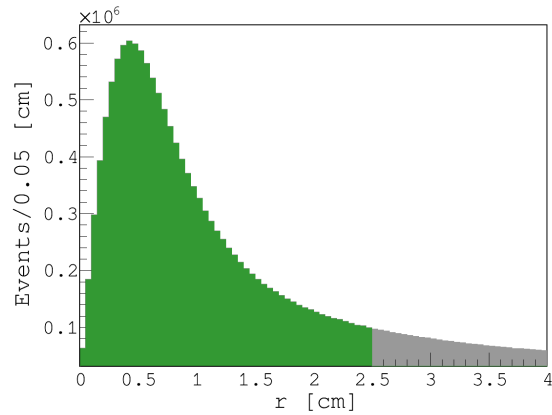
(d) Corrections' effects on Proton momenta.

Figure 3.1: The z and r distributions of  $pK^+\pi^+\pi^-[\pi^-]$  events. The blue region indicates the selected events.

An event's vertex timing is determined by averaging over the start counter vertex timing for every track in the event. Once the average time is determined, a triggering photon is selected using the prescription described earlier. The difference between the timing determined by the RF-corrected tagger (extrapolated accelerator time) and the start counter timing is then used to select the proper vertex time. Only events with a timing difference within 1 ns are selected as shown in Figure 3.3.



(a) The  $z$  vertex distribution



(b) The target cell radius

Figure 3.2: The  $z$  and  $r$  distributions of  $pK^+\pi^+\pi^-[X]$  events. The green region indicates the selected events.

### 3.1.3 Beta Cuts

As described in section 3.1.2, a significant number of CLAS events have more than one photon in the same beam bucket. This is taken care of by selecting the photon with the highest energy as the triggering photon. And while this method has high success rates, the wrong photon is sometimes selected. Selection of the wrong photon yields an incorrect value for the vertex start time, thus leading to "unphysical" speed measurements of tracks in the event. Unphysical speed measurements can be observed by examining the quantity  $\beta$ , which is determined using timing information from the start counter and the time of flight subdetectors. The stop time and position from the TOF are combined with the start time and position from the start counter to

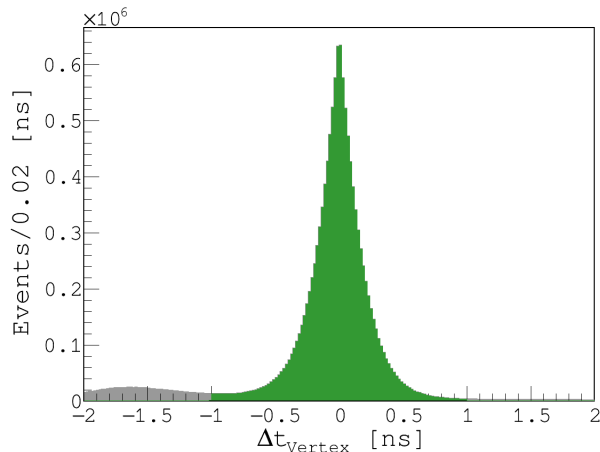


Figure 3.3: The difference in start counter time to the RF-corrected tagger vertex time of  $pK^+\pi^+\pi^-[\pi^-]$  events. The green region indicates the selected events.

get the total flight time of a particle. This time, combined with the distance the particle travels inside the detector, allows the determination of the speed of a charged track which gives  $\beta$  when divided by the speed of light as shown in Equation 3.1.

$$\beta = \frac{\text{particle speed } (v)}{\text{speed of light } (c)} = \frac{l_{TOF} - l_{SC}}{c(t_{TOF} - t_{SC})} \quad (3.1)$$

where  $l_{TOF}$  and  $l_{SC}$  are the path lengths from the vertex to the time of flight and start counter respectively, and  $t_{TOF}$  and  $t_{SC}$  are the respective hit times. Figure 3.4 shows the beta of  $\pi^+$  including the selected events. We seek to reduce this effect by selecting events with physical betas while taking into account timing resolution. Therefore, only events with  $\beta_{\pi^+} \geq 1.04$  are selected. The same selection is also performed for all the other tracks.

### 3.1.4 Beam Energy

The threshold photon beam energy required to produce the  $\Lambda K^+\pi^+\pi^-$  final state can be calculated using energy/momentum conservation. Assuming that the produced particles are at rest, the threshold center-of-momentum energy to produce the final states is simply the sum of all the rest masses of the final state particles. Therefore by applying energy/momentum conservation laws to the four vectors of the initial and final state particles, we could determine the minimum production energy using

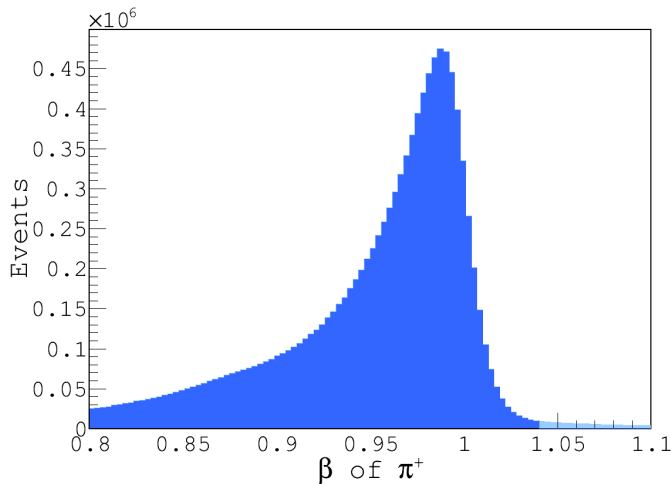


Figure 3.4: The *beta* distribution of  $\pi^+$  for all events. The darker blue region indicates the selected events.

$$E_\gamma = \frac{m_X^2 + m_r^2 - m_t^2 + 2m_X m_r}{2m_t} \quad (3.2)$$

where  $E_\gamma$  is the energy of the incident photon,  $m_X$  is the rest mass of the produced meson,  $m_r$  is the rest mass of the recoil baryon, and  $m_t$  is the rest mass of the target proton. To produce a  $\Lambda$  with a 1.4 GeV meson in the  $K^+\pi^+\pi^-$  system, photons with energies equal to or greater than 2.9 GeV are required. Information about the threshold production energy is important for making a beam selection, however it is not sufficient. The detector's configuration during the g12 run also plays a major role. For g12, photoproduced events were collected for energies between 1.1 and 5.5 GeV with the primary trigger configured to collect data for events with  $E \geq 4.4$  GeV. We therefore select events with beam energies higher than 4.4 GeV in correspondence with the detector configuration. Additionally, performing such a high beam energy cut enhances the t-channel peripheral production of mesons and comfortably sits above the regime of s-channel baryon production.

### 3.1.5 Kinematic Fitting

Kinematic fitting is a mathematical process that uses physical constraints, such as conservation of energy and momentum or vertex position to improve measured quantities. The fitter used in this analysis was developed by Dustin Keller [53] for CLAS data. It uses the Least Squares

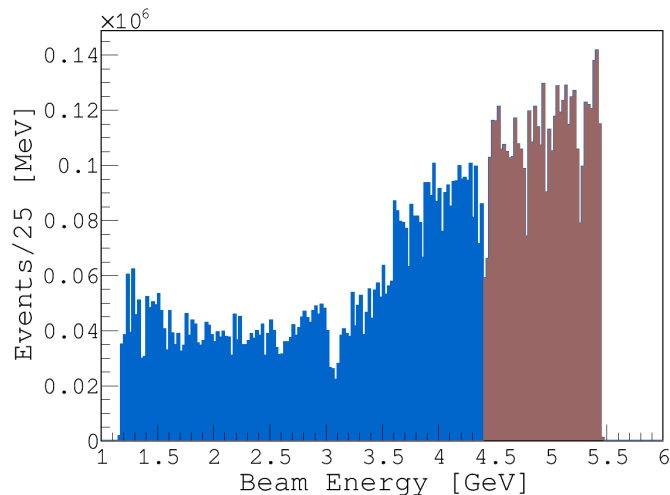


Figure 3.5: The beam profile of the  $pK^+\pi^+\pi^-[X]$  events. The brown area indicates the selected events.

Fitting techniques in conjunction with the method of Lagrange Multipliers to enforce the energy-momentum conservation, then performs a  $\chi^2$  minimization using the measured quantities. To kinematically fit the data in this analysis, the fitter is first provided with the kinematically corrected four-momenta and an initial calculated covariance matrix. This matrix contains information about the kinematic variables of reconstructed tracks, however, it does not account for multiple scattering errors and other energy losses. The fitter corrects for that by scaling the matrix elements and adjusting the kinematic variables to fall within the allowed constraints determined by the correlation matrix. A kinematic fit is generally categorized according to the number of constraints and variables included in the fitting procedure. For a  $k$  measured constraints and  $j$  unknown variables, the effective number of constraining elements is  $(k-j)$  and the fit is referred to as a " $(k-j)C$ " fit. For this analysis, the missing particle is hypothesized to be a " $\pi^-$ ". Therefore the three components of the missing particle momentum are treated as the unmeasured variables, while the energy-momentum conservation of the channel provides four measured constraints, categorizing the fit in hand as a " $1C$ " fit. To assess the quality of the fit, the fitter returns two quantities: the pulls (Equation 3.3) and the  $\chi^2$  distribution (Equation 3.4). The pull for the initial value,  $\eta_i$ , and final value,  $\eta_f$ , of the measured quantities is

$$z = \frac{\eta_i - \eta_f}{\sqrt{\sigma_{\eta_i}^2 - \sigma_{\eta_f}^2}} \quad (3.3)$$

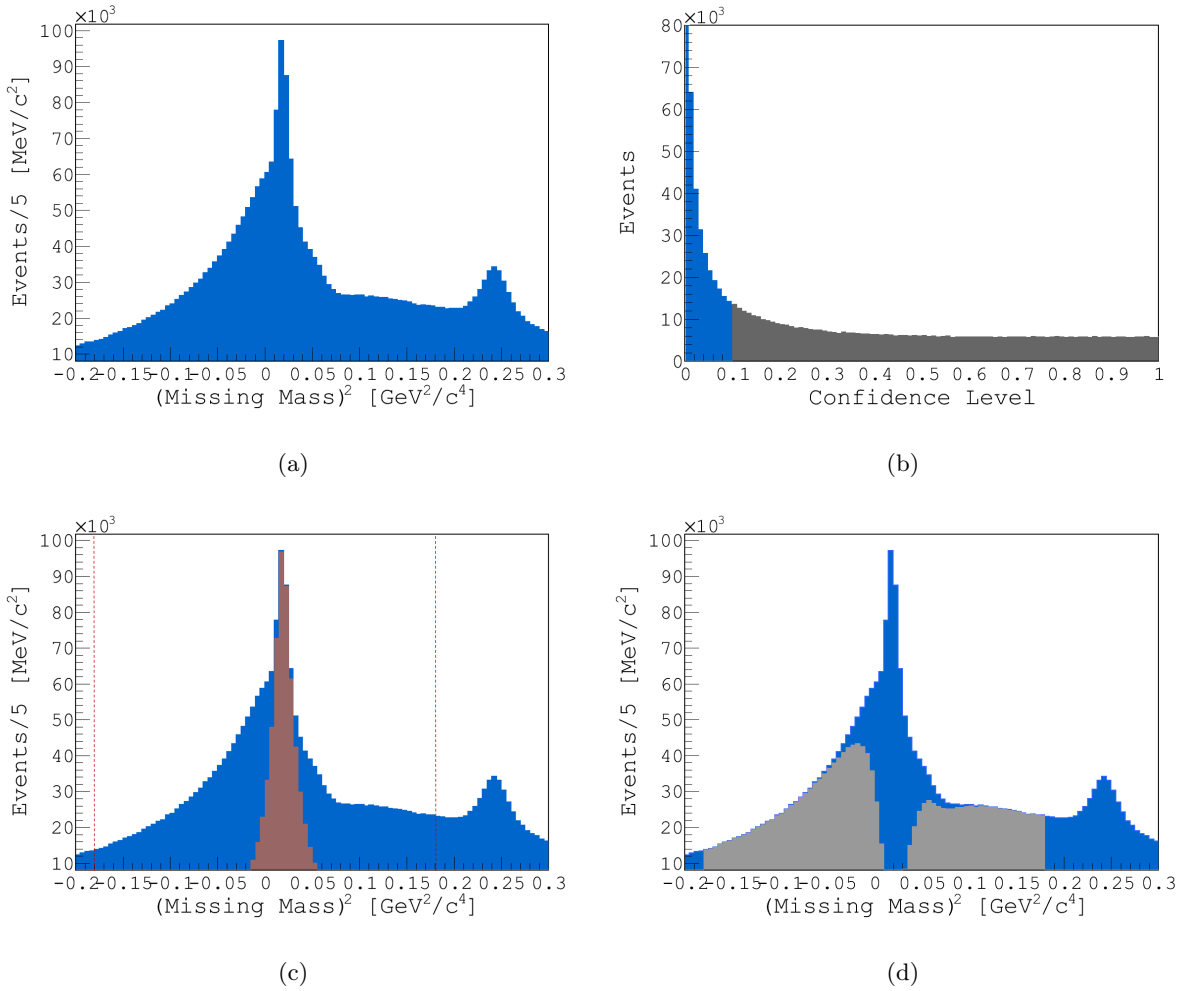


Figure 3.6: The missing mass squared off ( $pK^+\pi^+\pi^-$ ) distribution. The region between the two red lines indicates the fitted events. The dark gray region in Figure (b) represents the selected events. The shaded areas in Figures (c) and (d) represent the selected fitted events and the discarded fitted events respectively.

where  $\sigma_{\eta_i}^2$  and  $\sigma_{\eta_f}^2$  are the corresponding covariance matrix elements for  $\eta_i$  and  $\eta_f$  respectively. The pulls are expected to peak around 0 and to have a sigma close to 1. A significant deviation from the width or the mean of the pull distribution is an indication of wrongly estimated covariance matrix errors and scaling factors.

The confidence level, CL, is the integral of the  $\chi^2$  probability density function,  $f(z, n)$ , for  $n$  degrees of freedom;

$$CL = \int_{\chi^2}^{\infty} f(z, n) dz \quad (3.4)$$

A confidence level that is generally flat is an indication of a good fit. Events described by the hypothesis will result in a uniform distribution from 0 to 1, and those poorly described will result in a sharp peak at zero.

To decide which events to be kinematically fitted, we look at the squared invariant mass of the missing particle as shown Figure 3.6. The four-momentum of the missing particle, and the invariant mass are reconstructed using the four-momenta of the detected particles ( $P_{K^+} P_P P_{\pi^+} P_{\pi^-}$ ) and the tagged photon beam ( $P_\gamma$ ), according to the formulas below:

$$P_{Miss} = (P_\gamma + P_{Target}) - (P_{K^+} + P_P + P_{\pi^+} + P_{\pi^-}) \quad (3.5)$$

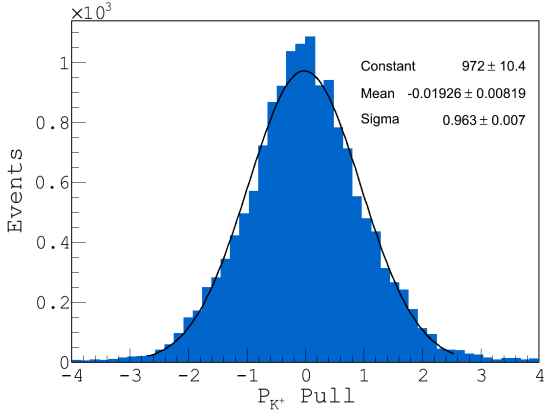
and

$$M_{Miss}^2 = |P_{Miss}^\mu \cdot P_{Miss,\mu}| \quad (3.6)$$

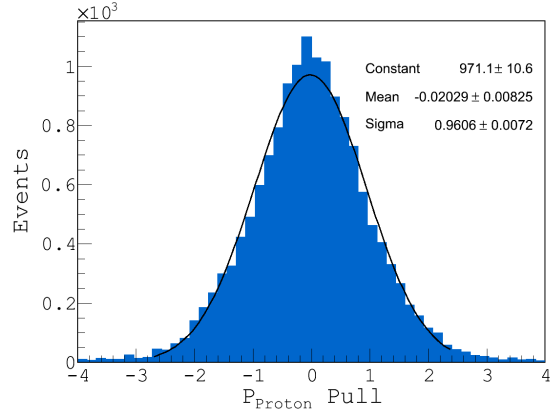
where  $M_{Miss}$  is the invariant mass of the missing particle and  $P_{Miss}$  is its four-momentum. The fitter is provided with events whose invariant mass squared is between -0.18 GeV and 0.18 GeV. This relatively large interval is arbitrarily chosen and takes the resolution of a pion into consideration. The enhancement around 0.24 GeV is a  $K^-$ , and corresponds to the  $\gamma p \rightarrow pK^+\pi^+\pi^- [K^-]$  channel. The final results for the  $pK^+\pi^+\pi^-\pi^-$  fit are summarized in Figure 3.6. The confidence level is as expected, mostly flat with a peak around zero that represents the poorly reconstructed events. The pulls in Figure 3.7 are centered around 0 and have a sigma close to 1, thus implying the good quality of the fit. The brown region in Figure 3.6(c) indicates events selected with a confidence level larger than 10%. The grey region in Figure 3.6(d) represents the discarded fitted events. About 25% of the fitted events are selected for the exclusive  $pK^+\pi^+\pi^-\pi^-$  analysis.

## 3.2 Final Event Selection

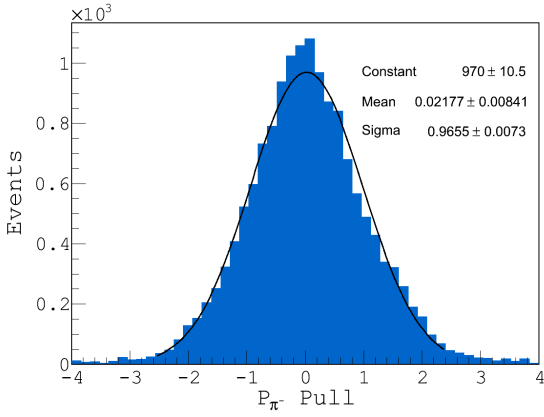
The main purpose of this analysis is to analyze the exclusive  $pK^+\pi^+\pi^-\pi^-$  final state in search for observable resonances in the  $K^+\pi^+\pi^-$  system peripherally produced off a  $\Lambda$  baryon.



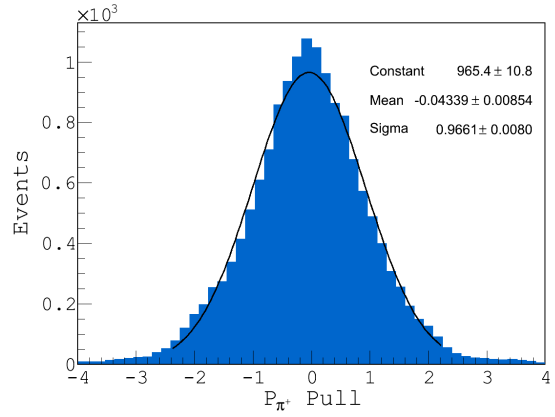
(a)  $K^+$  momentum pull.



(b) Proton momentum pull.



(c)  $\pi^-$  momentum pull.



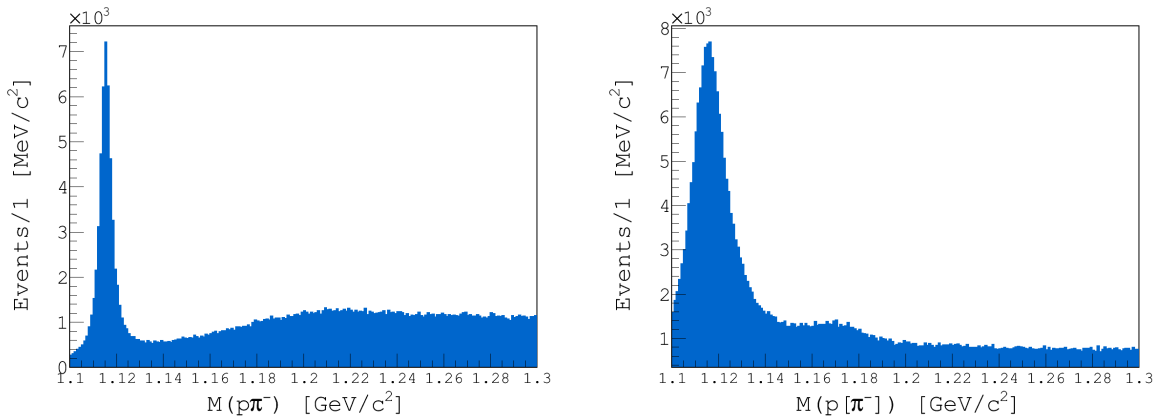
(d)  $\pi^+$  momentum pull.

Figure 3.7: The pulls of the kinematic fit related to the momenta of the particles. They are centered close to zero and have a sigma close to 1.

This is followed by performing a proper partial wave analysis to extract the dynamics and angular contributions of different strange states from the  $K^+\pi^+\pi^-$  final state. The success of the partial wave analysis heavily depends on our ability to isolate signals and reduce background from the meson system. In what follows, we discuss the different selections that were deemed essential to reduce the background and enhance the peripheral production of a  $(K\pi\pi)$  resonance.

### 3.2.1 $\Lambda \rightarrow p\pi^-$ Selection

The  $\Lambda$  baryon in this analysis is identified through its dominant decay mode:  $p\pi^-$ . In the exclusive  $pK^+\pi^+\pi^-\pi^-$ , one of the negatively charged pions is associated with the meson system,



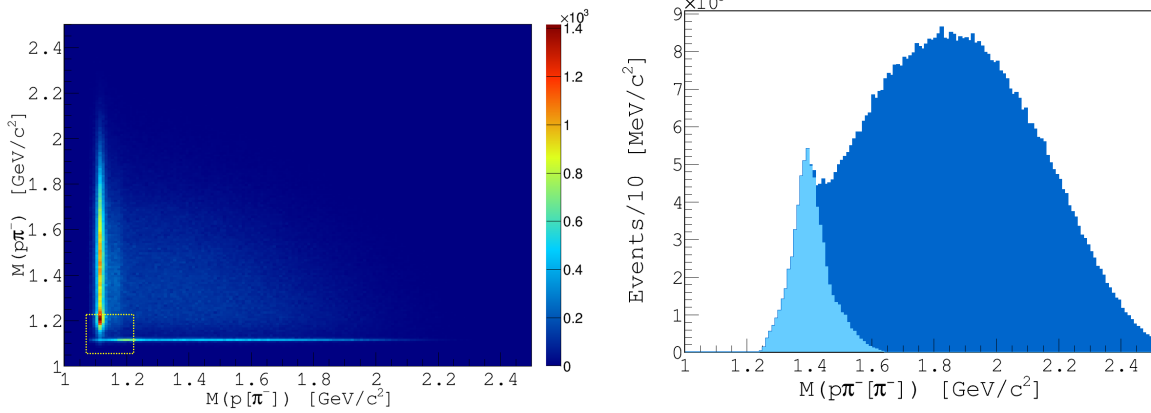
(a) The invariant mass of the  $(p\pi^-)$  system.

(b) The invariant mass of the  $(p\pi^-_{Missing})$  system.

Figure 3.8: The invariant masses of  $(p\pi^-)$  and  $(p[\pi^-])$  systems. Peaks around  $1.1 \text{ GeV}/c^2$  are clear indications of  $\Lambda$  baryons.

while the other originates from the  $\Lambda$  decay. To thoroughly understand the origin of either pion, we first examine the corresponding  $p\pi^-$  invariant mass spectra. Figure 3.8 clearly illustrates a  $\Lambda$  peak in both invariant mass distributions. The difference in the peak width is due to the nature of the resolution of the reconstructed missing pion. These two  $\Lambda$  peaks are clear indications that either pion can originate from the baryon vertex. To select these  $\Lambda$  events, we examine the two-dimensional plot of the  $p\pi^-$  and  $p[\pi^-]$  invariant masses, as shown in Figure 3.10. The vertical and horizontal narrow bands are representations of the  $\Lambda$  events. The area of overlap between 1-1.2 GeV constitute events where both pions overlap at small phase space. Such events could indicate a possible resonance coupling to  $\Lambda\pi^-$ . A sample of these events is chosen to examine the  $(p\pi^-\pi^-)$  system (Figure 3.9). The bright blue region represents the selected overlap area which evidently corresponds to the  $\Sigma^-(1385)$  baryon decaying to  $\Lambda\pi^-$ . These events are thus excluded from the final data selection, and only events enclosed inside the red boxes (Figure 3.10) are selected. About 30% of the selected  $\Lambda$ 's decay to a proton and a detected  $\pi^-$ .

Features of the selected events are shown in Figure 3.11. A peak in the lower  $(K\pi\pi)$  mass region is evident around 1.4 GeV. The large shoulder in the higher mass region, however, makes it hard to observe any other possible peaks except for a relatively small enhancement around 1.75 GeV. A clear and sharp  $K^*(892)$  sitting on a relatively large background is observed around 0.9 GeV in the  $(K^+\pi^-)$  system, with a small enhancement in the higher mass region peaking



(a) The invariant mass of  $(p\pi^-)$  versus the invariant mass of  $(p\pi^-)$ . (b) The invariant mass distribution of  $(p\pi^-\pi^-)$ .

Figure 3.9: The 2 dimensional plot of the invariant masses of  $(p\pi^-)$  and  $(p[\pi^-])$  (a), The invariant mass distribution of the  $(p\pi^-\pi^-)$  system (b). Events in bright blue in (b), correspond to the sample enclosed in the yellow box in (a).

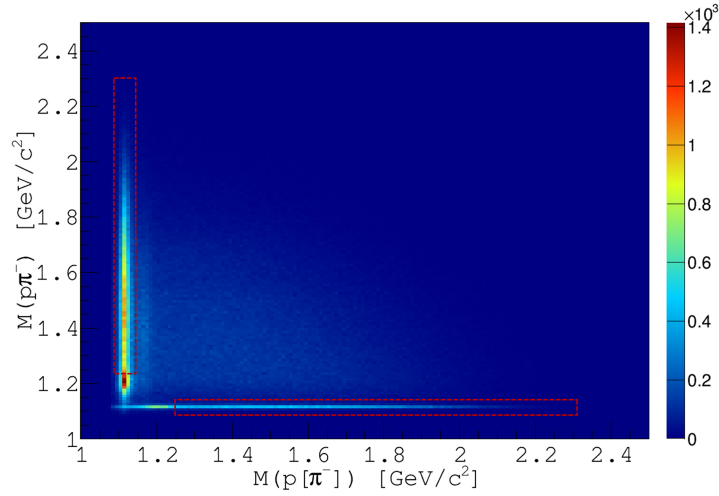
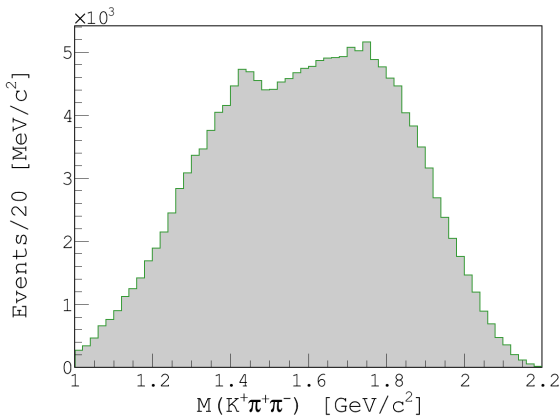
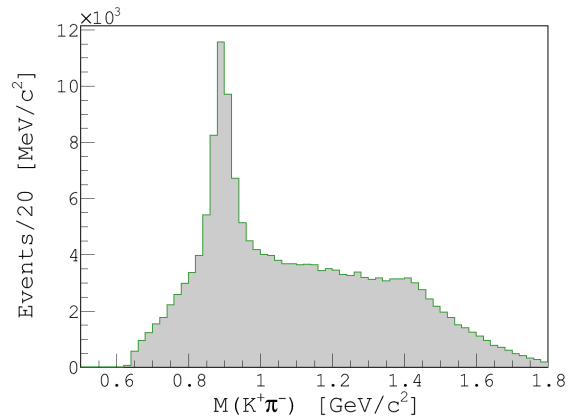


Figure 3.10: The invariant mass of  $(p\pi^-)$  versus the invariant mass of  $(p\pi^-)$ . Events enclosed inside the red boxes correspond to the  $\Lambda$  selection.

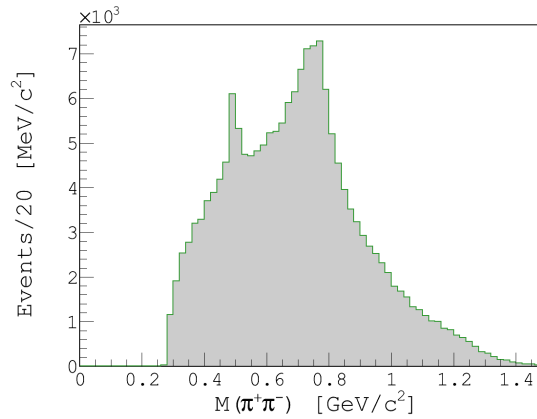
around 1.4 GeV. The peaks around 0.5 GeV and 0.75 GeV in the  $(\pi^+\pi^-)$  system correspond to  $K_s$  and  $\rho(770)$  respectively. The shoulder that the  $K_s$  sits on is due to reflections from  $K^+\pi^-$ . The presence of this state is an indication that the PID's of pions and kaons are compromised,



(a) The invariant mass of  $(K^+\pi^+\pi^-)$ .



(b) The invariant mass of  $(K^+\pi^-)$ .



(c) The invariant mass of  $(\pi^+\pi^-)$ .

Figure 3.11: The invariant mass of  $K^+\pi^+\pi^-$  (a),  $K^+\pi^-$  (b), and  $\pi^+\pi^-$  (c) for the exclusive  $\gamma p \rightarrow \Lambda K^+\pi^+\pi^-$  sample following the  $\Lambda$  selection.

this is due to limitations in the  $\pi/K$  separation in CLAS as discussed in section 2. Eliminating this effect is essential for obtaining a clean and reliable sample that would later be used for partial wave analysis.

### 3.2.2 Baryon Background Reduction

The main source of background in this analysis has been found to be baryonic in nature. As discussed in section 3.2,  $\Sigma(1385)^-$  was clearly present in the  $\Lambda\pi^-$  invariant mass, and it was eliminated by rejecting the area of overlap between the two  $\Lambda$ 's. This cut however did not completely eliminate the baryonic background. A major contribution from the  $\Sigma(1385)^+$  was

found in the invariant mass of  $\Lambda\pi^+$  as shown in Figure 3.13. This state corresponds to the  $\gamma p \rightarrow \Sigma(1385)K^*(892)$  channel. A two dimensional plot (Figure 3.12) of the  $(\Lambda\pi^+)$  and the  $(K^+\pi^-)$  invariant masses, shows the correspondence between the two states in that channel. To exclude this state, only events with a  $(\Lambda\pi^+)$  invariant mass greater than 1.47 GeV are chosen as shown in Figure 3.13.

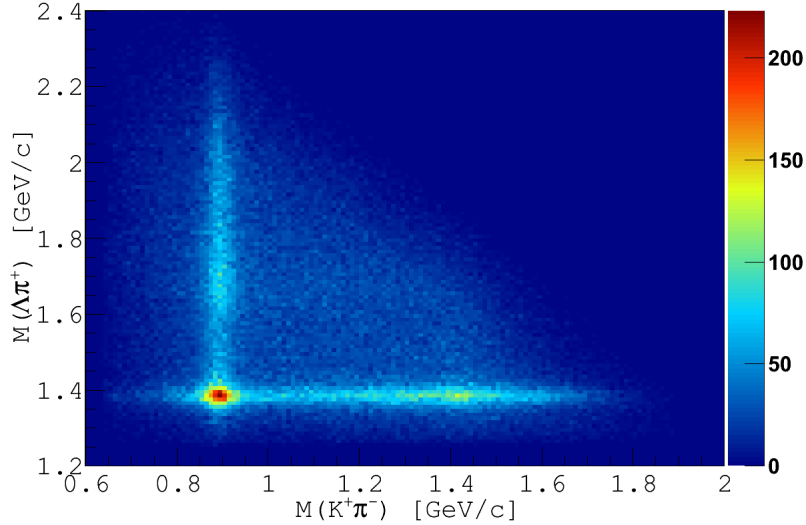


Figure 3.12: The invariant mass of  $\Lambda\pi^+$  versus the invariant mass of  $K^+\pi^-$ .

The effect of this cut on the features of the data is illustrated in Figure 3.14. The enhancement around 1.4 GeV in the  $K^+\pi^+\pi^-$  invariant mass is now more prominent, with the shoulder in the higher mass region relatively smaller. The small peak around 1.43 GeV in the  $K^+\pi^-$  invariant mass was eliminated with the cut, and the background on which the  $K^*(892)$  sits on is now less significant. The  $K_s$  and  $\rho$  in the  $\pi^+\pi^-$  invariant mass are still prominently present, sitting on a relatively large background.

### 3.2.3 Eliminating Particle Misidentification

As we discussed in section 3.2, one of the major sources of background is the misidentification of particles due to CLAS's limited  $\pi/K$  separation capabilities. As a matter of fact, CLAS is only capable of successfully separating pions from kaons up to 1.5 GeV momenta. Beyond this point, PID is compromised and pions can hardly be distinguished from kaons. This analysis, however, takes advantage of the strangeness enforcement in the meson vertex due to the recoil

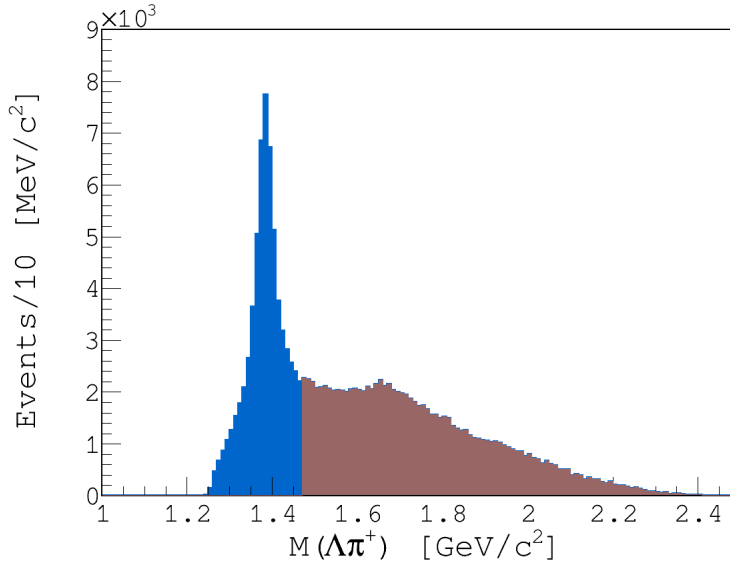


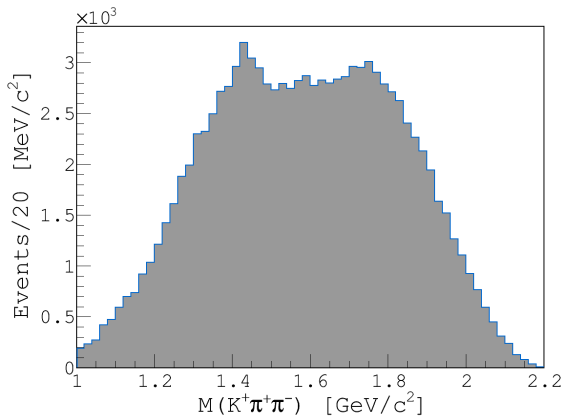
Figure 3.13: The invariant mass of  $\Lambda\pi^+$ . The area in brown corresponds to selected events.

$\Lambda$  in the baryon vertex. As a result of a good  $\Lambda$  selection from the initial data sample, the  $\pi/K$  separation at this point is expected to be better in the high momentum region. To visualize the relation between PID and momentum, a two dimensional plot of  $\beta$  of pions and kaons is plotted as a function of their corresponding momenta as shown in Figure 3.15.

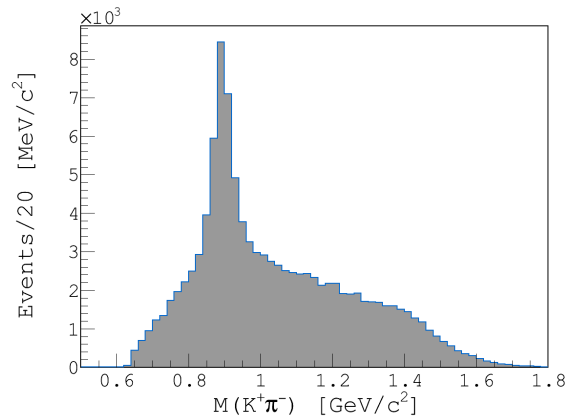
The bands in Figure 3.15 correspond to different particles. The difference in the shape is due to the nature of the relationship between the  $\beta$  of the particle and its mass as evident by equation 3.7 below:

$$\beta = \frac{p}{E} = \frac{p}{\sqrt{m^2 + p^2}} \quad (3.7)$$

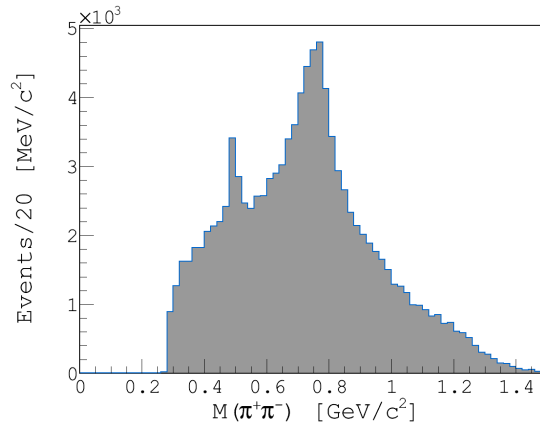
where  $p$  is the momentum of the particle and  $m$  is its mass. The separation momentum limit between  $\pi$  and  $K$  can be clearly seen in Figure 3.15. PID is compromised when the momenta of pions and kaons approach 1.9 GeV, making it hard to separate one from the other. As a result, it is more likely that higher momentum kaons are mislabeled pions. Misidentification was seen to severely affect the  $\pi^+\pi^-$  spectrum (Figure 3.16, as evident by the existence of a  $K_s$ ). To further investigate its origin, the mass of the  $\pi^+\pi^-$  system is plotted against the momentum of kaons as shown in Figure 3.16. The  $K_s$  is clearly more prominent in the higher momentum region as a result of particle of misidentification. To eliminate the effect of this phenomenon,



(a) The invariant mass of  $(K^+\pi^+\pi^-)$ .



(b) The invariant mass of  $(K^+\pi^-)$ .



(c) The invariant mass of  $(\pi^+\pi^-)$ .

Figure 3.14: The invariant mass of  $K^+\pi^+\pi^-$  (a),  $K^+\pi^-$  (b), and  $\pi^+\pi^-$  (c) for the exclusive  $\gamma p \rightarrow \Lambda K^+\pi^+\pi^-$  sample following the sigma elimination cut.

events with K momentum higher than 1.9 GeV are excluded from further analysis. The effect of this cut on the features of the data are shown in Figure 3.17.

Figure 3.17b shows a decrease in the background under the  $K^*(892)$ . Meanwhile the shoulder around 1.4 GeV is still present indicating the possibility of a  $K_2^*(1430)$  in that region. The  $K_s$  signal in the  $\pi^+\pi^-$  system is significantly reduced compared to its intensity in Figure 3.14c. The low mass region in the  $K^+\pi^+\pi^-$  system is not significantly affected by this cut, however the higher mass shoulder is now more defined compared to Figure 3.14(a).

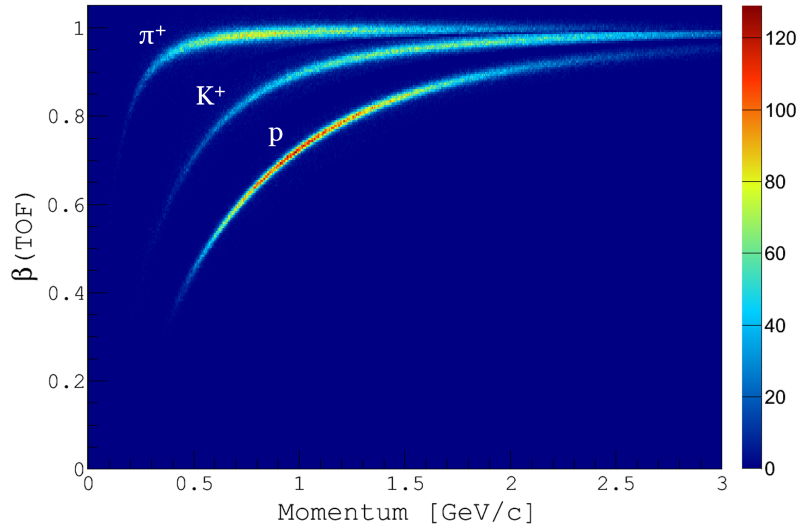


Figure 3.15: An illustration of the relation between momentum and PID. The momenta of proton,  $\pi$  and K (x-axis) are plotted against their respective  $\beta$ 's (y-axis).

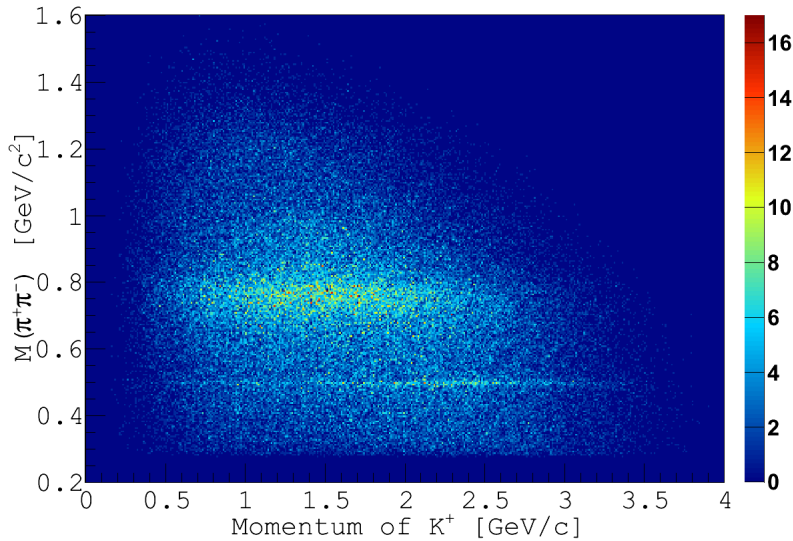
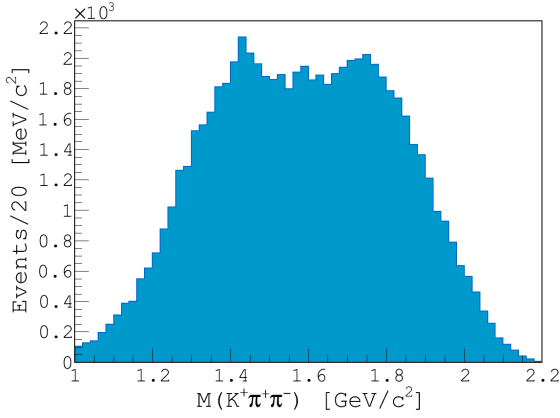


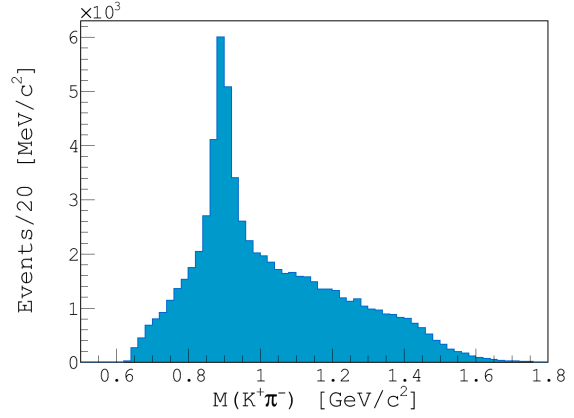
Figure 3.16: A two dimensional plot of the mass of  $\pi^+\pi^-$  as a function of the momenta of kaons. The  $K_s$  is clearly more prominent in the higher momentum region.

### 3.2.4 Momentum Transfer Cut

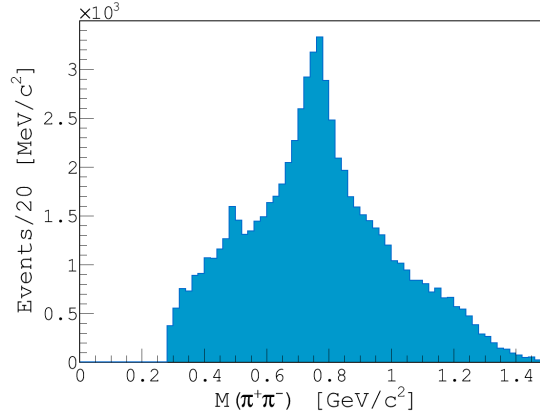
The last quantity to look at before finalizing data selection is the momentum transfer  $t$ . Being one of the Mandelstam variables,  $t$  provides essential information about the nature of the



(a) The invariant mass of  $(K^+\pi^+\pi^-)$ .



(b) The invariant mass of  $(K^+\pi^-)$ .



(c) The invariant mass of  $(\pi^+\pi^-)$ .

Figure 3.17: The invariant mass of  $K^+\pi^+\pi^-$  (a),  $K^+\pi^-$  (b), and  $\pi^+\pi^-$  (c) for the exclusive  $\gamma p \rightarrow \Lambda K^+\pi^+\pi^-$  sample following the K momentum cut.

interaction between the beam and the target. The Mandelstam variables  $s$ ,  $t$  and  $u$  are defined as follows:

$$\begin{aligned}
 s &= (p_\gamma^\mu + p_p^\mu)^2 = (p_X^\mu + p_\Lambda^\mu)^2 \\
 t &= (p_\gamma^\mu - p_X^\mu)^2 = (p_p^\mu - p_\Lambda^\mu)^2 \\
 u &= (p_\gamma^\mu - p_\Lambda^\mu)^2 = (p_p^\mu - p_X^\mu)^2
 \end{aligned} \tag{3.8}$$

where

- $p_\gamma^\mu$  is the four-momentum of the beam
- $p_p^\mu$  is the four-momentum of the target
- $p_\Lambda^\mu$  is the four-momentum of the recoil  $\Lambda$
- $p_X^\mu$  is the four-momentum of the  $K\pi\pi$  resonance

Figure 3.18 shows the distribution of the momentum transfer  $t$  for events that survived all the previous cuts. The distribution is expected to fall exponentially according to  $Ae^{-bt}$  for a peripheral meson production [51]. In photoproduction, the peripheral production of a meson occurs when the incident photon interacts with the cloud of virtual mesons around the nucleons rather than directly with the nucleon, thus transferring little momentum to it. With higher momentum transfer to the nucleon, it is more likely that this transferred momentum would cause the excitation of the nucleon. For these reasons, it is important to keep the transferred momentum to a minimum.

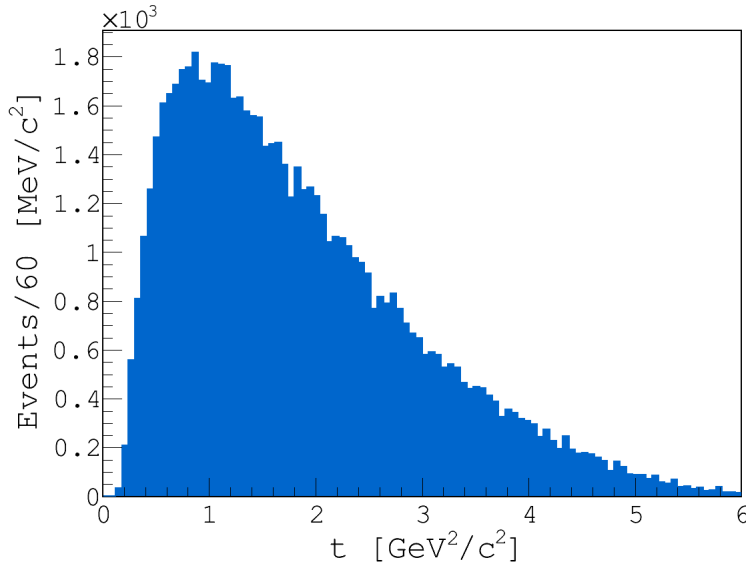


Figure 3.18: The momentum transfer  $t$ .

Instead of using the momentum transfer  $t$  for this selection, we use the quantity  $t'$  defined as

$$t' = t - t_{min}$$

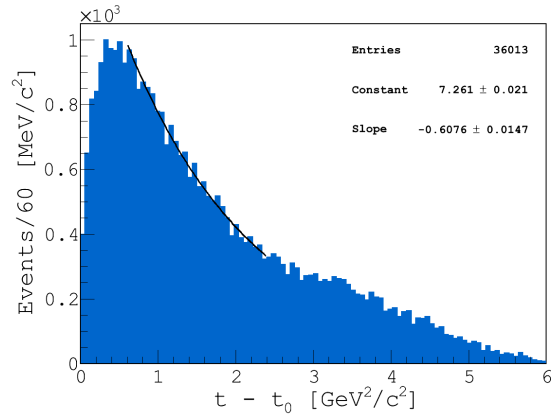
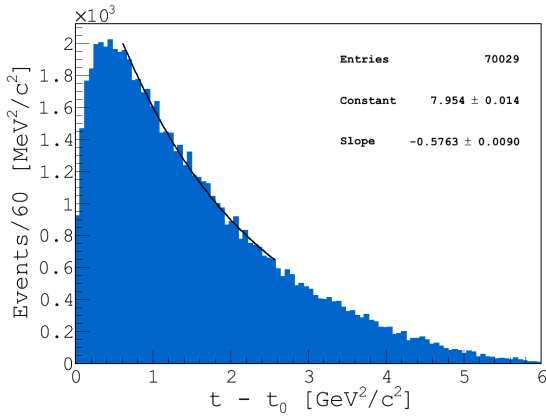
$$t_{min} = \left[ \frac{m_{\Lambda}^2 - m_X^2 - m_p^2}{2\sqrt{s}} \right] - (p_{\gamma}^{CM} - p_X^{CM})^2 \quad (3.9)$$

$t'$  is the excess momentum transfer and  $t_{min}$  is the minimum momentum transfer required to produce a resonance of mass  $m_X$  with momentum  $p_X^{CM}$  in the center-of-mass frame.  $p_{\gamma}^{CM}$  is the center-of-mass beam momentum,  $m_{\Lambda}$  is the mass of the recoil  $\Lambda$ , and  $m_p$  is the mass of the target proton. The excess momentum transfer  $t'$  is illustrated in Figure 3.22a. Similar to  $t$ , it falls exponentially with a sharp cut off close to zero due to the CLAS acceptance. Since  $t_{min}$  depends on the invariant mass of the resonance  $X$  in the  $K\pi\pi$  system, the slope of  $t'$  is expected to vary within the different regions of the  $K\pi\pi$  system and vice versa. In Figures 3.22b and 3.22c, the  $t'$  distribution is examined for two  $K\pi\pi$  mass regions. Slightly steeper slopes are observed in the low mass region compared to higher  $K\pi\pi$  mass events. This slight difference is irrelevant in peripheral production as only low momentum transfer events are chosen in order to enforce the exchange of a  $K^+$  between the baryon vertex and the meson vertex.

To determine the effectiveness of limiting the excess momentum transfer on reducing the background, the invariant masses of the  $K\pi$ ,  $\pi\pi$ , and  $K\pi\pi$  systems are examined over a range of cuts in  $t'$ . The results are presented in Figure 3.20. General features of the data remained the same for different  $t'$  cuts. Significant reductions in the background are observed specifically in the  $K^+\pi^-$  system where the  $K^*$  now sits on a relatively lower background. The same applies to the  $\pi^+\pi^-$  system where a significant decrease in background events is observed. While choosing a lower  $t'$  cut could possibly result in further background reductions, limited statistics dictated choosing the lowest  $t'$  cut to be  $0.6 \text{ GeV}^2/c^2$ . This range provides the analysis with a considerable number of events to perform a successful partial wave analysis, and is low enough to enhance the peripheral production of resonances in  $K\pi\pi$ .

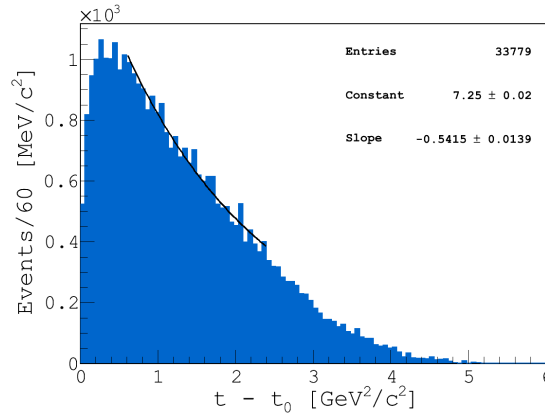
### 3.3 Features of the Final $\gamma p \rightarrow \Lambda K^+ \pi^+ \pi^-$ Sample

With the background now reduced to acceptable levels, the final features of this  $K^+\pi^+\pi^-$  system can be examined for resonances. Of the 164,418 exclusive  $\Lambda K^+\pi^+\pi^-$  events, 16,157 events survived our cuts, making this dataset the largest  $\Lambda K^+\pi^+\pi^-$  photoproduction dataset to date. A summary of the cuts and their corresponding selected number of events is presented in Table 3.1.



(a) The  $t'$  distribution for the full  $K\pi\pi$  mass range

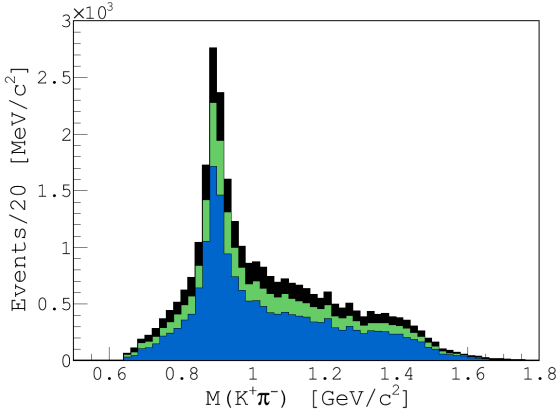
(b) The  $t'$  distribution for the low  $K\pi\pi$  mass range



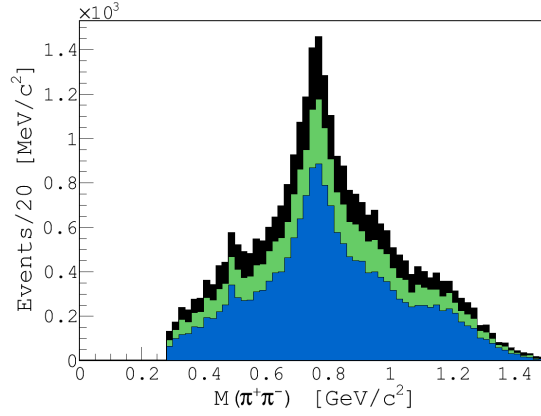
(c) The  $t'$  distribution for the high  $K\pi\pi$  mass range

Figure 3.19: Exponential fits for the  $t'$  distribution over the full  $K\pi\pi$  mass range (a), in the low mass region between 1 and 1.6 GeV (b), and in the high mass region between 1.6 and 2.2 GeV (c). the values of the slopes are  $-0.5763$ ,  $-0.6076$ , and  $-0.5415$  respectively.

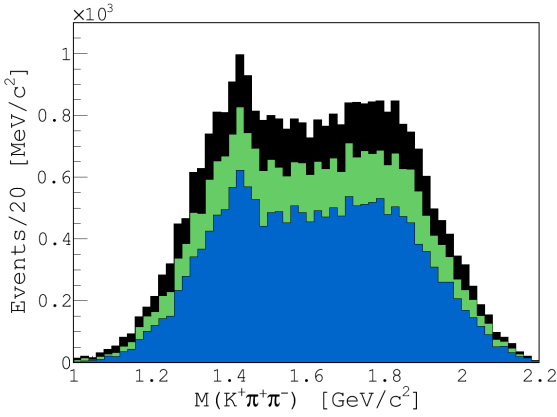
Past Kaon beam experiments have reported two dominating decay modes in the  $K\pi\pi$  system, the  $\rho K$  and  $K^*(892)\pi$  modes. The accepted  $K^+\pi^-\pi^0$  mass spectrum (Figure 3.20(a)) shows a sharp  $K^*(892)$  sitting on a relatively low background with a small enhancement around 1.4 GeV equivalent to the  $K_2^*(1430)$ . Figure 3.20(b) shows the accepted  $\pi^+\pi^-\pi^0$  mass distribution where a  $\rho(770)$  dominates sitting on a considerably high background, with a shoulder around 1.2 GeV assumed to be due to an  $f_2(1270)$ . The accepted  $K^+\pi^+\pi^-\pi^0$  mass distribution for this final selection is presented in Figure 3.21(a). A considerable enhancement in the low mass



(a) The  $t'$  distribution for the full  $K\pi\pi$  mass range



(b) The  $t'$  distribution for the low  $K\pi\pi$  mass range



(c) The  $t'$  distribution for the high  $K\pi\pi$  mass range

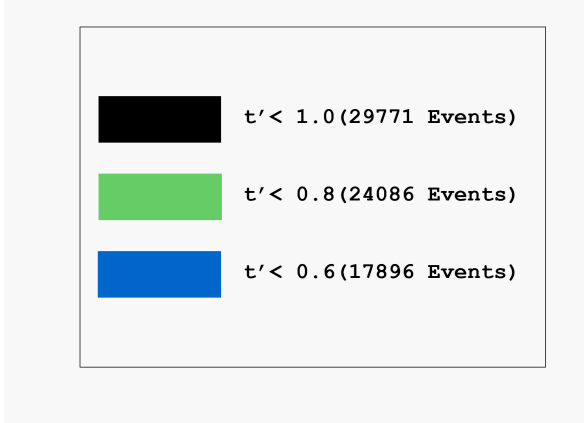
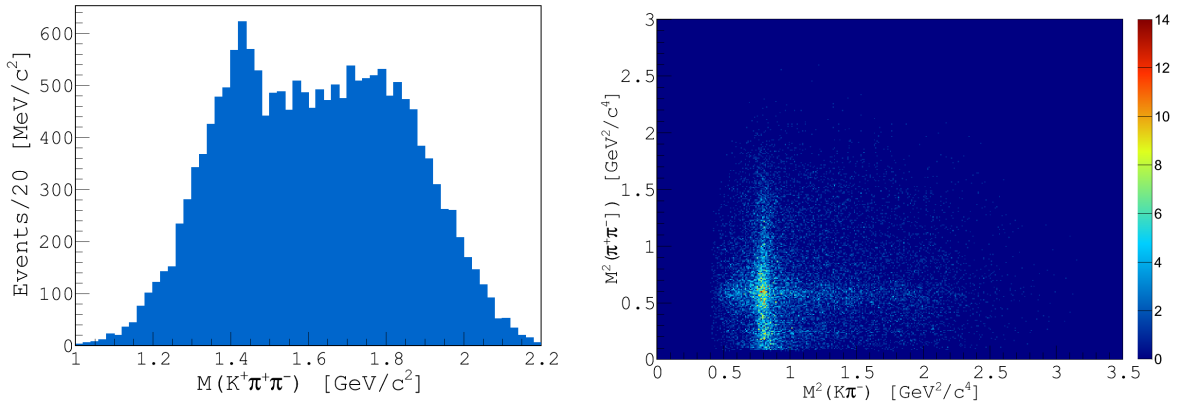


Figure 3.20: Features of the data: the invariant mass of  $K^+\pi^-$  in (a),  $\pi^+\pi^-$  in (b), and  $K^+\pi^+\pi^-$  in (c) for various  $t'$  selections. The final event sample uses the  $t'$  cut shown in blue.

region between 1.3 GeV and 1.5 GeV is evident, while the higher mass region does not exhibit clear resonance behavior except for a shoulder around 1.8 GeV. The final  $K^+\pi^+\pi^-$  sample consisted of 16,157 events from 164K events of the  $\Lambda K^+\pi^+\pi^-$  topology. With the background reduction finalized, and the features of the data thoroughly examined, a partial wave analysis was performed to extract resonance properties and understand the angular structure of the dataset.

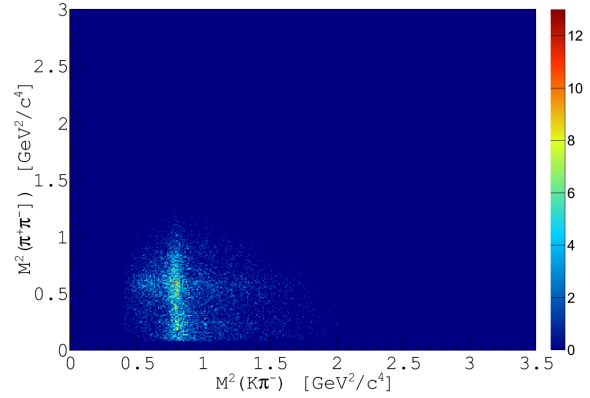
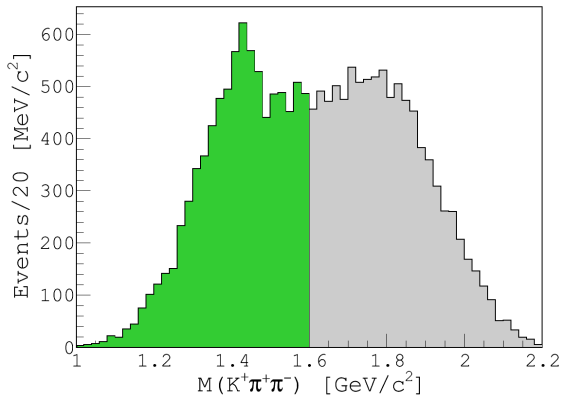
Table 3.1: A summary of the event counts before and after each cut used to select the final sample  $\gamma p \rightarrow \Lambda K^+ \pi^+ \pi^-$  events for PWA.

Description	Selection	Events In	Events Out
Vertex within target length	$-110 < z < -70$ cm	25,238,560	23,374,333
Vertex within target radius	$r < 2.5$ cm	23,374,333	14,155,638
Physical $\beta$ 's for all particles	$0 < \beta_{\pi,proton,K} < 1.04$	14,155,638	12,382,383
Event vertex timing	$ \Delta t  < 1.002$ ns	12,382,383	11,137,129
High beam energy	$E_\gamma > 4.4$ GeV	11,137,129	4,522,670
Kinfit $MM^2$ range	$-0.18 < MM^2 < 0.18$ GeV <sup>2</sup>	4,522,670	2,297,665
Confidence Level	CL > 0.1	2,297,665	596,583
Combined $\Lambda$ selection	$1.096 < M(p\pi^-) < 1.136$ GeV	596,583	160,007
Elimination of $\Sigma^+(1385)$	$M(\Lambda\pi^+) > 1.46$ GeV	160,007	98,812
PID Selection	$P_{K^+} < 1.9$ GeV	98,812	64,045
Low momentum transfer ( $t'$ )	$t' < 0.6$ GeV <sup>2</sup>	64,045	16,157

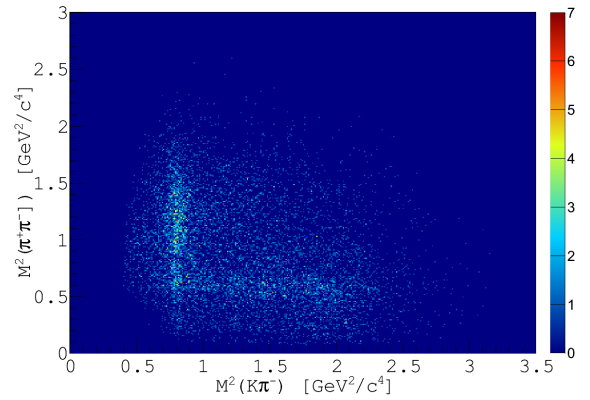
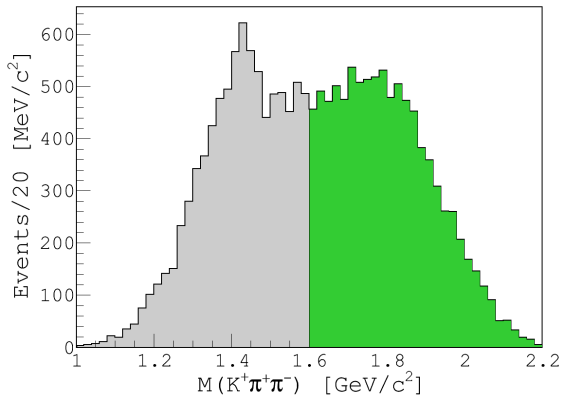


(a) The  $K^+ \pi^+ \pi^-$  invariant mass with low range selection. (b) The dalitz plot of  $K^+ \pi^+ \pi^-$  for low mass events.

Figure 3.21: The invariant mass of the final  $K^+ \pi^+ \pi^-$  sample used in the partial wave analysis (a), and the dalitz plot of this selected sample (b).



(a) The  $K^+\pi^+\pi^-$  invariant mass with low range selection. (b) The dalitz plot of  $K^+\pi^+\pi^-$  for low mass events.



(c) The  $K^+\pi^+\pi^-$  invariant mass with high range selection. (d) The dalitz plot of  $K^+\pi^+\pi^-$  for high mass events.

Figure 3.22: Dalitz distributions for the low  $K\pi\pi$  mass region (**top**), and high mass region **bottom**. Green regions on the left correspond to events used in the Dalitz plots on the right.

# CHAPTER 4

## PARTIAL WAVE ANALYSIS FORMALISM

The  $K\pi\pi$  meson system in this analysis has demonstrated resonance behavior in the low mass region, but did not provide definite identification of the state responsible for this peak. As a matter of fact, it is virtually impossible to identify this state by simply examining the invariant mass spectrum, as this mass region is populated with different known states such as the  $K^*(1400)$ ,  $K_1(1410)$ ,  $K_0^*(1430)$  and  $K_2^*(1430)$ . Since all of these states are candidates for the resonance enhancement around 1.4 GeV, a partial wave analysis is considered essential to this analysis. In this Chapter, a detailed description of the partial wave analysis framework is introduced.

### 4.1 Introduction

Partial wave analysis is a tool used to determine the contribution of different spin-parity states to the observed intensity distribution. It provides a framework to extract the resonance properties and understand the angular structure of the data sample in hand. It is essentially used to parametrize the amplitude of a spectrum as a function of the angular distributions of the decay products. We start examining the methodology of partial wave analysis by looking at the cross section, a quantity that is used to describe the intensity of production of a particular process; meaning a process with a higher cross section happens more often than a process with lower cross section. The general form of the cross section  $\sigma$  is

$$\sigma = \frac{n \times A_{H_2}}{2 \times n_\gamma \times l_t \times \rho_t \times N_A \times Acceptance} \quad (4.1)$$

where  $n$  is the number of observed  $\gamma p \rightarrow \Lambda K^+ \pi^+ \pi^-$  events,  $A_{H_2}$  is the mass number of the  $H_2$  atom,  $n_\gamma$  is the total number of photons on target,  $l_t$  is the length of the target,  $\rho_t$  is its mass density, and  $N_A$  is Avogadro's number. While this quantity is useful for general analysis purposes, providing the over-all cross section for a  $\gamma p \rightarrow \Lambda K^+ \pi^+ \pi^-$  event to occur at all combinations of angles and momenta. A detailed analysis of the cross section requires normalizing

this quantity to the available phase space for this reaction; that is, normalizing the unit cross section  $d\sigma$  to the unit scattering angle  $d\theta$ . This quantity is known as the differential cross section  $d\sigma/d\theta$ .

In the case of three final state mesons, the differential cross section tends to become more complicated, thus dictating the use of a model to describe the decay of the unknown resonance. We assume that the decay  $X \rightarrow K^+\pi^+\pi^-$ , illustrated in Figure 4.1, is well-described by the isobar model [67], it thus follows either of the forms below

$$\begin{aligned} X &\rightarrow Y\pi^+ \rightarrow K^+\pi^-\pi^+ \\ X &\rightarrow YK^+ \rightarrow \pi^+\pi^-K^+ \end{aligned} \tag{4.2}$$

where the resonance Y is the intermediate state isobar. The Lorentz-invariant phase space for this process is given by the form found in reference [69]

$$d\rho \propto d\Omega^* (p_Y d\Omega_X dm_X) (p_b d\Omega_Y dm_Y) \tag{4.3}$$

where  $\Omega^* = (\theta^*, \phi^*)$  represents the polar and azimuthal angles of the resonance X of mass  $m_X$  in the center-of-mass frame;  $\Omega_X = (\theta_X, \phi_X)$  denotes the angles describing the orientation of the momentum  $p_Y$  of the isobar of mass  $m_Y$  in the  $K\pi\pi$  rest frame;  $\Omega_Y = (\theta_Y, \phi_Y)$  denotes the angles corresponding to the momentum  $p_b$  of the bachelor particle in the isobar's helicity rest frame.

A full description of the three body system requires five variables [69]. In this framework four angles,  $\Omega = (\Theta, \Phi)$  and  $\Omega_Y = (\theta, \phi)$ , and the isobar mass  $m_Y$  are chosen. The angles  $\Omega = (\Theta, \Phi)$  are the polar and azimuthal angles describing the isobar orientation  $\vec{p}$  in the Gottfried-Jackson frame (the resonance X rest frame), where the z-axis is chosen to be in the direction of the beam in the X rest frame,  $y_{GJ}$  is defined as  $\hat{p}_\gamma \times \hat{p}_X$ , the normal to the production plane, and  $x_{GJ}$  is obtained by enforcing a right-handed coordinate system. Additionally, the angles  $\Omega_Y = (\theta, \phi)$  specify the orientation  $\vec{p}_b$  of one of the decay products of the isobar in the helicity frame (Isobar Y rest frame), where the z-axis is defined as  $\hat{p}_Y$  before the boost into the Y rest frame,  $\hat{y}_H$  is defined as  $\hat{z}_H \times \hat{p}_\gamma$ , and then  $\hat{x}_H$  is obtained by again enforcing a right-handed coordinate system with  $\hat{y}_H \times \hat{z}_H$ . Both reference frames are illustrated in Figure 4.2. The Lorentz-invariant phase space can now be written as

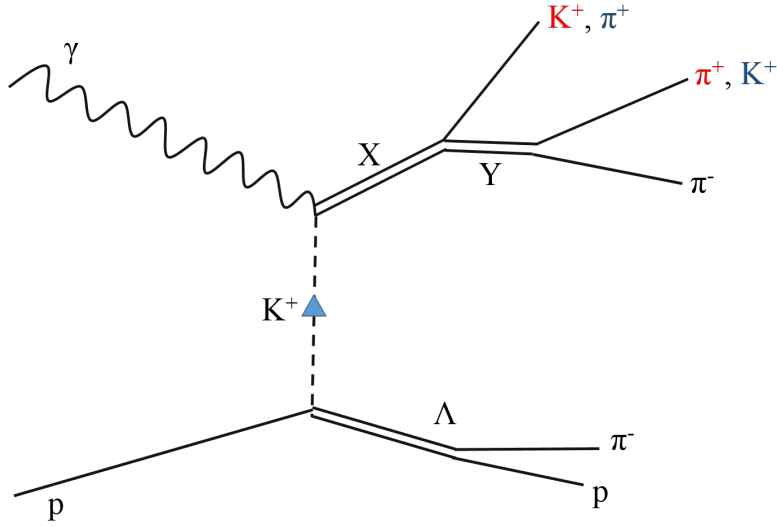


Figure 4.1: A Feynman Diagram illustrating the isobar model interpretation of a  $\gamma p \rightarrow \Lambda K^+ \pi^+ \pi^-$  decay. The incoming photon exchanges a  $K^+$  with the proton, which in turn leaves as a  $\Lambda$  that later decays to a  $p\pi^-$ , and peripherally produces a resonance  $X$ .  $X$  then decays to an isobar  $Y$  and a bachelor particle which could be either a  $\pi^+$  or a  $K^+$ . The isobar then decays to  $\pi^+\pi^-$  or  $K^+\pi^-$ .

$$d\rho \propto dt dm_X d\tau \quad (4.4)$$

where

- $\tau = \{\Omega, \Omega_Y, m_X\}$
- $d\tau = d\Omega d\Omega_Y dm_Y = d\Phi d\cos\Theta d\phi d\cos\theta dm_Y$
- $t = t_0 - 4|p_\gamma||p_X| \sin^2(\theta^*/2)$

Notice that the  $\Omega^* = (\theta^*, \phi^*)$  term has been replaced by the momentum transfer term. This is due to the fact that the reaction is independent of  $\phi^*$ , and can thus be integrated over. Then using the definition of  $t$ , the  $\theta^*$  dependence can be related to the momentum transfer. The differential cross-section can now be written as

$$\frac{d\sigma}{dt dm_X d\tau} \propto |\mathcal{M}|^2 p_Y p_b \quad (4.5)$$

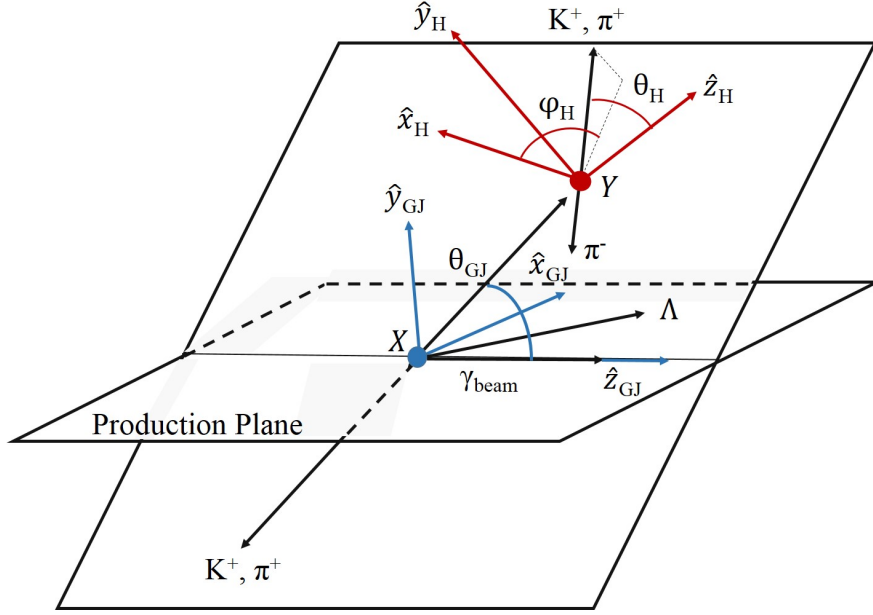


Figure 4.2: The definition of the Gottfried-Jackson reference frame (blue) and the Helicity reference frame (red) used in the calculation of decay amplitudes.

where

$$|\mathcal{M}|^2 = \mathcal{I}(\tau), \quad (4.6)$$

is the Lorentz-invariant transition amplitude.  $\mathcal{M}$  serves as a connection between the intensity distribution and the differential cross section. The purpose for this analysis is essentially to parametrize  $\mathcal{M}$  as a function of the Lorentz-invariant phase space and analyze the data for each bin given the corresponding momentum transfer  $t$  and the  $K\pi\pi$  mass  $m_X$ .

The transition amplitude  $\mathcal{M}$  can be written in terms of the transition operator  $\hat{T}$  as follows

$$\mathcal{M} = \langle out | \hat{T} | in \rangle \quad (4.7)$$

where "out" represents the final state ( $K^+\pi^+\pi^-\Lambda$ ) and "in" represents the initial state ( $\gamma p$ ).

The intensity distribution thus becomes

$$\mathcal{I}(\tau) = \sum_{\alpha} |\mathcal{M}|^2 = \sum_{\alpha} \langle out | \hat{T} | in \rangle (\langle out | \hat{T} | in \rangle)^* \quad (4.8)$$

and more precisely,

$$\mathcal{I}(\tau) = \sum_{\alpha} \langle out | \hat{T} | in \rangle \langle in | \hat{T}^{\dagger} | out \rangle \quad (4.9)$$

the operator  $|in\rangle \langle in|$  is then replaced with the initial spin density matrix operator,  $\hat{\rho}_{in}$ , and the intensity distribution becomes

$$\mathcal{I}(\tau) = \sum_{\alpha} \langle out | \hat{T} \hat{\rho}_{in} \hat{T}^{\dagger} | out \rangle \quad (4.10)$$

The index  $\alpha$  in this case represents all the quantum numbers needed to specify a mesonic state and its subsequent decay. These quantum numbers are

- J, the total angular momentum of X
- P, the parity of X
- M, the projection of J along the beam axis
- L, the angular momentum of the isobar Y and the bachelor particle ( $K^+$  or  $\pi^+$ )
- I, the isospin of X
- S, the spin of X,
- $\lambda$ , the helicity of the rest frame

Keeping our reaction in mind, the transition operator can be factorized into two parts: the production operator and the decay operator, such that

$$\mathcal{I}(\tau) \propto \sum_{\alpha} \langle out | \hat{T}_{decay} \hat{T}_{production} \hat{T}_{production}^{\dagger} \hat{T}_{decay}^{\dagger} | out \rangle \quad (4.11)$$

notice that the spin density matrix operator was dropped. This is due to the fact that the spin density matrix is block-diagonal in the case of an unpolarized photon beam. Inserting a complete orthogonal set of states,  $|X\rangle$  into Equation 4.11, we obtain:

$$\mathcal{I}(\tau) \propto \sum_{\alpha} \sum_{X, X'} \langle out | \hat{T}_d | X \rangle \langle X | \hat{T}_p \hat{T}_p^{\dagger} | X' \rangle \langle X' | \hat{T}_d^{\dagger} | out \rangle \quad (4.12)$$

The set of states,  $|X\rangle$ , are called partial waves, that can be described by the set of quantum number  $\alpha$ . This set spans all the possible intermediate states, therefore, the experimental goal

of finding the quantum numbers associated with the resonance is translated to measuring the partial wave amplitudes. Equation 4.12 can then be rewritten in a more simplified form

$$\mathcal{I}(\tau) = \sum_k \sum_{\alpha, \alpha'} A_\alpha(\tau) V_\alpha^k V_{\alpha'}^{k*} A_{\alpha'}^*(\tau) \quad (4.13)$$

where  $k$  is the rank of the spin density matrix. The term  $\langle out | \hat{T}_d | X \rangle$  is replaced by the decay amplitude  $A_\alpha(\tau)$  for a given wave  $\alpha$ . The decay amplitudes will be discussed in more details in Section 4.2. Similarly, the term  $\langle X | \hat{T}_p | X' \rangle$  is replaced by the production amplitudes  $V_\alpha^k$  which contain the hadronic QCD-based interaction that can not be calculated. More details about the production amplitudes can be found in Section 4.3. A more detailed explanation of the phenomenology of partial wave analysis can be obtained from reference [69].

## 4.2 Decay Amplitudes

The decay amplitudes for a resonance decaying into three or more particles can be calculated using the isobar model. This model assumes a series of sequential decays. The resonance  $X$  first decays to an intermediate unstable isobar and a stable bachelor particle, then the isobar subsequently decays into other stable particles. We assume that there are no interactions between the final state particles after they are produced through sequential decays and that all the final state particles are spinless.

The decay amplitudes  $A_\alpha(\tau)$  are calculated in the helicity formalism in a frame-by-frame, decay-by-decay fashion. In the isobar model, the decay amplitude contains information that describe the angular nature of a  $J^P$  state as well as the mass dependence of the isobar. The decay amplitude can then be rewritten to include separate terms containing this information.  $A_\alpha(\tau)$  thus becomes

$$A_\alpha(\tau) = A_\alpha(\Omega_X, \Omega_Y) A_\alpha(m_Y) \quad (4.14)$$

where  $\Omega_X$  denotes the angles describing the orientation of the momentum of the isobar in the  $X$  rest frame, and  $\Omega_Y$  denotes the angles describing the orientation of one of the decay particles of the isobar in the helicity rest frame.

The angular term of the decay amplitude can be described by the Wigner D-functions and their corresponding d-functions.  $A_\alpha(\Omega_X, \Omega_Y)$ , from reference [69], is defined as

$$A_\alpha(\Omega_X, \Omega_Y) = \tilde{l}\tilde{s} \sum_{\lambda} D_{M_X \lambda}^{J*}(\phi_X, \theta_X, \phi_Y) d_{\lambda 0}^J(\theta_Y) C(l 0 s \lambda | J \lambda) \quad (4.15)$$

where the D-functions are defined as

$$D_{MM'}^J(\alpha, \beta, \gamma) = e^{-im'\alpha} d_{MM'}^J(\beta) e^{-i\gamma} \quad (4.16)$$

More information on Winger functions can be found in Appendix E. The symbols J and  $M_X$  represent the total angular momentum and its z projection. The symbols s and  $\lambda$  are the spin and the helicity of the isobar, and  $C(l 0 s \lambda | J \lambda)$  is the corresponding Clebsch-Gordon coefficient. The quantum numbers J, S and L are defined as

$$\begin{aligned} J &= L_{Total} + S_{Total} \\ L_{Total} &= L_Y + L_b \end{aligned} \quad (4.17)$$

$$S_{Total} = S_Y + S_b$$

The mass dependent term of the decay amplitude  $A_\alpha(m_Y)$ , as defined by reference [69] is

$$A_\alpha(m_Y) = F_l(p_X) F_s(p_b) \psi(m) \quad (4.18)$$

where  $\psi(m)$  is the fully relativistic Breit-Wigner distribution

$$\psi(m) = \frac{m_0 \Gamma_0}{m_0^2 - m^2 - im_0 \Gamma_Y(m)} \quad (4.19)$$

and

$$\Gamma_Y = \Gamma_0 \frac{m_0 p F_s^2(q)}{m p_0 F_0^2(q_0)} \quad (4.20)$$

where q and  $q_0$  are the COM breakup momentum for a resonance of mass m and  $m_0$ , respectively. The functions  $F_l(p)$  are the Blatt-Weisskopf angular momentum barrier factors [60].

The parity conservation in this production process is taken into account by introducing the reflectivity basis into the angular term of the decay amplitude. This basis change will bring the density matrix into a block diagonal form. The reflectivity basis in reference [69] is defined by

$$|\epsilon JPM\rangle = [ |JPM\rangle - \epsilon P(-1)^{J-M} |JP - M\rangle ] \theta(M) \quad (4.21)$$

where P is the parity of the state  $|JPM\rangle$  and

$$\begin{aligned} \theta(M) &= \frac{1}{\sqrt{2}}, \quad M > 0 \\ &= \frac{1}{2}, \quad M = 0 \\ &= 0, \quad M < 0 \end{aligned} \quad (4.22)$$

The reflectivity  $\epsilon$  is here defined such that it coincides with the naturality  $\eta$  such that

$$\epsilon = \eta = P(-1)^J \quad (4.23)$$

It should be noted that

$$|\epsilon JPM\rangle = 0 \quad \text{for } m = 0; \quad \text{if } \epsilon = P(-1)^J \quad (4.24)$$

Additionally, states of opposite reflectivities do not interfere, as they are in separate blocks of the block-diagonal spin-density matrix. Rewriting Wigner D-functions in the reflectivity basis yields

$${}^\epsilon D_{M_X \lambda}^{JP*}(\phi_X, \theta_X, \phi_Y) = \theta(M) [D_{M_X \lambda}^{J*}(\phi_X, \theta_X, \phi_Y) - \epsilon P(-1)^{J-M} D_{-M_X \lambda}^{J*}(\phi_X, \theta_X, \phi_Y)] \quad (4.25)$$

Since  $P = (-1)^{l+s+1}$ , the new form of the D-functions can be rearranged and Equation 4.15 becomes

$${}^\epsilon A_\alpha(\Omega_X, \Omega_Y) = \tilde{l}\tilde{s} \sum_\lambda \theta(M) [D_{M_X \lambda}^{J*} - \epsilon P(-1)^{J-M} D_{-M_X \lambda}^{J*}] d_{\lambda 0}^J(\theta_Y) C(l0s\lambda|J\lambda) \quad (4.26)$$

The mass dependent term of the decay amplitude is unaffected by this change of axis, and Equation 4.14 can be written as

$${}^\epsilon A_\alpha(\tau) = {}^\epsilon A_\alpha(\Omega_X, \Omega_Y) A_\alpha(m_Y) \quad (4.27)$$

The final form of the decay amplitudes can now be used and the values of  $\Omega_X$ ,  $\Omega_Y$  and  $m_Y$  for each event can be determined using the four vectors of the final data sample. The decay amplitudes are complex numbers and are expected to be different for every wave, even waves with opposite reflectivities as seen in Equation 4.27.

An example of the dependence of the decay amplitude of  $1^+D, \rho K^+$  on the invariant mass of the  $K\pi\pi$  sample is illustrated in Figure 4.3. To obtain the values on the y-axis, the diagonal terms of the normalization integral of  $1^+D, \rho K^+$  for the raw and accepted Monte Carlo samples are determined. These terms are essentially the squared moduli of the decay amplitudes for every wave normalized to the number of events in the sample. Once extracted from the normalization integral in every bin, the squared modulus can be plotted against its corresponding  $K\pi\pi$  mass. The overall plot gives an idea about the phase space available for the chosen wave. As we mentioned before, we expect the reflectivities of the same wave to have equal contributions, which essentially means they would have similar decay amplitude variations in term of the  $K\pi\pi$  mass. Moreover, comparing the plot of the accepted Monte Carlo (left) to the plot of the raw Monte Carlo (right), we are able to see the effect of acceptance on this wave. With the decay amplitudes in hand, the fitter can now determine the production amplitudes,  ${}^{\epsilon k}V_\alpha$ , using the extended maximum likelihood method.

### 4.3 Production Amplitudes

Unlike the decay amplitudes which can be calculated directly from the data sample, the production amplitudes, also complex numbers, are considered a weight on each partial decay amplitude of the final mix and are parameters to be fit to the data, and depend on the rank of the spin density matrix. The production amplitudes,  ${}^{\epsilon k}V_\alpha$ , are generally a function of  $m_X$  and  $t$ , but we study the dependence in  $m_X$  by performing a partial wave analysis in narrow bins of  $m_X$ . Then by performing a maximum likelihood fit, we extract the production amplitudes, to later use them to study the contribution of the waves in the fit by studying their intensities using

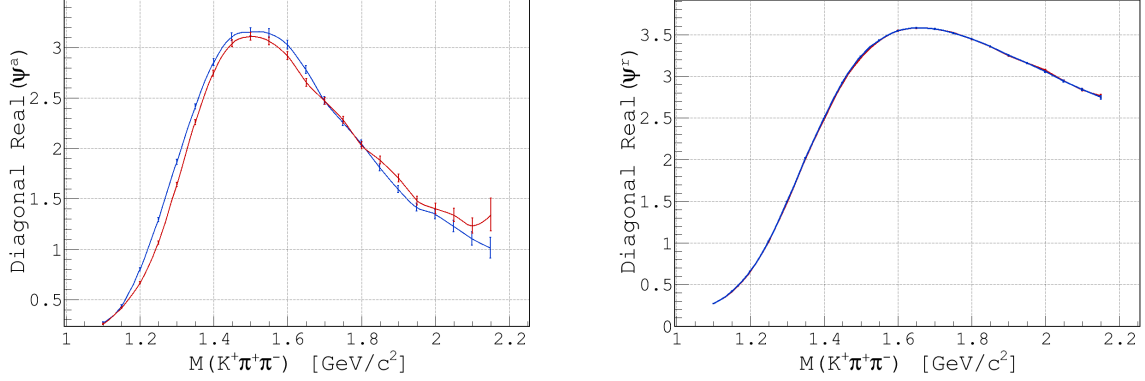


Figure 4.3: The variation of the decay amplitude of the  $1^+D, \rho K^+$  as a function of the invariant mass of the  $K^+\pi^+\pi^-$  system for accepted Monte Carlo events (**left**) and raw Monte Carlo events (**right**). The blue lines correspond to the positive reflectivity  $1^+D, \rho K^+$  wave, while the red lines corresponds to the negative reflectivity of the same wave. Notice that the decay amplitudes of both reflectivities on the right are almost identical making it hard to distinguish them in this plot.

$$\mathcal{I}(\tau) = \sum_k \sum_{\epsilon} \sum_{\alpha, \alpha'} \epsilon^k V_{\alpha}^* \epsilon^k V_{\alpha} \epsilon A_{\alpha}^*(\tau) \epsilon A_{\alpha}(\tau) \quad (4.28)$$

where  $\epsilon$  denotes the eigenvalues of reflectivity,  $\alpha$  is the set of the state's quantum numbers, and  $k$  is the rank of the spin density matrix  $\epsilon^k \rho_{\alpha\alpha'}$ . The spin density matrix contains all the spin information available about a given quantum system. The diagonal elements give the probabilities of different states, while the off-diagonal elements give information about the interference between different states. The reflectivity basis diagonalizes the spin density matrix, thus forcing opposite reflectivities to occupy different blocks. As a result, states with differing reflectivities do not interfere with each other. The spin density matrix rank, usually referred to using Roman numerals, depends on the exchanged particle between the baryon and meson vertex. In most cases, the rank of the spin density matrix is simply one, for a pomeron exchange. The spin density matrix is defined in terms of the production amplitudes as

$$\epsilon^k \rho_{\alpha\alpha'} = \sum_k \epsilon^k V_{\alpha} \epsilon^k V_{\alpha'}^* \quad (4.29)$$

In what follows, we exhibit the form of the likelihood function used in our partial wave analysis, as well as the normalization integrals for raw and accepted Monte Carlo events. The

maximum likelihood method is a statistical procedure that can be used to match a parameterized model to a sample of data. The likelihood function, defined by reference [69], for finding "n" events of a given bun with a finite acceptance is

$$\mathcal{L} \propto \left[ \frac{\tilde{n}^n}{n!} e^{-\tilde{n}} \right] \prod_i^n \left[ \frac{\mathcal{I}(\tau_i)}{\int \mathcal{I}(\tau) \eta(\tau) d\tau} \right] \quad (4.30)$$

where  $\eta(\tau)$  is the acceptance of the detector. In other words, it is the ability of the detector to measure n number of events given their associated values of  $\tau$ . The factors dependent on the number of observed events can be reduced by applying the definition of the expectation value,

$$\tilde{n} = \int \mathcal{I}(\tau) d\tau \quad (4.31)$$

and the likelihood function can be then reduced to

$$\mathcal{L} \propto \left[ \prod_i^n \mathcal{I}(\tau_i) \right] \exp \left[ \int \mathcal{I}(\tau) \eta(\tau) d\tau \right] \quad (4.32)$$

then taking the log of the likelihood function,

$$\log \mathcal{L} \propto \sum_i^n \log \mathcal{I}(\tau_i) - \int \mathcal{I}(\tau) \eta(\tau) d\tau \quad (4.33)$$

The function  $\mathcal{I}(\tau)$  can be replaced by the form obtained in Equation 4.28. The acceptance  $\eta(\tau)$  can be determined by taking a sample of raw Monte Carlo events generated uniformly according to the available  $K\pi\pi$  phase space, and passing it through the detector simulation, taking into account the detector's inefficiencies and geometry. Events that survive the CLAS simulation and reconstruction process are then used to determine the detector's acceptance. These events are referred to as accepted Monte Carlo events. Using the raw and accepted Monte Carlo events, and their corresponding decay amplitudes, we can calculate the normalization integrals according to the equations below

$$\begin{aligned} \epsilon^k \psi_{\alpha\alpha'}^r &= \frac{1}{n_r} \sum_i^{n_r} \epsilon A_\alpha(\tau_i)^\epsilon A_\alpha^*(\tau_i) \\ \epsilon^k \psi_{\alpha\alpha'}^a &= \frac{1}{n_a} \sum_i^{n_a} \epsilon A_\alpha(\tau_i)^\epsilon A_\alpha^*(\tau_i) \end{aligned} \quad (4.34)$$

where  ${}^{\epsilon k}\psi_{\alpha\alpha'}^r$  are the normalization integrals of the *raw Monte Carlo* events and  $n_r$  is their corresponding number. Likewise,  ${}^{\epsilon k}\psi_{\alpha\alpha'}^a$  are the normalization integrals of the *accepted Monte Carlo* events and  $n_a$  is their corresponding number. The production amplitude parameters are also normalized via

$$V \rightarrow \sqrt{\frac{n}{\eta_x}} \quad (4.35)$$

The final form of the log of the likelihood function in terms of the new parameters and the normalization integrals is

$$\log \mathcal{L} = \sum_i^n \log \left[ \sum_{k\epsilon\alpha,\alpha'} {}^{\epsilon k}V_\alpha^* {}^{\epsilon k}V_\alpha {}^\epsilon A_\alpha^*(\tau_i) {}^\epsilon A_\alpha(\tau_i) \right] - n \left[ \sum_{k\epsilon\alpha,\alpha'} {}^{\epsilon k}V_\alpha^* {}^{\epsilon k}V_\alpha {}^{\epsilon k}\psi_{\alpha\alpha'}^a \right] \quad (4.36)$$

and the normalization condition is of the form

$$\sum_{\alpha\alpha'} V_\alpha V_\alpha^* \psi_{\alpha\alpha'}^a = 1 \quad (4.37)$$

This normalization allows the fitted production amplitudes to independent of variations among different bins. In other words, a set of fitted  $V_\alpha$ 's in a given bin can be used as a starting value for the neighboring bins. The final quantity we examine is the predicted number of events in a given bin, also known as the event yield. This quantity is essential to examine the contribution of a wave or a coalition of different waves. The event yield is proportional to the square of the production amplitude and the raw normalization integrals. One can examine the event yield for a single wave or a coherent sum of waves. To find this predicted number, acceptance is taken into consideration by scaling the number of data to the inverse of the acceptance in a specific bin, as it is illustrated below

$$\mathcal{N} = n_d \frac{n_r}{n_a} \sum_{\alpha\alpha'} V_\alpha V_\alpha^* {}^\epsilon \psi_{\alpha\alpha'}^r \quad (4.38)$$

where  $\alpha$  is a set of all the quantum numbers that characterize a wave or a set of waves. By plotting  $\mathcal{N}$  as a function of the  $K\pi\pi$  mass, we are granted access to features of waves and their contributions to the overall mass spectrum. In general, resonances take the form of peaks behaving as a relativistic Breit-Wigner amplitude. Once a peak is deemed significant enough, it could be fitted to a Breit-Wigner distribution and its physical characteristics such as the mass

and decay width can be determined. The phase difference can be used to determine whether this peaks is a manifestation of a resonance or simply a leak from other waves. It should be noted that for a partial wave analysis to be conclusive and successful, a large data set is required. Typical partial wave analysis datasets include on the order of millions of events. This allows access to more rigorous results especially when the meson system mass is binned very narrow bins. It will be shown in the next chapter, that even though our dataset was not large, a partial wave analysis was carried out by binning the data in larger-than-usual sizes thus limiting the ability to observe clean and significant phase motion between waves.

## 4.4 Summary

We have seen that the partial wave analysis can be a powerful tool to understand the dynamics of the data and to study the contribution of various states to the meson system under study. The framework used for this partial wave analysis is done assuming that the data is well-described by the isobar model in the helicity formalism using the reflectivity basis. Our observed intensity distribution  $\mathcal{I}(\tau)$  is decomposed into a sum of independent production and decay amplitudes,

$$\mathcal{I}(\tau) = \sum_k \sum_{\epsilon} \sum_{\alpha, \alpha'} \epsilon^k V_{\alpha}^* \epsilon^k V_{\alpha} \epsilon A_{\alpha}^*(\tau) \epsilon A_{\alpha}(\tau) \quad (4.39)$$

The decay amplitudes for each wave are calculated for each data event in the helicity formalism in a frame-by-frame, decay-by-decay fashion. In the isobar model, the decay amplitude contains information the describe the angular nature of a  $J^P$  state as well as the mass dependence of the isobar. The production amplitudes depend on the mass of the meson system  $m_X$  and the momentum transfer  $t$  and are determined by maximizing the likelihood function. The likelihood function includes the production amplitudes, decay amplitudes, and normalization integrals and has the following form

$$\log \mathcal{L} = \sum_i^n \log \left[ \sum_{k \in \alpha, \alpha'} \epsilon^k V_{\alpha}^* \epsilon^k V_{\alpha} \epsilon A_{\alpha}^*(\tau_i) \epsilon A_{\alpha}(\tau_i) \right] - n \left[ \sum_{k \in \alpha, \alpha'} \epsilon^k V_{\alpha}^* \epsilon^k V_{\alpha} \epsilon^k \psi_{\alpha \alpha'}^a \right] \quad (4.40)$$

The partial wave analysis procedure, including the set of waves, software tools, binning, and background parameterization is covered in details in the following chapter.

## CHAPTER 5

# PARTIAL WAVE ANALYSIS PROCEDURE AND RESULTS

A partial wave analysis was performed on the selected  $K^+\pi^+\pi^-$  events to extract the significantly contributing waves from the spectrum. In this chapter, the specifics of the partial wave analysis procedure are discussed in details, followed by results from a fit where the most prominent waves are included. Further details related to wave selection, data binning, and fit quality check will be also discussed.

### 5.1 Experimental Acceptance

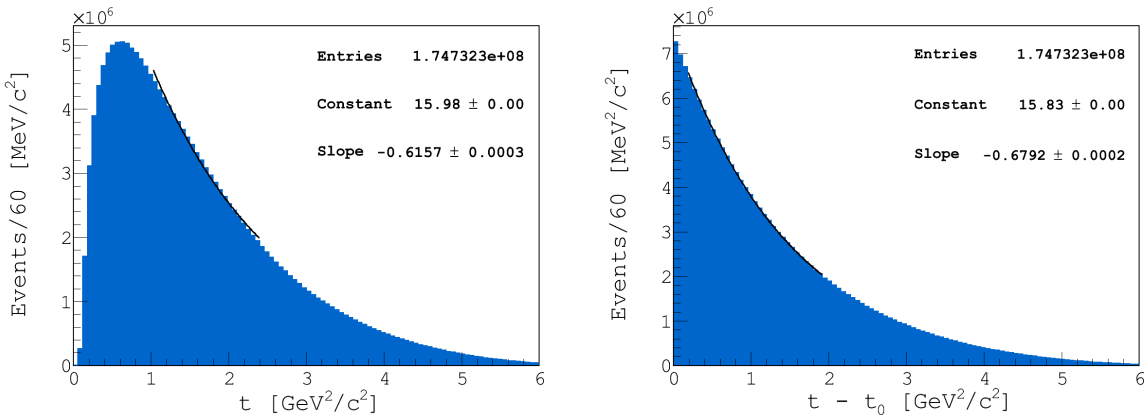
The first step in the partial wave analysis procedure is determining the acceptance of the CLAS detector which is essential for the normalization of the likelihood function. This is necessary to ensure that the wave intensities resulting from a fit are due to physics and to accurately represent the detector's ability to see events in a kinematic region. To accomplish this,  $\gamma p \rightarrow \Lambda K^+\pi^+\pi^-$  events are randomly and uniformly generated across the *phase space* accessible by the  $K^+\pi^+\pi^-$  system. In other words, the decay of X to  $K^+\pi^+\pi^-$  is generated such that the  $\theta$  and  $\phi$  of the isobar Y and the bachelor in the Gottfreid-Jackson frame are isotropic. The  $\Lambda$  was generated with a mass of  $1.115 \text{ GeV}/c^2$  and a width of  $10 \text{ KeV}/c^2$  to match the  $p\pi^-$  mass distribution of the data. We also implemented the detachment of the  $\Lambda$  vertex into our simulation to ensure that the acceptance is simulated properly (More details on the vertex detachment can be found in Appendix C). The mass of X was generated over the  $K^+\pi^+\pi^-$  invariant mass range from  $1.0$  to  $2.2 \text{ GeV}/c^2$  in  $5 \text{ MeV}/c^2$  wide bins containing events the would be enough to yield accepted events that are 50 times the number of data events in every bin. It is qualitatively important to generate Monte Carlo in narrow mass bins, narrower than the smallest practical bin size for data, as it ensures our ability to normalize fits in a variety of bin sizes by merging bins of Monte Carlo as well as reduce the effect of bin migration. Is is equally as important to generate a large Monte Carlo dataset to minimize any statistical uncertainties in the fit results. The latter effect can be seen in Figure 4.3 where the errors are seen to be higher towards the

end of the  $K^+\pi^+\pi^-$  mass where the number of generated events is substantially low compared to other bins.

The simulated events are also generated with momentum transfer dependence. As we previously discussed in Section 3.2.4, our experimental data also had an exponential distribution in  $t$  with a slope close to  $0.55 \text{ GeV}^2/c^4$ . This slope was shown to be constant across different regions in the  $K^+\pi^+\pi^-$  system when fitting the momentum transfer distribution over the same range. As a result, the raw Monte Carlo events were generated with a  $t$  slope of 0.69 that would later be reconstructed to be 0.56 after passing the generated events through the detector simulation and smearing programs. The raw Monte Carlo dataset contained around 174 million  $\gamma p \rightarrow \Lambda K^+\pi^+\pi^-$  events generated with a bremsstrahlung photon beam of energies between 4.4 and 5.45 GeV. The generated events were then fed to the detector simulation package, GSIM (a GEANT based model of CLAS) [50], where the detector's responses are simulated. GSIM takes each particle's information and generates a track of it inside the detector, thus providing hits according to the detector efficiencies. Events that passed through GSIM were then passed through GPP to smear the detector signals as so to match the resolution of the detectors used to take data. Events were then run through the reconstruction package A1C to reconstruct the simulated tracks. Further details about the different simulation packages and how to run them can be found in reference [50]. The final accepted Monte Carlo dataset consisted of 774838 events after reconstruction and applying data selection cuts.

The slope of the fitted  $t$  distribution in Figure 5.1, is different from the slope that we input into genr8 because it is modified by the available phase space. The input slope can be extracted from the  $t'$  distribution where this effect is corrected for. The raw Monte Carlo sample was generated without angular dependence, in other words it was generated flat in the available phase space. The absence of any angular dependence can be observed in Figure 5.2 where features of the generated Monte Carlo events are illustrated. The uniformity of the phase space can be seen in the Dalitz plots for different regions of the  $K^+\pi^+\pi^-$ . Similarly, the uniformity in the physics angles can be seen in Figures 5.6 and 5.7. Raw Monte Carlo events are used to determine the raw normalization integrals. While these normalization integrals do not contribute to the minimization of the likelihood function or the fit, they are essential to produce acceptance-corrected intensity distributions.

The detector simulation and reconstruction software used to obtain the accepted Monte Carlo sample is analogous to the CLAS simulation packages used in other experiments with a

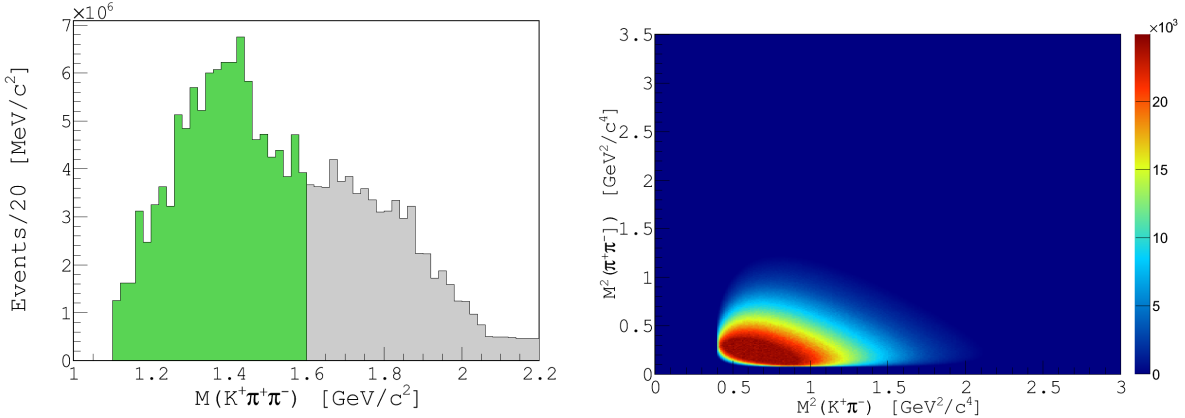


(a) The momentum transfer  $|t|$  of the raw MC. (b) The excess momentum transfer  $|t'|$  of the raw MC.

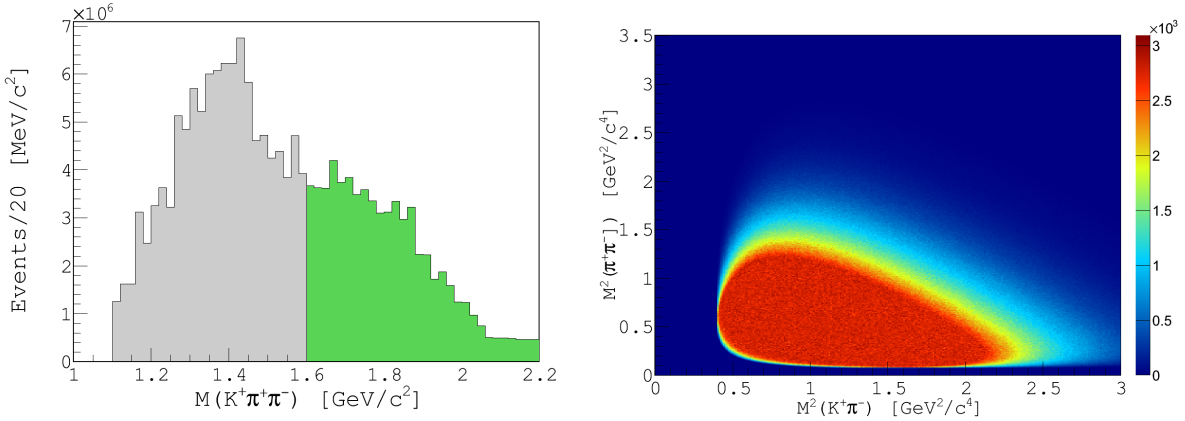
Figure 5.1: The momentum transfer  $|t|$  (a) and the excess momentum transfer  $|t'|$  (b) for the raw Monte Carlo sample. Both distributions are fitted to an exponential function thus yielding slopes of 0.615 and 0.679 for the accepted and raw Monte Carlo samples respectively.

handful of tweaks. These variations include taking into account the repositioning of the target cell for the g12 experiment, as well as accounting for any dead cells and paddles in various sub-detectors. The latter is taken care of in the GPP package during the smearing of simulated events after they passed through the GSIM package. It is of great importance to make sure that the simulation packages simulate all efficiencies in the detector's components properly. Luckily, this could be checked by plotting the lab angles  $\theta$  and  $\phi$  against each other, then comparing the distributions to those of the final data sample. These plots have been used in the past to perform fiducial cuts based on the exclusion of events lying outside the regions where the acceptance is optimal. Such cuts are not performed in this analysis as they were found to have little to no effect on the partial wave analysis results. Fiducial regions can be seen in Figures 5.8 and 5.9. Regions where the acceptance is compromised in the accepted Monte Carlo plots is due to simulated inefficiencies in various detector sectors. The presence of such gaps is an indication of a simulation that best describes the data.

Features of the final accepted Monte Carlo sample are illustrated in Figure 5.5. Comparing the Dalitz plots of Figure 5.5 to their equivalences in Figure 5.2, we can see the effect of acceptance on various regions of the  $K^+\pi^+\pi^-$  invariant mass. This variation can be obtained by simply dividing the number of accepted events in a certain  $K^+\pi^+\pi^-$  mass bin by the number of



(a) The  $K^+\pi^+\pi^-$  invariant mass with low range selection. (b) The dalitz plot of  $K^+\pi^+\pi^-$  for low mass events.



(c) The  $K^+\pi^+\pi^-$  invariant mass with high range selection. (d) The dalitz plot of  $K^+\pi^+\pi^-$  for high mass events.

Figure 5.2: Dalitz distributions for the low  $K\pi\pi$  mass region (**top**), and high mass region **bottom** for the raw Monte Carlo dataset. Green regions on the left correspond to events used in the Dalitz plots on the right.

raw events in the respective raw mass bin. In other words, in every  $50 \text{ MeV}/c^2$  bin we determine

$$\text{Acceptance} = \frac{\text{Number of Accepted Monte Carlo Events}}{\text{Number of Raw Monte Carlo Events}} \quad (5.1)$$

The acceptance is represented in Figure 5.3. The acceptance varies relatively smoothly over the  $K^+\pi^+\pi^-$  mass as it increases from 0.0005 in the low mass region to 0.0043 in the higher mass region. The effect of acceptance can be also seen when comparing the momentum transfer distributions for the raw and accepted Monte Carlo events. Accepted Monte Carlo events are

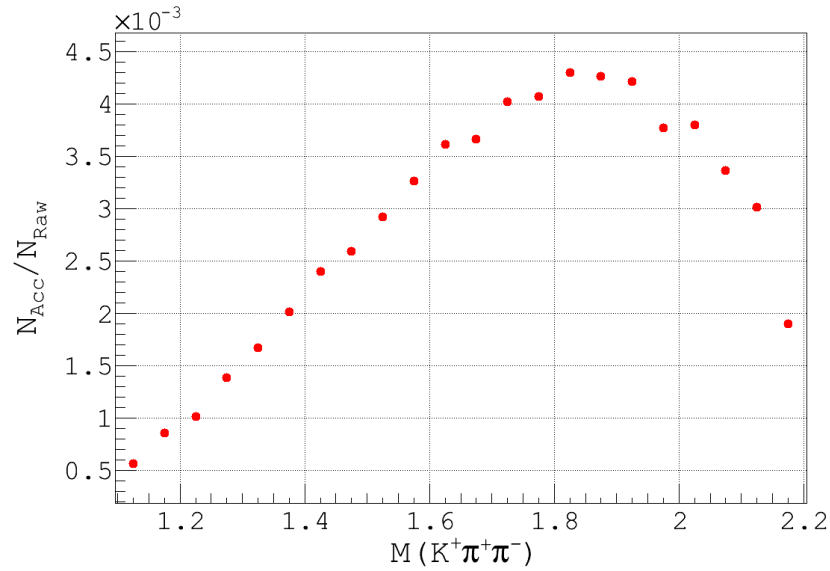
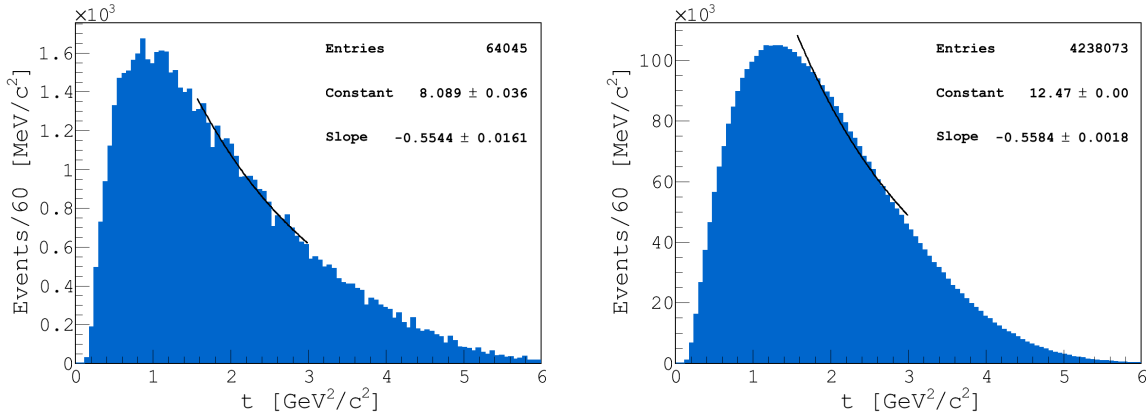


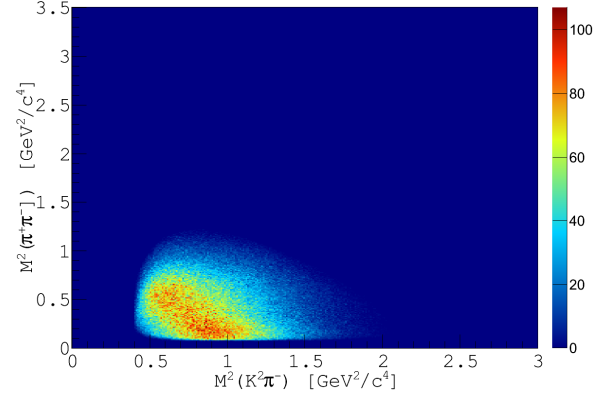
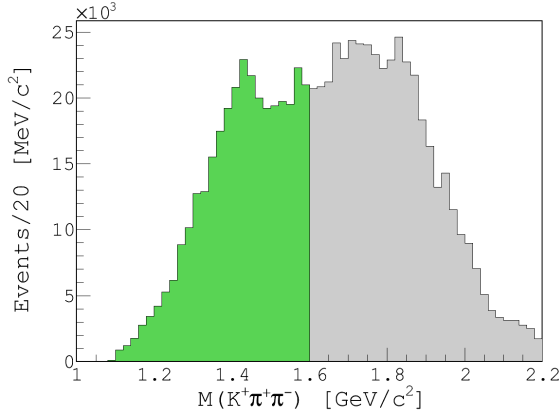
Figure 5.3: The CLAS acceptance for the  $\gamma p \rightarrow \Lambda K^+ \pi^+ \pi^-$  events as a function of  $K^+ \pi^+ \pi^-$  mass.



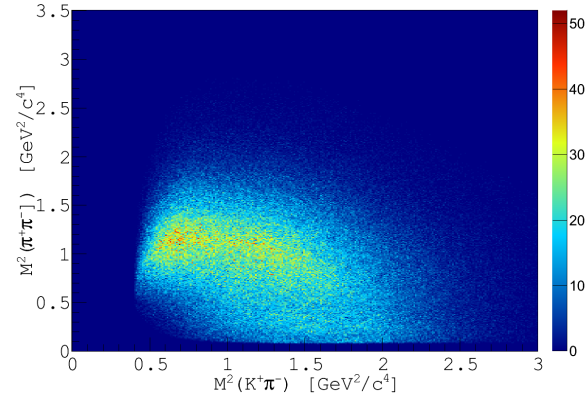
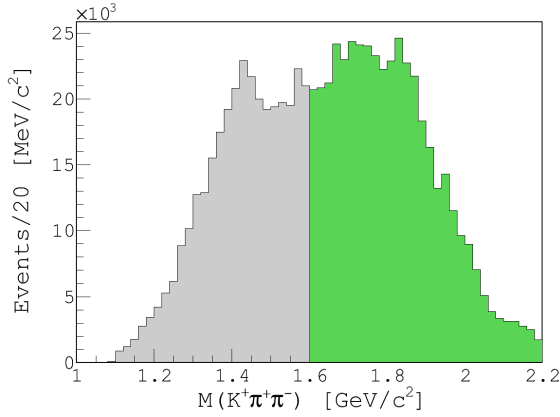
(a) The momentum transfer  $|t|$  distribution of the data. (b) The momentum transfer  $|t|$  distribution of the accepted Monte Carlo.

Figure 5.4: The momentum transfer  $|t|$  distribution of the data (a) and of the accepted Monte Carlo (b). The slopes are in approximate agreement at 0.554 for data and 0.558 for the accepted Monte Carlo.

used to calculate the accepted normalization integrals that go into the Likelihood function. They are essential in the sense that they provide information about the phase space available for each wave, in addition to their crucial role in the minimization of the likelihood function.

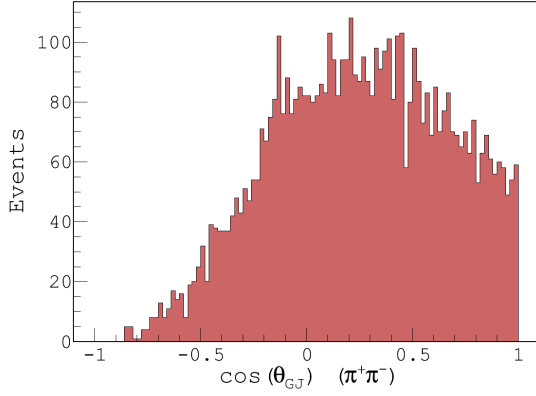


(a) The  $K^+\pi^+\pi^-$  invariant mass with low range selection. (b) The dalitz plot of  $K^+\pi^+\pi^-$  for low mass events.

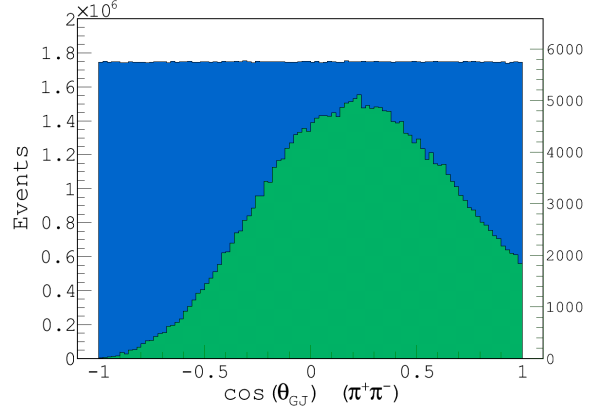


(c) The  $K^+\pi^+\pi^-$  invariant mass with high range selection. (d) The dalitz plot of  $K^+\pi^+\pi^-$  for high mass events.

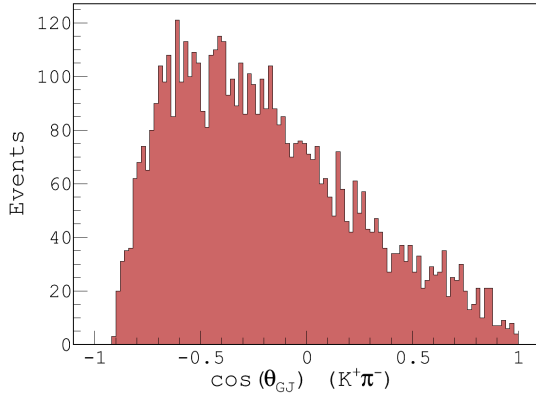
Figure 5.5: Dalitz distributions for the low  $K\pi\pi$  mass region (**top**), and high mass region **bottom** for the accepted Monte Carlo dataset. Green regions on the left correspond to events used in the Dalitz plots on the right.



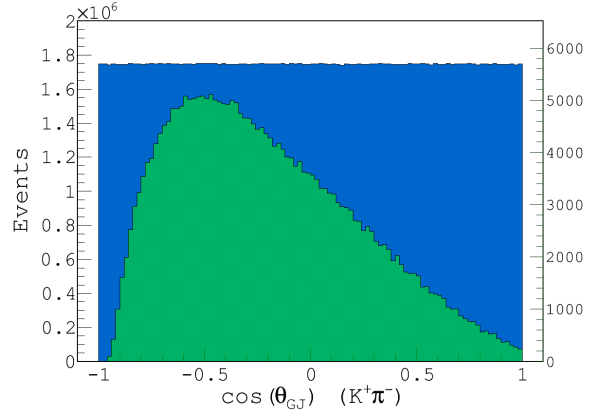
(a)  $\cos\theta_{GJ}$  of  $\pi^+\pi^-$  for data events.



(b)  $\cos\theta_{GJ}$  of  $\pi^+\pi^-$  for MC events.

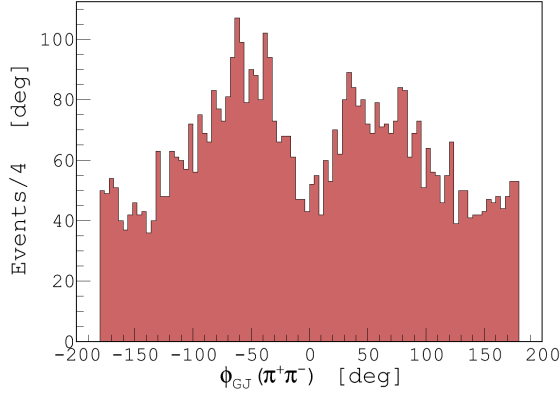


(c)  $\cos\theta_{GJ}$  of  $K^+\pi^-$  for data events.

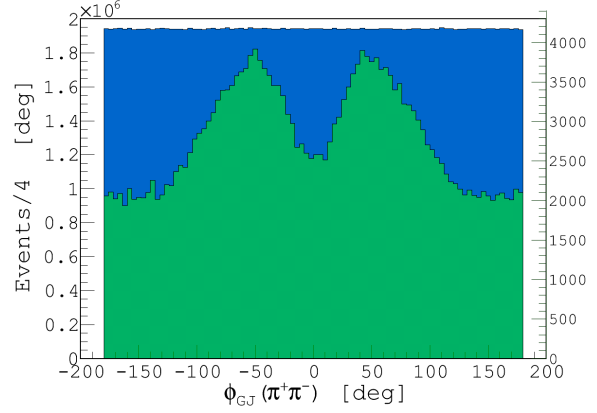


(d)  $\cos\theta_{GJ}$  of  $K^+\pi^-$  for MC events.

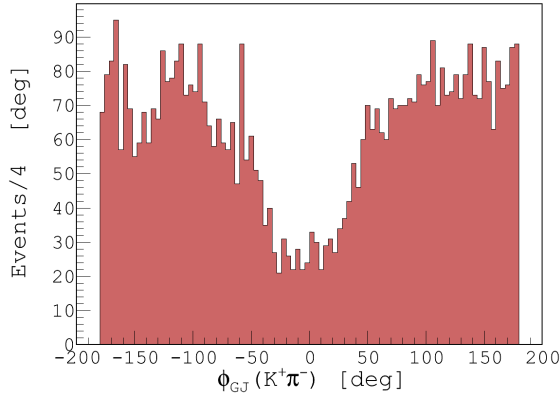
Figure 5.6: The Gottfried-Jackson angles for the data and Monte Carlo Samples. The flat **blue** distribution is the  $\cos\theta_{GJ}$  of  $(\pi^+\pi^-)$  in (b) and  $(K^+\pi^-)$  in (d) for the raw Monte Carlo sample, while the **green** distributions are the  $\cos\theta_{GJ}$  of  $(\pi^+\pi^-)$  in (b) and  $(K^+\pi^-)$  in (d) for the accepted Monte Carlo.



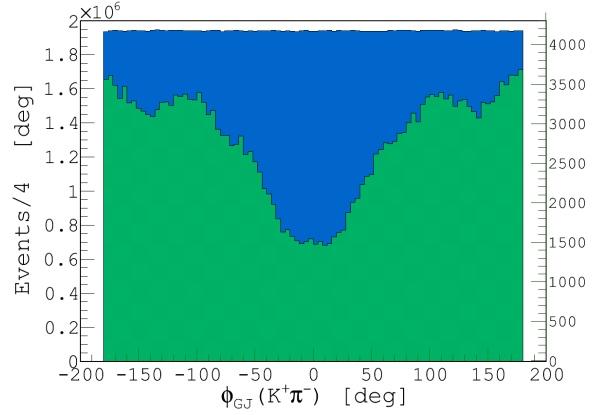
(a)  $\phi_{GJ}$  of  $\pi^+\pi^-$  for data events.



(b)  $\phi_{GJ}$  of  $\pi^+\pi^-$  for MC events.

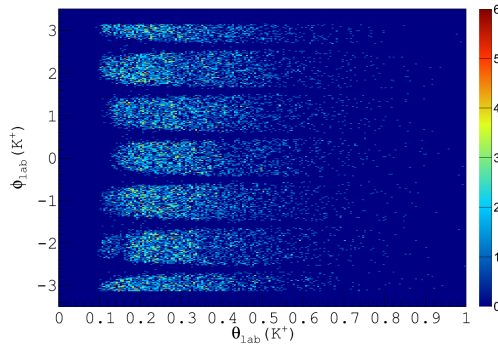


(c)  $\phi_{GJ}$  of  $K^+\pi^-$  for data events.

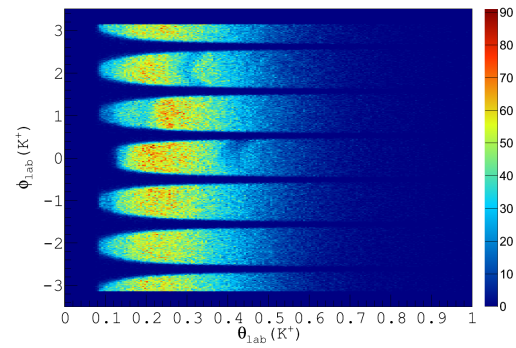


(d)  $\phi_{GJ}$  of  $K^+\pi^-$  for MC events.

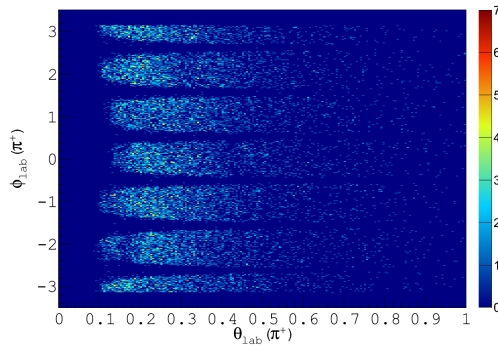
Figure 5.7: The Gottfreid-Jackson angles for the data and Monte Carlo Samples. The flat **blue** distribution is the  $\phi_{GJ}$  of  $(\pi^+\pi^-)$  in (b) and  $(K^+\pi^-)$  in (d) for the raw Monte Carlo sample, while the **green** distributions are the  $\phi_{GJ}$  of  $(\pi^+\pi^-)$  in (b) and  $(K^+\pi^-)$  in (d) for the accepted Monte Carlo.



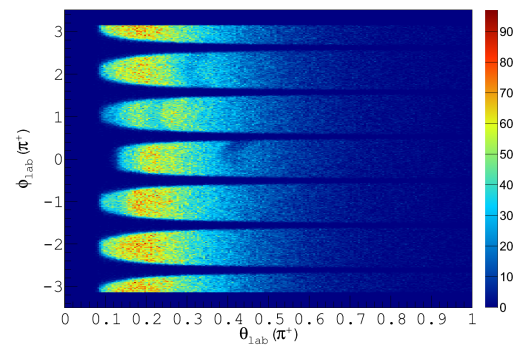
(a) The data  $(\phi_{lab}, \theta_{lab})$  distribution of  $K^+$ .



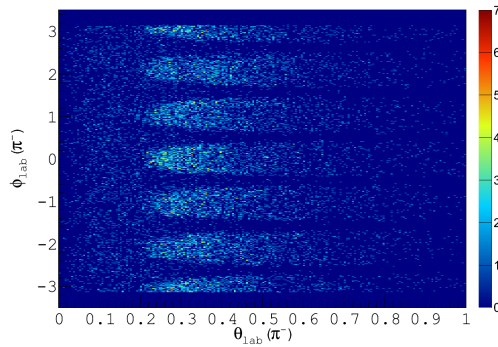
(b) The accepted  $(\phi_{lab}, \theta_{lab})$  distribution of  $K^+$ .



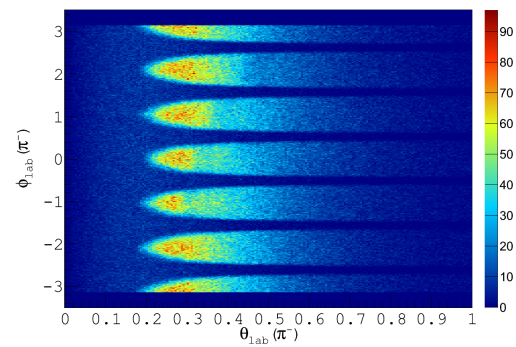
(c) The data  $(\phi_{lab}, \theta_{lab})$  distribution of  $\pi^+$ .



(d) The accepted  $(\phi_{lab}, \theta_{lab})$  distribution of  $\pi^+$ .

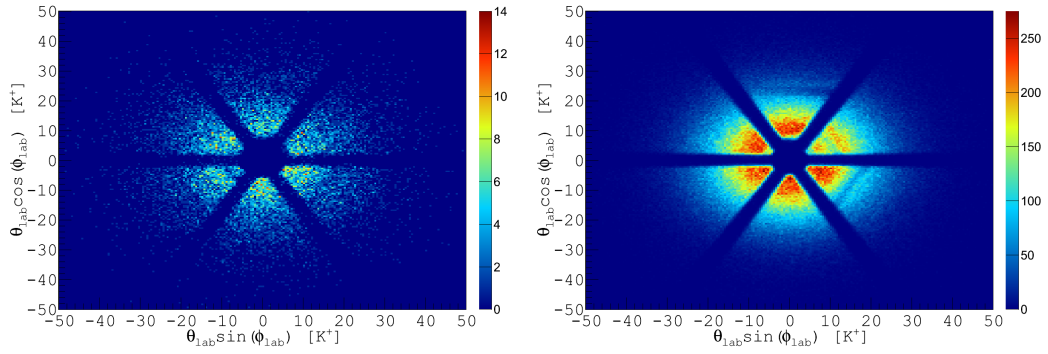


(e) The data  $(\phi_{lab}, \theta_{lab})$  distribution of  $\pi^-$ .

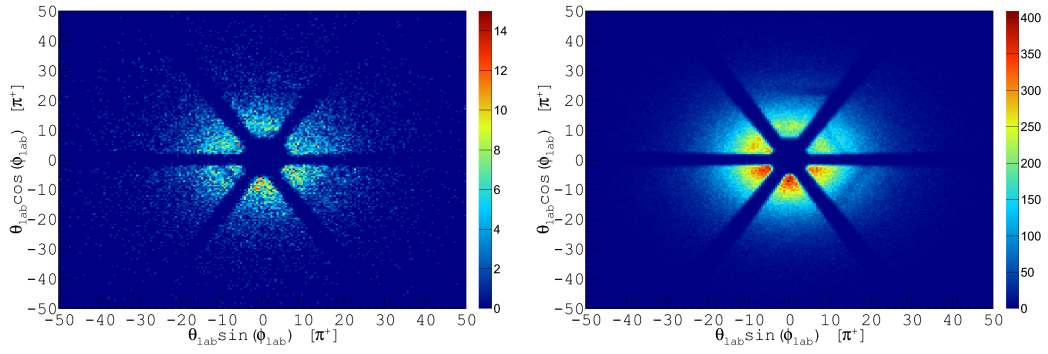


(f) The accepted  $(\phi_{lab}, \theta_{lab})$  distribution of  $\pi^-$ .

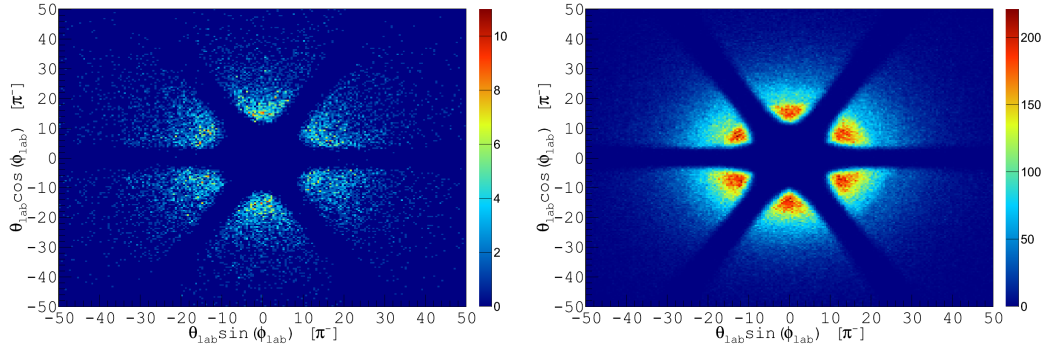
Figure 5.8: The  $(\phi_{lab}, \theta_{lab})$  angular distributions of all detected particles for both the data and the accepted Monte Carlo events.



(a) The data  $(\phi_{lab}, \theta_{lab})$  distribution of  $K^+$ . (b) The accepted  $(\phi_{lab}, \theta_{lab})$  distribution of  $K^+$ .



(c) The data  $(\phi_{lab}, \theta_{lab})$  distribution of  $\pi^+$ . (d) The accepted  $(\phi_{lab}, \theta_{lab})$  distribution of  $\pi^+$ .



(e) The data  $(\phi_{lab}, \theta_{lab})$  distribution of  $\pi^-$ . (f) The accepted  $(\phi_{lab}, \theta_{lab})$  distribution of  $\pi^-$ .

Figure 5.9: The  $(\phi_{lab}, \theta_{lab})$  angular distributions of all detected particles for both the data (right) and the accepted Monte Carlo (left) events, plotted as so to reflect the geometry of the CLAS detector.

## 5.2 Fitting Procedure

In this section we discuss the details of the PWA fitting procedure including the PWA package we used, the preparation of the dataset and our binning choice, minimization of the likelihood function and the software used, intensity errors estimation, the criteria for selecting waves to include in the fit, and our fit quality check methods.

### 5.2.1 The FSU PWA Toolkit

The PWA software toolkit used in this analysis is analogous to the PWA package developed at Brookhaven for the "E852" experiment. The programs in this kit were designed by Dr. Paul Eugenio using object-oriented methods to produce objects that would later be implemented using C++. The toolkit consists of a range of programs, each utilized to perform a specific task, that can be executed using a shell-based script developed by the user. Using this kit, a partial wave analysis can be performed by executing four major programs: **sliceGamp**, **gamp**, **pwaInts**, and **pwaFit**. This kit relies on the user to create the necessary directories and soft links to insure reliable communication between its programs. A Graphical User Interface was developed by the author to facilitate and speed up this procedure.

The partial wave analysis starts by supplying the sliceGamp package with a data file containing a set of events in a gamp format [63]. This data file is essentially an ascii file that includes the four vectors of the final state particles and the beam, their charges, and their "Gamp ID". SliceGamp reads the file and outputs another gamp formatted file containing events that fall within a user defined bin into a subdirectory. We execute sliceGamp for the g12 dataset and the Monte Carlo datasets independently but following the same binning criteria. The sliced data files are then supplied to gamp. Gamp is responsible of generating decay amplitudes for every event we include in the fit. To execute gamp, an input key file which contains a list of amplitudes to calculate and a data file containing events for which the amplitude is to be determined, are required. Gamp uses the four vectors to calculate the mass and momentum transfer "t" in addition to the angular properties of every event. The key file supplies gamp with the decay structure of the wave and the quantum numbers necessary to determine the amplitudes according to the prescription we outlined in Section 4.2. The output is an amplitude file for every wave in the waveset in every bin. This is done for the data as well as the raw and accepted

Monte Carlo. Since it is time consuming and requires extensive computing power, this step is only done once regardless of any changes in the wave set as long as the binning doesn't change and the amplitude for the added wave is available.

After generating the decay amplitudes with `gamp`, the raw and accepted Monte Carlo amplitudes are used to calculate the normalization integrals. This is done by executing a program called `pwaInts`. The decay amplitudes are provided to `pwaInts` alongside a set of waves to find the normalization integrals for. The `pwaInts` program then extracts the complex numbers from the amplitude files and calculates the integrals in every bin, based on the methodology explained in Section 4.2. A change in the number of waves to include in the fit, requires recalculating the normalization integrals for the raw and accepted Monte Carlo events. Following the successful calculation of the normalization integrals, the user can now execute the fitter by running the `pwaFit` program. The fitter uses the data decay amplitudes and the accepted normalization integrals to construct the likelihood function in an event-by-event manner. It requires supplying starting values for the fitting parameters, or more specifically the production amplitudes, by the user. A minimization software called "MINUIT" then minimizes the negative log of the likelihood function and returns the fitting parameters that best describe the data and waves included in the fit. MINUIT also provides estimated statistical errors that come from the likelihood fit, which can later be used to determine the statistical errors on the predicted intensities. More Details on MINUIT and the minimization of the likelihood function are discussed in Section 5.2.3.

The fitter finishes by providing the user with a file containing information about the number of events in each bin, the normalization integrals for the raw and accepted Monte Carlo, the error estimates on the likelihood fit, and the production amplitudes. The intensity for each wave, or a combination of waves, is then constructed using

$$\mathcal{N} = n_d \frac{n_r}{n_a} \sum_{\alpha\alpha'} V_\alpha V_{\alpha'}^* \epsilon_\alpha \psi_{\alpha\alpha'}^r \quad (5.2)$$

where  $V_\alpha$  are the production amplitudes (fit parameters), and  $\psi_{\alpha\alpha'}^r$  are the raw normalization integrals. The **pwaFitView** graphical user interface is then used to visualize intensities and relative phase motion between different waves.

### 5.2.2 Preparation of the $\gamma p \rightarrow \Lambda K^+ \pi^+ \pi^-$ Dataset

The preparation of the 16K selected  $\gamma p \rightarrow \Lambda K^+ \pi^+ \pi^-$  events begins with binning the data in the  $K\pi\pi$  invariant mass. The binning choice is governed by two factors: to maximize the number of events in every bin, and to insure that the bins are not too large that waves would not be able to assume their natural decay widths. Ideally, we would like to choose the finest bin size possible as it validates our assumption that the production amplitudes' dependence on the  $K\pi\pi$  system is constant. Furthermore, narrow bins are ideal when waves that fall in close proximity to each other are expected. It is also vital that the bins contain enough events so that the fitter's chances of finding a global minimum are increased. Indeed, the lower the number of events in a bin, the more likely the fitter converges the likelihood function to a local minimum. Additionally, a low number of events would result in higher errors due to statistical fluctuations.

Motivated by the fact that we only have 16K events to fit, we decided that binning our data in 100 MeV bins from 1.1 - 2.2 GeV is the most ideal choice for our analysis. At this rate, we were able to maintain around 1.5K events per bin in the area of interest in the  $K\pi\pi$  system. Choosing such wide bins, however, is problematic as it runs close to the decay widths of some of the states we expect most contribution from. Therefore, we were not able to choose narrower bins without drastically reducing the number of events per bin, but we were able to work around this problem by binning our data in 100 MeV bins again, only this time starting from 1.15 MeV to 2.25 MeV. This is not equivalent to binning the data in 50 MeV bins, but it is equivalent to performing two fits, thus allowing the study of the systematics of the PWA. At the end, both fits were performed simultaneously but independently, and their results were combined together to observe the intensities.

The final fitted dataset consisted 16K  $K^+ \pi^+ \pi^-$  events from 1.1 GeV to 2.2 GeV distributed among 11 bins, then binned again starting from a 50 MeV shifted bin to cover a range between 1.15 GeV and 2.25 GeV also distributed among 11 bins. The largest bin contained 2533 events from 1.4 GeV to 1.5 GeV, while the smallest bin housed 25 events from 2.15 GeV to 2.25 GeV. The decay amplitudes for every event were generated using **gamp** independently in a bin-by-bin manner. The set of allowed states for the  $K^+ \pi^+ \pi^-$  system is described in Section 5.2.4.

### 5.2.3 Minimization of The Likelihood Function and Error Estimation

We want to minimize the likelihood function to determine the parameters (production amplitudes) that best describe our data in a reliable and rapid manner. To do so, we adopt the use

of a package called **MINUIT** [54] to minimize the negative logarithm of the likelihood function. MINUIT is a physics analysis tool that was developed by Frederick James at CERN about 25 years ago. The software was originally written in Fortran, but has recently been re-implemented in an object oriented way using C++. MINUIT provides a set of tools for minimizing a chi-square, likelihood, or user-defined function and for special error analysis. A multi-parameter function can be supplied to the software with a crude assumption of the unknown parameters' starting values, **MIGRAD** (one of MINUIT's processors) is then called to minimize the function. When the function converges to a minimum, the fit parameters are found and MIGRAD provides the user with an estimation of the error matrix. The returned values are the real and imaginary parts of the production amplitudes in each bin for every wave included in the fit. The returned values are then implemented into the predicted intensities to study the contribution of waves to the  $K\pi\pi$  system, according to

$$\mathcal{N} = n_d \frac{n_r}{n_a} \sum_{\alpha\alpha'} V_\alpha V_{\alpha'}^* \epsilon \psi_{\alpha\alpha'}^r \quad (5.3)$$

The errors on the predicted intensities are of two natures, systematic and statistical. The systematic components come mostly from the truncation on the rank and on the number of partial waves included in a fit. The systematic errors are estimated by comparing different sets ( $j = 1, \dots, N$ ), of intensities,  $I_j$ , and calculate their variance using

$$\sigma_{sys}^2 = \frac{1}{N} \sum_{j=1}^N (\hat{I} - I_j)^2 \quad (5.4)$$

where  $\hat{I}$  is the average intensity of  $N$  wave sets. The statistical errors, on the other hand, come from the likelihood fit. They are derived by using the errors on the fit parameters that MINUIT outputs when it successfully minimizes the likelihood function. The statistical errors on the predicted  $\mathcal{N}$  values are calculated using the variance obtained by propagating errors through Equation 5.3. Recalling that the production amplitudes ( $V_\alpha$ ) are complex numbers, we can rewrite them as

$$V_\alpha = v_{\alpha R} + i v_{\alpha I} \quad (5.5)$$

where  $v_{\alpha R}$  is the real part of the production amplitude and  $v_{\alpha I}$  is the imaginary part, and  $\alpha = 1, \dots, n$ , where  $n$  is the total number of partial waves. Therefore, Equation 5.3 can be rewritten as

$$\mathcal{N} = n_d \frac{n_r}{n_a} \sum_{\alpha\alpha'} (v_{\alpha R} + i v_{\alpha I})(v_{\alpha R} - i v_{\alpha I})^\epsilon \psi_{\alpha\alpha'}^r \quad (5.6)$$

Then propagating the errors from  $v_{\alpha R}$  and  $v_{\alpha I}$  to  $\mathcal{N}$ , we obtain

$$\sigma_{stat}^2 = \mathcal{J} \cdot \mathcal{E} \cdot \mathcal{J}^T \quad (5.7)$$

where  $\mathcal{E}$  is the covariance matrix, more specifically, the error matrix produced by MINUIT, and  $\mathcal{J}$  is the Jacobian. The diagonal terms correspond to the errors for a single wave production amplitude, while the off-diagonal terms are a representation of the correlation between various production amplitudes. The Jacobian,  $\mathcal{J}$ , is a symmetric  $(2n) \times (2n)$  matrix. The error matrix generally has the following form

$$\mathcal{E} = \begin{bmatrix} \sigma^2(v_{1R}) & \sigma(v_{1R}, v_{1I}) & \cdots & \sigma(v_{1R}, v_{nR}) & \sigma(v_{1R}, v_{nI}) \\ \sigma(v_{1R}, v_{1I}) & \sigma^2(v_{1I}) & \cdots & \sigma(v_{1I}, v_{nR}) & \sigma(v_{1I}, v_{nI}) \\ \cdots & \cdots & \cdots & \cdots & \cdots \\ \cdots & \cdots & \cdots & \cdots & \cdots \\ \sigma(v_{nR}, v_{1R}) & \sigma(v_{nR}, v_{1I}) & \cdots & \sigma^2(v_{nR}) & \sigma(v_{nR}, v_{nI}) \\ \sigma(v_{nI}, v_{1R}) & \sigma(v_{nI}, v_{1I}) & \cdots & \sigma(v_{nI}, v_{nR}) & \sigma^2(v_{nI}) \end{bmatrix} \quad (5.8)$$

where the diagonal terms,  $\sigma^2(v_{\alpha R(I)})$ , are the standard variance of  $v_{\alpha R(I)}$ , and the off-diagonal terms  $\sigma(v_{\alpha R(I)}, v_{\alpha I(R)})$  represent the covariance between  $v_{\alpha R(I)}, v_{\alpha I(R)}$ . The Jacobian  $\mathcal{J}$  is an  $\alpha \times 2n$  vector of the form

$$\mathcal{J} = \left[ \cdots \quad \frac{\partial \mathcal{N}}{\partial v_{\alpha R}} \quad \frac{\partial \mathcal{N}}{\partial v_{\alpha I}} \quad \cdots \right] \quad (5.9)$$

the partial derivative of the predicted intensity can be determined using Equation 5.6,

$$\frac{\partial \mathcal{N}}{\partial v_{\alpha R(I)}} = 2 \times \sum_{j=1}^n \epsilon \psi_{\alpha j}^r v_{jR(I)} \quad (5.10)$$

Finally, the total error on the predicted intensity  $\mathcal{N}$  is obtained by using

$$\sigma_{\mathcal{N}}^2 = \sigma_{sys}^2 + \sigma_{stat}^2 \quad (5.11)$$

In a similar manner, we can estimate the error on the phase difference between two waves. The phase difference is defined as:

$$\Delta\phi = \arctan\left(\frac{Im(V_1V_2^*)}{Re(V_1V_2^*)}\right) \quad (5.12)$$

The errors in the phase difference can be determined by error propagation taking  $\Delta\phi$  as a function of the fitted  $V_1$  and  $V_2^*$  values. Replacing  $Re(V_1V_2^*)$  with  $a$  and  $Im(V_1V_2^*)$  with  $b$ , we can write the statistical error on the phase difference as

$$\sigma_{\Delta\phi}^2 = \left(\frac{\partial\delta\phi}{\partial a}\right)^2 \sigma_a^2 + \left(\frac{\partial\delta\phi}{\partial b}\right)^2 \sigma_b^2 + 2\left(\frac{\partial\delta\phi}{\partial a}\right)\left(\frac{\partial\delta\phi}{\partial b}\right)\sigma_{ab}^2 \quad (5.13)$$

where

$$\frac{\partial\Delta\phi}{\partial a} = \frac{a}{a^2 + b^2}; \quad \text{and} \quad \frac{\partial\Delta\phi}{\partial b} = \frac{-b}{a^2 + b^2}; \quad (5.14)$$

The errors in  $a$  and  $b$  can be derived using the error matrix MINUIT provides (Equation 5.8).

Hence,

$$\sigma_{a(b)}^2 = \mathcal{J}_{a(b)} \cdot \mathcal{E} \cdot \mathcal{J}_{a(b)}^T \quad (5.15)$$

and

$$\sigma_{ab}^2 = \mathcal{J}_a \cdot \mathcal{E} \cdot \mathcal{J}_b^T \quad (5.16)$$

The Jacobians  $\mathcal{J}_a$  and  $\mathcal{J}_b$  have the following form

$$\mathcal{J}_a = (v_{2R}, v_{2I}, v_{1R}, v_{1I}) \quad \text{and} \quad \mathcal{J}_b = (-v_{2I}, v_{2R}, v_{1I}, -v_{1R}) \quad (5.17)$$

where  $v_{1I(R)}$  and  $v_{2I(R)}$  are the imaginary and real parts of the complex numbers  $V_1$  and  $V_2$ .

Error analysis plays an important role in determining the quality of the fit, as it serves as a tool to assess the minimization of the likelihood function. Abnormally large errors, for instance, are an indication that MINUIT converged the likelihood function to a local minimum. This effect could be reduced by performing the fit multiple times with randomly generated starting values of the fit parameters, then choosing the production amplitudes where the likelihood function was the lowest in every bin and subsequently best errors.

#### 5.2.4 Wave Selection

The decision to include and exclude waves from a fit has a great impact on its likelihood to successfully describe the data. Ideally, we would like to include a large number of waves to get the best description of the angular structure of the data, however, we are constrained by the available statistics. In our case, the 16K events demand reducing the wave set down to the most important and most contributing waves required by the data. The final  $K^+\pi^+\pi^-$  invariant mass showed significant structure in the lower mass region and exhibited a shoulder behavior in the higher mass region, the  $K^+\pi^+\pi^-$  system is thus divided into two mass regions, and both regions are fitted independently. In what follows, the method we use to construct the waves and our choice of isobars, are described.

**Parametrization of the Isobars:** The decay of the  $K^+\pi^+\pi^-$  resonance will be described in a subsequent decays manner via the isobar model as we previously outlined. This translates to a decay of a resonance to an isobar and  $K^+$  or  $\pi^+$  bachelor particle. The isobar, in turn, would then decay to a  $K^+\pi^-$  or a  $\pi^+\pi^-$  preserving charge, angular momentum, isospin, parity, and energy. Experiments that explored the  $K\pi\pi$  system in the past, observed major contributions from the  $\rho(770)$ , the  $K^*(892)$ , and the  $K_2^*(1430)$  to the decay of several excited strange mesons. In order to include any isobars in our partial wave set, it is important to observe indications of these isobars in the  $K^+\pi^-$  and  $\pi^+\pi^-$  invariant mass spectrum. This means, that peaks or possible shoulder behavior around the mass of the isobar should exist for the isobar to be included in the construction of the partial waves.

Table 5.1: The full set of isobars considered to contribute to the invariant mass distributions of  $K^+\pi^-$  and  $\pi^+\pi^-$  subsystems. Isobars that were present in our data, and were essential for the success of the PWA, are marked in red.

$J^P$	State Name	Decay Channel	Model
$0^+$	$f_0(600)$	$\pi^+ \pi^-$	Breit-Wigner
$0^+$	$f_0(980)$	$\pi^+ \pi^-$	Breit-Wigner
$0^+$	$f_0(1370)$	$\pi^+ \pi^-$	Breit-Wigner
$0^+$	$f_0(1500)$	$\pi^+ \pi^-$	Breit-Wigner
$0^+$	$K(800)$	$K^+ \pi^-$	Breit-Wigner
$0^+$	$K_0^*(1430)$	$K^+ \pi^-$	Breit-Wigner
$1^-$	$\rho(770)$	$\pi^+ \pi^-$	Breit-Wigner
$1^-$	$\rho(1450)$	$\pi^+ \pi^-$	Breit-Wigner
$1^-$	$K^*(892)$	$K^+ \pi^-$	Breit-Wigner
$1^-$	$K^*(1680)$	$K^+ \pi^-$	Breit-Wigner
$2^+$	$f_2(1270)$	$\pi^+ \pi^-$	Breit-Wigner
$2^+$	$K_2^*(1430)$	$K^+ \pi^-$	Breit-Wigner

Table 5.1 summarizes the set of isobars considered to contribute to the observed  $K^+\pi^-$  and  $\pi^+\pi^-$  mass spectrum. All of these waves were parameterized with relativistic Breit-Wigner functions. For this analysis, except for the  $K_2^*(1430)$  and the  $f_2(1270)$ , all of the higher mass isobars were excluded from the partial wave analysis, due to the absence of any indications of their existence in our data. The  $f_0(600)$  and its strange equivalent the  $K(800)$  were also excluded from the fit that we found to describe the data the best. Instead of these states, we used an isotropic flat background. Results from a fit that included these states are shown in Appendix A.1.

**Waves construction and selection:** The partial wave set for the  $K^+\pi^+\pi^-$  system was constructed by combining the isobars (marked red) in Table 5.1 and a bachelor particle. As we mentioned earlier, candidate waves must conserve all the symmetries of the strong interaction in their production. For this analysis, we will rely on angular momentum, isospin, and parity to construct these states. We start off by using the initial state of the photon ( $J^P = 1^-$ ) and the proton ( $J^P = \frac{1}{2}^+$ ) and assuming an exchange of a  $K^+$  between the baryon and meson vertex. The dominance of a kaon exchange translates to a rank I spin density matrix. The photon and

the recoil baryon have the freedom to interact with any relative orbital angular momentum thus allowing all spins to be produced. The parity of the resonance should be constructed in a way that it is conserved when the resonance decays to an isobar and a bachelor. Although commonly used in partial wave analysis for  $3\pi$  systems, the G and C parities are dropped here as a result of the absence of such symmetries in strange states. Therefore, we only use the following quantum numbers and physical properties to construct our waves and their corresponding amplitudes:

- J, the total spin of the resonance.
- P, the parity of the resonance.
- L, the relative angular momentum of the isobar Y and the bachelor particle ( $K^+$  or  $\pi^+$ )
- I, the isospin of the resonance.
- s, the spin of the isobar (in most cases  $l=s$ , as we have spinless final state particles)
- l, the relative angular momentum between the two daughters of the isobar.
- $[\omega_0, \Gamma_0]$ , the central mass and width of the isobar as determined by PDG [16].

Each wave will also be characterized by its reflectivity  $\epsilon$ . The isospin and total spin of a state follow the usual selection rules

$$|I_I - I_B| \leq I \leq |I_I + I_B| \quad (5.18)$$

and

$$|L - S| \leq J \leq |L + S| \quad (5.19)$$

The total parity of a resonance is determined using

$$P = P_I \cdot P_B \cdot (-1)^L \quad (5.20)$$

where  $P_I$  is the parity of the isobar and  $P_B$  is the parity of the bachelor particle. To illustrate how a wave is constructed in more details, we propose an example where we look for a state that decays to a  $\rho(770)K^+$  in an S-wave. An S-wave translates to an angular momentum  $L = 0$  between the isobar and the bachelor particle. The  $\rho$  has a spin  $S_\rho = 1$ , while the  $K^+$  is spinless. The total spin  $S$  for this system is therefore 1. Per Equation 5.19, the total spin  $J$  of the state is therefore 1. The parity is determined using Equation 5.20, thus the parity of this state is

$P = (-1) \cdot (-1) \cdot (-1)^0 = 1$ . Finally, the reflectivity of this state can be either +1 or -1 and is determined using Equation 4.23. In this case, the reflectivity is -1 which means that this is an unnatural state. In conclusion, a state that decays to a  $\rho(770)K^+$  in an S-wave has a  $J^P$  equal to  $1^+$ . A state where the resonance decays to a  $K^*(892)\pi^+$  in an S-wave is constructed in the same manner and has the same form  $J^P = 1^+$ .

We could construct as many states as we wish and include them in our fit. However, as we explained before, statistical limitations prohibit us from doing so. Therefore, we only include states that are required to describe the data. We therefore exclude any waves with high total spin from our fits as our data does not provide the phase space needed by higher spin states, we therefore bound our states to  $J \leq 4$ . We also exclude waves with  $J=0$ , because the production of such states with a photon beam is not possible with the exchange of a spin-0 particle between the baryon and meson vertexes. Similarly,  $m=0$  is excluded from all other  $J^P$ 's. We also exclude any  $M > 1$  spin projections from the final fit as they were not required by the data. All the waves that could have possibly contributed to our data are compiled in Table A.2.

Although we could systematically decide which waves can be included in our fits, the process of choosing a "good" wave set remains a matter of iterating through different wave combinations. We therefore began with a small wave set including only the lowest angular momentum  $L = 0$  waves. We then studied the intensities of these waves and gradually added other waves while excluding ones that were not required by the data. It should be noted that in rare occasions, excluding an insignificant wave from the fit had an effect on the intensities of other waves, in this case, the wave was kept in the fit. Looking back at our final  $K^+\pi^+\pi^-$  invariant mass spectrum in Figure 3.21(a), we recall that the most significant structure is evident in the lower mass region between 1.3-1.5 GeV. In general, the low mass region of a  $K\pi\pi$  system is heavily populated with states that have been observed in a handful of experiments with kaon or pion beams. As a matter of fact, states such as the  $K_1(1270)$  and  $K_1(1400)$  have been observed to dominate this mass region [26] [29] [30] [31]. Additionally, the higher mass region has showed no resonating behavior, except for a shoulder around 1.8 GeV. As a result, we limited our states in the higher mass region to the waves we included in the lower mass region and two  $2^-$  waves decaying primarily to  $K_2^*(1430)\pi^+$  and  $f_2(1270)K^+$  in an S wave. We excluded  $1^+$  D-waves from all fits after observing that most of the  $1^+$  intensity is concentrated in S-waves.

The final wave set consisted of 13 waves, including an isotropic flat background, in the 1.1 - 1.6 GeV mass region, and 17 waves in the 1.6 - 2.2 GeV mass region. The 4 waves difference

Table 5.2: The full set of waves expected to contribute in the partial wave analysis. Waves in red correspond to the ones that we included in the final fit where the best results were obtained. The check marks indicate the region where a wave is included in the partial wave analysis. Keep in mind that except for the flat background, every wave has two reflectivities.

<b>L</b>	$J^P$	<b>Isobar</b>	<b>Bachelor</b>	<b>1.1 - 1.6 GeV</b>	<b>1.6 - 2.2 GeV</b>
S	$0^-$	$f_0(600)$	$K^+$		
	$0^-$	$K^*(800)$	$\pi^+$		
	1 <sup>+</sup>	$\rho(770)$	$K^+$	✓	✓
	1 <sup>+</sup>	$K^*(892)$	$\pi^+$	✓	✓
	$2^-$	$f_2(1270)$	$K^+$		✓
	$2^-$	$K_2^*(1430)$	$\pi^+$		✓
P	$1^+$	$f_0(600)$	$K^+$		
	$1^+$	$K^*(800)$	$\pi^+$		
	1 <sup>-</sup>	$\rho(770)$	$K^+$	✓	✓
	1 <sup>-</sup>	$K^*(892)$	$\pi^+$	✓	✓
	$2^-$	$\rho(770)$	$K^+$		
	$2^-$	$K^*(892)$	$\pi^+$		
D	$1^+$	$\rho(770)$	$K^+$		
	$1^+$	$K^*(892)$	$\pi^+$		
	2 <sup>+</sup>	$\rho(770)$	$K^+$	✓	✓
	2 <sup>+</sup>	$K^*(892)$	$\pi^+$	✓	✓
Flat	Isotropic			✓	✓

is due to the addition of the  $2^-$  waves exclusively in the higher mass region as they will not contribute in any way to the masses below their production threshold of 1.6 GeV. The  $f_0(600)$  and the  $K^*(800)$  isobars were not chosen for the final wave set as they were observed to have inhomogeneous behavior whenever a wave was excluded or included. While previous experiments included these waves, in addition to a flat background, we decided to remove them when a flat background was included, as they were found to cause an ambiguity. Results where these waves replace the flat background are presented in Appendix A.1.

### 5.2.5 Fit Quality

In Section 5.2.3, we mentioned that intensity errors give insight about the quality of the fit. They, however, are not a qualitatively reliable test for the quality of the fit. Statistical limitations can significantly affect the quality of the fit and the error estimations, and due to the low number of events in each bin, MINUIT might converge to a local minimum thus giving incorrect values for the production amplitudes. Several strategies have been implemented in this PWA procedure to guarantee best results. The first strategy dictates performing a mass independent fit multiple times with random starting values for the production amplitudes, then fitting every bin independently. This is followed by selecting as the correct minimum, the fit that returns the smallest likelihood value. We employed this strategy in our fits and noticed marginal effect on their quality, potentially due to the complexity of the structure of the likelihood space.

The second strategy is to track up and down bins in  $K\pi\pi$ . A bin, generally with the highest statistics or most stable results, is chosen to initialize the fitter. Random starting values are supplied to the fitter so it can start fitting from the chosen bin. The fit parameters that the fitter then returns, are used as starting values for the neighboring bin. The fitter tracks up the mass spectrum or down depending on the user's preference. This method ensures rapid convergence for subsequent bins, as production amplitudes tend to vary smoothly over the  $K\pi\pi$  mass range as we showed in Figure 4.3. For this analysis, the 1.5-1.6 bin was chosen as a starting point, mainly because it gave the most stable likelihood results and for being a point of separation for the two mass regions. The fitter then tracked down from 1.6 GeV to 1.1 GeV fitting the mass region with the wave selection shown in Table A.2. Similarly, the fitter tracked up the bins from 1.5 GeV to 2.2 GeV fitting this mass region with the selected waves. This strategy significantly enhanced the fit results, mainly because it starts with a bin that has higher number of events compared to bin 1.1-1.2 GeV where only a handful of events are accessible.

Both of the methods above were employed in this analysis to guarantee best final results. The fit was performed a number of times with different fit parameters starting values and from different initial bins to study consistency. To qualitatively estimate how well the fit describes the data, weighted Monte Carlo distributions were generated. This method gives the most concise quality check as it takes into account the angular dependencies of the fitted waves and the acceptance of the detector to illustrate how well the "mock data" describes the real data. To generate weighted Monte Carlo distributions, we start off with a set of accepted Monte Carlo

events that we used in the fitter to find the weight  $W_{i,\alpha}$  for each wave  $\alpha$  in every event  $i$

$$W_i = \sum_{\alpha,\alpha'} V_\alpha^* V_{\alpha'} A_{i,\alpha}^* A_{i,\alpha'} \quad (5.21)$$

where V and A are the production and decay amplitudes. One then finds the sum of weights over  $\alpha$  for every event thus quantifying the kinematics with the fitted production amplitudes. The total weight for every event is then normalized to the maximum weight in a bin to obtain a number between 0 and 1 for each event. The dividend is then compared to a random number  $r$  between 0 and 1, if

$$r > \frac{W_i}{W_{max}} \quad (5.22)$$

is satisfied, the event is kept. The weighted Monte Carlo sample is thus reduced to  $N$  events in total, where  $N$  is the number of events in the real data. When analyzing these events, various distributions are generated to compare them to distributions from the experimental data. Ideally, including a large set of waves in our fit gives the best predicted distributions as the angular structure of the data would be adequately described. However, statistical limitations dictate leaving only the most significant waves in our fits. Predicted distributions for this analysis are shown in Section 5.3.6.

## 5.3 Fit Results

A mass independent partial wave analysis was carried out on 16K  $\gamma p \rightarrow K^+ \pi^+ \pi^-$  events from the CLAS g12 experiment using an event based likelihood fit. The fit was performed multiple times with different wave sets to determine the partial waves which make the most significant contributions to describing our data. Results presented below are from the fit where the most significant waves which were required to describe the data. The fit quality was assessed by stability tests, by performing several fits with random starting parameters in each bin, as well as results of the predicted distributions. All the intensities below have been corrected for acceptance.

### 5.3.1 The Total Intensity

The coherent sum over all waves gives the total intensity in Figure 5.11. The total intensity is an illustration of an acceptance corrected  $K^+ \pi^+ \pi^-$  invariant mass distribution. Effects of acceptance can be seen when comparing Figures 5.11 and 3.21(a). The shoulder in the higher mass

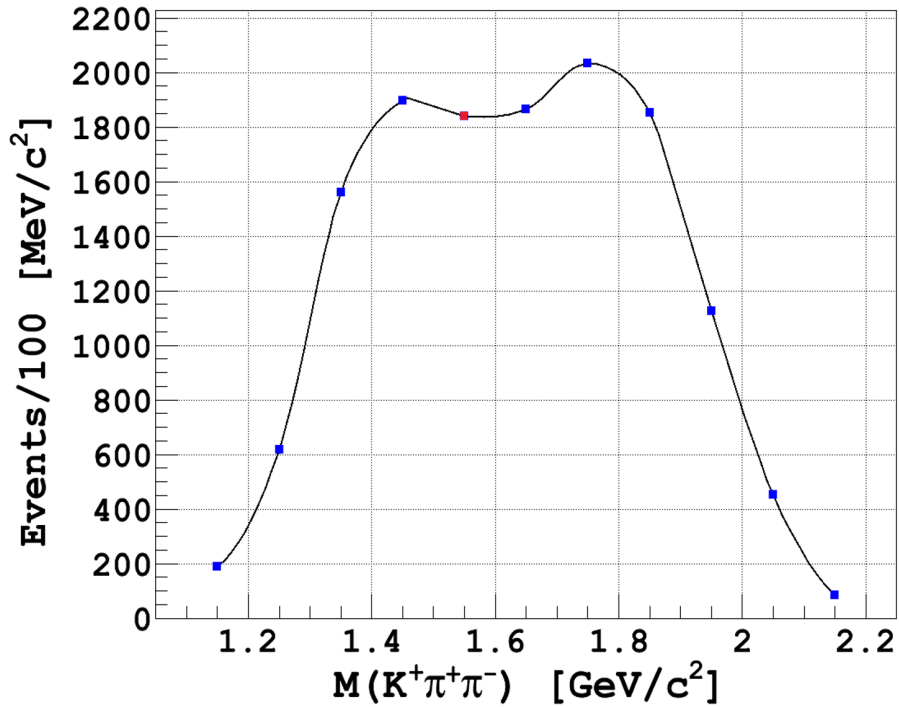


Figure 5.10: The values of the likelihood function at its minimum for each bin in the fit we are presenting. The red point indicates the location of the bin which we used in our tracking process. A total of hundred fits were performed in that bin to determine the minimum of the likelihood function.

region was reduced, while the lower mass region peak became more prominent. The acceptance corrected  $K\pi\pi$  mass distribution can be also determined by simply finding the product of the number of events in every bin in Figure 3.21(a) and the inverse of the acceptance. A rather easy way to determine the acceptance is by dividing the number of accepted Monte-Carlo events in every bin in  $K\pi\pi$ , by the number of raw Monte Carlo events in the same bin.

### 5.3.2 $1^+S$ Waves

**Discussion:** The  $1^+$  waves showed significant structures in both mass regions for both decay modes. Figure 5.12 illustrates the intensity of the coherent sum of all  $1^+S$  waves included in the fit. One can observe a very prominent peak in the lower mass region, thus consistently peaking where the  $K\pi\pi$  invariant mass in Figure 3.21(a) most dominantly peaks. A shoulder in the higher mass region between 1.6 and 1.8 GeV is also observed. Both peaks were found to be stable regardless of any changes in fitting parameters or permutations of waves. The structure

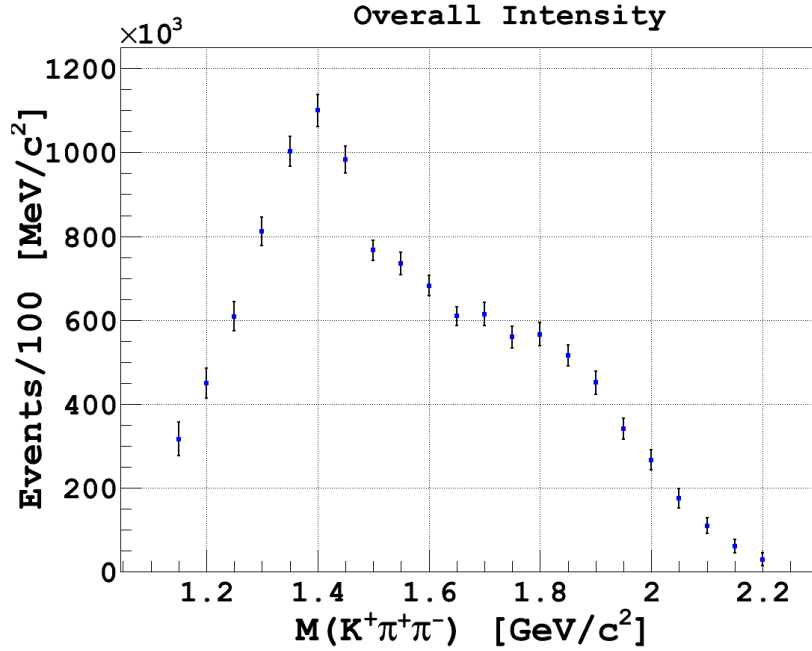


Figure 5.11: The acceptance corrected total intensity of all the partial waves in the fit. To determine the total intensity, the coherent sum of all the partial waves is calculated.

around 1.35 GeV falls in a range where to the  $K_1(1270)$  and  $K_1(1400)$  have been observed. Both of these states have been found to exist between 1.2 GeV and 1.4 GeV. They are also rather broad with decay widths around 100 GeV for the  $K_1(1270)$  and 170 GeV for the  $K_1(1400)$  [16]. Taking our binning choice into account and the proximity at which these two states exist, it would be difficult to separate their contributions to the  $1^+$  intensity in the lower mass region. We could however use their branching ratios to possibly distinguish them by studying different partial waves contributions to the  $1^+S$  intensity.

When we examine the  $1^+S \rho(770)K^+$  wave intensity in Figure 5.13(a), we notice that this wave exhibits resonating structures in both mass regions. An enhancement around 1.35 GeV and a broader more prominent enhancement peaking around 1.7 GeV are evident. The lower mass region in the  $1^+S K^*(892)\pi^+$  wave is dominated by a structure peaking around 1.35 GeV as well. While the low mass structures in both waves could be representations of the same state, it is difficult to draw a conclusion. We mentioned earlier that this  $K\pi\pi$  mass region has been thoroughly studied by a handful of experiments using a hadronic beam. Most of these studies reported confirmation of the  $K_1(1270)$  and  $K_1(1400)$  in this region whenever separation was possible. According to reference [16], the  $K_1(1400)$  state decays primarily (94% of the time)

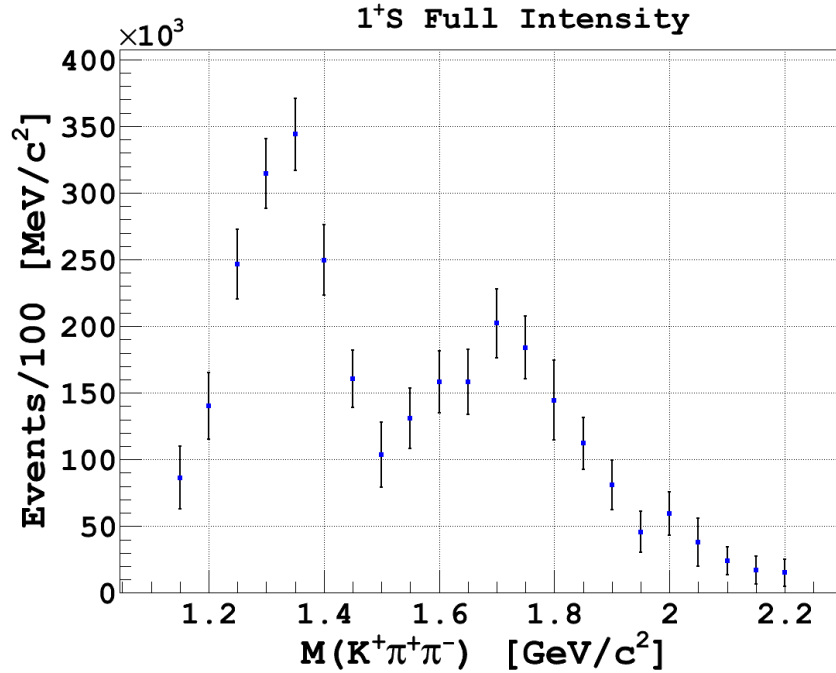
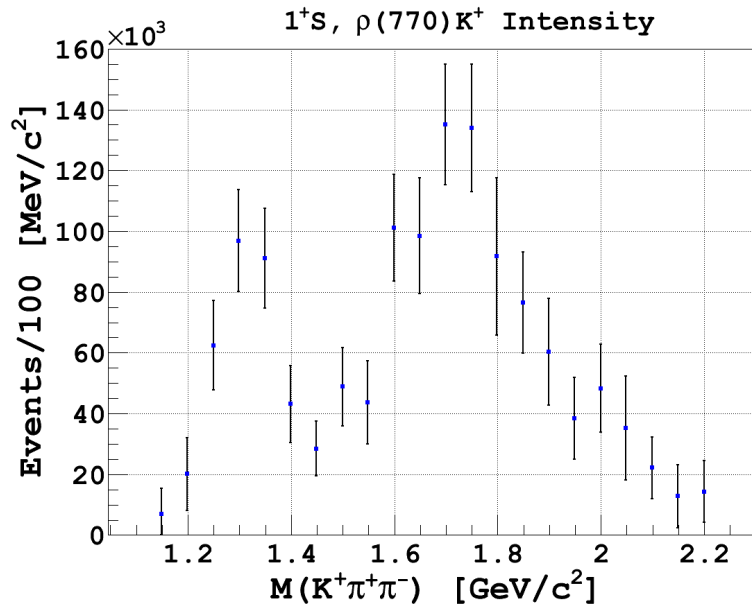


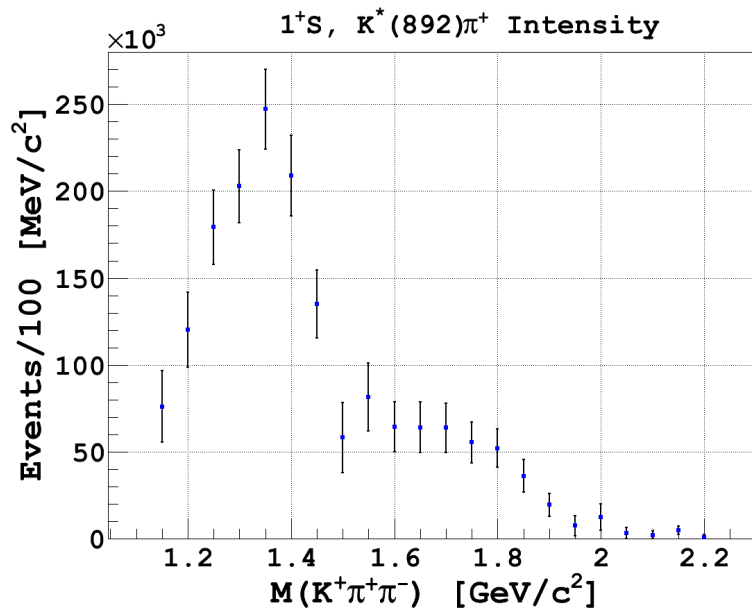
Figure 5.12: The acceptance corrected total intensity of all  $1^+S$  waves included in this fit. This intensity includes the coherent sum of amplitudes of  $1^+S$  wave decaying to a  $\rho(770)K^+$  or a  $K^*(892)\pi^+$ .

through  $K^*(892)\pi$ , while the  $K_1(1270)$  decays dominantly through  $\rho(770)K$ . We fitted the  $1^+SK^*(892)\pi^+$  intensity to a mass-dependent Breit-Wigner distribution to get more reliable mass and width results and possibly identify the state. The results are shown in Figure 5.14(a). The mass obtained ( $1.347 \pm 0.015$  GeV) and the width ( $0.224 \pm 0.062$  GeV) were found to be close to the properties of one of the  $1^+$  states reported in this region, i.e. the  $K_1(1400)$ 's. If we take into account decay properties of the  $K_1(1400)$  reported in reference [16], the width of the  $1^+SK^*(892)\pi^+$  enhancement is in good agreement with the width of the reported state. Similarly, the mass we obtained from our fit falls within the mass limits reported by other experiments for the  $K_1(1400)$ . A similar structure was observed in the  $1^+S\rho(770)K^+$  as we will discuss below.

Both peaks in the  $1^+S, \rho(770)K^+$  wave intensity were also fitted as shown in Figure 5.14(b). This wave was not fitted with a simple Breit-Wigner. We instead used the K-matrix formalism. More particularly, we relied on the P-vector approximation of the K-matrix formalism as outlined by reference [61]. The fit yielded a mass of  $1.313 \pm 0.027$  GeV and a width of a  $0.1463 \pm 0.016$

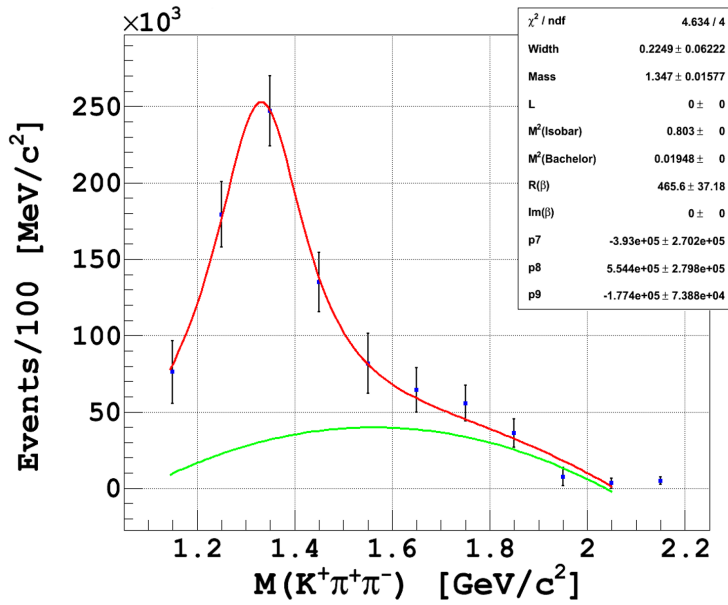


(a) The  $1^+S, \rho(770)K^+$  wave intensity.

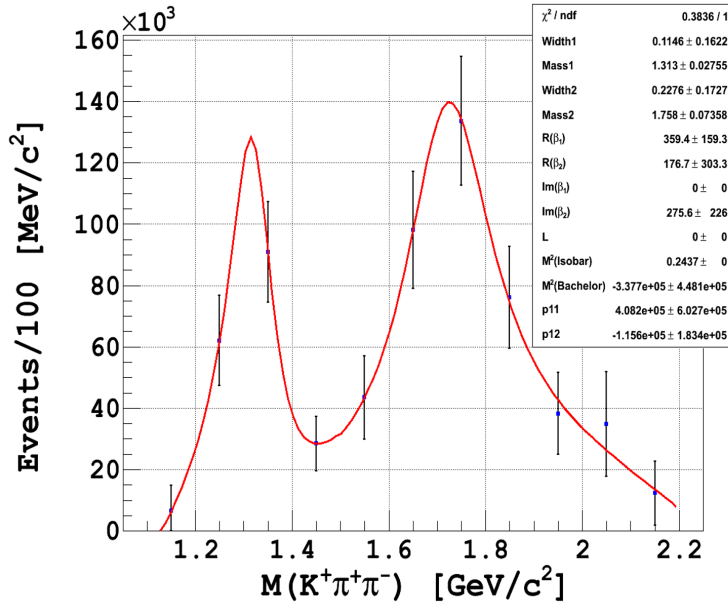


(b) The  $1^+S, K^*(892)\pi^+$  wave intensity.

Figure 5.13: The acceptance corrected total intensities  $1^+S$  waves decaying to  $\rho(770)K^+$  (a) and  $K^*(892)\pi^+$ (b).



(a) The  $1^+S, K^*(892)\pi^+$  wave intensity.



(b) The  $1^+S, \rho(770)K^+$  wave intensity.

Figure 5.14: The acceptance corrected intensities of the  $1^+S$  with a relativistic Breit-Wigner fit of the low mass structure in  $1^+S, K^*(892)\pi^+$  (a) and a K-matrix fit of both structures in  $1^+S, \rho(770)K^+$  (b).

GeV for the lower mass structure, and a mass of  $1.758 \pm 0.075$  GeV with a broad width of  $0.227 \pm 0.017$  GeV for the higher mass structure. Keep in mind that these parameters do not represent the masses and widths of the actual resonances. The actual resonance properties are determined using the fitted values of the K-matrix as we explain in Appendix D. Comparing the actual resonance properties from the lower mass region of this wave ( $m=1.33 \pm 0.027$  GeV and  $\Gamma=0.144 \pm 0.021$  GeV) to those from  $1^+SK^*(892)\pi^+$ , we notice only a slight difference in both the mass and the width. And while the mass and width of the low-mass structure in the  $1^+S, \rho(770)K^+$  wave are significantly closer to those of the  $K_1(1400)$  state, a conclusion about whether this state is a  $K_1(1270)$  or  $K_1(1400)$  can not be confidently drawn.

The fitted broad peak in  $1^+S\rho(770)K^+$  had a mass of  $1.734 \pm 0.032$  GeV and a width of  $0.2279 \pm 0.036$  GeV and was not found to be explicitly consistent with any states in Reference [16]. This state, however, does possess some similarities to the reported, yet unconfirmed,  $K_1(1650)$  having a mass close to the suggested average of 1.65 GeV and a width close to the 0.250 GeV broad width. It should be noted that this structure was very stable against any changes in the set of waves included in the fit. It was also present when the flat background was swapped for the  $0^-\sigma K^+$  and/or  $0^-K^*(800)\pi^+$  waves.

**Conclusion:** The  $1^+S$  exhibited very distinct and stable resonating behavior in both mass regions. A resonance coupling strongly to the  $K^*(892)\pi^+$  decay mode was observed to have a mass =  $1.347 \pm 0.015$  GeV and a width =  $0.224 \pm 0.062$  GeV. The  $\rho(770)K^+$  decay mode also exhibited resonating behavior in the low mass region with a mass =  $1.33 \pm 0.027$  GeV and a width =  $0.144 \pm 0.021$  GeV. The resonance around 1.7 GeV was observed to couple strongly to the  $\rho(770)K^+$  decay mode and had a mass =  $1.734 \pm 0.032$  GeV and a width =  $0.2279 \pm 0.036$  GeV. Similarities were found between the high mass broad structure in the  $1^+S\rho(770)K^+$  wave and the  $K_1(1650)$ .

### 5.3.3 $1^-P$ Waves

**Discussion:** The  $1^-P$  wave consistently showed strong resonating behavior in the lower mass region. The peak around 1.4 GeV in Figure 5.15 was found to be most pronounced in the  $1^-PK^*(892)\pi^+$  wave. Additionally, the  $1^-P$  wave showed stable behavior regardless of any addition or elimination of other waves. The prominent peak around 1.4 GeV seemed to couple strongly to the  $K^*(892)\pi^+$  mode, while the  $1^-P\rho(770)K^+$  wave exhibited no resonating behavior.

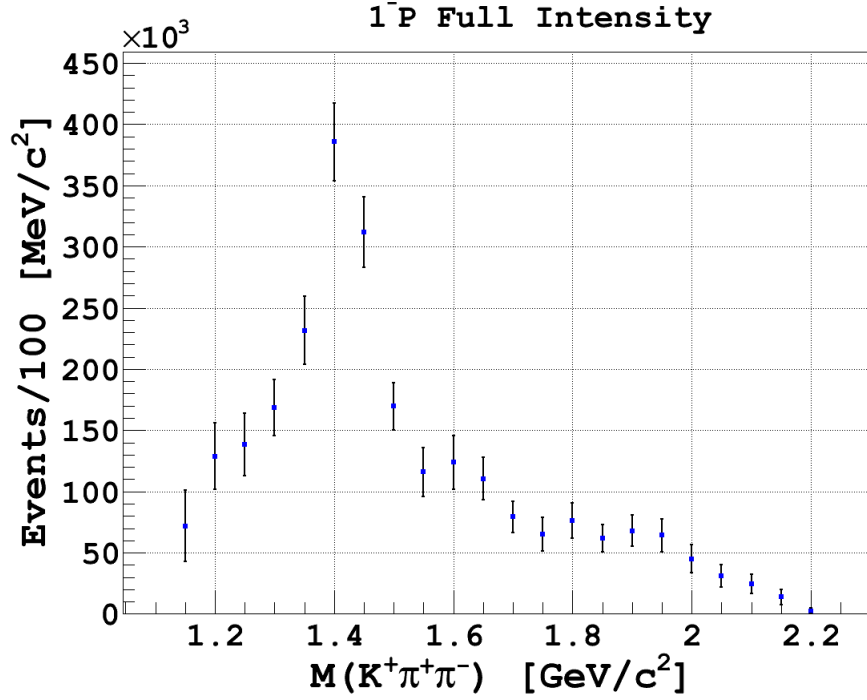
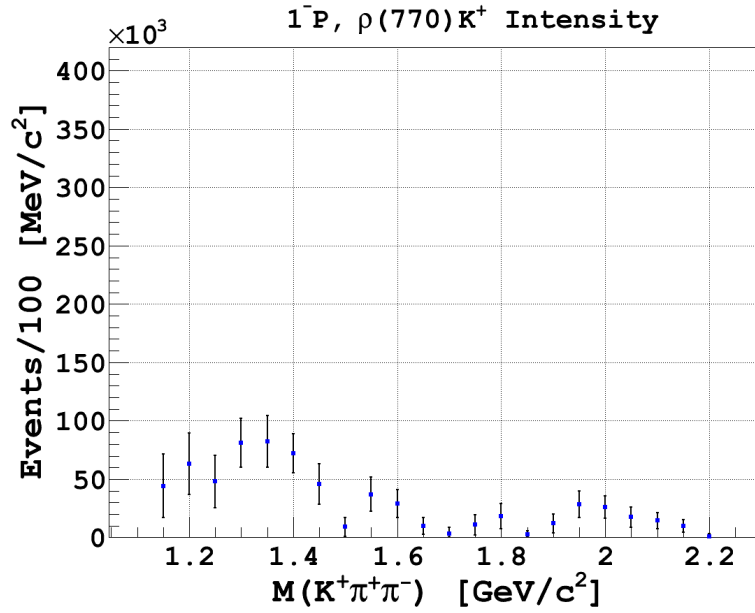


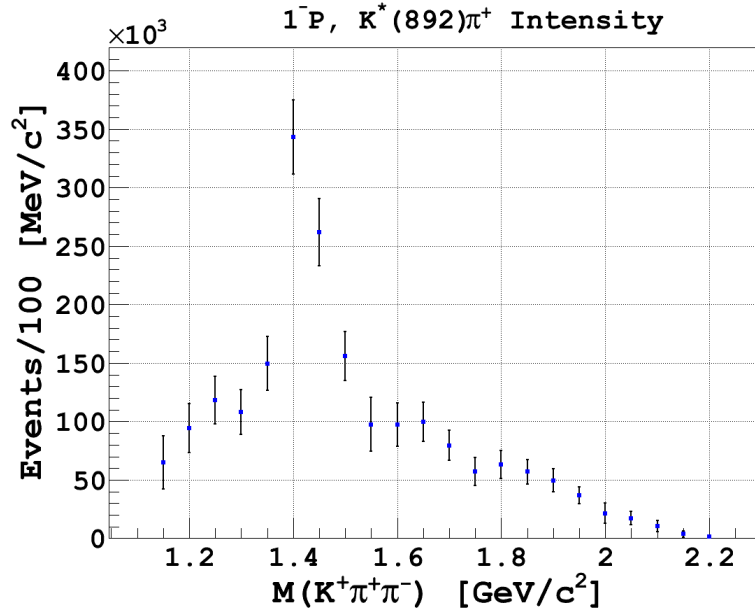
Figure 5.15: The acceptance corrected total intensity of all  $1^-P$  waves included in this fit. This intensity includes the coherent sum of amplitudes of  $1^-P$  wave decaying to a  $\rho(770)K^+$  or a  $K^*(892)\pi^+$ .

Figure 5.16 shows the intensities of  $1^-P, \rho(770)K^+$  and  $1^-P, K^*(892)\pi^+$ . One can observe of how strongly the  $1^-P$  wave couples to the  $K^*(892)\pi^+$  decay mode. The main structure in Figure 5.16b is centered around 1.4 GeV. A Similar behavior was not present in Figure 5.16a. We are only presenting the results of  $1^-P\rho(770)K^+$  for completion. From Figure 5.17 we can obtain the results of a mass dependent analysis of this structure. The fit yields a mass of  $1.429 \pm 0.024$  GeV and a width of  $0.097 \pm 0.072$  GeV, very close to the 1.414 GeV average mass but substantially narrower than the 0.232 GeV average width of the  $K^*(1410)$  state as reported by reference [16]. Decay properties of this structure were found to be in good agreement with the  $K^*(1410)$ , decaying primarily to  $K^*(892)\pi^+$ .

**Conclusion:** An enhancement was found in the  $1^-P$  wave around 1.43 GeV. This wave evidently coupled strongly to the  $K^*(892)\pi^+$  decay mode. Upon performing a mass dependent analysis on the low mass structure in the  $1^-P, K^*(892)\pi^+$  wave intensity, we found agreement between this structure and the  $K_1(1410)$  state in terms of mass and branching ratios.



(a) The  $1^-P, \rho(770)K^+$  wave intensity.



(b) The  $1^-P, K^*(892)\pi^+$  wave intensity.

Figure 5.16: The acceptance corrected total intensities  $1^-P$  waves decaying to  $\rho(770)K^+$  (a) and  $K^*(892)\pi^+$  (b).

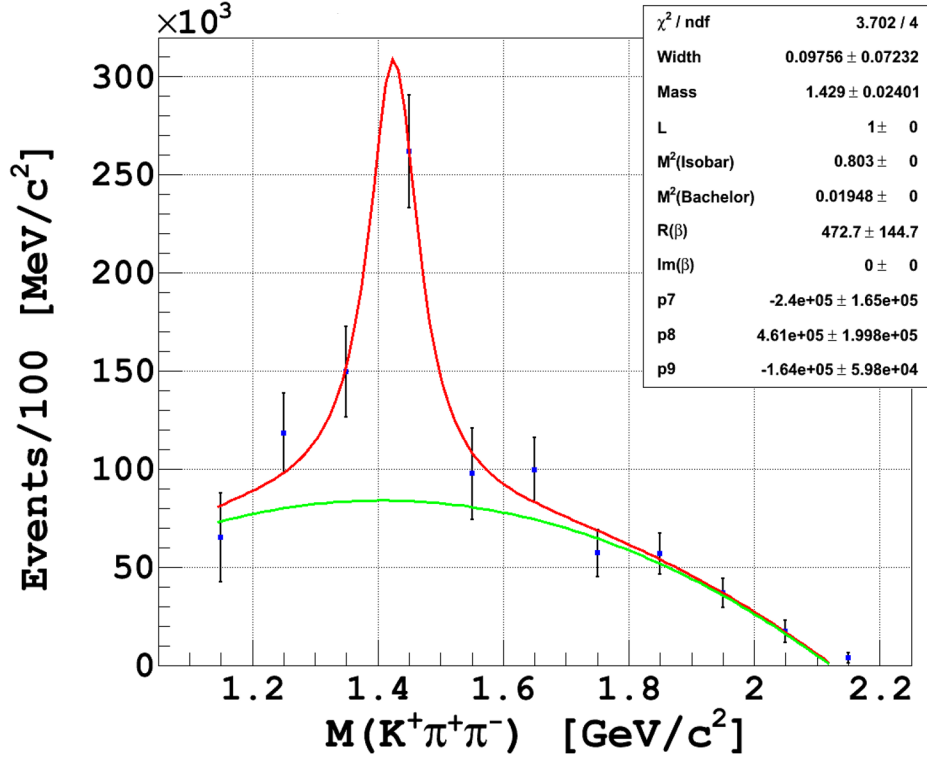


Figure 5.17: The acceptance corrected total intensity of all  $1^-P$  waves included in this fit. This intensity includes the coherent sum of amplitudes of  $1^-P$  wave decaying to a  $\rho(770)K^+$  or a  $K^*(892)\pi^+$ .

### 5.3.4 $2^+D$ Waves

**Discussion:** Also included in this fit are the  $2^+D$  waves. The  $2^+$  wave has been extensively observed in the  $K\pi\pi$  system in several kaon beam experiments [12][26][32]. It has been observed to strongly couple to the  $K^*(892)\pi$  mode, and primarily dominate the lower mass region via the  $K_2^*(1430)$  state. The overall intensity of the  $2^+D$  wave is shown in Figure 5.18. A significant enhancement can be seen in the lower mass region around 1.5 GeV. The  $2^+D$  intensity for the  $\rho(770)K^+$  and the  $K^*(892)\pi^+$  decay modes are shown in Figures 5.19(a) and 5.19(b). Both intensities exhibit broad enhancements between 1.4 and 1.6 GeV, however the  $\rho(770)K^+$  was not as stable, therefore none of the enhancements it exhibited were considered for a mass dependent analysis. The  $2^+DK^*(892)\pi^+$  intensity was fitted with a mass-dependent relativistic Breit-Wigner as shown in Figure 5.20. The resulting parameters ( $m=1.49 \pm 0.012$  GeV and  $\Gamma=0.141$

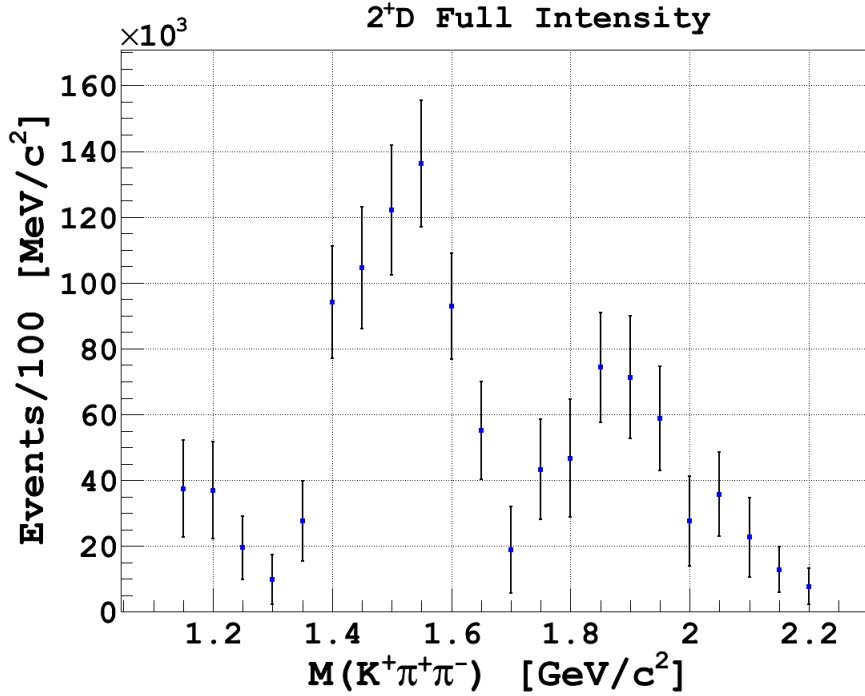


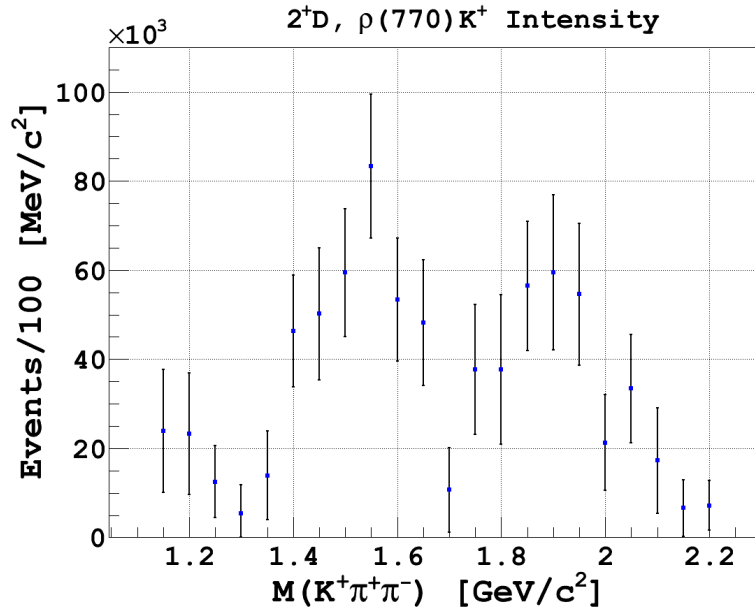
Figure 5.18: The acceptance corrected total intensity of all  $2^+D$  waves included in this fit. This intensity includes the coherent sum of amplitudes of  $2^+D$  wave decaying to a  $\rho(770)K^+$  or a  $K^*(892)\pi^+$ .

$\pm 0.042$  GeV) are in close agreement with the only reported  $2^+$  state around 1.4 GeV, the  $K_2^*(1430)$ . If we compare the width of the enhancement we obtained with the reported range of widths for the  $K_2^*(1430)$ , we notice a good agreement.

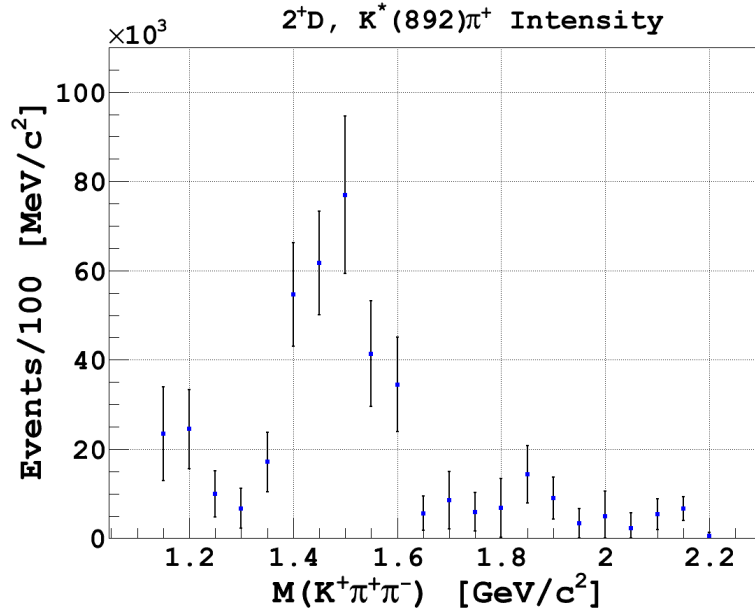
**Conclusion:** A stable structure in the low mass region, that strongly couples to the  $K^*(892)\pi^+$  mode, was found in the  $2^+D$  wave. This enhancement was fitted with a mass-dependent relativistic Breit-Wigner, and the yielded parameters were found to be in close agreement with the mass and width of the confirmed  $K_2^*(1430)$  state. The resonating behavior in the  $\rho(770)K^+$  wave was not considered for a mass dependent analysis due to the instability of the results.

### 5.3.5 $2^-S$ Waves

**Discussion:** The  $2^-$  wave was added to the fit mainly to account for the shoulder the  $K^+\pi^+\pi^-$  invariant mass exhibits around 1.8 GeV. The most heavily reported  $2^-$  resonance around 1.8 GeV is the  $K_2(1770)$  which reportedly dominantly decays to  $K_2^*(1430)\pi$ . For this



(a) The  $2^+D, \rho(770)K^+$  wave intensity.



(b) The  $2^+D, K^*(892)\pi^+$  wave intensity.

Figure 5.19: The acceptance corrected total intensities  $2^+D$  waves decaying to  $\rho(770)K^+$  (a) and  $K^*(892)\pi^+$  (b).

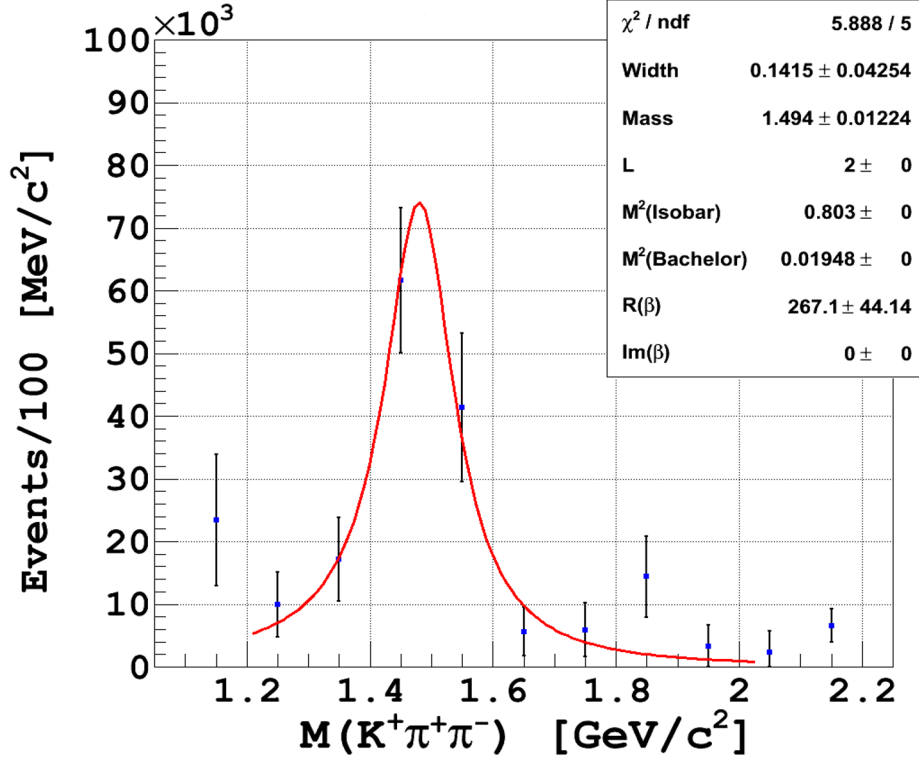


Figure 5.20: The acceptance corrected intensity of the  $2^+ DK^*(892)\pi^+$  wave fitted with a mass-dependent relativistic Breit-Wigner and a second degree polynomial.

reason, we only included  $2^-S$  waves decaying to  $K_2^*(1430)\pi$  or  $f_2(1770)K^+$ , in our fits. We also refrained from including these waves below the  $K_2(1770)$  production threshold at 1.5 GeV. Figure 5.21 shows the coherent sum of both  $2^-S$  waves. An enhancement is evident between 1.6 GeV and 1.9 GeV. This behavior is more pronounced in the  $K_2^*(1430)\pi^+$  as shown in Figure 5.22(a).

We fitted the structure in Figure 5.22(a) with a mass-dependent relativistic Breit-Wigner 5.23 resulting in a mass =  $1.759 \pm 0.03$  GeV and a decay width  $\Gamma = 0.167 \pm 0.076$  GeV, which were found to be in close agreement with the reported average mass (1.773 GeV) and width (0.186 GeV) of the  $K_2^*(1430)\pi^+$  state [16]. We excluded any  $2^-P$  waves, decaying through  $\rho(770)K$  and  $K^*(892)\pi$ , from our final fit as they were not required by the data.

**Conclusion:** The  $2^-S$  wave accounted for the higher mass shoulder exhibited by the  $K^+\pi^+\pi^-$  system. It strongly coupled to the  $K_2^*(1430)\pi^+$  mode and had a mass =  $1.759 \pm 0.03$  GeV and a width =  $0.167 \pm 0.076$  GeV. The  $K_2(1770)$  state is considered to be a good

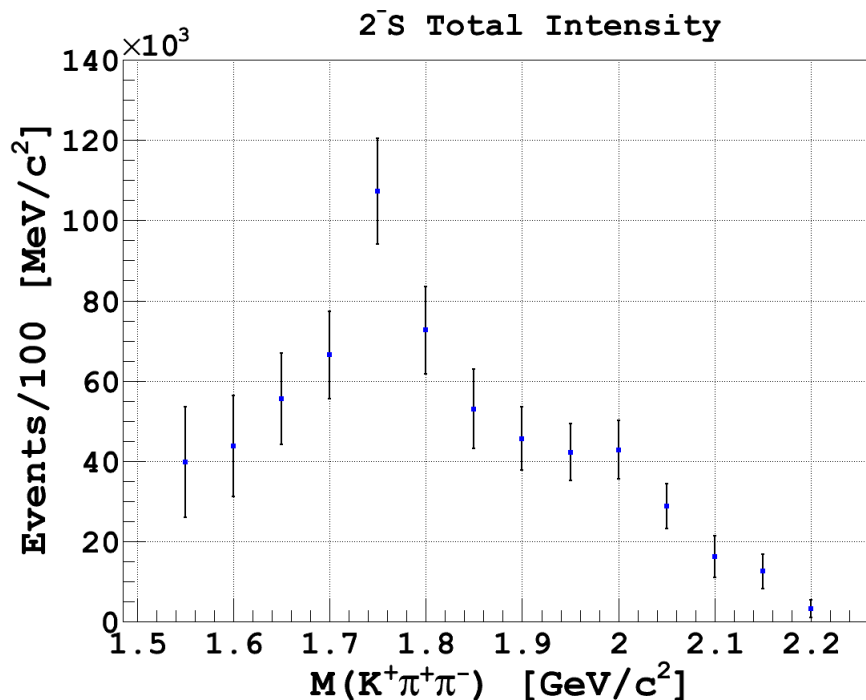
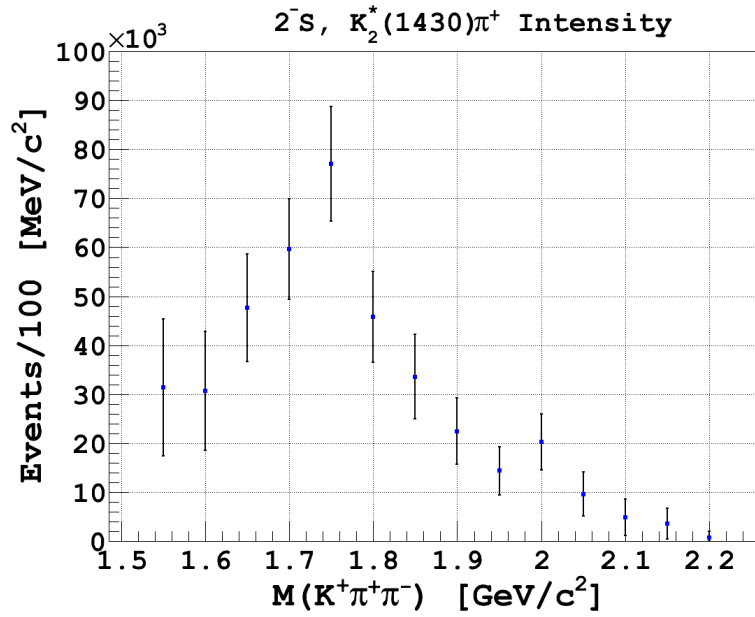


Figure 5.21: The acceptance corrected total intensity of all  $2^-S$  waves included in this fit. This intensity includes the coherent sum of amplitudes of  $2^-S$  wave decaying to a  $f_2(1270)K^+$  or a  $K_2^*(1432)\pi^+$ .

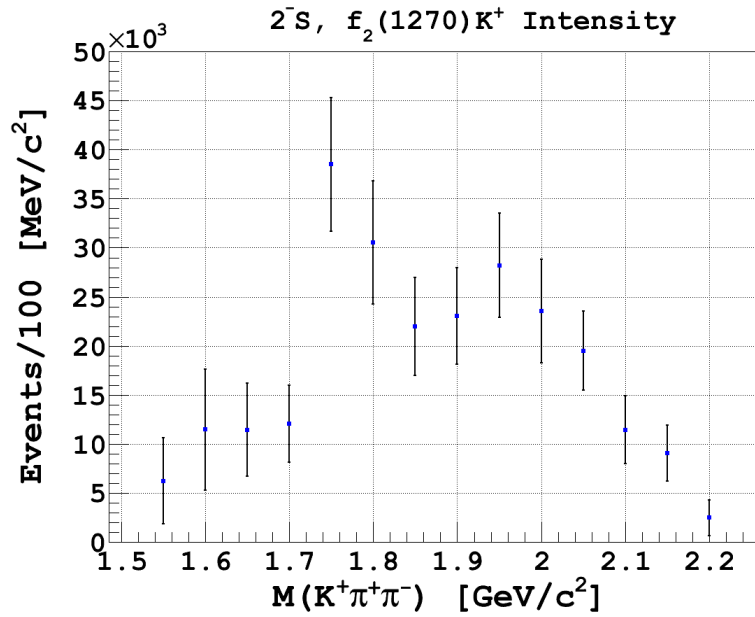
candidate for this structure.

### 5.3.6 Predicted Distributions

The qualities of the fits were determined by weighing the accepted Monte Carlo according to the procedure outlined in Section 5.2.5. Various features of the data and weighed Monte Carlo are presented in Figure 5.24. The predicted  $K^+\pi^-$  and  $\pi^+\pi^-$  masses overlap quite well with their corresponding data distributions. The higher  $\pi^+\pi^-$  mass shoulder was also reproduced by the fit, primarily because of the inclusion of the  $f_2(1270)K^+$  decay mode in most of our fits. Comparing the angular distributions of the data to those from the weighted Monte Carlo, we notice a good agreement between the angles  $(\phi_{GJ}, \theta_{GJ})$  in the Gottfried-Jackson frame. A study was performed on small discrepancy in figure 5.25(a) to test its effect on the PWA results. The region of discrepancy in  $\phi_{GJ}$  for the  $(K^+\pi^-)$  system was excluded from the data and the accepted Monte Carlo, and a partial wave analysis was performed on the new dataset with the



(a) The  $2^-S, K_2^*(1430)\pi^+$  wave intensity.



(b) The  $2^-S, f_2(1430)K^+$  wave intensity.

Figure 5.22: The acceptance corrected total intensities  $2^+D$  waves decaying to  $K_2^*(1430)\pi^+$  (a) and  $f_2(1430)K^+$ (b).

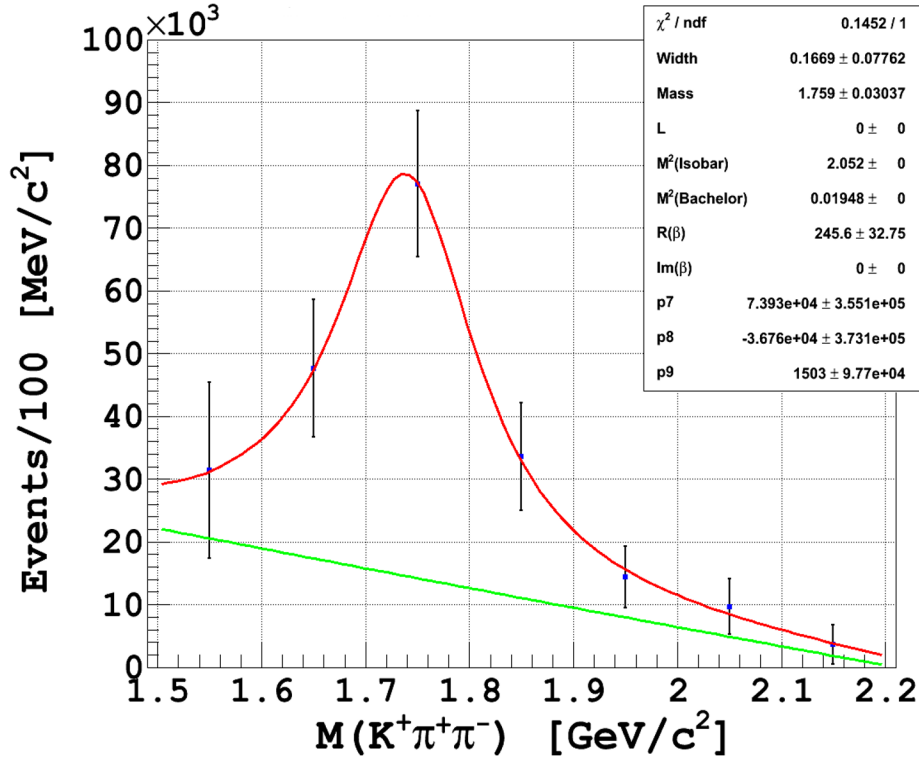
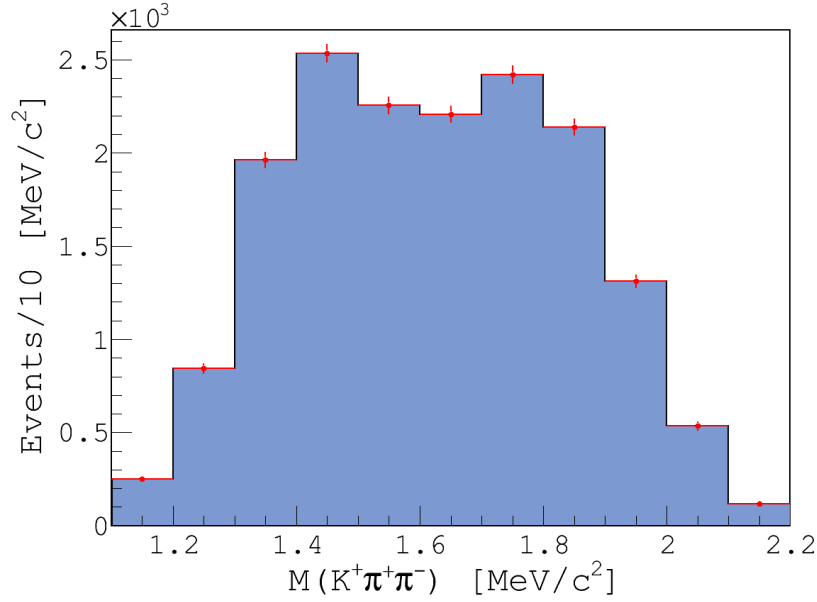
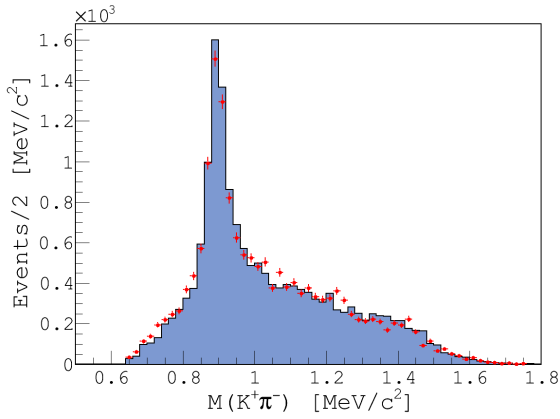


Figure 5.23: The acceptance corrected intensity of the  $2^-SK_2^*(1430)\pi^+$  wave fitted with a mass-dependent relativistic Breit-Wigner and a second degree polynomial.

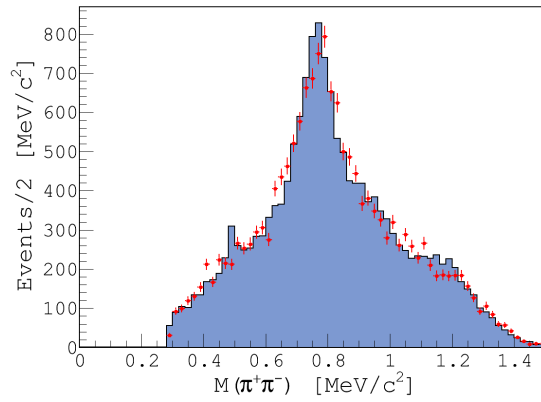
waves we presented earlier. The resulting intensities showed no significant deviations from the intensities of the waves presented in section 5.3. The predicted helicity angles are also in good agreement with the corresponding data distributions as shown in Figure 5.26. Therefore we can deduce that the waves included in this fit properly describe the data.



(a) The  $K^+\pi^+\pi^-$  invariant mass.

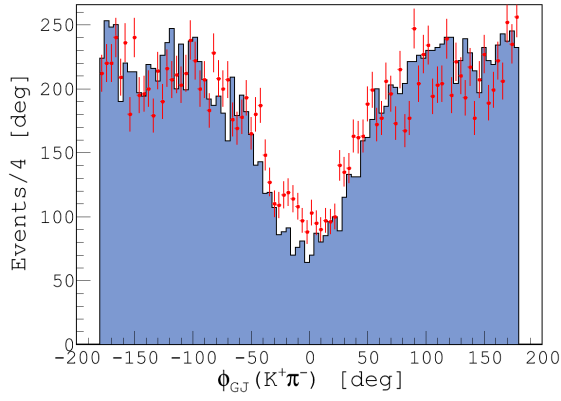


(b) The  $K^+\pi^-$  invariant mass.

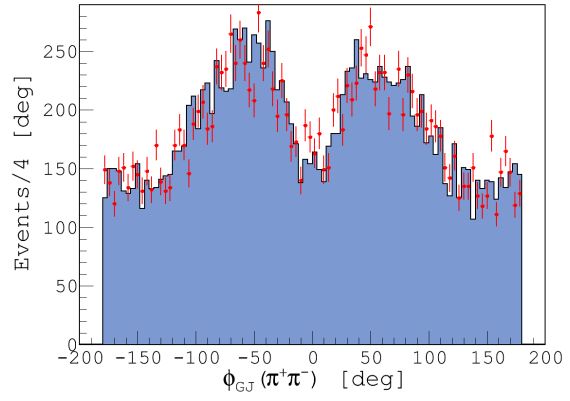


(c) The  $\pi^+\pi^-$  invariant mass.

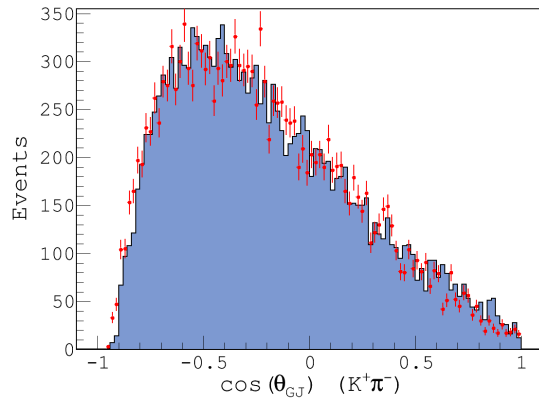
Figure 5.24: Features of the fitted data events (blue) and the predicted distributions (red points) for the  $\gamma p \rightarrow \Lambda K^+\pi^+\pi^-$  sample.



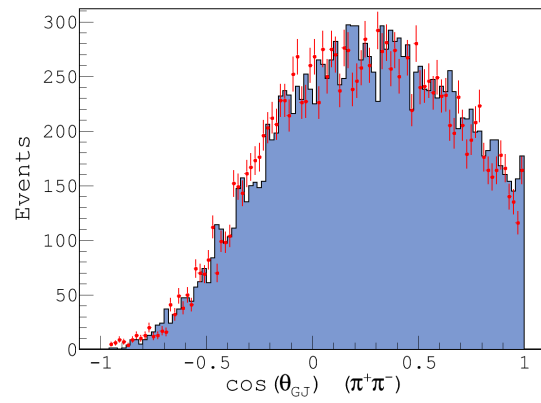
(a) The GJ angle  $\phi$  of  $K^+\pi^-$ .



(b) The GJ angle  $\phi$  of  $\pi^+\pi^-$ .

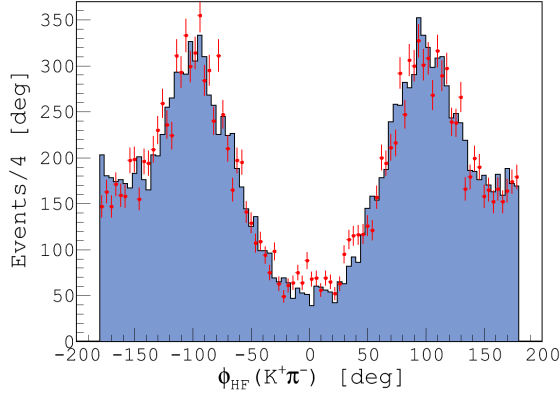


(c) The GJ  $\cos(\theta)$  of  $K^+\pi^-$ .

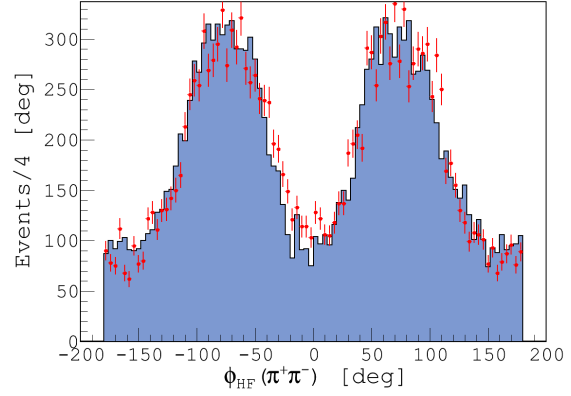


(d) The GJ  $\cos(\theta)$  of  $\pi^+\pi^-$ .

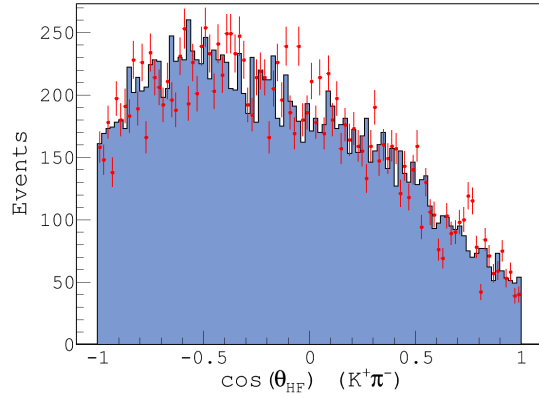
Figure 5.25: The measured (blue) and predicted (red points) angular distributions in the Gottfried-Jackson frame.



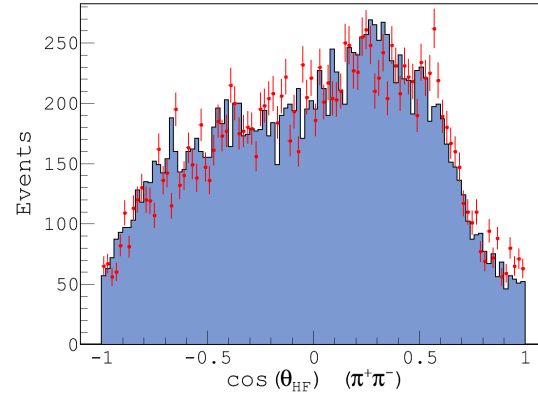
(a) The HF angle  $\phi$  of  $K^+\pi^-$ .



(b) The HF angle  $\phi$  of  $\pi^+\pi^-$



(c) The HF  $\cos(\theta)$  of  $K^+\pi^-$



(d) The HF  $\cos(\theta)$  of  $\pi^+\pi^-$

Figure 5.26: The measured (blue) and predicted (red points) angular distributions in the Helicity frame. The angular distributions of the  $K^+\pi^-$  system were determined using the  $K^+$  as a spectator, and those of the  $\pi^+\pi^-$  system were determined using the  $\pi^+$  as a spectator.

# CHAPTER 6

## SUMMARY

A mass independent partial wave analysis of the reaction  $\gamma p \rightarrow \Lambda K^+ \pi^+ \pi^-$  was performed using the first and only photoproduction dataset available for  $E_\gamma \in [4.40 \text{ GeV}, 5.45 \text{ GeV}]$ . The main motivation for this analysis was to search for excited strange states that have never been photoproduced before. This includes all excited states except for the  $K^*(892)$ . Our fit results showed strong evidence of leading strange states such as the  $K_1(1270)$  decaying in a  $1^+S$  wave an strongly coupling to the  $\rho(770)K$  mode, and the  $K_1(1400)$  dominantly coupling to  $K^*(892)$ . A prominent and rather broad structure was also found in the  $1^+S, \rho(770)K^+$  wave, peaking in the higher mass region. A good candidate for such a resonance is the  $K_1(1650)$  state that has been reported but not confirmed.

The  $1^-P, K^*(892)\pi^+$  wave exhibited resonating behavior around 1.4 GeV. Such a structure was not observed in the  $\rho(770)K^+$  decay mode. And while these branching properties are consistent with the  $K^*(1410)$ , the structure observed in our fits was found to be narrower than the reported average width.

Complimentary waves such as the  $2^+D, K^*(892)\pi$  and the  $2^+D, \rho(770)K$  showed evidence of resonating behavior as well. The  $2^+D, K^*(892)\pi$  in particular was stable and peaked around 1.45 GeV. A mass-dependent Breit-Wigner fit of this structure showed strong correlation with the  $K_2^*(1430)$  state. The  $2^+D, \rho(770)K$  wave on the other hand, did not show strong stability and showed significant distortion with the exclusion/inclusion of other waves. As a result, we did not feel confident in interpreting the  $2^+D, \rho(770)K$  structures. A strong enhancement was seen in the  $2^-S, K_2^*(1430)\pi$  intensity in agreement with the  $K_2(1770)$ .

Due to statistical limitations of the data, significant partial wave phase motions were unable to be measured. Drawing conclusions about resonant nature based solely on intensity is limited, however the stability of the exhibited structures to the addition or exclusion of others waves, is a strong evidence that these structures have resonating natures. The quality of the fit was assessed by weighing a sample of accepted Monte Carlo to the fit parameters, then comparing its features with the features of the data sample used in for PWA. The included waves were found to describe the angular and mass dependent structure of the data quite well.

Table 6.1: Summary of the resonant structures observed in the partial waves, along with any possible states that could account for them.

$J^P$	Decay Channel	Mass [ $GeV/c^2$ ]	Width [ $GeV/c^2$ ]
$1^+$	$\rho(770)K$	$1.33 \pm 0.03$	$0.14 \pm 0.02$
$1^+$	$\rho(770)K$	$1.73 \pm 0.03$	$0.23 \pm 0.04$
$1^+$	$K^*(892)\pi$	$1.35 \pm 0.02$	$0.22 \pm 0.06$
$1^-$	$K^*(892)\pi$	$1.43 \pm 0.02$	$0.1 \pm 0.07$
$2^+$	$K^*(892)\pi$	$1.49 \pm 0.01$	$0.14 \pm 0.04$
$2^-$	$K_2^*(1430)\pi$	$1.76 \pm 0.03$	$0.17 \pm 0.08$

Phase motion was not used in this analysis due to instability. This is a result of the statistical limitations that this channel suffered from. Drawing a conclusion about a wave based solely on its intensity behavior might not be enough, however the stability of the exhibited structures to the addition or exclusion of other waves, is a strong evidence that these structures have resonating natures. Additionally, the quality of the fit was assessed by weighing a sample of accepted Monte Carlo to the fit parameters, then comparing its features to the features of the data sample used in this fit. The included waves were thus found to describe the angular structure of the data quite well.

This analysis, with limited number of events, was able to show evidence of the production of a handful of excited strange states, thus giving an impression of what to expect in a similar channel with higher statistics. With larger number of events, and higher beam energies, experiments such as GlueX will be able to extend the study of the  $K\pi\pi$  system and present a more complete understanding of a  $K^+\pi^+\pi^-$  system produced off a  $\Lambda$ .

# APPENDIX A

## EXTENDED PWA RESULTS

A series of different PWA fits for the  $\gamma p \rightarrow \Lambda K^+ \pi^+ \pi^-$  channel are presented in this chapter.

### A.1 PWA Fit with $0^- S$ waves

The flat background in this fit is replaced by the  $0^- S$  wave decaying to  $f_0(600)K^+$  and  $K^*(800)\pi^+$  waves.

Table A.1: The full set of waves included in this partial wave analysis. The check marks indicate the region where a wave is included in the partial wave analysis. Keep in mind that except for the flat background, every wave has two reflectivities.

L	$J^P$	Isobar	Bachelor	1.1 - 1.6 GeV	1.6 - 2.2 GeV
	$0^-$	$f_0(600)$	$K^+$	✓	✓
	$0^-$	$K^*(800)$	$\pi^+$	✓	✓
S	$1^+$	$\rho(770)$	$K^+$	✓	✓
	$1^+$	$K^*(892)$	$\pi^+$	✓	✓
	$2^-$	$f_2(1270)$	$K^+$		✓
	$2^-$	$K_2^*(1430)$	$\pi^+$		✓
P	$1^+$	$f_0(600)$	$K^+$		
	$1^+$	$K^*(800)$	$\pi^+$		
	$1^-$	$\rho(770)$	$K^+$	✓	✓
	$1^-$	$K^*(892)$	$\pi^+$	✓	✓
D	$1^+$	$\rho(770)$	$K^+$		
	$1^+$	$K^*(892)$	$\pi^+$		
	$2^+$	$\rho(770)$	$K^+$	✓	✓
	$2^+$	$K^*(892)$	$\pi^+$	✓	✓

### A.1.1 $1^+S$ Waves

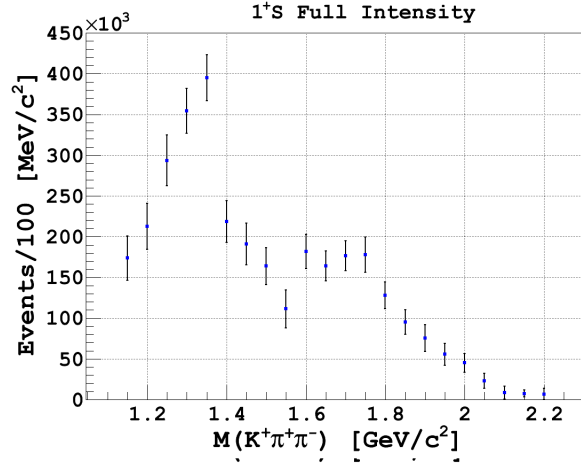
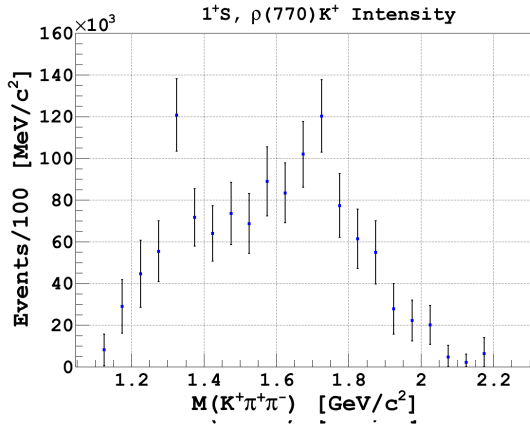
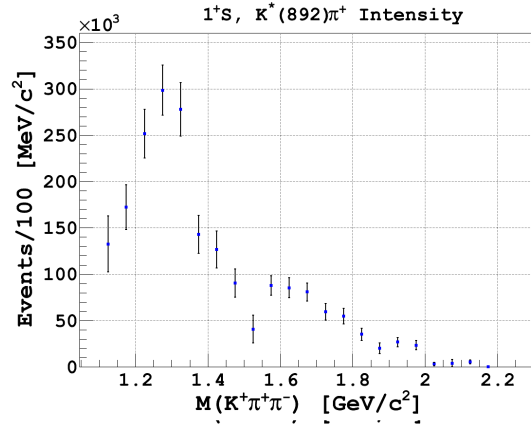


Figure A.1: The acceptance corrected total intensity of all  $1^+S$  waves included in this fit. This intensity includes the coherent sum of amplitudes of  $1^+S$  wave decaying to a  $\rho(770)K^+$  or a  $K^*(892)\pi^+$ .



(a) The  $1^+S, \rho(770)K^+$  wave intensity.



(b) The  $1^+S, K^*(892)\pi^+$  wave intensity.

Figure A.2: The acceptance corrected total intensities  $1^+S$  waves decaying to  $\rho(770)K^+$  (a) and  $K^*(892)\pi^+$  (b).

### A.1.2 $1^-P$ Waves

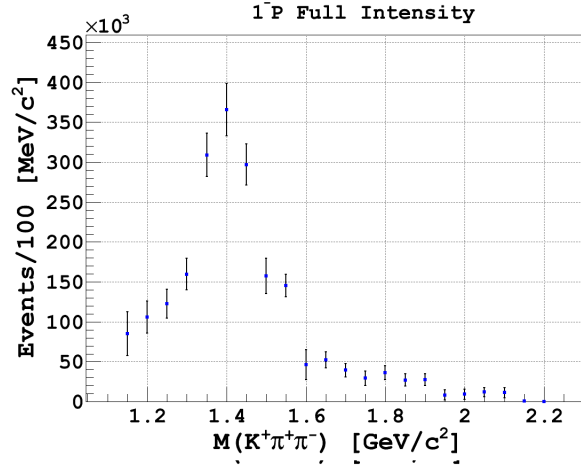
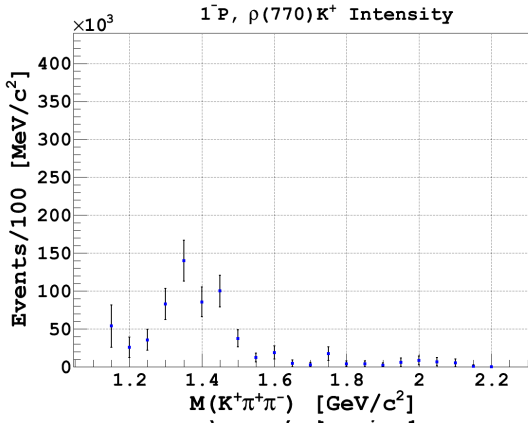
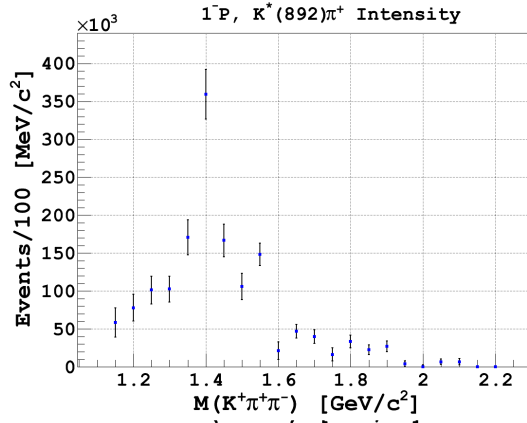


Figure A.3: The acceptance corrected total intensity of all  $1^-P$  waves included in this fit. This intensity includes the coherent sum of amplitudes of  $1^-P$  wave decaying to a  $\rho(770)K^+$  or a  $K^*(892)\pi^+$ .



(a) The  $1^-P, \rho(770)K^+$  wave intensity.



(b) The  $1^-P, K^*(892)\pi^+$  wave intensity.

Figure A.4: The acceptance corrected total intensities  $1^-P$  waves decaying to  $\rho(770)K^+$  (a) and  $K^*(892)\pi^+$  (b).

### A.1.3 $2^+D$ Waves

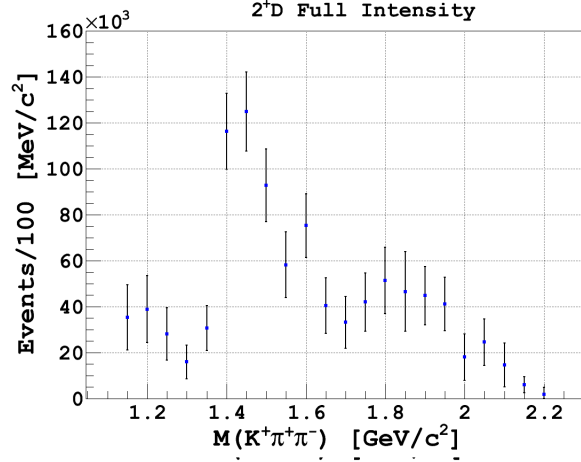
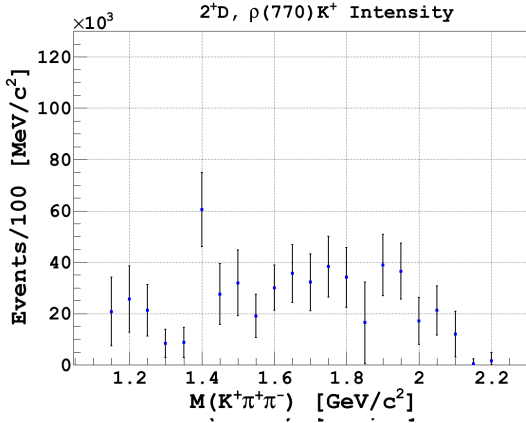
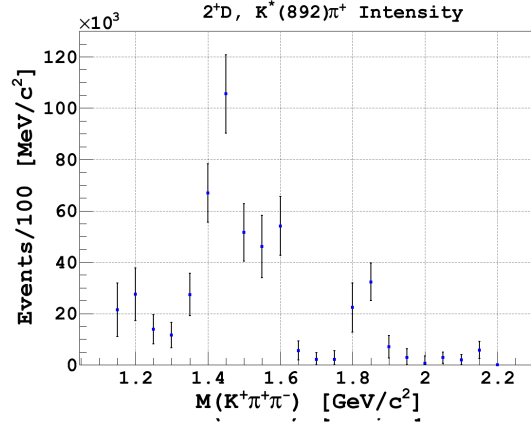


Figure A.5: The acceptance corrected total intensity of all  $1^-P$  waves included in this fit. This intensity includes the coherent sum of amplitudes of  $1^-P$  wave decaying to a  $\rho(770)K^+$  or a  $K^*(892)\pi^+$ .



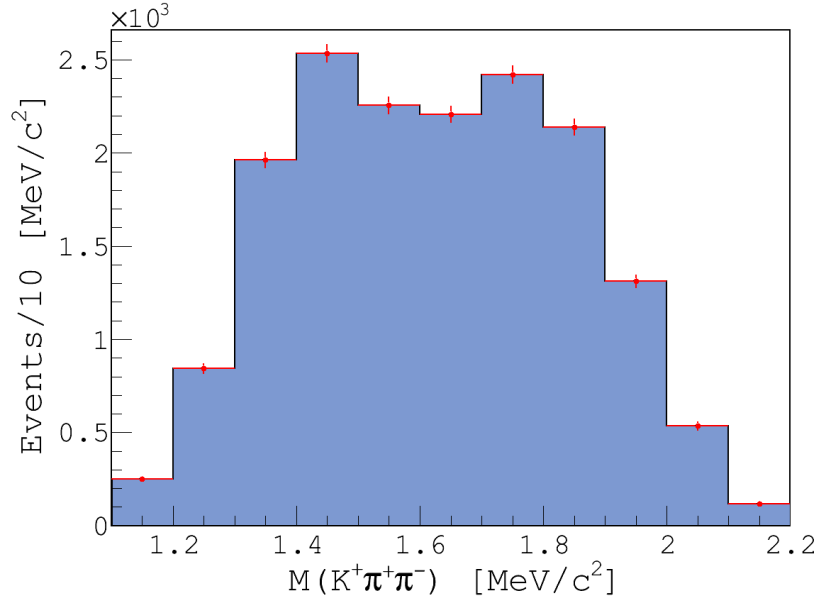
(a) The  $2^+D, \rho(770)K^+$  wave intensity.



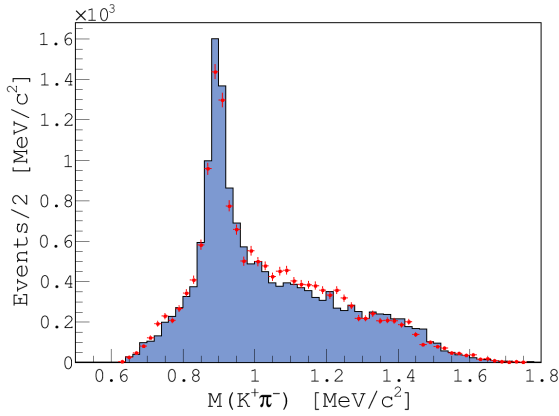
(b) The  $2^+D, K^*(892)\pi^+$  wave intensity.

Figure A.6: The acceptance corrected total intensities  $2^+D$  waves decaying to  $\rho(770)K^+$  (a) and  $K^*(892)\pi^+$  (b).

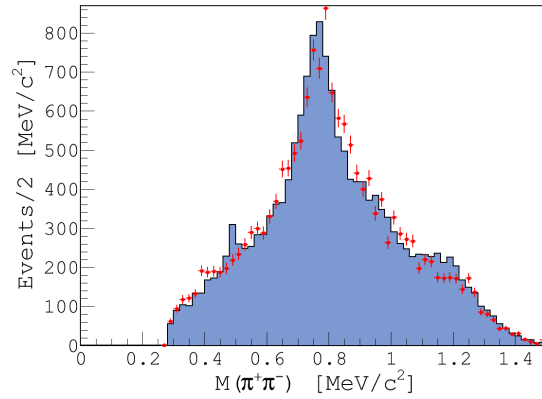
### A.1.4 Predicted Distributions



(a) The  $K^+\pi^+\pi^-$  invariant mass.



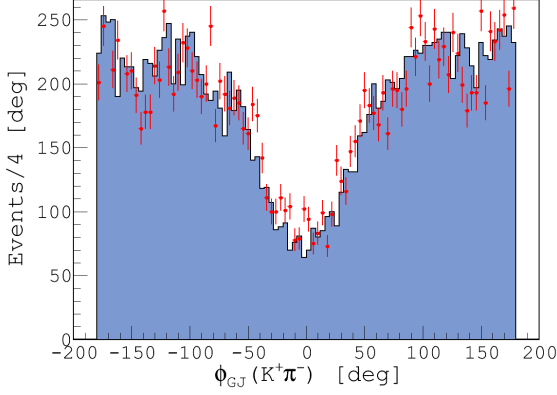
(b) The  $K^+\pi^-$  invariant mass.



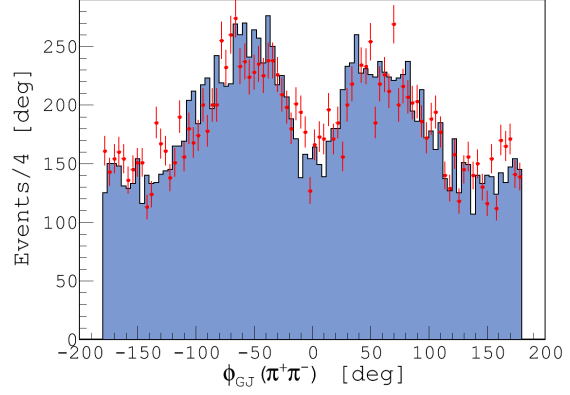
(c) The  $\pi^+\pi^-$  invariant mass.

Figure A.7: Features of the fitted data events (blue) and the predicted distributions (red points) for the  $\gamma p \rightarrow \Lambda K^+\pi^+\pi^-$  sample.

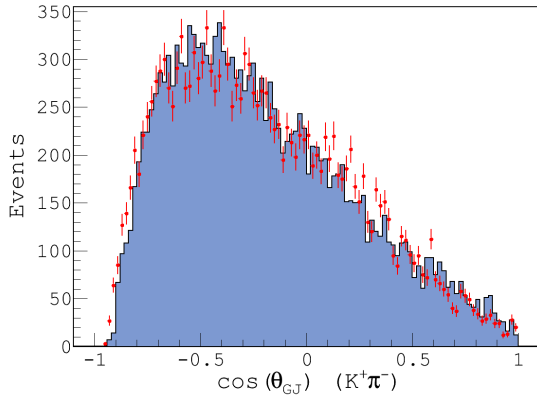
**Discussion:** Major structures that were observed in the fit we presented in Section 5.3, were also observed in this fit. The flat background was replaced with the isotropic  $0^-S$  wave. The only slight difference in waves behavior was found in the  $1^-S, \rho(770)K^+$  where the lower mass enhancement was relatively less prominent when compared to that in Figure 5.13(a). The



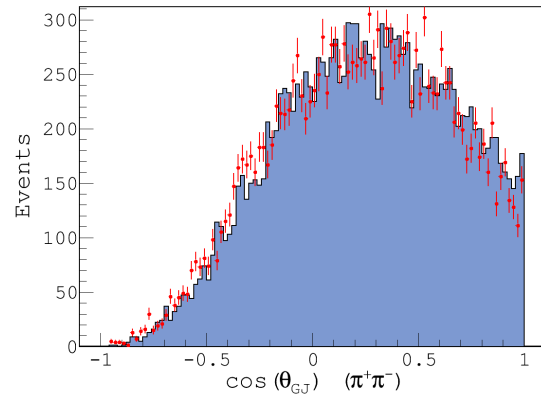
(a) The GJ angle  $\phi$  of  $K^+\pi^-$ .



(b) The GJ angle  $\phi$  of  $\pi^+\pi^-$ .



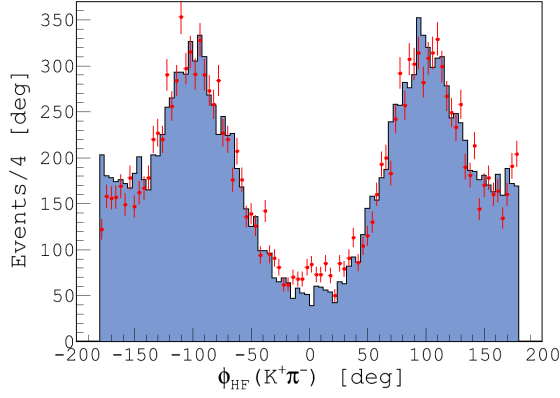
(c) The GJ  $\cos(\theta)$  of  $K^+\pi^-$ .



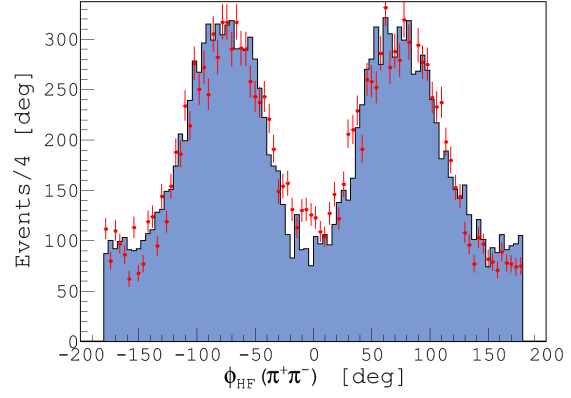
(d) The GJ  $\cos(\theta)$  of  $\pi^+\pi^-$ .

Figure A.8: The measured (blue) and predicted (red points) angular distributions in the Gottfried-Jackson frame.

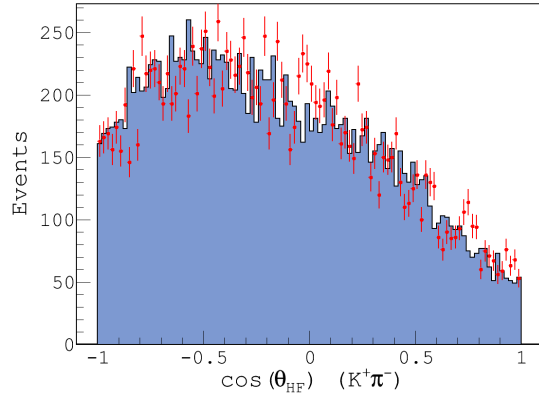
unstable structures we observed in the  $2^+D, \rho(770)K^+$  in Figure 5.19(a) was also absent from Figure A.6(a). Generally speaking, one can replace the flat background with the isotropic  $0^-S$  wave; however, this would require an in-depth study of the parametrization of the  $\sigma(600)$  and  $K^*(800)$ . In this fit, for the sake of simplicity, both mesons were parametrized with broad Breit-Wigners.



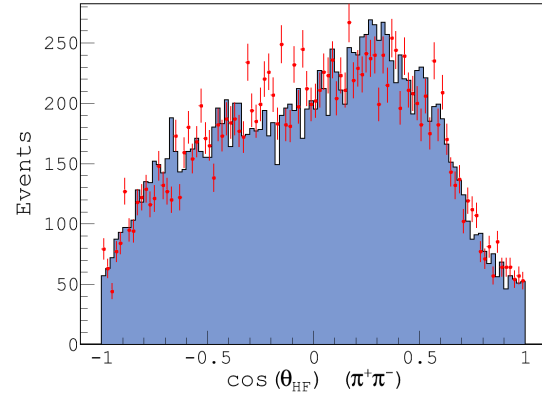
(a) The HF angle  $\phi$  of  $K^+\pi^-$ .



(b) The HF angle  $\phi$  of  $\pi^+\pi^-$ .



(c) The HF  $\cos(\theta)$  of  $K^+\pi^-$ .



(d) The HF  $\cos(\theta)$  of  $\pi^+\pi^-$ .

Figure A.9: The measured (blue) and predicted (red points) angular distributions in the Helicity frame. The angular distributions of the  $K^+\pi^-$  system were determined using the  $K^+$  as a spectator, and those of the  $\pi^+\pi^-$  system were determined using the  $\pi^+$  as a spectator.

## A.2 PWA Fit with 50 MeV Bins

The flat background is used in this fit. The only change is the width of the bins.

Table A.2: The full set of waves included in this partial wave analysis. The check marks indicate the region where a wave is included in the partial wave analysis. Keep in mind that except for the flat background, every wave has two reflectivities.

L	$J^P$	Isobar	Bachelor	1.1 - 1.6 GeV	1.6 - 2.2 GeV
S	1 <sup>+</sup>	$\rho(770)$	$K^+$	✓	✓
	1 <sup>+</sup>	$K^*(892)$	$\pi^+$	✓	✓
	2 <sup>-</sup>	$f_2(1270)$	$K^+$		✓
	2 <sup>-</sup>	$K_2^*(1430)$	$\pi^+$		✓
P	1 <sup>+</sup>	$f_0(600)$	$K^+$		
	1 <sup>+</sup>	$K^*(800)$	$\pi^+$		
	1 <sup>-</sup>	$\rho(770)$	$K^+$	✓	✓
	1 <sup>-</sup>	$K^*(892)$	$\pi^+$	✓	✓
D	1 <sup>+</sup>	$\rho(770)$	$K^+$		
	1 <sup>+</sup>	$K^*(892)$	$\pi^+$		
	2 <sup>+</sup>	$\rho(770)$	$K^+$	✓	✓
	2 <sup>+</sup>	$K^*(892)$	$\pi^+$	✓	✓
Flat	Isotropic			✓	✓

**Discussion:** A fit including the waves discussed in Section 5.3 but with 50 MeV bins was performed. Larger statistical uncertainties as well as instability of some waves were observed. This is mainly due to the further statistical limitations arising from fitting with smaller bins. However, the major structures that were observed in our previous 100 MeV binned fits, were observed here. The low and high mass structures in the  $1^+S, \rho(770)K^+$  wave were also observed in this fit, as evident by Figure A.11(a). Other waves exhibited behaviors very comparable to those of the corresponding waves in the fit in Section 5.3. We did not seek this binning choice in our fits mainly because of concerns of reliability arising from the rather large errors and the discrepancies between the predicted and observed angular distributions.

## A.2.1 $1^+S$ Waves

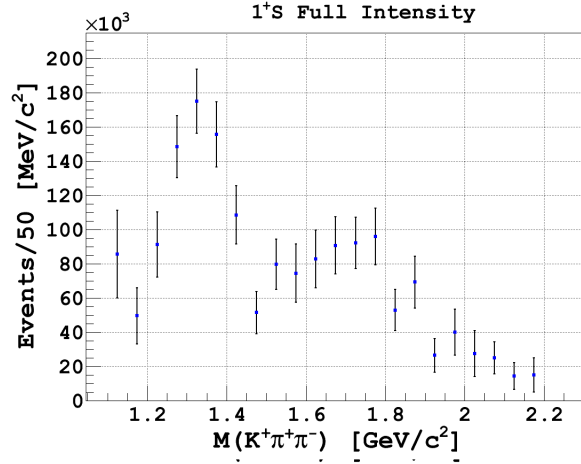
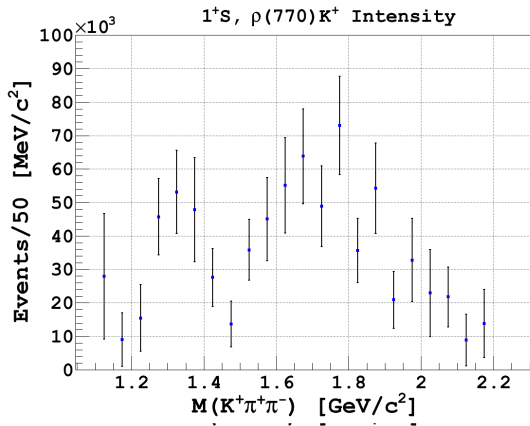
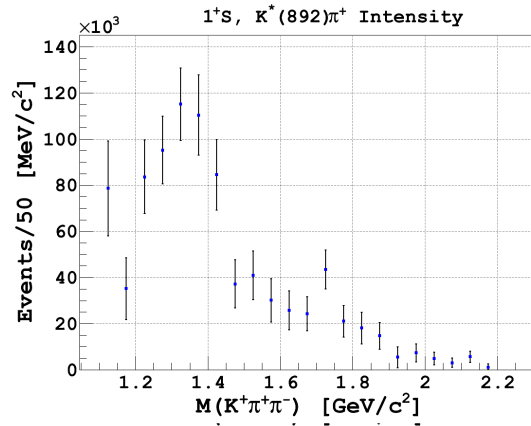


Figure A.10: The acceptance corrected total intensity of all  $1^+S$  waves included in this fit. This intensity includes the coherent sum of amplitudes of  $1^+S$  wave decaying to a  $\rho(770)K^+$  or a  $K^*(892)\pi^+$ .



(a) The  $1^+S, \rho(770)K^+$  wave intensity.



(b) The  $1^+S, K^*(892)\pi^+$  wave intensity.

Figure A.11: The acceptance corrected total intensities  $1^+S$  waves decaying to  $\rho(770)K^+$  (a) and  $K^*(892)\pi^+$  (b).

## A.2.2 $1^-P$ Waves

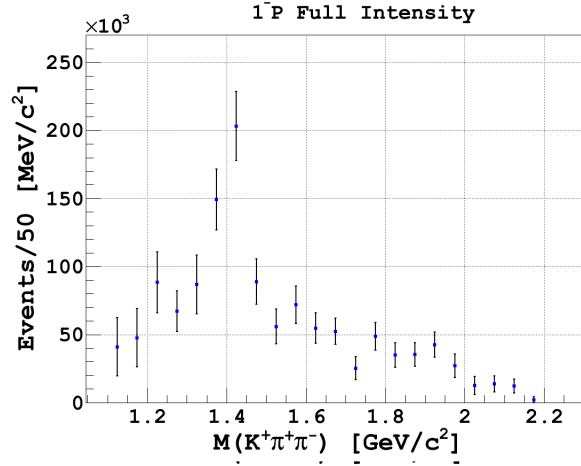
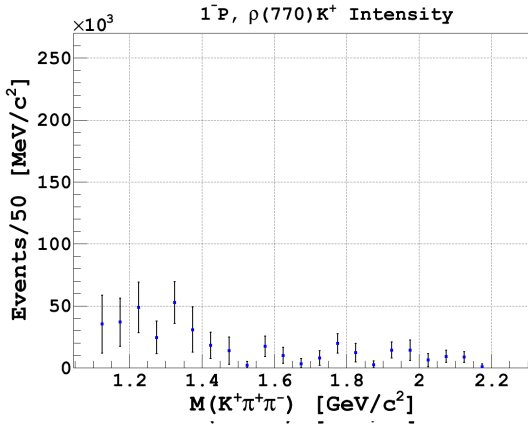
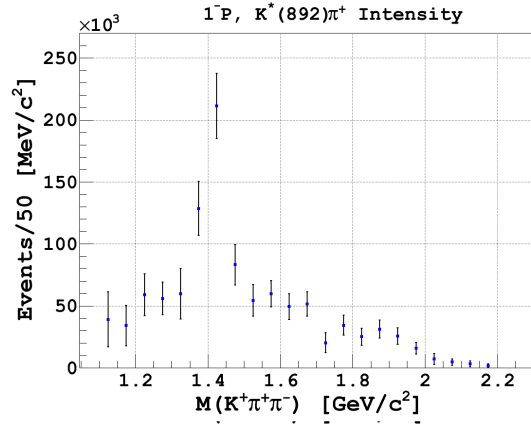


Figure A.12: The acceptance corrected total intensity of all  $1^-P$  waves included in this fit. This intensity includes the coherent sum of amplitudes of  $1^-P$  wave decaying to a  $\rho(770)K^+$  or a  $K^*(892)\pi^+$ .



(a) The  $1^-P, \rho(770)K^+$  wave intensity.



(b) The  $1^-P, K^*(892)\pi^+$  wave intensity.

Figure A.13: The acceptance corrected total intensities  $1^-P$  waves decaying to  $\rho(770)K^+$  (a) and  $K^*(892)\pi^+$  (b).

### A.2.3 $2^+D$ Waves

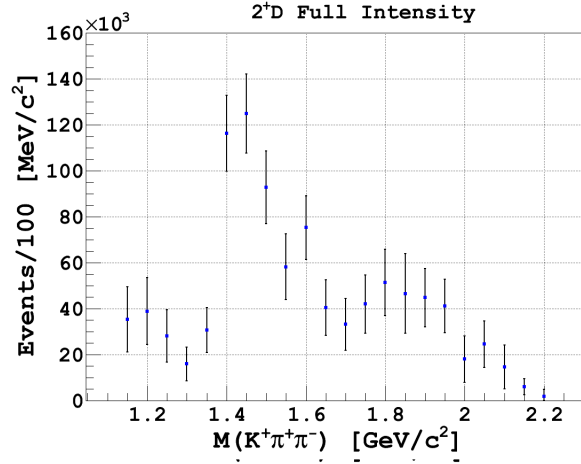
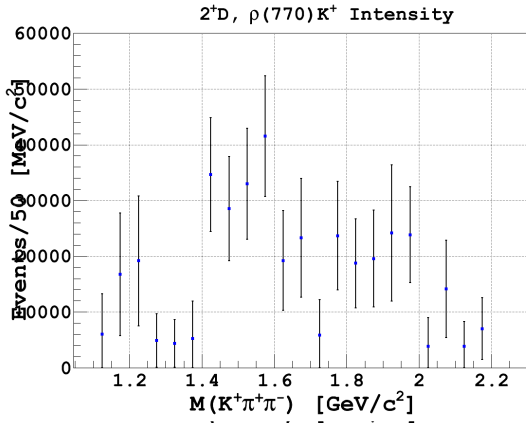
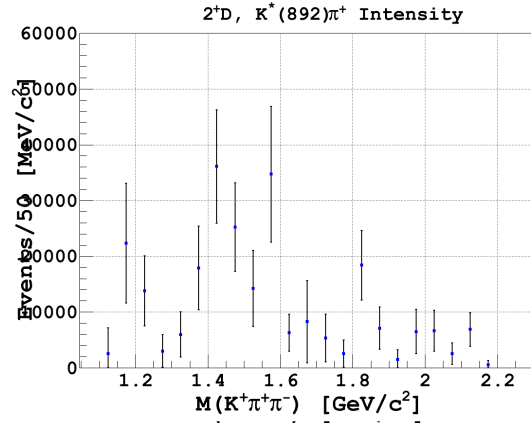


Figure A.14: The acceptance corrected total intensity of all  $1^-P$  waves included in this fit. This intensity includes the coherent sum of amplitudes of  $1^-P$  wave decaying to a  $\rho(770)K^+$  or a  $K^*(892)\pi^+$ .



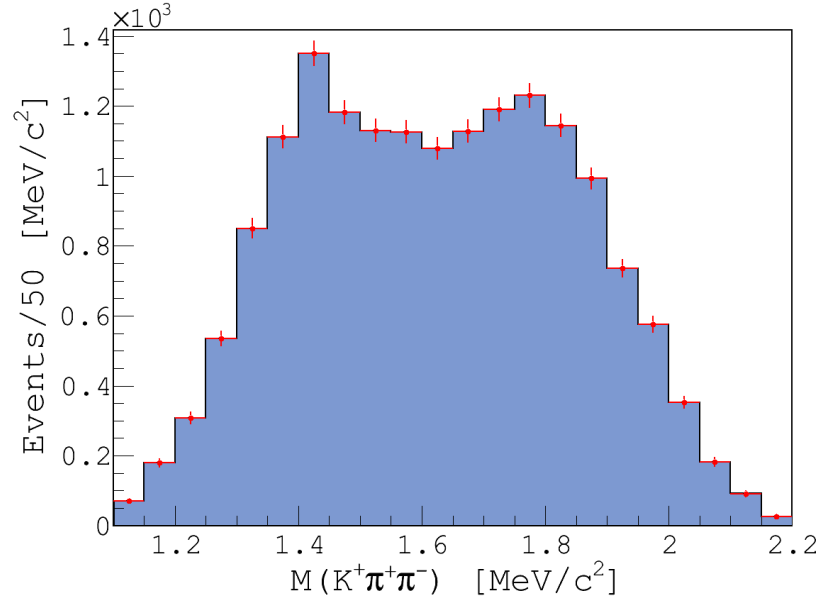
(a) The  $2^+D, \rho(770)K^+$  wave intensity.



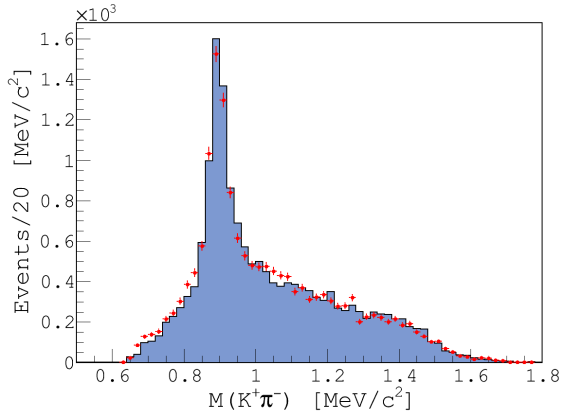
(b) The  $2^+D, K^*(892)\pi^+$  wave intensity.

Figure A.15: The acceptance corrected total intensities  $2^+D$  waves decaying to  $\rho(770)K^+$  (a) and  $K^*(892)\pi^+$  (b).

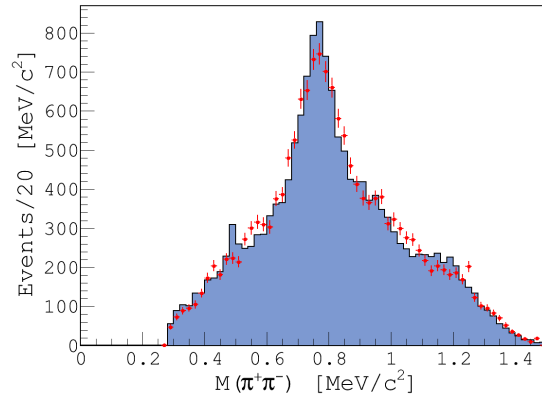
## A.2.4 Predicted Distributions



(a) The  $K^+\pi^+\pi^-$  invariant mass.

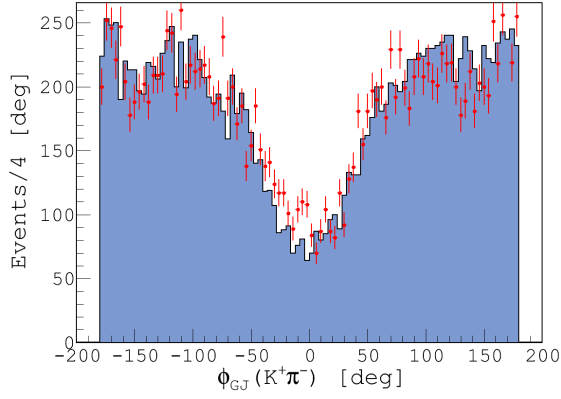


(b) The  $K^+\pi^-$  invariant mass.

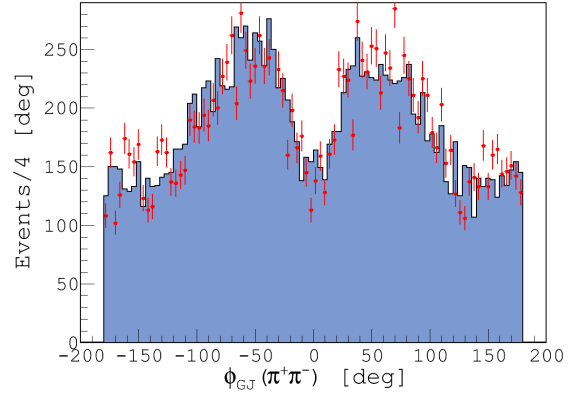


(c) The  $\pi^+\pi^-$  invariant mass.

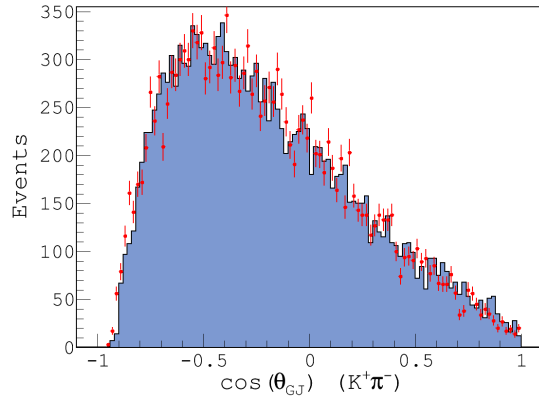
Figure A.16: Features of the fitted data events (blue) and the predicted distributions (red points) for the  $\gamma p \rightarrow \Lambda K^+\pi^+\pi^-$  sample.



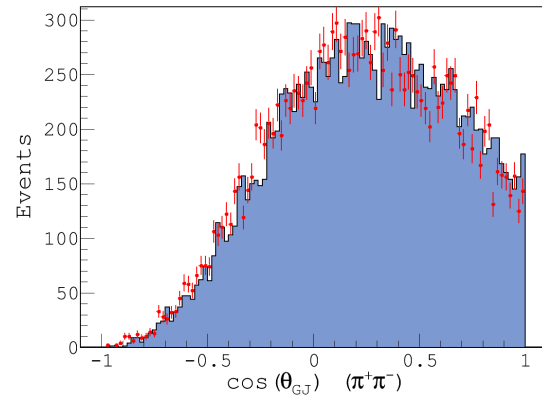
(a) The GJ angle  $\phi$  of  $K^+\pi^-$ .



(b) The GJ angle  $\phi$  of  $\pi^+\pi^-$ .

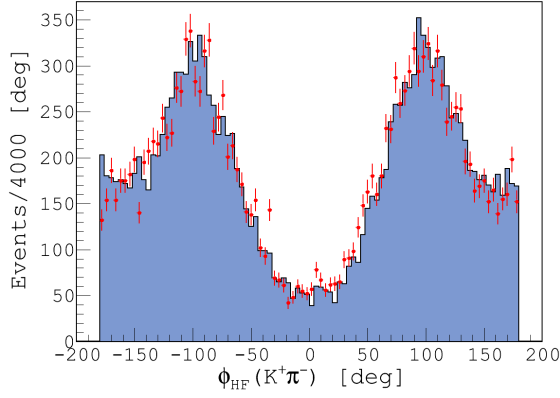


(c) The GJ  $\cos(\theta)$  of  $K^+\pi^-$ .

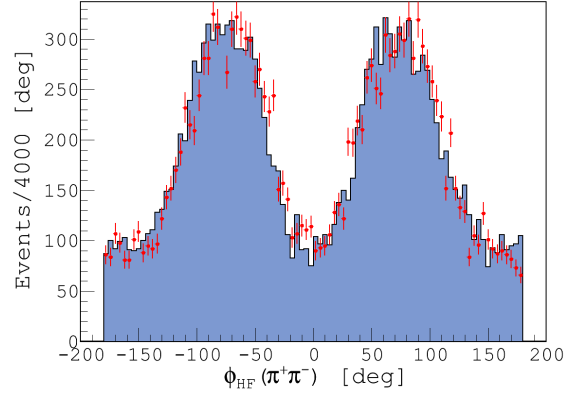


(d) The GJ  $\cos(\theta)$  of  $\pi^+\pi^-$ .

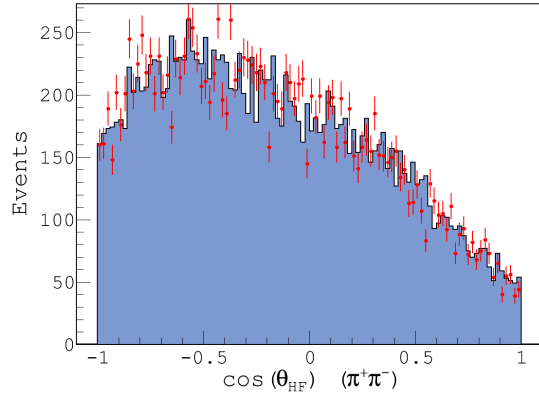
Figure A.17: The measured (blue) and predicted (red points) angular distributions in the Gottfried-Jackson frame.



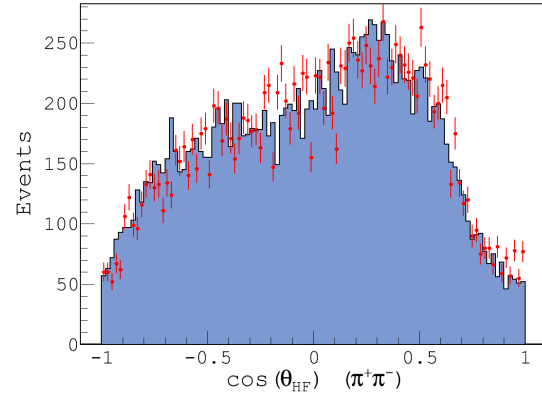
(a) The HF angle  $\phi$  of  $K^+\pi^-$ .



(b) The HF angle  $\phi$  of  $\pi^+\pi^-$



(c) The HF  $\cos(\theta)$  of  $K^+\pi^-$



(d) The HF  $\cos(\theta)$  of  $\pi^+\pi^-$

Figure A.18: The measured (blue) and predicted (red points) angular distributions in the Helicity frame. The angular distributions of the  $K^+\pi^-$  system were determined using the  $K^+$  as a spectator, and those of the  $\pi^+\pi^-$  system were determined using the  $\pi^+$  as a spectator.

# APPENDIX B

## THE GLUEX EXPERIMENT

GlueX is a particle physics experiment at the Thomas Jefferson National Accelerator Facility (Jlab), Newport News, Virginia. The main goal of GlueX is understanding the nature of color confinement in quantum chromodynamics (QCD). Confinement of quarks and gluon is a unique property of QCD and understanding it requires understanding the nature of gluonic field binding the quarks together inside a hadron. GlueX aims to search for hybrids and exotic mesons to understand confinement as these states manifest gluonic degrees of freedom. GlueX will use a coherent bremsstrahlung photon beam incident on a liquid hydrogen target to produce these meson states. Photoproduction is expected to be particularly effective in producing exotic hybrids, and GlueX is expected to provide the largest photoproduction dataset to date. The GlueX detector and its housing hall were the most recent addition to Jlab's facilities and were part of the 12 GeV upgrade.

### B.1 The 12 GeV Upgrade

The Continuous Electron Beam Accelerator Facility (CEBAF) has operated at 6 GeV since 1995 and has served over 1400 users for at least 17 years. The last 6 GeV at Jlab was successfully completed in the spring of 2012. Ever since, the CEBAF facility and the three halls (A, B, and C) have undergone various upgrades and improvements. The 12 GeV upgrade aimed to double the operating electron energy by adding 10 new cryomodules to existing 40 cryomodules in free space at the end of each linac, and by upgrading the magnets in the original 9 arcs to higher fields. In addition, a new arc had to be added to provide an additional pass to deliver a 12 GeV beam to hall D. The upgrade also included adding 10 new RF stations to power the 10 new cryomodules, doubling the refrigerator capacity, modifications to the extraction system to support the higher energy beams, and a new beamline connecting the Hall D to the baseline accelerator [55]. The upgrade was finalized in 2015 and first commissioning runs in all four halls were performed. The new beam support system will carry a beam of energies up to 11 GeV to halls A, B and C, as well as a 12 GeV beam to hall D where the GlueX detector is housed.

A tagged photon beam of energies up to 9 GeV will then be delivered on the target in hall D. Different components of the 12 GeV upgrade on CEBAF can be seen in Figure B.1. More details about the GlueX detector and the construction of the time of flight detector at Florida State University will be discussed in the next section.

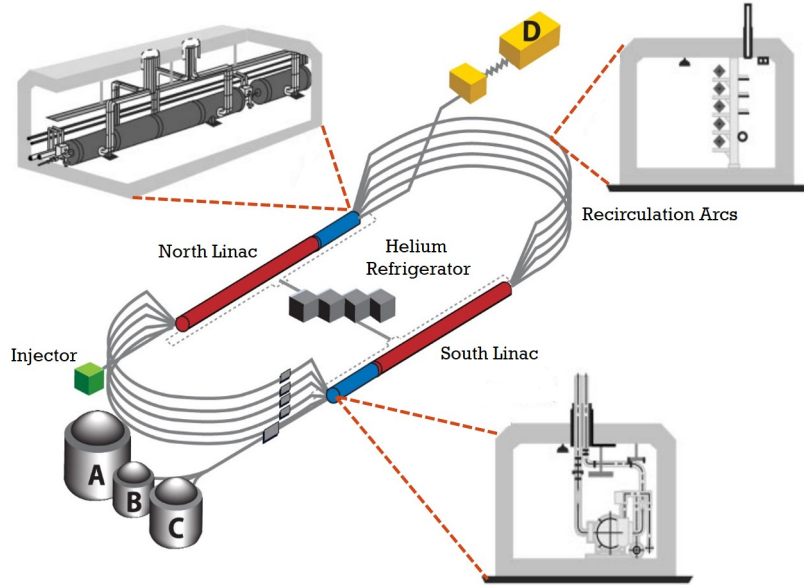


Figure B.1: Schematic CEBAF accelerator overview, including modifications for the 12 GeV update.

## B.2 The GlueX Detector

The GlueX detector is an azimuthally symmetric and nearly hermetic detector for charged particles and photons and is shown in Figure B.2. The detector is housed in hall D at Jefferson lab and is made of 6 subdetectors, each of which performs tasks related to tracking or particle identification. The process of producing the photons beam, and the detection of the charged particles is similar to the process followed by CLAS. A 12 GeV electron beam is supplied to the tagger hall in front of hall D to produce a photon beam via bremsstrahlung radiation. Electrons first pass through a diamond radiator, then into a dipole magnet that tags the energy of the scattered electrons, which later is used to get information about the energies of the produced photons. The diamond radiator is aligned in such a way that it produces a coherent

bremsstrahlung in the 8.4 GeV to 9.0 GeV range. The coherent photons are linearly polarized relative to the crystal axes of the diamond. Coherent photons then travel through an 80 m long vacuum beamline before making their way to hall D. The photon beam then passes through a 3.4 mm diameter collimator to remove off-axis photons while also providing fast feedback on the beam positioning. Before reaching the target cell in the detector, the photons also travel through a pair spectrometer system that is used to monitor both the energy and intensity of the photon beam [56].

The photon beam enters hall D and is directly incident on a 30 cm liquid hydrogen target. The largest element of the GlueX detector is a solenoid superconducting magnet. The solenoid is a 73-inch warm bore superconducting device that produces a nominal maximum central field of 2.0 Tesla along the direction of the beam. Surrounding the target is a 30-element scintillator detector called the start counter [57][58]. The start counter provides a start signal for time of flight measurements with 300 ps resolution, and it also identifies the beam pulse associated with the observed event. It is located in close proximity to the target so it is independent of particle momenta and trajectories. Immediately surrounding the start counter is the central drift chamber [59]. Also referred to as the straw tube chamber, the CDC is a 1.5 m long and 1.2 m in diameter. The CDC is made of 3522 1.6 cm straws, forming 28 layers 12 of which are straight and 16 are stereo. The central drift chamber provides position measurements along the charged tracks with 150  $\mu\text{m}$  accuracy in the  $r - \phi$  plane. It also provides  $dE/dx$  information for charged tracks and has a good  $\pi/p$  separation up to 1 GeV/c.

Downstream of the CDC is the forward drift chamber system. The FDC system is made of four separate packages each of which is based on six layers of planar drift chambers with both anode and cathode readouts [64]. These readouts allow the drift chambers to reconstruct a three-dimensional space point which is essential for tracking in the high-magnetic field environment. Surrounding these tracking detectors and inside the solenoid is the barrel calorimeter. It is a lead-scintillating fiber calorimeter with readout on both the upstream and downstream layers [64]. The timing information from the BCAL is used to provide time-of-flight information for particles interacting in the BCAL and can be used to global particle identification of charged particles and photons. The second calorimeter in GlueX is the forward calorimeter (FCAL) [66]. The FCAL consists of 2800 lead-glass crystals each 45 cm long. The crystals are stacked such that the active area of the FCAL is circular. The FCAL is sensitive to photons of  $E_\gamma \geq 100$  MeV. Upstream from the FCAL is the time of flight detector which was constructed at Florida State University

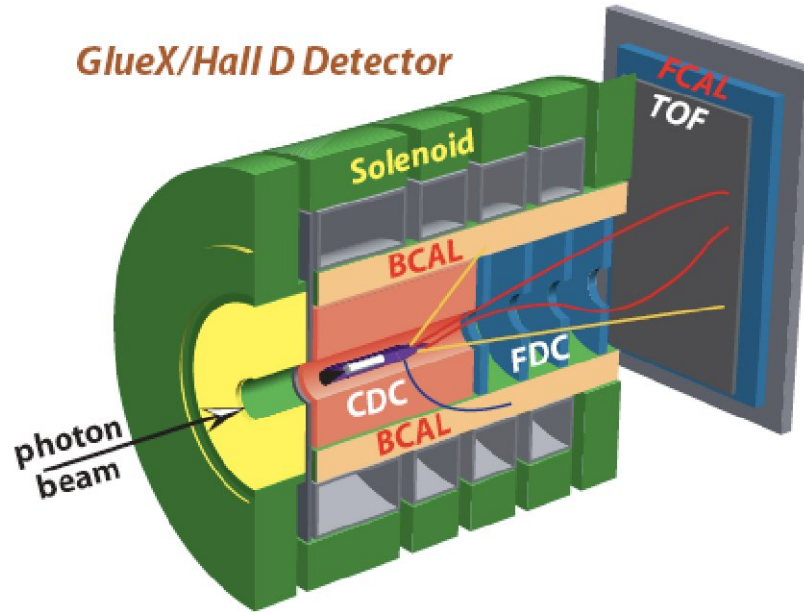


Figure B.2: Schematic CEBAF accelerator overview, including modifications for the 12 GeV update.

and will be discussed in the following section. For more information about the subsystems of the detectors, refer to References [56][57][58][59][64][66].

### B.3 The Time of Flight Detector

The construction and assembly of the time of flight detector (TOF) was a year long project from May 2013 to May 2014. The construction section was completely performed at Florida State University by a number of graduate and undergraduate students under the supervision of Dr. Paul Eugenio and Dr. Alexander Ostrovidov. The most recent effort on the time of flight includes commissioning and calibration which will not be covered in this section. This section will include a brief description of various construction steps which the author of this document had a leading role in.

The main purpose of the time of flight detector is to provide timing and energy loss measurements. Timing information from the TOF are combined with timing information from the

start counter to determine the identity of a particle in the same fashion CLAS's time of flight detector operated (refer to Section 2.4.4). The TOF detector for GlueX consists of two layers of scintillator paddles with readout using photomultiplier tubes on both sides. Each layer consists of

- 38  $2.54 \times 6.00 \times 252.00$  (cm) scintillator modules with PMT's mounted on both ends.
- 4  $2.54 \times 3.00 \times 252.00$  (cm) scintillator modules with PMT's mounted on both ends.
- 4  $2.54 \times 6.00 \times 120.00$  (cm) scintillator modules with PMT's mounted on one end.

The half-width and half-length modules go in the center region of both layers, where the half-length modules account for the beam hole in the middle of each layer as shown in Figure B.3. The scintillation material used in the modules is Eljen's EJ200. Each full length module is made of an EJ200 scintillator bar with a light guide, that is fabricated from the same material by the FSU machine shop, attached to either end. Each of the half length modules had only one light guide attached to its scintillator bar.

Producing the modules was a combined effort process and was done in four different steps. the first step included the fabrication and polishing of the light guides. Polishing the light guides with highest quality was crucial to guarantee the highest performance from a module. A smooth and scratch-free surface eliminated any light dispersion effect that could seriously compromise the performance of the modules. Next, the dimensions of scintillator bars were measured individually. This was done to ensure dimension measurement consistency between all the modules. Each scintillator bar was examined for scratches and deformities, then covered with plastic wrap and prepared for the next step. The next step included attaching the polished light guides to the scintillator bars using EJ500 optical cement (Figure B.4). Finished modules were then wrapped with a layer of 3M's Enhanced Specular Reflector (ESR) film, which serves as a reflector of the photons produced by particles that transverse the module, so that these photons could reach the PMT at the end of the module. Wrapped modules were then inspected for the quality of the ESR wrapping before photomultiplier tubes were attached to their ends. A Silicon RTV mixture was used to mount PMT's on the ends of the modules (Figure B.5). After several hours of curing, the glued PMT/lightguide joints were cheked for quality. Joints that exhibited any form of irregularity were redone. Finally, finished modules were wrapped with a

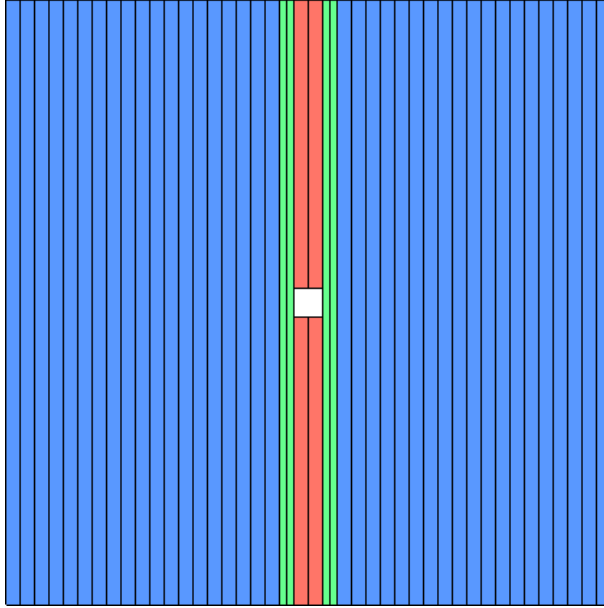


Figure B.3: Schematic of a layer of the Time of Flight detector. Blue colored bars represent the full width - full length modules. The green colored bars represent the half width modules, and the red colored bars represent the half length modules. The white box in the middle represents the beam hole.

layer of Tedlar PVF film. The Tedlar layer is added to eliminate any contamination from visible light.

The position of a module in an individual layer depended on its efficiency and performance. Modules with highest efficiency, essentially those that had high gain PMT's attached to them, were placed in the middle of the layer and closer to the beam beam hole. One with lowest efficiencies where thus placed on the edges. The Assembly of the TOF detector took place in hall D at Jefferson Lab, and was completed in 4 months. Several modifications to the original design had to be done, but we will not cover them here. The finished detector was lifted to its place in front of the forward drift chamber shortly after all the modules were put in their corresponding positions. Finally, with the detector in place, it was ready to be cabled and connected to its DAQ system. Two cables were driven from each PMT to the platform behind the FDC where the DAQ system was housed. The signal cable from the PMT was connected to a splitter that would send the signal to an FDC crate and a TDC crate simultaneously, while the high voltage cable was connected to a channel in the HV crate. The detector was then turned on and was given a first assessment of performance to check for any light leaks or



Figure B.4: An illustration of the different steps of polishing that the light guides had to go through. Several sand papers were used in the process, leading to the shades variation observed above.



Figure B.5: The method used to attach PMT to light guides is illustrated in this photo. After the Silicon RTV was applied, the PMT/Light guide joint was held together using the device shown in this photo. Constant pressure had to be applied to the joint to ensure best results.

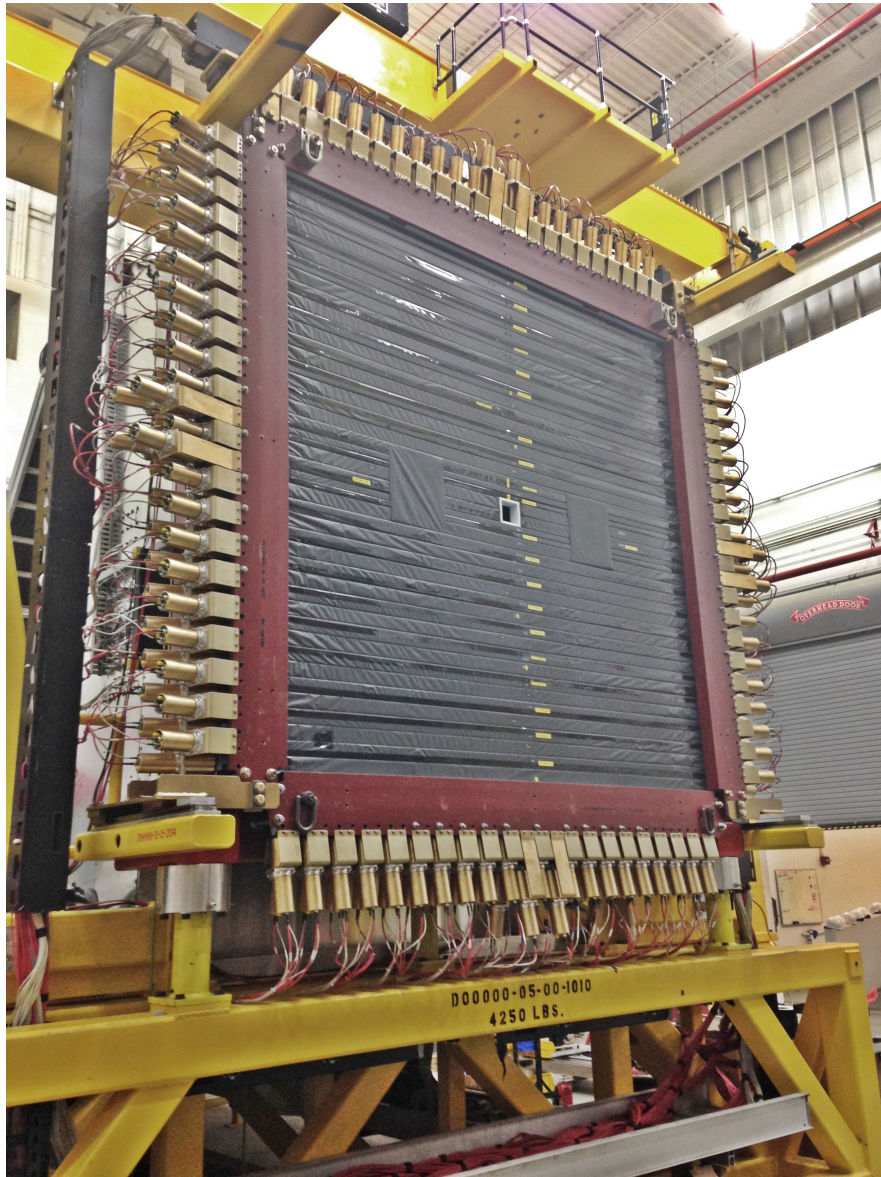


Figure B.6: The completed time of flight proudly fashioned in garnet and gold (FSU's official colors), as it gloriously resides in its final position.

cabling ambiguities. Several cabling ambiguities and light leaks were found and then corrected for accordingly. The Time of Flight detector currently operates with a 95 ps resolution and has been operating without any problems. The final form and position of the detector can be seen in Figure B.6.

## APPENDIX C

### DETACHED VERTEX SIMULATION

When generating Monte Carlo for our partial wave analysis, we needed to ensure that we were accurately simulating the detector's response to this channel. To do so, we had to account for the detached vertex of the  $\Lambda$  baryon. Since the  $\Lambda$  decays to a  $p\pi$  pair via weak interaction, it would travel for a considerable distance before it decays. As a result, the proton and the pion would originate from a vertex that is detached from the original event vertex. Genr8 does not account for vertex information and all vertex information is provided by gamp2part. Gamp2part inserts random vertex information to the generated Monte Carlo but in a common vertex fashion. A detached vertex was inserted into its code following the prescription detailed below.

To simulate the detachment of the vertex of  $\Lambda$ , random numbers were generated with an exponential probability distribution of the  $\Lambda$  lifetime in its rest frame. The probability distribution is

$$F(t) = F_{rest}(t) = \alpha e^{-\alpha t} \quad (\text{C.1})$$

where  $\alpha$  is the decay constant and is related to the mean lifetime  $\tau$  by

$$\tau = \frac{1}{\alpha} \quad (\text{C.2})$$

we can then generate a random variable  $x$  between 0 and 1 and relate it to the probability distribution by

$$x = \int_0^t f(z) dz \quad (\text{C.3})$$

The relation above relates the source random variable and the known target random variable. If we plug Equation C.1 into the equation above, we get

$$x = \int_0^t \alpha e^{-\alpha z} dz \quad (\text{C.4})$$

or,

$$x = \alpha \left( \frac{-1}{\alpha} \exp^{-\alpha t} + \frac{1}{\alpha} \right) = 1 - e^{-\alpha t} \quad (\text{C.5})$$

Inverting the above equation,

$$t = \frac{\ln(1-x)}{-\alpha} \quad (\text{C.6})$$

Then substituting  $\alpha$  using Equation C.2, yields

$$t = -\tau \ln(1-x) \quad (\text{C.7})$$

The random number  $t$  represents the  $\Lambda$  lifetime at rest. We can relate the lab and rest frame using the Lorentz factor  $\gamma$  such that

$$t = t_{rest} = \frac{t_{lab}}{\gamma} \quad (\text{C.8})$$

where  $\gamma$  is

$$\gamma = \frac{1}{\sqrt{1-v^2/c^2}} = \frac{1}{\sqrt{1-\beta^2}} \quad (\text{C.9})$$

where  $v$  is the relative velocity between inertial reference frames and can be measured using the momentum of  $\Lambda$ ,  $c$  is the speed of light, and  $\beta$  is

$$\beta = \frac{v}{c} = \frac{p}{\sqrt{p^2 + m^2 c^2}} \quad (\text{C.10})$$

We can rewrite  $t_{lab}$  in natural units as

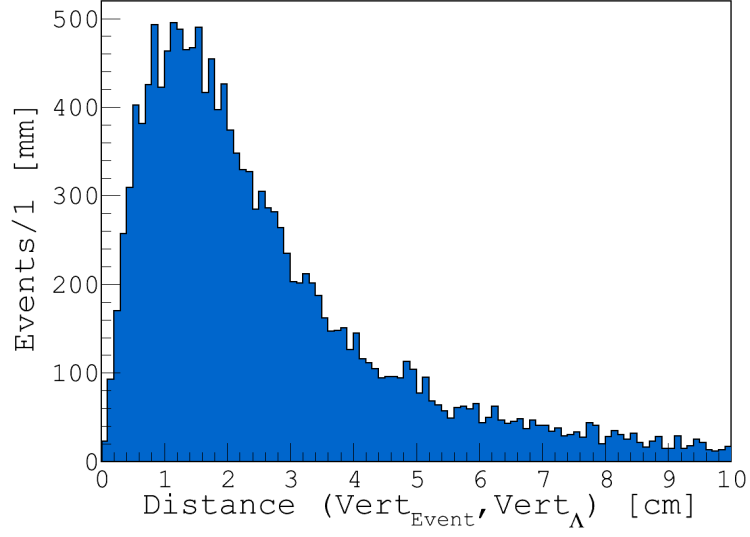
$$t_{lab} = \frac{t_{rest}}{\sqrt{1 - \frac{p^2}{p^2 + m^2}}} \quad (\text{C.11})$$

Finally, the distance that  $\Lambda$  flies between its creation and decay is given by,

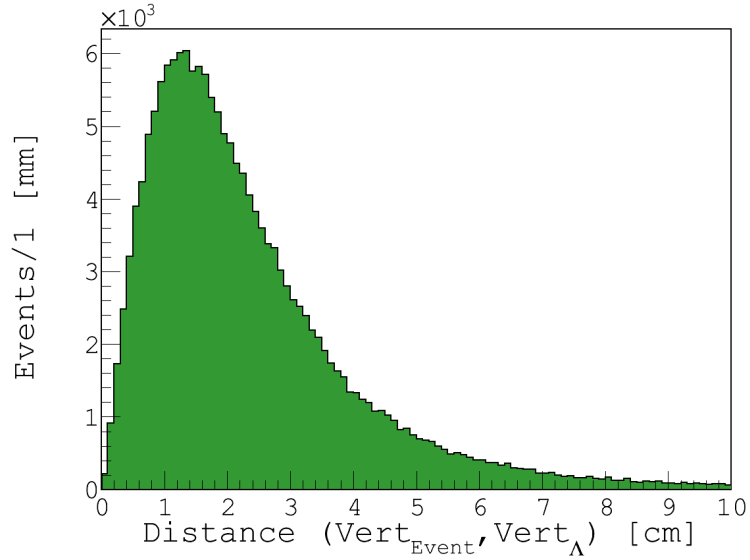
$$D = c\beta t_{lab} = \frac{c\gamma p t_{rest}}{E} \quad (\text{C.12})$$

Figure C.1 shows the distance distribution for the data and the accepted simulated Monte Carlo. The  $\Lambda$  distance is determined by using the vertex of the proton and the vertex of the event as provided by the TBTR bank. The distance is then determined using

$$D = \sqrt{(x_p - x_{event})^2 + (y_p - y_{event})^2 + (z_p - z_{event})^2} \quad (\text{C.13})$$



(a) The Distance between  $\Lambda$  and event vertex for Data.



(b) The Distance between  $\Lambda$  and event vertex for MC.

Figure C.1: Distributions of the distance between the  $\Lambda$  vertex and the event vertex for the Data sample (a) and the accepted Monte Carlo sample (b).

# APPENDIX D

## THE K-MATRIX FORMALISM

The Breit-Wigner parameterization is valid for a single isolated resonance decaying into one channel above threshold, however in the real world, resonances can overlap within one channel, can decay into more than one channel, and can be in the vicinity of thresholds of each other. As a result, the unitarity of the scattering S-matrix is violated. And while this violation is marginal in the case of narrow isolated and distant resonances, it becomes more severe when the resonances become broader and overlap. As a result, a new formalism was proposed a long time ago to study overlapping and multiple-channel resonances, it is formally referred to as the K-Matrix formalism. The K-matrix formalism provides a framework through which the unitarity of the S-matrix of two body processes can be imposed, something that can not be achieved by the simple sum of two Breit-Wigners. Additionally, this formalism can be extended beyond scattering problems to cover cases of resonance production in complex reactions via the P-vector approach. More information about the K-Matrix and P-vectors formalism can be found in reference [65].

Consider a two-body scattering of the form  $ab \rightarrow cd$ . Then the differential cross section can be written in terms of the invariant amplitude  $\mathcal{M}$  or more precisely, the scattering amplitude  $f$  as follows

$$\frac{d\sigma_{fi}}{d\Omega} = \frac{1}{(8\pi)^2 m^2} \left(\frac{q_f}{q_i}\right) |\mathcal{M}_{fi}|^2 = |f_{fi}(\Omega)|^2 \quad (\text{D.1})$$

where  $i$  and  $f$  represent the initial and final states,  $\Omega$  denotes the spherical coordinates and  $m$  is the center of mass energy. The  $q$ 's are the initial and final breakup momenta. The scattering amplitude can be expanded to

$$f_{fi}(\Omega) = \frac{1}{q_i} \sum_j (2J+1) T_{fi}^J(s) D_{\lambda\mu}^{J*}(\phi, \theta, 0) \quad (\text{D.2})$$

where  $\lambda = \lambda_a - \lambda_b$  and  $\mu = \lambda_c - \lambda_d$  are represented in terms of the helicities of the particles. Integrating the differential cross section in Equation D.1, the total cross section in the partial

wave J becomes

$$\sigma_{fi}^J = \left(\frac{4\pi}{q_i^2}\right) (2J+1) |T_{fi}^J(s)|^2 \quad (\text{D.3})$$

The initial and final states can be written as

$$\begin{aligned} |i\rangle &= |ab, JM\lambda_a\lambda_b\rangle \\ |f\rangle &= |cd, JM\lambda_c\lambda_d\rangle \end{aligned} \quad (\text{D.4})$$

where M is the z-component of the total spin J in the overall CM frame. These states are normalized according to

$$\langle f|i\rangle = \delta_{ij} \quad (\text{D.5})$$

The amplitude that the initial state  $|i\rangle$  would end up in the final state  $|i\rangle$  is

$$S_{fi} = \langle f|S|i\rangle \quad (\text{D.6})$$

where S is called the scattering operator. We can then define the transition operator through

$$S = I + 2iT \quad (\text{D.7})$$

where I is the identity operator. Conservation of probability leads to the unitarity of the scattering operator

$$S S^\dagger = S^\dagger S = I \quad (\text{D.8})$$

Using the unitarity of S, one gets

$$T - T^\dagger = 2iT^\dagger T = 2iTT^\dagger \quad (\text{D.9})$$

As a result T becomes Hermitian. We can introduce a new operator called K of the form

$$K^{-1} = T^{-1} + iI \quad (\text{D.10})$$

K is therefore also Hermitian i.e.  $K = K^\dagger$ . Due to time reversal invariance, K is real and symmetric. We can rewrite T in terms of K as

$$T = (I - iK)^{-1}K \quad (\text{D.11})$$

The K-matrix elements are representations of resonances  $\alpha$  (poles) in decay channels i and j, and can be written as

$$K_{ij} = \sum_{\alpha} \frac{g_{\alpha i}(m)g_{\alpha j}(m)}{m_{\alpha}^2 - m^2} \quad (\text{D.12})$$

where

$$g_{\alpha i}(m) = \gamma_{\alpha i} \sqrt{m_{\alpha} \Gamma_{\alpha}^0} B_{l_{\alpha i}}(q_i, q_{\alpha i}) \sqrt{\rho_i} \quad (\text{D.13})$$

$m_{\alpha}$  is the mass of the pole and  $\Gamma_{\alpha}$  is its decay width. It should be noted that these do not necessarily correspond to the properties of the resonances. The physical properties of the real resonances can be obtained from the poles of the T-matrix. In the case of two overlapping resonances, the K-matrix becomes

$$K = \frac{m_A \Gamma_A(m)}{m_A^2 - m^2} + \frac{m_B \Gamma_B(m)}{m_B^2 - m^2} \quad (\text{D.14})$$

where the relative decay amplitude  $\Gamma_{\alpha}(m)$  is

$$\Gamma_{\alpha}(m) = \Gamma_{\alpha 0} \left( \frac{m_{\alpha}}{m} \right) \left( \frac{q}{q_{\alpha}} \right) B_{\alpha}(q, q_{\alpha})^2 \quad (\text{D.15})$$

As we mentioned earlier, the K-matrix formalism can be extended beyond the formation of resonances (s-channel resonances) to cover the case of production of resonances by introducing the P-vectors. According to reference [61], the P-vectors can be written as

$$P = \sum_{\alpha} \frac{\beta_{\alpha} m_{\alpha} \Gamma_{\alpha}^0 B_{\alpha}^l}{m_{\alpha}^2 - m^2} \quad (\text{D.16})$$

where  $\beta_{\alpha}$  are complex numbers that account for the phase between the poles and carry the production information of a resonance  $\alpha$ . Moreover, the production amplitude P can be transformed into the resulting invariant amplitude F using

$$F = (I - iK)^{-1} P \quad (\text{D.17})$$

or more precisely,

$$F = \frac{\sum_{\alpha} \frac{\beta_{\alpha} m_{\alpha} \Gamma_{\alpha}^0 B_{\alpha}^l}{m_{\alpha}^2 - m^2}}{1 - i \sum_{\alpha} \frac{m_{\alpha} \Gamma_{\alpha}^0}{m_{\alpha}^2 - m^2} \frac{\rho}{\rho_{\alpha}} \left| \frac{F_l(q)}{F_l(q_{\alpha})} \right|^2} \quad (\text{D.18})$$

Recall that a relativistic Breit-Wigner amplitude is defined as,

$$BW_{\alpha} = \beta_{\alpha} \frac{m_{\alpha} \Gamma_{\alpha}^0}{m_{\alpha}^2 - m^2 - im_{\alpha} \Gamma_{\alpha}(m)} B_{\alpha}^l \quad (\text{D.19})$$

We can now rearrange the F amplitude and rewrite it in terms of the relativistic Breit-Wigner amplitude as

$$F = \sum_{\alpha} \frac{BW_{\alpha}}{1 - z_{\alpha}} \quad (\text{D.20})$$

where  $z_{\alpha}$  is defined as

$$z_{\alpha}(m) = i \frac{m_{\alpha}^2 - m^2}{m_{\alpha}^2 - m^2 - im_{\alpha}\Gamma_{\alpha}(m)} \left( \sum_{\beta \neq \alpha} K_{\beta} \right) \quad (\text{D.21})$$

Again in order to find the mass and width of the actual resonances, we have to find the T poles. This could be achieved by solving for m in the following equation

$$\prod_{\alpha} (1 - z_{\alpha}(m)) = 0 \quad (\text{D.22})$$

Solving  $z_{\alpha}(m) = 1$  yields a complex solution of the form  $m = mass - i\frac{\Gamma}{2}$ . Generally speaking, the mass and width obtained from the T-poles are expected to be rather close to the ones obtained from the F-poles. This prediction was illustrated in our partial wave analysis results for the  $1^+S\rho K$  wave, where two resonances in close proximity were fitted with an F amplitude to determine their masses and widths.

# APPENDIX E

## WIGNER-D FUNCTIONS

The Wigner-D function gives the matrix elements of the rotation operator  $\mathcal{R}$  in the  $jm$ -representation. Given a set of Euler angles  $(\alpha, \beta, \gamma)$ , a rotation of a state of total spin  $J$ , referred to as  $|jm\rangle$ , can be expressed in a complete space basis as

$$\mathcal{R} = \sum_{m'} D_{m'm}^J(\alpha, \beta, \gamma) |Jm'\rangle \quad (\text{E.1})$$

the Wigner-D functions are defined as the coefficients in this expansion. Therefore we can also express

$$\mathcal{R} = e^{-i\alpha J_x} e^{-i\beta J_y} e^{-i\gamma J_z} \quad (\text{E.2})$$

and

$$D_{m'm}^J(\alpha, \beta, \gamma) = \langle Jm' | e^{-i\alpha J_x} e^{-i\beta J_y} e^{-i\gamma J_z} |Jm\rangle \quad (\text{E.3})$$

or

$$D_{m'm}^J(\alpha, \beta, \gamma) = e^{-im'\alpha} \langle Jm' | e^{-i\beta J_y} |Jm\rangle e^{-im\gamma} \quad (\text{E.4})$$

The angles  $\alpha$  and  $\beta$  can be thought of as the polar angles  $\phi$  and  $\theta$  respectively. We choose  $\gamma = 0$  thus adopting the convention in Reference [70], and define the Wigner-d functions as

$$d_{m'm}^J(\beta) = \langle Jm' | e^{-i\beta J_y} |Jm\rangle \quad (\text{E.5})$$

then the Wigner-D functions can be written as

$$D_{m'm}^J(\alpha, \beta, \gamma) = e^{-im'\alpha} d_{m'm}^J(\beta) e^{-im\gamma} \quad (\text{E.6})$$

The  $d_{m'm}^J(\beta)$  functions were calculated by Wigner and they have the following form

$$\begin{aligned}
d_{m'm}^J(\beta) &= C \sum_S \frac{(-1)^S}{(J-m'-S)!(J+m-S)!(S+m'-m)!S!} \\
&\times \left[ \cos\left(\frac{\beta}{2}\right) \right]^{2J+m-m'-2S} \times \left[ -\sin\left(\frac{\beta}{2}\right) \right]^{m'-m+2S}
\end{aligned} \tag{E.7}$$

where  $C = [(J+m)!(J-m)!(J+m')!(J-m')!]^{\frac{1}{2}}$ . The sum is over the values of the integer  $S$  for which the factorials  $\geq 0$ . The Wigner-D functions can be normalized such that

$$\int d\Omega D_{m'_1 m_1}^{J_1 \star} D_{m'_2 m_2}^{J_2} = \frac{8\pi^2}{2J_1 + 1} \delta_{J_1 J_2} \delta_{m'_1 m'_2} \delta_{m_1 m_2} \tag{E.8}$$

The following properties can be assigned to these functions [62]

- $D_{m'm}^{J\star}(\alpha, \beta, \gamma) = (-1)^{m'-m} D_{-m'-m}^J(\alpha, \beta, \gamma)$
- $D_{m'_1 m_1}^{J_1} D_{m'_2 m_2}^{J_2} = \sum_{J_3, m'_3, m_3} (J_1 m'_1 J_2 m'_2 | J_3 m'_3) (J_1 m_1 J_2 m_2 | J_3 m_3) D_{m'_3 m_3}^{J_3}$

The factors in parentheses are the Clebsch-Gordan coefficients (Appendix D). The normalization relation is

$$\int d\Omega D_{m'_1 m_1}^{J_1 \star} D_{m'_2 m_2}^{J_2} D_{m'_3 m_3}^{J_3 \star} = \frac{8\pi^2}{2J_3 + 1} (J_1 m'_1 J_2 m'_2 | J_3 m'_3) (J_1 m_1 J_2 m_2 | J_3 m_3) \tag{E.9}$$

# APPENDIX F

## CLEBSCH-GORDAN COEFFICIENTS

Suppose we have two angular momentum states  $|J_1 m_1\rangle$  and  $|J_2 m_2\rangle$ . We want to add these two states to form a state of angular momentum  $|J m\rangle$ , such that  $J = J_1 \oplus J_2$ . These states are related by a linear relation given by,

$$|J m\rangle = \sum_{m_1 m_2} (J_1 m_1 J_2 m_2 | J m) |J_1 m_1\rangle |J_2 m_2\rangle \quad (\text{F.1})$$

where the coefficients  $(J_1 m_1 J_2 m_2 | J m)$  are the Clebsch-Gordan coefficients, and  $m = m_1 + m_2$ . An expression of these coefficients was derived by Wigner [62]

$$\begin{aligned} (J_1 m_1 J_2 m_2 | J m) &= \delta_{m, m_1 + m_2} \\ &\times \left[ (2J + 1) \frac{(J + J_1 - J_2)! (J - J_1 + J_2)! (J_1 + J_2 - J)! (J + m)! (J - m)!}{(J + J_1 + J_2 + 1)! (J_1 - m_1)! (J_1 + m_1)! (J_2 - m_2)! (J_2 + m_2)!} \right]^{\frac{1}{2}} \\ &\times \sum_S \frac{(-1)^{S+J+m}}{S!} \frac{(J + m_1 + J_2 - S) (J_1 - m_1 + S)!}{J - (J_1 + J_2 - S)! (J + m - S)! (S + J_1 - J_2 - m)!} \end{aligned} \quad (\text{F.2})$$

Then using the orthogonality relations, we can write the reciprocal relations

$$|J_1 m_1\rangle |J_2 m_2\rangle = \sum_J (J_1 m_1 J_2 m_2 | J m) |J m\rangle \quad (\text{F.3})$$

Some important symmetry properties can be extracted from these formulas,

- $(J_1 m_1 J_2 m_2 | J m) = (-1)^{J_1 + J_2 - J} (J_1 - m_1 J_2 - m_2 | J - m)$
- $(J_1 m_1 J_2 m_2 | J m) = (-1)^{J_1 + J_2 - J} (J_2 m_2 J_1 m_1 | J m)$
- $(J_1 m_1 J_2 m_2 | J m) = (-1)^{J_1 - m_1} \left[ \frac{2J+1}{2J_2+1} \right]^{\frac{1}{2}} (J_1 m_1 J - m | J_2 - m_2)$

Note: A square-root sign is to be understood over *every* coefficient, e.g., for  $-8/15$  read  $-\sqrt{8/15}$ . Notation:  $\begin{matrix} J & J & \dots \\ M & M & \dots \end{matrix}$

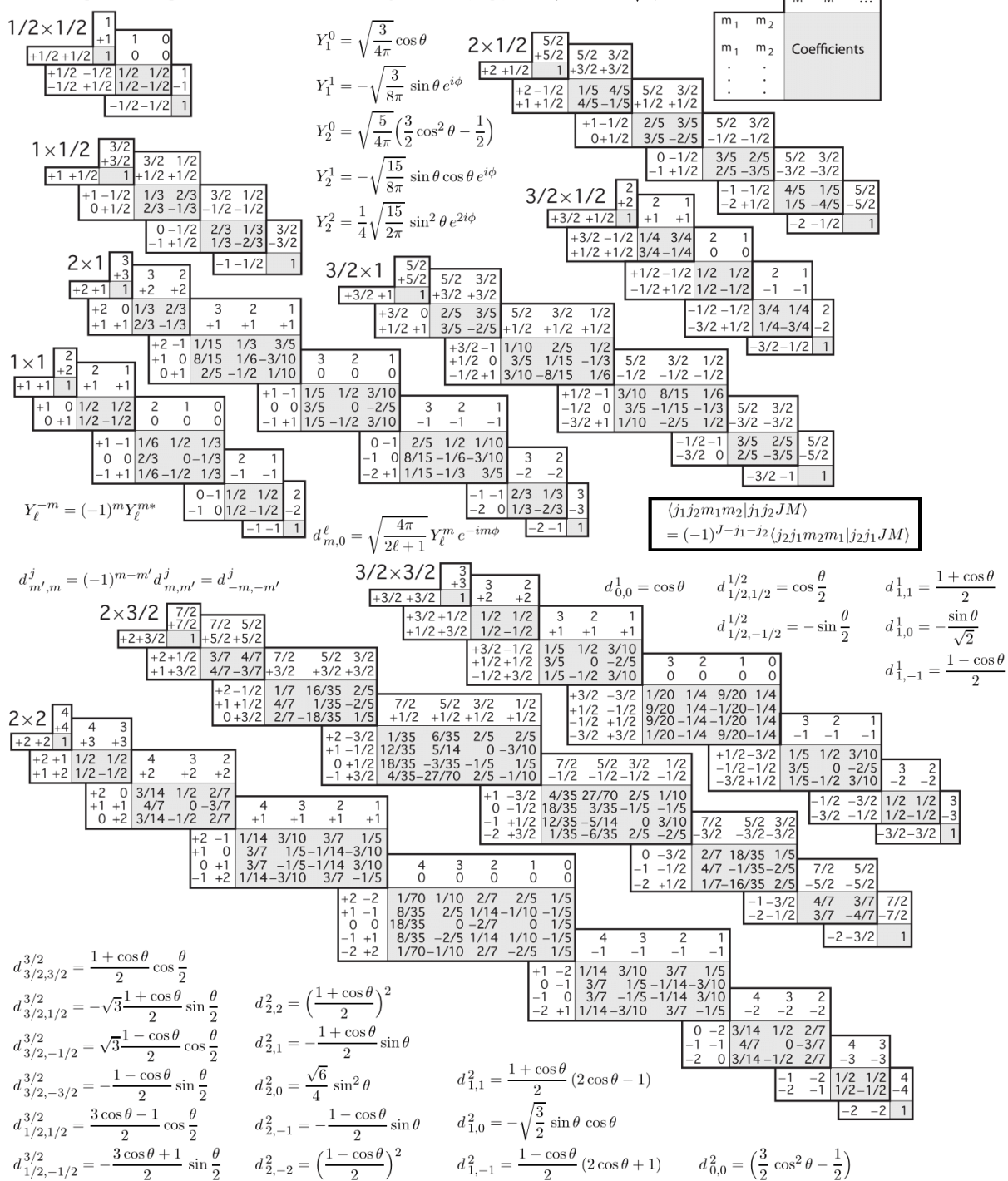


Figure F.1: The Clebsch-Gordan coefficients table with the Wigner-d functions and the spherical harmonics  $Y_l^m$ . Image source [16].

## REFERENCES

- [1] Lüscher, Martin. "Lattice QCD from quark confinement to asymptotic freedom." *Annales Henri Poincaré*. Vol. 4. No. 1. Birkhäuser-Verlag, 2003.
- [2] D. J. Gross, F. Wilczek, *Phys. Rev. Lett.* 30 (1973) 1343
- [3] H. D. Politzer, *Phys. Rev. Lett.* 30 (1973) 1346
- [4] S. Weinberg: *Physica* 96 A, 327 (1979)
- [5] J. Gasser and H. Leutwyler: *Nucl. Phys. B* 250, 465 (1985)
- [6] S. Scherer. Introduction to chiral perturbation theory. *Adv. Nucl. Phys.*, 27:277, 2003.
- [7] Hideki Yukawa. On the interaction of elementary particles. *Proc. Phys. Math. Soc. Jap.*, 17:4857, 1935.
- [8] M. Gell-Mann. A schematic model of baryons and mesons. *Phys. Lett.*, 8(3):214215, (1964).
- [9] G. Zweig. CERN preprint 8419/Th412, 8182/Th401.
- [10] B.B. Brandt et al. Form factors in lattice QCD. arXiv:heplat/1106.1554v1, 2011.
- [11] C. M. G. Lattes, G. P. S. Occhialini, and C. F. Powell. OBSERVATIONS ON THE TRACKS OF SLOW MESONS IN PHOTOGRAPHIC EMULSIONS. 2. *Nature*, 160:486492, 1947.
- [12] Jasinski, P. Analysis of diffractive dissociation of  $K^-$  into  $K^+\pi^-\pi^-$  on a liquid hydrogen target at the COMPASS spectrometer. Diss. Mainz U., 2012.
- [13] E. Rutherford. The scattering of  $\alpha$  and  $\beta$  particles by matter and the structure of the atom. *Phil. Mag.*, 21:669688, 1911.
- [14] J. Chadwick. POSSIBLE EXISTENCE OF A NEUTRON. *Nature*, 129:312, 1932.
- [15] C. M. G. Lattes, G. P. S. Occhialini, and C. F. Powell. OBSERVATIONS ON THE TRACKS OF SLOW MESONS IN PHOTOGRAPHIC EMULSIONS. 1. *Nature*, 160:453456, 1947.
- [16] K. A. Olive *et al.* [Particle Data Group Collaboration], *Chin. Phys. C* **38**, 090001 (2014). doi:10.1088/1674-1137/38/9/090001
- [17] Y. C. Chao et al., *Journal of Physics: Conference Series*, 299 (2011).
- [18] Christoph W. Leemann et al., *Annu. Rev. Nucl. Part. Sci.*, 2001 51,413-50 (2001).

- [19] B. A. Mecking et al., [CLAS Collaboration], NIM A 503 3, 513 (2003).
- [20] G. W. Brandenburg *et al.*, Phys. Rev. Lett. **36**, 703 (1976). doi:10.1103/PhysRevLett.36.703
- [21] S. Stepanyan et al., [CLAS Collaboration] NIM A 572, 654 (2007).
- [22] D. I. Sober et al., [CLAS Collaboration] NIM A 440, 263 (2001).
- [23] G. D. Rochester and C. C. Butler. EVIDENCE FOR THE EXISTENCE OF NEW UNSTABLE ELEMENTARY PARTICLES. Nature, 160:855857, 1947.
- [24] E.S. Smith et al., [CLAS Collaboration] NIM A 432, 265 (1999).
- [25] Frame, D., et al. "A spin-parity analysis of the  $\phi K^+$  system produced in the reaction  $K + p \rightarrow \phi K + p, \phi \rightarrow K + K$  at 13 GeV/c." Nuclear Physics B 276.3 (1986): 667-705.
- [26] G. Otter *et al.* [Aachen-Berlin-CERN-London-Vienna Collaboration], Nucl. Phys. B **147**, 1 (1979).
- [27] Y. G. Sharabian et al., [CLAS Collaboration] NIM A 556, 246 (2006).
- [28] M. D. Mesteyar et al., [CLAS Collaboration] NIM A 449, 81 (2000).
- [29] C. Fernandez *et al.* [CERN-College de France-Madrid-Stockholm Collaboration], Z. Phys. C **16**, 95 (1982). doi:10.1007/BF01572258
- [30] C. Daum *et al.* [ACCMOR Collaboration], Nucl. Phys. B **187**, 1 (1981).
- [31] D. Aston *et al.*, Phys. Lett. B **149**, 258 (1984). doi:10.1016/0370-2693(84)91595-8
- [32] D. Aston *et al.*, Nucl. Phys. B **292**, 693 (1987).
- [33] Y. M. Antipov *et al.* [CERN-Serpukhov Boson Spectrometer Group Collaboration], Nucl. Phys. B **86**, 381 (1975).
- [34] ATLAS Collaboration. Observation of a new particle in the search for the Standard Model Higgs boson with the ATLAS detector at the LHC, Physics Letters B, Volume 716, Issue 1, 17 September 2012, Pages 1-29, ISSN 0370-2693, <http://dx.doi.org/10.1016/j.physletb.2012.08.020>.
- [35] B. Mecking et al. The CEBAF large acceptance spectrometer (CLAS). Nucl. Instrum. Methods A 503, 513, 2003.
- [36] Jefferson Laboratory. The JLab Picture Exchange. <http://www1.jlab.org/ul/jpix>.
- [37] Jefferson Laboratory. <http://www1.jlab.org/>.

- [38] C. W. Leemann, D. R. Douglas, and G. A. Kraft. The Continuous Electron Beam Accelerator Facility: CEBAF at the Jefferson Laboratory. *Ann. Rev. Nucl. Part. Sci.*, 51:413450, 2001.
- [39] D.I. Sober et al. The bremsstrahlung tagged photon beam in Hall B at JLab. *Nucl. Inst. Meth. A* 440, 263 (2000).
- [40] D. I. Sober et al. The bremsstrahlung tagged photon beam in Hall B at JLab. *Nucl. Instrum. Meth.*, A440:263284, 2000.
- [41] S. Christo. The g11a Target Cell, [http://www.jlab.org/christo/g11a\\_target.html](http://www.jlab.org/christo/g11a_target.html).
- [42] J. T. Goetz. Hyperon Photoproduction from Threshold to 5.4 GeV with the CEBAF Large Acceptance Spectrometer. PhD thesis, University of California Los Angeles, 2010.
- [43] C. Bookwalter. A Search for Exotic Mesons in  $\gamma p \rightarrow \pi^+ \pi^+ \pi^- n$  with CLAS at Jefferson Lab. PhD thesis, Florida State University, 2012.
- [44] Y. G. Sharabian et al. A new highly segmented start counter for the CLAS detector. *Nucl. Instrum. Meth.*, A556:246258, 2006.
- [45] G. Adams et al. The CLAS Cherenkov detector. *Nucl. Instrum. Meth.*, A465:414427, 2001.
- [46] M. Amarian et al. The CLAS forward electromagnetic calorimeter. *Nucl. Instrum. Meth.*, A460:239265, 2001.
- [47] P. Eugenio, C. Salgado, D. Weygand [CLAS Collaboration], Proposal for g12, E-04-005,(2003).
- [48] E. Pasyuk, CLAS NOTE 2007-016 (2007).
- [49] E. Pasyuk. Energy loss corrections for charged particles in clas. CLAS-NOTE, (2007-016), (2007).
- [50] J. Goetz, CLAS g12 analysis note, CLAS NOTE, November, (2012).
- [51] R. Mattuck. A Guide to Feynman Diagrams in the Many-Body Problem. Courier Dover Publications, (1976).
- [52] H. Bichsel. Passage of particles through matter, (2006).
- [53] D. Keller, CLAS NOTE 2010-015 (2010).
- [54] F. James and M. Roos. Minuit: A System for Function Minimization and Analysis of the Parameter Errors and Correlations. *Comput. Phys. Commun.*, 10:343-367, 1975.
- [55] Pilat, F. "The 12 GeV Energy Upgrade at Jefferson Laboratory." *Energy* (1910): 2.

- [56] F. Barbosa, C. Hutton, A. Sitnikov, A. Somov, S. Somov, and I. Tolstukhin, Nucl. Instrum. Methods A795, 376380 (2015).
- [57] F. Barbosa, J. McKisson, J. McKisson, Y. Qiang, E. Smith, and C. Zorn, Nucl. Instrum. Methods A695, 100104 (2012).
- [58] O. Soto, R. Rojas, S. Kuleshov, H. Hakobyan, A. Toro, and W. Brooks, Nucl. Instrum. Methods A732, 431436 (2013).
- [59] Y. Van Haarlem, C. A. Meyer, F. Barbosa, B. Dey, D. Lawrence, V. Razmyslovich, E. S. Smith, G. Visser, T. Whitlatch, G. Wilkin, and B. Zihlmann, Nucl. Instrum. Methods A622, p. 142 (2010).
- [60] Frank von Hippel and C. Quigg. Centrifugal-barrier effects in resonance partial decay widths, shapes, and production amplitudes. Phys. Rev. D, 5:624638, Feb 1972.
- [61] Aitchison, I. J. R. "The K-matrix formalism for overlapping resonances." Nuclear Physics A 189.2 (1972): 417-423.
- [62] M.E. Rose, Elementary Theory of Angular Momentum, Dover Pub., 1995.
- [63] John P. Cummings and Dennis P. Weygand. An object-oriented approach to partial wave analysis. eprint only, 2003.
- [64] V. V. Berdnikov, S. V. Somov, L. Pentchev, and B. Zihlmann, Instrum. Exp. Tech. 58, p. 25 (2015).
- [65] Chung, S. U., et al. "Partial wave analysis in K-matrix formalism." Annalen der Physik 507.5 (1995): 404-430.
- [66] K. Moriya et al., Nucl. Instrum. Methods A726, 6066 (2013).
- [67] D. Herndon, P. Soding, and R. J. Cashmore. A GENERALIZED ISOBAR MODEL FORMALISM. Phys. Rev., D11:3165, 1975.
- [68] J. T. Goetz.  $\Xi$  Hyperon Photoproduction from Threshold to 5.4 GeV with the CEBAF Large Acceptance Spectrometer. PhD thesis, University of California Los Angeles, 2010.
- [69] S. U. Chung. Formulas for Partial-Wave Analysis, Version II. Unpublished BNL preprint BNL-QGS-93-05, September 1999.
- [70] Chung, Suh Urk. Spin formalisms. No. BNL-QGS-02-0900. Brookhaven Nat. Lab., 2008.

## BIOGRAPHICAL SKETCH

The Author was born in Beirut, Lebanon, and graduated from Jamil Rawwas High school in Beirut. He earned his undergraduate degree in applied physics from the Lebanese University in Hadath, Lebanon, before coming to Florida State University to pursue a PhD in experimental hadronic physics.